



US Army Corps
of Engineers
Waterways Experiment
Station

Technical Report SL-98-1
March 1998

Performance of Lightly Reinforced Concrete Intake Towers Under Selected Loadings

by Richard Charles Dove

19980305 088

DTIC QUALITY INSPECTED 4

Approved For Public Release; Distribution Is Unlimited

The contents of this report are not to be used for advertising, publication, or promotional purposes. Citation of trade names does not constitute an official endorsement or approval of the use of such commercial products.

The findings of this report are not to be construed as an official Department of the Army position, unless so designated by other authorized documents.



PRINTED ON RECYCLED PAPER

Technical Report SL-98-1
March 1998

Performance of Lightly Reinforced Concrete Intake Towers Under Selected Loadings

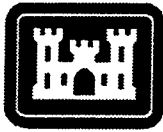
by Richard Charles Dove

U.S. Army Corps of Engineers
Waterways Experiment Station
3909 Halls Ferry Road
Vicksburg, MS 39180-6199

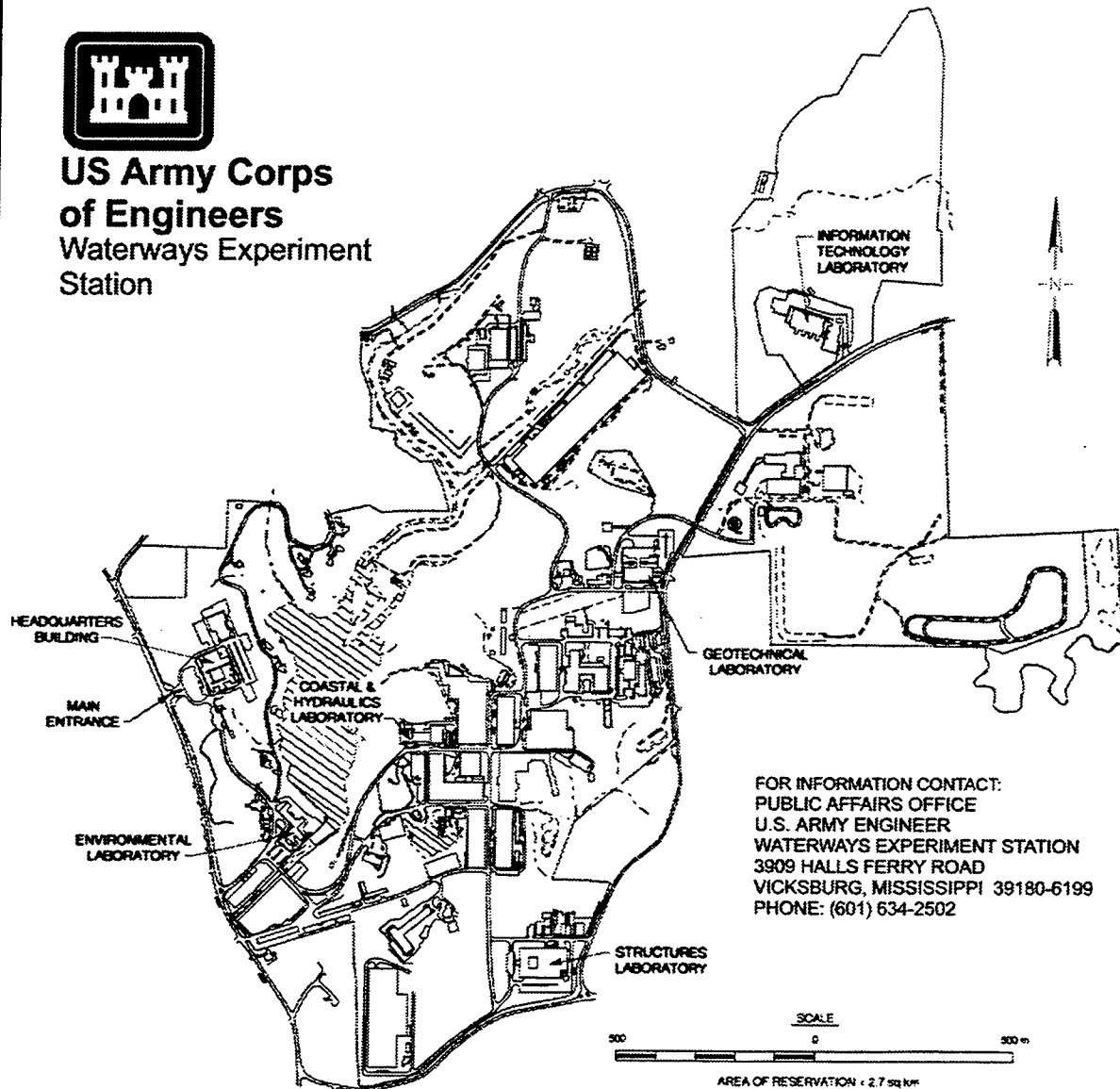
Final report

Approved for public release; distribution is unlimited

Prepared for U.S. Army Corps of Engineers
Washington, DC 20314-1000



**US Army Corps
of Engineers**
Waterways Experiment
Station



FOR INFORMATION CONTACT:
PUBLIC AFFAIRS OFFICE
U.S. ARMY ENGINEER
WATERWAYS EXPERIMENT STATION
3909 HALLS FERRY ROAD
VICKSBURG, MISSISSIPPI 39180-6199
PHONE: (601) 634-2502

Waterways Experiment Station Cataloging-in-Publication Data

Dove, Richard C.

Performance of lightly reinforced concrete intake towers under selected loadings / by Richard Charles Dove ; prepared for U.S. Army Corps of Engineers.

284 p. : ill. ; 28 cm. — (Technical report ; SL-98-1)

Includes bibliographical references.

1. Intakes (Hydraulic engineering) 2. Earthquakes and hydraulic structures. 3. Reinforced concrete. I. United States. Army. Corps of Engineers. II. U.S. Army Engineer Waterways Experiment Station. III. Structures Laboratory (U.S. Army Engineer Waterways Experiment Station) IV. Title. V. Series: Technical report (U.S. Army Engineer Waterways Experiment Station) ; SL-98-1.

TA7 W34 no.SL-98-1

Preface

The research reported herein was sponsored by Headquarters, U.S. Army Corps of Engineers, under Research Program 387 - Earthquake Engineering - Structures, Work Unit 32911, Nonlinear Dynamic Response and Failure Mechanisms of Intake Towers.

This research effort was conducted during the period October 1993 to December 1997. All work was carried out by Dr. Richard C. Dove, Structural Mechanics Division (SMD), Structures Laboratory (SL), U.S. Army Engineer Waterways Experiment Station (WES), under general supervision of Dr. Bryant Mather, Director, SL; Dr. Reed Mosher, Chief, SMD, SL, and Dr. Robert L. Hall, Chief, Research Analysis Group, SMD. This research was conducted and the report was written by Dr. Dove in partial fulfillment of the requirements for the degree of Doctor of Philosophy at Mississippi State University.

At the time of publication of this report, Director of WES was Dr. Robert W. Whalin. Commander was COL Robin R. Cababa, EN.

ACKNOWLEDGEMENTS

The author would like to acknowledge his sincere gratitude to the many people involved in the research contained herein and in the preparation of this dissertation. My committee chairman, Dr. Krishnan Balasubramaniam, is thanked for his assistance in guiding me through the dissertation process. The other members of the committee, Dr. R. Ralph Sinno, Dr. William Jones, Dr. Reed Freeman, and Dr. Stan Woodson, are all thanked for their invaluable aid and guidance. Thanks are also due to Dr. Jack Moehle, of the University of California, for his assistance with the displacement-based analysis technique. The research that formed the basis of this dissertation was sponsored by Headquarters, U.S. Army Corps of Engineers, and was conducted at the Structural Mechanics Division (SMD), Structures Laboratory (SL), U.S. Army Engineer Waterways Experiment Station (WES). Special thanks are extended to the supervisory and technical staff at WES, without whose support and assistance this research would not have been possible. Specific thanks are extended to Dr. Bryant Mather, Director, SL, Dr. Reed Mosher, Chief, SMD, SL, and Dr. Robert Hall, Chief, Research Analysis Group, SMD, SL, and Program Manager of the Earthquake Engineering Program.

TABLE OF CONTENTS

	Page
PREFACE	i
ACKNOWLEDGEMENTS	iii
LIST OF TABLES	vii
LIST OF FIGURES	viii
CHAPTER	
1 INTRODUCTION	1
Objective	2
Approach	3
2 ANALYSIS OF EXISTING INTAKE TOWER INVENTORY	7
Database Development	7
Summary Statistics	13
3 EXPERIMENTAL DESCRIPTION	21
Experiment Configuration	21
ITS-1 Instrumentation Configuration	29
ITS-2 and ITS-3 Instrumentation Configuration	35
Test Article Construction	38
ITS-1 and ITS-2 Material Properties	47
ITS-3 Material Properties	48
Experimental Procedure	49
4 ITS-1 EXPERIMENTAL RESULTS	51
Introduction	51
Structural Response	51
Active Instrumentation Response	55
Load Response	56

CHAPTER	Page
Deflection Response.....	59
Strain Response.....	62
Modal Response.....	75
5 ITS-2 EXPERIMENTAL RESULTS	87
Introduction.....	87
Structural Response.....	87
Active Instrumentation Response.....	98
Load Response	98
Deflection Response.....	103
Strain Response.....	107
Modal Response.....	108
6 ITS-3 EXPERIMENTAL RESULTS	116
Introduction.....	116
Structural Response.....	117
Active Instrumentation Response.....	122
Load Response	123
Deflection Response.....	125
Strain Response.....	128
Modal Response.....	130
7 EXPERIMENTAL ANALYSIS	138
ITS-1 Analysis	142
ITS-2 Analysis	148
ITS-3 Analysis	152
Modification of Deflection-Based Analysis.....	155
8 SUMMARY, CONCLUSIONS, AND RECOMMENDATIONS.....	167
Summary	167
Conclusions.....	168
Recommendations.....	169
REFERENCES	170

APPENDIX	Page
A INVENTORY ANALYSIS RESULTS	171
B MATERIAL PROPERTIES.....	182
C STRAIN CONTOURS.....	188
D MODE SHAPES	237
E DISPLACEMENT ANALYSIS PLOTS.....	243

LIST OF TABLES

TABLE	Page
1. Description of intake tower database parameters.....	12
2. ITS-2 yield and plastic hinge lengths.....	165
3. ITS-3 yield and plastic hinge lengths.....	165
4. ITS-2 strain penetration length determination.	169
5. ITS-3 strain penetration length determination.	169
B1. Tensile test results for reinforcement steel used in ITS-1 and ITS-2.....	187
B2. Concrete properties of ITS-1.....	188
B3. Concrete properties of ITS-2.....	189
B4. Tensile test results for reinforcement steel used in ITS-3.....	190
B5. Concrete properties of ITS-3.....	191

LIST OF FIGURES

FIGURE	Page
1. Lost Creek Intake Tower during construction.	2
2. Large-Scale Load Frame.	5
3. Typical rectangular intake tower.	9
4. Overall experimental layout.	23
5. ITS-1 vertical load hydraulic ram and roller assemblies.	23
6. ITS-2 and ITS-3 vertical load hydraulic ram and roller assemblies.	24
7. Model dimensions and configuration.	26
8. Tower section reinforcement layout.	27
9. Reinforcing bar details.	28
10. Location of strain gages mounted on exterior reinforcing layer, on west (compression) side of ITS-1 structure.	31
11. Location of strain gages mounted on exterior of wall, on west (compression) side of ITS-1 structure.	32
12. Location of strain gages mounted on exterior reinforcing layer, on north side of ITS-1 structure.	32
13. Location of strain gages mounted on exterior reinforcing layer, on east (tension) side of ITS-1 structure.	33
14. Location of strain gages mounted on inner reinforcing layer, on east (tension) side of ITS-1 structure.	33

FIGURE	Page
15. Plan view and elevation view of deflection gage locations on ITS-1 structure.....	34
16. Location of strain gages placed on the vertical reinforcing at the base of the ITS-2 and ITS-3 structure. Gage designations containing the letter "B" were located at the base, those with "A" at 2 in. above the base.....	36
17. Location of strain gages mounted on exterior reinforcing layer, on east and west sides of ITS-2 and ITS-3 structures.....	37
18. Plan view of deflection gage locations on ITS-2 and ITS-3 structures.	37
19. Side view of deflection gage locations on ITS-2 and ITS-3 structures.	38
20. Base slab reinforcement, ITS-2.....	39
21. View of model reinforcement, after base slab concrete placement, ITS-2.	40
22. Completed reinforcing cage for ITS-1.....	42
23. Completed reinforcing cage for ITS-2.....	43
24. Completed reinforcing cage for ITS-3.....	44
25. East side of complete ITS-2 structure.....	45
26. West side of complete ITS-2 structure.....	46
27. Lazon modal survey system.....	49
28. ITS-1, post-experiment view of north wall, imposed top deflection of 2 in.....	52
29. ITS-1, post-experiment view of east (tension) wall, imposed top deflection of 2 in.....	53
30. ITS-1, post-experiment view of south wall, imposed top deflection of 2 in.....	53
31. ITS-1, post-experiment view of west (compression) wall, imposed top deflection of 2 in.....	54
32. ITS-1, close-up view of interior south-east corner , imposed top deflection of 2 in.....	54

FIGURE	Page
33. ITS-1, close-up view of south-east corner, imposed top deflection of 2 in.	55
34. Horizontal load versus horizontal loader deflection.	56
35. Horizontal deflection at various elevations, plotted against imposed loader deflection.	59
36. Approximate structure deflected shape just prior to cracking.	61
37. Structure deflected shapes after cracking.....	61
38. Distribution of vertical strain in outermost reinforcing bars in the east (tension) wall up to initial yielding.	64
39. Distribution of vertical strain in outermost reinforcing bars in the north wall up to initial yielding.	64
40. Distribution of vertical strain in outermost reinforcing bars in the west (compression) wall at 2 in. elevation, up to final deflection.	65
41. Vertical strain measured on outside of west (compression) wall at 2 in. elevation. .	66
42. Vertical strain measured on outside of west (compression) wall at 12 in. elevation.	67
43. Vertical strain measured up side of structure, 3 in. from the center of east (tension) wall, including bottom gage.	69
44. Vertical strain measured up side of structure, 3 in. from the center of east (tension) wall without the bottom gage.	69
45. Vertical strain measured up side of structure, 21 in. from the center of east (tension) wall without the bottom gage.	70
46. Vertical strain measured up side of structure, 3 in. from the center of west (compression) wall, including bottom gage.	71
47. Vertical strain measured up side of structure, 21 in. from the center of west (compression) wall, including bottom gage.	71
48. Vertical strain distribution at base of structure for a horizontal loader deflection of 0.15 in.	73

49. Vertical strain distribution at base of structure for a horizontal loader deflection of 0.18 in.....	74
50. Frequency response function for undamaged ITS-1 structure.....	80
51. Bending mode for undamaged ITS-1 structure at 46 Hz.....	81
52. Ovaling mode for undamaged ITS-1 structure at 69 Hz.....	81
53. Torsional mode for undamaged ITS-1 structure at 121 Hz.....	82
54. Localized response associated with cold joint for undamaged ITS-1 structure at 200 Hz.....	82
55. Second bending mode for undamaged ITS-1 structure at 440 Hz.....	83
56. Frequency response function for damaged ITS-1 structure.....	83
57. Bending and rocking mode for damaged ITS-1 structure at 14 Hz.....	84
58. Bending and rocking mode for damaged ITS-1 structure at 20 Hz.....	84
59. Torsional mode for damaged ITS-1 structure at 34 Hz.....	85
60. Rocking about center of gravity for damaged ITS-1 structure at 81 Hz.....	85
61. Second bending mode for damaged ITS-1 structure at 429 Hz.....	86
62. Variation of first four modes of vibration during loading of ITS-1 structure.....	86
63. ITS-2 pre-experiment view of north wall.....	88
64. ITS-2 view of north wall, imposed top deflection of 2 in. towards the west.....	89
65. ITS-2 view of north wall, imposed top deflection of 2 in. towards the east.....	89
66. ITS-2 pre-experiment view of west wall.....	90

FIGURE	Page
67. ITS-2 view of west wall, imposed top deflection of 2 in. towards the west.	90
68. ITS-2 view of west wall, imposed top deflection of 2 in. towards the east.	91
69. ITS-2 pre-experiment view of south and east walls.....	91
70. ITS-2 view of south and east walls, imposed top deflection of 2 in. west.....	92
71. ITS-2 view of south and east walls, imposed top deflection of 2 in. east.....	92
72. ITS-2 pre-experiment close-up view of interior south-east corner.	93
73. ITS-2 close-up view of interior south-east corner, imposed top deflection of 2 in. towards the west.....	93
74. ITS-2 close-up view of interior south-east corner, imposed top deflection of 2 in. towards the east.....	94
75. Base of ITS-2 model with tower section removed.....	94
76. Close-up view of failure plane under east wall of ITS-2.	95
77. Close-up view of failure plane under north wall of ITS-2.....	95
78. Close-up view of failure plane under south wall of ITS-2.....	96
79. Close-up view of failure plane under west wall of ITS-2.	96
80. ITS-2, typical failed reinforcing bar.	97
81. Failure surface at bottom of ITS-2 tower section.	97
82. Horizontal load versus horizontal loader deflection.	100
83. ITS-2 energy dissipation per load cycle, as measured by area inside of load- deflection curve.	102
84. Observed ductility for ITS-1 and ITS-2 as related to the imposed deflection.	102
85. Observed ductility for ITS-2 as related to the measured top deflection.	103

FIGURE	Page
86. ITS-2 measured horizontal deflection at various elevations.....	105
87. ITS-2 measured horizontal deflection at various elevations, normalized by height on the structure.....	105
88. Deflected shape of ITS-2 at the top of the first eight excursions, as measured by the horizontal deflection gages.....	106
89. Correlation coefficients for linear and second-order curve fits to the deflected shape of ITS-2 at the top of the first eight excursions.....	106
90. ITS-2 frequency response function from pre-experiment survey.....	110
91. ITS-2 frequency response function from post-experiment survey.....	111
92. Change of first bending mode with increasing damage for ITS-2 model.....	114
93. Change of first torsional mode with increasing damage for ITS-2 model.....	114
94. Change of second bending mode with increasing damage for ITS-2 model.....	115
95. ITS-3 pre-experiment view of north and west walls.....	118
96. ITS-3 view of north and west walls, imposed top deflection of 1.6 in. towards the west.....	118
97. ITS-3 view of north and west walls, imposed top deflection of 1.6 in. towards the east.....	119
98. ITS-3 pre-experiment view of south and east walls.....	119
99. ITS-3 view of south and east walls, imposed top deflection of 1.6 in. towards the west.....	120
100. ITS-3 view of south and east walls, imposed top deflection of 1.6 in. towards the east.....	120
101. ITS-3 pre-experiment close-up view of interior south-east corner.....	121

FIGURE	Page
102. ITS-3 close-up view of interior south-east corner, imposed top deflection of 1.6 in. towards the west.....	121
103. ITS-3 close-up view of interior south-east corner, imposed top deflection of 1.6 in. towards the east.....	122
104. Horizontal load versus measured horizontal deflection.	123
105. ITS-3 measured horizontal deflection at various elevations.	126
106. ITS-3 measured horizontal deflection at various elevations, normalized by height on the structure.	127
107. Deflected shape of ITS-3 at the top of the first ten excursions, as measured by the horizontal deflection gages.	127
108. Correlation coefficients for linear and second-order curve fits to the deflected shape of ITS-3 at the top of the first ten excursions.	128
109. ITS-3 frequency response function from pre-experiment survey.	131
110. ITS-3 frequency response function from post-failure survey.	132
111. ITS-3 frequency response function from post-experiment survey.....	134
112. Change of first bending mode with increasing damage for ITS-2 and ITS-3 models.	136
113. Change of first torsional mode with increasing damage for ITS-2 and ITS-3 models.	136
114. Change of second bending mode with increasing damage for ITS-2 and ITS-3 models.	137
115. Suggested applicability of the displacement-based analysis technique.	139
116. Assumed flexural response.	141
117. Observed and calculated ITS-1 response as related to imposed horizontal deflections.	144

FIGURE	Page
118. Relationship of ductility ratio to reinforcing steel ultimate strain and plastic hinge length, for ITS-1 model with invariant yield response.	147
119. Observed and calculated ductility for ITS-1 and ITS-2 as related to the imposed deflection.....	148
120. ITS-2 measured and calculated ductility as related to measured top deflection. ...	149
121. ITS-3 measured and calculated ductility as related to measured top deflection. ...	154
122. Proposed curvature relationship.....	157
123. Assumed flexural response.	164
A1. Distribution of towers by decade of design/construction.....	172
A2. Distribution of towers by total height.	172
A3. Distribution of rectangular towers by ratio of total height to base width.	173
A4. Distribution of rectangular towers by ratio of height to base width for parallel and perpendicular axis directions.	173
A5. Distribution of nonrectangular towers by ratio of total height to base width.....	174
A6. Distribution of nonrectangular towers by ratio of height to base width for parallel and perpendicular axis directions.	174
A7. Distribution of critical sections by height above critical section.	175
A8. Distribution of rectangular tower critical sections by normalized wall thickness.	175
A9. Distribution of rectangular tower critical sections by normalized wall thickness for parallel and perpendicular axis directions.	176
A10. Distribution of nonrectangular tower critical sections by wall thickness.....	176
A11. Distribution of rectangular tower critical sections by wall area to gross area ratio.	177

FIGURE	Page
A12. Distribution of rectangular tower critical sections by wall area to gross area ratio for parallel and perpendicular axis directions.	177
A13. Distribution of rectangular tower critical sections by normalized vertical steel percentage of walls.	178
A14. Distribution of rectangular tower critical sections by normalized vertical steel percentage of walls for parallel and perpendicular axis directions.	178
A15. Distribution of rectangular tower critical sections by normalized horizontal steel percentage of walls.	179
A16. Distribution of rectangular tower critical sections by normalized horizontal steel percentage of walls for parallel and perpendicular axis directions.	179
A17. Distribution of nonrectangular tower critical sections by vertical steel percentage of walls.	180
A18. Distribution of nonrectangular tower critical sections by horizontal steel percentage of walls.	180
A19. Distribution of all critical sections by moment required to initiate cracking of section.	181
C1. ITS-2 base strains, imposed deflection -0.1 in., cumulative travel of 0.1 in., that is, the top of the first leg of the first load cycle.	189
C2. ITS-2 base strains, imposed deflection 0.0 in., cumulative travel of 0.2 in., that is, the bottom of the first leg of the first load cycle.	190
C3. ITS-2 base strains, imposed deflection 0.1 in. and a cumulative imposed travel of 0.3 in., that is, the top of the second leg of the first load cycle.	191
C4. ITS-2 base strains, imposed deflection 0.0 in., cumulative travel of 0.4 in., that is, the bottom of the second leg of the first load cycle.	192
C5. ITS-2 base strains, imposed deflection -0.2 in., cumulative travel of 0.6 in., that is, the top of the first leg of the second load cycle.	193
C6. ITS-2 base strains, imposed deflection 0.0 in., cumulative travel of 0.8 in., that is, the bottom of the first leg of the second load cycle.	194

C7. ITS-2 base strains, imposed deflection 0.2 in., cumulative travel of 1.0 in., that is, the top of the second leg of the second load cycle.	195
C8. ITS-2 base strains, imposed deflection 0.0 in., cumulative travel of 1.2 in., that is, the bottom of the second leg of the second load cycle.	196
C9. ITS-2 base strains, imposed deflection -0.3 in., cumulative travel of 1.5 in., that is, the top of the first leg of the third load cycle.	197
C10. ITS-2 base strains, imposed deflection 0.0 in., cumulative travel of 1.8 in., that is, the bottom of the first leg of the third load cycle.	198
C11. ITS-2 base strains, imposed deflection 0.3 in., cumulative travel of 2.1 in., that is, the top of the second leg of the third load cycle.	199
C12. ITS-2 strains at 2 in. elevation, imposed deflection -0.1 in., cumulative travel of 0.1 in., that is, the top of the first leg of the first load cycle.	200
C13. ITS-2 strains at 2 in. elevation, imposed deflection 0.0 in., cumulative travel of 0.2 in., that is, the bottom of the first leg of the first load cycle.	201
C14. ITS-2 strains at 2 in. elevation, imposed deflection 0.1 in., cumulative travel of 0.3 in., that is, the top of the second leg of the first load cycle.	202
C15. ITS-2 strains at 2 in. elevation, imposed deflection 0.0 in., cumulative travel of 0.4 in., that is, the bottom of the second leg of the first load cycle.	203
C16. ITS-2 strains at 2 in. elevation, imposed deflection -0.2 in., cumulative travel of 0.6 in., that is, the top of the first leg of the second load cycle.	204
C17. ITS-2 strains at 2 in. elevation, imposed deflection 0.0 in., cumulative travel of 0.8 in., that is, the bottom of the first leg of the second load cycle.	205
C18. ITS-2 strains at 2 in. elevation, imposed deflection 0.2 in., cumulative travel of 1.0 in., that is, the top of the second leg of the second load cycle.	206
C19. ITS-2 strains at 2 in. elevation, imposed deflection 0.0 in., cumulative travel of 1.2 in., that is, the bottom of the second leg of the second load cycle.	207
C20. ITS-2 strains at 2 in. elevation, imposed deflection -0.3 in., cumulative travel of 1.5 in., that is, the top of the first leg of the third load cycle.	208

FIGURE

Page

C21. ITS-2 strains at 2 in. elevation, imposed deflection 0.0 in., cumulative travel of 1.8 in., that is, the bottom of the first leg of the third load cycle.	209
C22. ITS-2 strains at 2 in. elevation, imposed deflection 0.3 in., cumulative travel of 2.1 in., that is, the top of the second leg of the third load cycle.	210
C23. ITS-3 base strains, imposed deflection -0.1 in., cumulative travel of 0.1 in., that is, the top of the first leg of the first load cycle.	211
C24. ITS-3 base strains, imposed deflection 0.0 in., cumulative travel of 0.2 in., that is, the bottom of the first leg of the first load cycle.	212
C25. ITS-3 base strains, imposed deflection 0.1 in., cumulative travel of 0.3 in., that is, the top of the second leg of the first load cycle.	213
C26. ITS-3 base strains, imposed deflection 0.0 in., cumulative travel of 0.4 in., that is, the bottom of the second leg of the first load cycle.	214
C27. ITS-3 base strains, imposed deflection -0.2 in., cumulative travel of 0.6 in., that is, the top of the first leg of the second load cycle.	215
C28. ITS-3 base strains, imposed deflection 0.0 in., cumulative travel of 0.8 in., that is, the bottom of the first leg of the second load cycle.	216
C29. ITS-3 base strains, imposed deflection 0.2 in., cumulative travel of 1.0 in., that is, the top of the second leg of the second load cycle.	217
C30. ITS-3 base strains, imposed deflection 0.0 in., cumulative travel of 1.2 in., that is, the bottom of the second leg of the second load cycle.	218
C31. ITS-3 base strains, imposed deflection -0.3 in., cumulative travel of 1.5 in., that is, the top of the first leg of the third load cycle.	219
C32. ITS-3 base strains, imposed deflection 0.0 in., cumulative travel of 1.8 in., that is, the bottom of the first leg of the third load cycle.	220
C33. ITS-3 base strains, imposed deflection 0.3 in., cumulative travel of 2.1 in., that is, the top of the second leg of the third load cycle.	221
C34. ITS-3 base strains, imposed deflection 0.0 in., cumulative travel of 2.4 in., that is, the bottom of the second leg of the third load cycle.	222

C35. ITS-3 base strains, imposed deflection -0.4 in., cumulative travel of 2.8 in., that is, the top of the first leg of the fourth load cycle.	223
C36. ITS-3 strains at 2 in. elevation, imposed deflection -0.1 in., cumulative travel of 0.1 in., that is, the top of the first leg of the first load cycle.....	224
C37. ITS-3 strains at 2 in. elevation, imposed deflection 0.0 in., cumulative travel of 0.2 in., that is, the bottom of the first leg of the first load cycle.	225
C38. ITS-3 strains at 2 in. elevation, imposed deflection 0.1 in., cumulative travel of 0.3 in., that is, the top of the second leg of the first load cycle.....	226
C39. ITS-3 strains at 2 in. elevation, imposed deflection 0.0 in., cumulative travel of 0.4 in., that is, the bottom of the second leg of the first load cycle.	227
C40. ITS-3 strains at 2 in. elevation, imposed deflection -0.2 in., cumulative travel of 0.6 in., that is, the top of the first leg of the second load cycle.	228
C41. ITS-3 strains at 2 in. elevation, imposed deflection 0.0 in., cumulative travel of 0.8 in., that is, the bottom of the first leg of the second load cycle.	229
C42. ITS-3 strains at 2 in. elevation, imposed deflection 0.2 in., cumulative travel of 1.0 in., that is, the top of the second leg of the second load cycle.....	230
C43. ITS-3 strains at 2 in. elevation, imposed deflection 0.0 in., cumulative travel of 1.2 in., that is, the bottom of the second leg of the second load cycle.....	231
C44. ITS-3 strains at 2 in. elevation, imposed deflection -0.3 in., cumulative travel of 1.5 in., that is, the top of the first leg of the third load cycle.	232
C45. ITS-3 strains at 2 in. elevation, imposed deflection 0.0 in., cumulative travel of 1.8 in., that is, the bottom of the first leg of the third load cycle.....	233
C46. ITS-3 strains at 2 in. elevation, imposed deflection 0.3 in., cumulative travel of 2.1 in., that is, the top of the second leg of the third load cycle.	234
C47. ITS-3 strains at 2 in. elevation, imposed deflection 0.0 in., cumulative travel of 2.4 in., that is, the bottom of the second leg of the third load cycle.	235
C48. ITS-3 strains at 2 in. elevation, imposed deflection -0.4 in., cumulative travel of 2.8 in., that is, the top of the first leg of the fourth load cycle.	236

FIGURE	Page
D1. ITS-2 pre-experiment first bending mode at 44 Hz.	238
D2. ITS-2 pre-experiment torsional mode at 121 Hz.....	238
D3. ITS-2 pre-experiment higher order torsional mode at 157 Hz.	238
D4. ITS-2 pre-experiment second bending mode at 457 Hz.....	238
D5. ITS-2 post-experiment first bending mode at 23 Hz.....	239
D6. ITS-2 post-experiment torsion mode at 94 Hz.....	239
D7. ITS-2 post-experiment higher order torsion mode at 157 Hz.	239
D8. ITS-2 post-experiment second order bending mode at 340 Hz.....	239
D9. ITS-3 pre-experiment first bending mode at 51 Hz.	240
D10. ITS-3 pre-experiment torsional mode at 143 Hz.....	240
D11. ITS-3 pre-experiment second bending mode at 440 Hz.....	240
D12. ITS-3 post-failure first bending mode at 23 Hz.	241
D13. ITS-3 post-failure torsional mode at 45 Hz.....	241
D14. ITS-3 post-failure higher order torsional mode at 155 Hz.....	241
D15. ITS-3 post-failure second bending mode at 426 Hz.....	241
D16. ITS-3 post-experiment first bending mode at 17 Hz.....	242
D17. ITS-3 post-experiment torsional mode at 32 Hz.	242
D18. ITS-3 post-experiment higher order torsional mode at 152 Hz.	242
D19. ITS-3 post-experiment wall bending mode at 421 Hz.	242
E1. Initial stiffness of ITS-2 structure generated from imposed deflection and measured load.	244

FIGURE	Page
E2. ITS-2 plastic deflection approximated by subtracting estimated elastic from total deflection.	244
E3. Vertical deflection measured at base of ITS-2 model.	245
E4. Curvature at base of ITS-2 model calculated from vertical deflections and internal strains.	245
E5. Plastic hinge length, calculated from experimental elastic and plastic deflection and curvature.	246
E6. Section curvature generated from vertical strains at a 6 in. elevation.	246
E7. Section curvature generated from vertical strains at a 12 in. elevation.	247
E8. Section curvature generated from vertical strains at an 18 in. elevation.	247
E9. Section curvature generated from vertical strains at a 24 in. elevation.	248
E10. Section curvature generated from vertical strains at a 48 in. elevation.	248
E11. Section curvature generated from vertical strains at a 72 in. elevation.	249
E12. Slope of the curvature triangle at various elevations.	249
E13. Average slope of the curvature triangle for 12 in. to 72 in. elevations.	250
E14. Curvature at the base of ITS-2 as derived from the estimated initial structural stiffness.	250
E15. Curvature at the base of ITS-2 as derived from the estimated initial structural stiffness compared to that derived from body strain measurements.	251
E16. Comparison of imposed and measured horizontal deflections to the deflection calculated from the strains measured in ITS-2 model.	251
E17. ITS-3 section curvature generated from vertical strains at a 24 in. elevation.	252
E18. ITS-3 section curvature generated from vertical strains at a 48 in. elevation.	252

FIGURE	Page
E19. ITS-3 average slope of the curvature triangle for 24 in. and 48 in. elevations.....	253
E20. Comparison of imposed and measured horizontal deflections to the deflection calculated from the strains measured in ITS-3 model.....	253

CHAPTER 1

INTRODUCTION

In the event of an earthquake, it is vitally important that the catastrophic failure of a dam and subsequent sudden release of the reservoir be prevented. An important part of the prevention of such a failure is maintaining the ability to control the release of water after the earthquake. If a dam is damaged, the prompt and controlled lowering of the water level will remove hydrostatic pressure and help to prevent the propagation of the damage into a catastrophic failure. For most earthen dams, and some concrete dams, the release of water is controlled through a reinforced concrete intake tower (Figure 1). The functional survival of such towers is the main concern of this research effort.

The success of the tower in resisting failure is dependent upon the magnitude of the earthquake loads and the structural details controlling the nonlinear dynamic response and failure mechanisms of the specific tower. Currently, available analysis techniques and engineering guidance for intake towers may not properly include these factors. The evaluation and/or development of better design and analysis procedures and guidance is the primary goal of the research reported here.

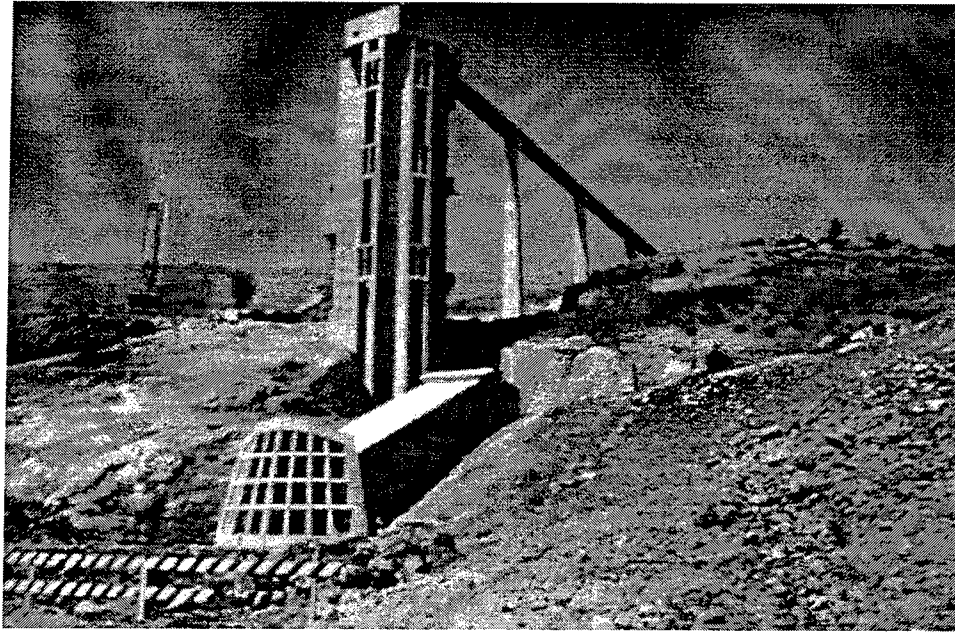


Figure 1. Lost Creek Intake Tower during construction.

Objective

The overall objective of this research is to understand the nonlinear response of existing, lightly reinforced intake towers. The ultimate objective is the evaluation and/or development of approximate or simplified analysis procedures for the evaluation of the ductility of existing intake towers.

There were two phases in the fulfillment of this ultimate objective. The first phase was a statistical analysis of the inventory of existing intake towers. The specific objective of this tower inventory analysis was to quantify the distribution and variation of the structural characteristics of the U.S. Army Corps of Engineers' inventory of existing intake towers as relating to their earthquake location hazard. This analysis was used to assist in the identification of possible failure mechanisms and to help quantify the extent

of the problem of the seismic response of existing towers. The information generated was used in planning the second phase of this research effort, the Intake Tower Substructure (ITS) experimentation series. The objectives of these experiments were to observe the response of scale models of typical intake towers, quantify the ductility available, and use the information generated for the development of approximate and/or simplified analysis procedures for the evaluation of the ductility of existing intake towers.

Approach

The approach of the tower inventory analysis was to build upon an initial effort conducted under the Repair, Evaluation, Maintenance and Rehabilitation Research (REMR) Program 120, Work Unit 32642. This initial study was performed to identify the characteristics of the intake towers of Corps dams as they relate to Uniform Building Code [1] seismic zones. This initial inventory effort included information compiled in 1993 by Mr. Dave Illias, U.S. Army Engineer District, Portland. Additional information was gathered from a search of design memoranda and inspection reports found in the U.S. Army Engineer Waterways Experiment Station (WES) research library. The National Inventory of Dams was also consulted. Of the 162 intake towers identified in this study, 77 were in seismic zones 2 and greater, as defined by the Uniform Building Code. The available information on the properties of these 77 towers was statistically analyzed. The tower characteristics included in the analysis were: total height, clear height, major and minor widths, height-to-width ratio, and concrete wall thickness.

In conducting the initial survey, it was evident that only limited structural information was available from the sources cited. As a result, the first step in the tower inventory analysis was to obtain structural drawings of the 77 towers of interest from the corresponding Corps districts. In all, 13 district offices were contacted, and all responded by sending the requested drawings and information. These drawings formed the basis of the inventory analysis conducted. Each drawing was analyzed to determine the geometric and material properties of the towers; this information was entered in a database, and a statistical analysis was performed on the data to summarize the results. The results were used to design the three experiments conducted in the next phase of the research.

The first ITS experiment (ITS-1) consisted of the one-way static loading to failure of a 1/8th scale model of a typical intake tower configuration. ITS-2 consisted of the cyclic application of a static bending load to a 1/8th scale model of a typical intake tower configuration. This model was constructed to be as similar as possible to the model in the ITS-1 experiment. ITS-3 also consisted of the cyclic application of static bending loads to a 1/8th scale model of a typical intake tower configuration; but, in this case the steel reinforcement percentages and material strengths were changed to reflect an upper bound of expected values. All experiments took place in the Large-Scale Load Frame constructed to conduct these and subsequent experiments. The frame was designed to withstand a load of 200 kips vertically and 400 kips horizontally at the maximum specimen height of 20 ft. This load capacity is based upon preliminary analysis of 1/8th

to 1/6th scale models of intake towers spanning the structural characteristics of interest.

Figure 2 shows the Large-Scale Load Frame.

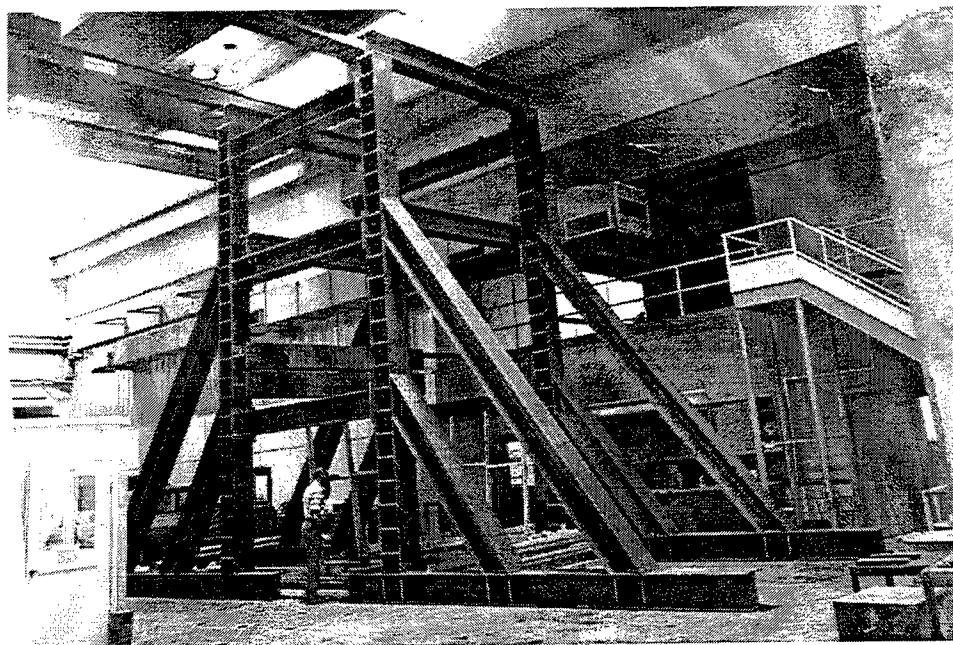


Figure 2. Large-Scale Load Frame.

Three specific structural responses were identified for study. The first is the overall ductility response of the models under one-way and cyclic excursion loads. Basically, the ductility response can be defined as the load-deflection or moment-curvature relationship of the model as it deflects into the plastic range to failure. The ductility of a structure is often given as the ratio of total deflection or curvature at failure, to the maximum elastic deflection or curvature.

The second area of interest is the response of the base of the model. The base of a cantilever structure is where moment loads are greatest and is obviously a critical section.

In actual towers, a construction joint is usually found at this critical section. The conjunction of maximum loads with a construction joint indicates that the response of the joint may have a major influence on the ductility response of the structure. For this reason, emphasis was given to modeling the joint and gathering data on its response.

Measurements of the response of the base region of the structure also contribute to the development of simplified methods of analysis. Early on, a displacement-based analysis method was identified as very promising for application to problems of this type. This method attempts to explicitly consider earthquake-induced structural displacements. A major component of this analysis procedure is the plastic hinge length. For a tower model, the plastic hinge length can be defined as the height of the zone at the base of the tower, over which plastic rotations must occur, so that the total deflection at the top of the tower is equal to the deflection due to elastic and plastic rotations. The plastic hinge length is an empirical and analytical parameter; and thus, the measurement of the distribution of stresses and strains in the plastic hinge zone and monitoring of the progression of the formation of the plastic hinge were expected to be important.

The third area of interest is the dynamic characteristics of the model. Modal surveys of the experiment models before, during, and after experimentation were conducted. These surveys were used to quantify the changes in the mode shapes and frequencies due to the damage accumulated during experimentation.

CHAPTER 2

ANALYSIS OF EXISTING INTAKE TOWER INVENTORY

The inventory analysis began with an examination of the structural drawings of the towers of interest. It was evident that these structures were relatively complex and the structural configuration varied considerably from tower to tower. However, the towers were similar enough that descriptive parameters could be developed that would allow meaningful comparisons among the population. These parameters were determined for each tower and incorporated into a spreadsheet/database, and descriptive statistics were developed.

Database Development

Many parameters must be known to conduct a ductility analysis of a concrete intake tower. The parameters needed include the geometric and material properties of the tower, as well as the expected loading. To develop and/or validate ductility analysis

procedures for existing towers, the variation of these parameters in the tower population must be well understood. The generation of this spreadsheet was part of an effort to quantify the variation of important structural parameters in the population of existing Corps intake towers in areas of significant seismic risk. Statistical measures of this variability were used in the planning and design of experimentation and analysis efforts.

For most intake structures, the geometry varies considerably throughout the height of the tower. It is common to have a very massive substructure at lower elevations with a much less massive tower at higher elevations (Figure 3). The substructure typically consists of the intake (including trash racks) and outlet conduit. The towers usually contain water-quality gates and all flow-rate control mechanisms. A superstructure is often located at the top of the tower. The superstructure usually extends above the service bridge and is commonly where the control station is located. This superstructure is normally above the maximum water surface and is often a structurally distinct component of the intake tower.

Since most intake structures vary considerably in cross section throughout the height of the tower, it was necessary to determine certain critical cross sections where the tower would be most likely to fail. The most common critical cross section was at the intersection of the tower and the substructure. In some cases, the geometry of a tower led to the identification of two critical sections; one for bending about the flow axis, as well as one for bending about an axis perpendicular to the flow. The flow axis is defined as the direction of the flow of the water through the conduit. For most rectangular

towers, these two axes coincided with the major axes of the structure. Both sections were included in the spreadsheet for any tower with two critical sections.

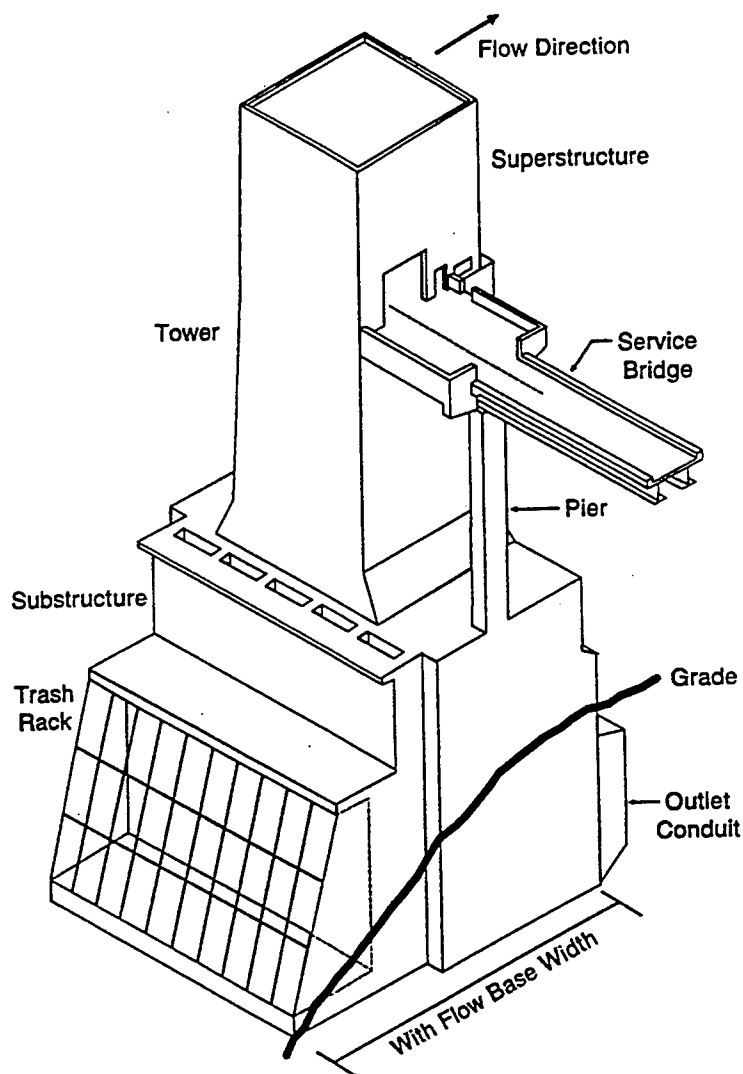


Figure 3. Typical rectangular intake tower.

The selection of critical sections was made by inspection and was based upon apparent large changes in stiffness at the lowest elevation in the free standing (not

embedded) part of the tower. These cross sections were not intended to identify an exact point of failure for an individual tower, rather they were meant to identify a cross section typical of one in an expected failure zone.

Once the critical cross sections were chosen, some idealization was needed to concisely represent the structure. For rectangular cross sections, the structure was idealized as a series of shear walls. Each section has shear walls in the direction of flow and in the direction perpendicular to the flow. This idealization ignores relatively minor variations in thickness, small penetrations, and other minor departures of the actual geometry from that of an assumed rectangular section. The rectangular section was always chosen as a conservative approximation of the typical actual section. From the chosen wall section, the typical wall reinforcement was identified, and both the vertical percent of steel (ρ_v) and horizontal percent of steel (ρ_h) were calculated based on a unit width of the section. These ratios are meant to provide a rough estimate of the actual reinforcement. Special rebar placed for cutouts, corners, etc. was not considered. The selection of typical reinforcement was complicated by the fact that additional reinforcement was usually present in the transition zone between the substructure and the tower. To overcome this problem, the reinforcement was chosen at the lowest point above the critical section which appeared to represent the typical reinforcing. For circular and octagonal sections, a similar process was followed for the identification of reinforcement. Vertical steel percentage (ρ_v) was calculated as the total reinforcement

divided by the area of concrete, while horizontal steel percentage (ρ_h) was calculated using a unit width of the section.

Determining the area properties of sections required a number of assumptions and simplifications due to the complexity of the geometry of individual critical cross sections. Most of these assumptions consisted of regularizing the geometry by neglecting the contribution of relatively minor structural components such as small wing walls or penetrations. It was not practical to completely describe all such simplifications in the spreadsheet. A record was kept of the assumptions made for each tower for later reference. All pertinent data and calculations were also recorded. All information was obtained from as-built drawings and other available literature such as design memoranda.

Table 1 describes the parameters presented in the spreadsheet and briefly explains how they were determined. All heights are measured from the base of the structure unless otherwise indicated. The base of the structure is defined as the lowest point of concrete common to the entire intake structure.

Table 1. Description of intake tower database parameters.

PROJECT	DAM OR RESERVOIR FOR WHICH PARAMETERS ARE GIVEN
DISTRICT	CORPS DISTRICT WHICH THE PROJECT IS LOCATED IN
YEAR BUILT	APPROXIMATE YEAR WHICH THE PROJECT WAS BUILT
ZONE	SEISMIC ZONE THE PROJECT IS LOCATED IN (FROM 1991 ZONING)
TYPE	SHAPE OR DESCRIPTION. R=RECTANGULAR, C=CIRCULAR, O=OCTAGONAL, I=INCLINED, COL=COLUMN SUPPORTED
MAXIMUM POOL	HEIGHT OF MAXIMUM POOL
CONSERVATION POOL	HEIGHT OF NORMAL POOL
MINIMUM POOL	MINIMUM EXPECTED POOL
TOTAL HEIGHT	HEIGHT TO HIGHEST POINT OF STRUCTURE
BASE WIDTH PARALLEL WITH FLOW	WIDTH AT BASE ALONG THE FLOW AXIS, INCLUDING TRASH RACKS, NOT INCLUDING TRANSITION CONDUIT UNLESS SUFFICIENTLY RIGID
BASE WIDTH PERPENDICULAR WITH FLOW	WIDTH AT BASE ALONG AN AXIS PERPENDICULAR TO FLOW, THROUGH THE MAXIMUM WIDTH OF THE BASE
BASE TO SERVICE BRIDGE	HEIGHT FROM THE BASE TO THE SERVICE BRIDGE FLOOR
BASE TO CRITICAL SECTION	HEIGHT FROM THE BASE TO THE ASSUMED CRITICAL SECTION, NOTE THERE MAY BE TWO SUCH HEIGHTS, SEE EXPLANATION ABOVE
BASE TO TOP OF CONDUIT	HEIGHT FROM THE BASE TO THE POINT OF EXTENSION OF THE TRANSITION CONDUIT OUTWARD FROM THE MAIN SUBSTRUCTURE
BASE TO AVERAGE EMBEDMENT	HEIGHT FROM THE BASE TO THE APPROXIMATE AVERAGE ELEVATION OF EMBEDMENT
f_y	YIELD STRENGTH OF REINFORCING BARS USED IN THE STRUCTURE
f'_c	CONCRETE COMPRESSIVE STRENGTH AFTER 28 DAYS
CLEAR HEIGHT AT CRITICAL SECTION	HEIGHT DIFFERENCE FROM TOP OF THE STRUCTURE TO THE CRITICAL SECTION
CRITICAL SECTION WIDTH PARALLEL TO FLOW	WIDTH OF STRUCTURE AT CRITICAL SECTION IN DIRECTION OF FLOW, THIS INFORMATION IS OMITTED FOR CIRCULAR AND OCTAGONAL SECTIONS
CRITICAL SECTION WIDTH PERPENDICULAR TO FLOW	WIDTH OF STRUCTURE AT CRITICAL SECTION IN THE DIRECTION PERPENDICULAR TO FLOW, SEE NOTE ABOVE
A_g AT CRITICAL SECTION	GROSS AREA OF CRITICAL CROSS SECTION, CALCULATED AS PRODUCT OF MAXIMUM WIDTHS IN BOTH DIRECTIONS FOR RECTANGULAR SECTIONS, APPROXIMATE AREA ENCLOSED BY SECTION FOR OTHER GEOMETRIES
N.A. DISTANCE PARALLEL WITH FLOW	THE MAXIMUM DISTANCE BETWEEN NEUTRAL AXIS AND EXTREME FIBER OF THE CRITICAL SECTION IN THE DIRECTION OF FLOW
N.A. DISTANCE PERPENDICULAR TO FLOW	THE MAXIMUM DISTANCE BETWEEN NEUTRAL AXIS AND EXTREME FIBER OF THE CRITICAL SECTION PERPENDICULAR TO THE DIRECTION OF FLOW
I_g ABOUT FLOW AXIS	MOMENT OF INERTIA ABOUT CENTROIDAL AXIS PARALLEL-TO-FLOW
I_g ABOUT AXIS PERPENDICULAR TO FLOW	MOMENT OF INERTIA ABOUT CENTROIDAL AXIS PERPENDICULAR-TO-FLOW
LENGTH	LENGTH OF WALL WITH ASSUMED CONSTANT THICKNESS
THICKNESS	THICKNESS OF WALL CORRESPONDING TO LENGTH ABOVE
VERTICAL STEEL INSIDE FACE	TYPICAL VERTICAL STEEL REINFORCEMENT USED ON THE INSIDE FACE OF THE WALL AS VIEWED FROM THE CENTROID OF THE STRUCTURE, SEE EXPLANATION ABOVE
VERTICAL STEEL OUTSIDE FACE	TYPICAL VERTICAL STEEL REINFORCEMENT USED ON THE OUTSIDE FACE OF THE WALL AS VIEWED FROM THE CENTROID OF THE STRUCTURE, SEE EXPLANATION ABOVE
ρ_v VERTICAL	CALCULATED GROSS VERTICAL REINFORCEMENT RATIO
HORIZONTAL STEEL INSIDE FACE	TYPICAL HORIZONTAL STEEL REINFORCEMENT USED ON THE INSIDE FACE OF THE WALL AS VIEWED FROM THE CENTROID OF THE STRUCTURE, SEE EXPLANATION ABOVE
HORIZONTAL STEEL OUTSIDE FACE	THE TYPICAL HORIZONTAL STEEL REINFORCEMENT USED ON THE INSIDE FACE OF THE WALL AS VIEWED FROM THE CENTROID OF THE STRUCTURE, SEE EXPLANATION ABOVE
ρ_h HORIZONTAL	CALCULATED GROSS HORIZONTAL REINFORCEMENT RATIO
COVER INSIDE FACE	CLEAR DISTANCE BETWEEN REINFORCEMENT AND FACE OF WALL FOR INSIDE FACE AS VIEWED FROM CENTROID OF STRUCTURE
COVER OUTSIDE FACE	CLEAR DISTANCE BETWEEN REINFORCEMENT AND FACE OF WALL FOR EXTERIOR FACE AS VIEWED FROM CENTROID OF STRUCTURE
AREA OF SHEAR WALL	AREA CALCULATED AS PRODUCT OF LENGTH BY THICKNESS OF RECTANGULAR SECTIONS, NOT APPLICABLE TO NONRECTANGULAR SECTIONS

Summary Statistics

The summary statistics of average and standard deviation were included in the intake tower spreadsheet containing the primary intake tower characteristics. Additional summary statistics and a graphical presentation of the distribution of several significant characteristics can be seen in Appendix A. Secondary characteristics derived from the primary characteristics will be presented and summarized.

Figure A1 shows the distribution of the decade of design of the examined towers. The date of design was taken as the initial date of the as-built drawings for each tower. The distribution shows that the majority of the towers were designed in the 1950 to 1970 time span. The average design date was 1960, with a standard deviation of 11 years. This information may be useful in the examination of the codes and design criteria applied to these towers.

The distribution of the total height of the towers is shown in Figure A2. Height is a very important factor in the earthquake analysis of a structure in that the fundamental frequency of response of a structure with a given mass and stiffness distribution is largely dependent upon the height. The mean total height for the tower population was 165.5 ft, with a standard deviation of 63.3 ft.

A characteristic related to the total height is the height-to-base ratio. This parameter is important in the consideration of possible rigid-body overturning of the towers and was defined as the ratio of the total height of a tower divided by the length of

the base of the tower. For most towers, two major axis directions can be defined as the parallel-to-flow direction and the perpendicular-to-flow direction. In both rectangular and nonrectangular towers, the base length may be different for these two major axes; hence, two height-to-base ratios were calculated for each tower. Figure A3 shows the distribution of height-to-base ratios for rectangular towers. Figure A4 shows the distribution of height-to-base ratios for rectangular towers with both axis directions shown separately. The mean ratio for the parallel-to-flow direction was 2.49, the standard deviation was 0.84, the minimum was 0.91, and the maximum was 5.27. The mean ratio for the perpendicular-to-flow direction was 3.31, the standard deviation was 0.98, the minimum was 1.34, and the maximum was 6.29. Similarly, Figure A5 shows the distribution of height-to-base ratios for nonrectangular towers. Figure A6 shows the distribution of height-to-base ratios for nonrectangular towers with both axis directions shown separately. In this case, the mean ratio for the parallel-to-flow direction was 3.23, the standard deviation was 0.72, the minimum was 2.31, and the maximum was 4.43. The mean ratio for the perpendicular-to-flow direction was 4.02, the standard deviation was 1.54, the minimum was 2.38, and the maximum was 7.97. In both rectangular and nonrectangular towers, the height-to-base ratio indicates that overturning would be more likely in the direction parallel to the flow than in the perpendicular direction.

For each tower in the database, at least one location was identified as a critical section where failure was most likely to occur. The first critical section parameter to be examined is the clear height, the distance from the bottom of the critical section to the top

of the tower. The clear height is significant in that the vertical dead load, as well as the horizontal earthquake loads, are directly dependent upon the mass of the structure above the critical section. Figure A7 shows the distribution of clear heights for all towers. The mean clear height was 93.79 ft, the standard deviation was 44.35 ft, the minimum was 19.07 ft, and the maximum was 209.00 ft.

The next parameter to be examined was the normalized wall thickness. Most rectangular towers can be considered as shear-wall-type structures containing from two to six parallel shear walls in each direction. Often these parallel walls were of similar thickness and had a fairly uniform thickness along the length. However, many critical sections contained walls that were not uniform. For the purpose of obtaining an average shear wall thickness at a given critical section in a given direction, the normalized wall thickness was calculated. For the rectangular towers, this parameter is defined as the thickness of each shear wall at a critical section in a given direction, multiplied by each wall length, and then summed and divided by the sum of the wall lengths. In this way, a single average wall thickness was developed for each critical section in each direction normalized by the length of the individual walls. This is not intended to define the total properties of the critical section itself as it does not indicate the number of walls in the section. Figure A8 shows the distribution of normalized wall thickness for rectangular towers. Figure A9 shows the distribution of normalized wall thickness for rectangular towers with both axis directions shown separately. The mean normalized thickness for the parallel-to-flow direction was 3.29 ft, the standard deviation was 2.11 ft, the

minimum was 1.06 ft, and the maximum was 15.47 ft. The mean normalized wall thickness for the perpendicular-to-flow direction was 3.35 ft, the standard deviation was 2.06 ft, the minimum was 1.05 ft, and the maximum was 15.75 ft.

For all the nonrectangular towers included in this analysis, the critical sections were circular or octagonal and hence had an identifiable single actual wall thickness. Figure A10 shows the distribution of wall thickness for nonrectangular cross-sections. The mean wall thickness was 3.30 ft, the standard deviation was 1.43 ft, the minimum was 2.00 ft, and the maximum was 6.5 ft.

In considering rectangular towers as shear wall structures, it is interesting to compare the properties of the towers with shear wall buildings. Wood [2] discusses a parameter called the wall area ratio that attempts to quantify the contribution of shear walls to the earthquake resistance of a building by calculating the ratio, the area of the shear walls in a given direction to the gross area of the building. This same reference indicates that for U.S. building construction, it is not unusual for this parameter to be as low as 0.005. In comparison, Chilean buildings with low steel percentages, large areas of shear walls, and good earthquake resistance had ratios that varied from 0.015 to 0.03. Figure A11 shows the distribution of wall area ratios for rectangular towers. Figure A12 shows the distribution of wall area ratios for rectangular towers with both axis directions shown separately. The mean wall area ratio for the parallel-to-flow direction was 0.242, the standard deviation was 0.101, the minimum was 0.113, and the maximum was 0.560. The mean wall area ratio for the perpendicular-to-flow direction

was 0.252, the standard deviation was 0.098, the minimum was 0.083, and the maximum was 0.593. These numbers are about an order of magnitude greater than Chilean buildings and two orders of magnitude above U.S. buildings. This may or may not bode well for the earthquake resistance of intake towers, but it does point out that care should be taken in applying criteria or analysis techniques generated for buildings to intake towers.

The next group of parameters examined was the steel percentages. As with the shear wall thickness, the steel percentages for rectangular towers were normalized to account for nonuniformities in wall thickness. For the purpose of obtaining an average vertical or horizontal steel percentage at a given critical section in a given axis direction, the normalized steel percentage was calculated. For the rectangular towers, this parameter was defined as the vertical or horizontal steel percentage for a wall at a critical section in a given axis direction, multiplied by each wall area, and then summed and divided by the sum of the wall areas. In this way, a single average vertical and horizontal steel percentage was developed for each critical section, in each axis direction, normalized by the area of the individual walls. As with the normalized wall thickness, this information was useful in the development of the experimentation and analysis programs. Again, this was not intended to define the properties of the specific critical section itself, since it does not indicate the number of walls in the section. Figure A13 shows the distribution of normalized vertical steel percentage for rectangular towers. Figure A14 shows the distribution of normalized vertical steel percentage for rectangular

towers with both axis directions shown separately. The mean normalized vertical steel percentage for the parallel-to-flow direction was 0.280 percent, the standard deviation was 0.178 percent, the minimum was 0.075 percent, and the maximum was 1.040 percent. The mean normalized vertical steel percentage for the perpendicular-to-flow direction was 0.281 percent, the standard deviation was 0.166 percent, the minimum was 0.056 percent, and the maximum was 0.761 percent. Figure A15 shows the distribution of normalized horizontal steel percentage for rectangular towers. Figure A16 shows the distribution of normalized horizontal steel percentage for rectangular towers with both axis directions shown separately. The mean normalized horizontal steel percentage for the parallel-to-flow direction was 0.380 percent, the standard deviation was 0.251 percent, the minimum was 0.118 percent, and the maximum was 1.758 percent. The mean normalized horizontal steel percentage for the perpendicular-to-flow direction was 0.366 percent, the standard deviation was 0.161 percent, the minimum was 0.068 percent, and the maximum was 1.022 percent.

For all the nonrectangular towers included in this analysis, the critical sections were circular or octagonal and hence had identifiable actual vertical and horizontal steel percentages. Figure A17 shows the distribution of vertical steel percentage for nonrectangular cross sections. The mean vertical steel percentage for nonrectangular

sections was 0.286 percent, the standard deviation was 0.155 percent, the minimum was 0.083 percent, and the maximum was 0.576 percent. Figure A18 shows the distribution of horizontal steel percentage for nonrectangular cross sections. The mean horizontal steel percentage for nonrectangular sections was 0.303 percent, the standard deviation was 0.148 percent, the minimum was 0.104 percent, and the maximum was 0.732 percent.

The final parameter to be examined was the cracking moment of the critical section. The cracking moment, as described by Wang and Salmon [3], was calculated using Equation 1, where f_r is defined as the modulus of rupture calculated as per Equation 2, I_g is the gross moment of inertia of the uncracked section without reinforcement, and y_t is the distance from the neutral axis to the extreme fiber of the concrete in tension. In Equation 2, the concrete strength (f'_c) is in lb /in.² and was assumed to be 3,000 lb /in.² for all towers. The cracking moment can be considered as a measure of the initial stiffness of the critical section and is dependent only on the geometry of the section and concrete strength. Figure A19 shows the distribution of the cracking moment about the flow direction axis and the axis perpendicular to the flow direction. The mean cracking moment about the flow direction axis was 1.63 kip-ft, the standard deviation was 1.28 kip-ft, the minimum is was 0.15 kip-ft, and the maximum was 6.16 kip-ft. The mean cracking moment about the axis perpendicular to the flow direction axis was 1.62 kip-ft, the standard deviation was 1.28 kip-ft, the minimum is 0.13 kip-ft, and the maximum was 5.78 kip-ft.

$$M_{cr} = \frac{f_r I_g}{y_t} \quad (1)$$

$$f_r = 7.5 \sqrt{f'_c} \quad (2)$$

CHAPTER 3

EXPERIMENTAL DESCRIPTION

Experiment Configuration

The dimensions, configuration, and structural parameters of the experimental components were selected to model typical prototype structures in the existing inventory rectangular intake towers. The prototype structures modeled would have a clear height of 80 ft, wall thickness of 3.75 ft, wall area to gross area ratio of 0.21, vertical steel ratios of 0.18 percent (ITS-1 and ITS-2) and 0.36 percent (ITS-3), horizontal steel ratios of 0.24 percent (ITS-1 and ITS-2) and 0.48 percent (ITS-3), and material properties commonly found in the existing towers. The clear height, wall thickness, and wall area to gross area ratio were selected to be representative of the center of the distribution of existing towers. The steel percentages and material properties were selected to envelop the upper and lower ranges of the expected values.

Figure 4 shows the overall experiment layout for the experiments. The 50-kip hydraulic loader, mounted horizontally, was used to provide loading at the top of the experimental models. This 50-kip loader is servocontrolled and is capable of applying a variety of load/time and deflection/time histories including load reversals, a capability utilized in the ITS-2 and ITS-3 experiments. The loader assembly incorporated a load cell for measurement of the applied load, as well as a deflection gage for control of the input motions. The vertically mounted 50-kip rams provided simulation of the dead load of the full-scale tower. The magnitude of this vertical load was selected to increase the vertical stress level at the base of the model tower to be the same as that at the base of a prototype tower 80 ft tall. The vertical load applied was a total of 66 kips. This simulated dead load was held constant throughout each experiment and was applied through a roller assembly to minimize lateral restraint of the top of the model (Figure 5 and Figure 6). A simple assembly, consisting of a single roller, was used in ITS-1, while a multi-roller assembly, offering less rolling resistance, was used in ITS-2 and ITS-3.

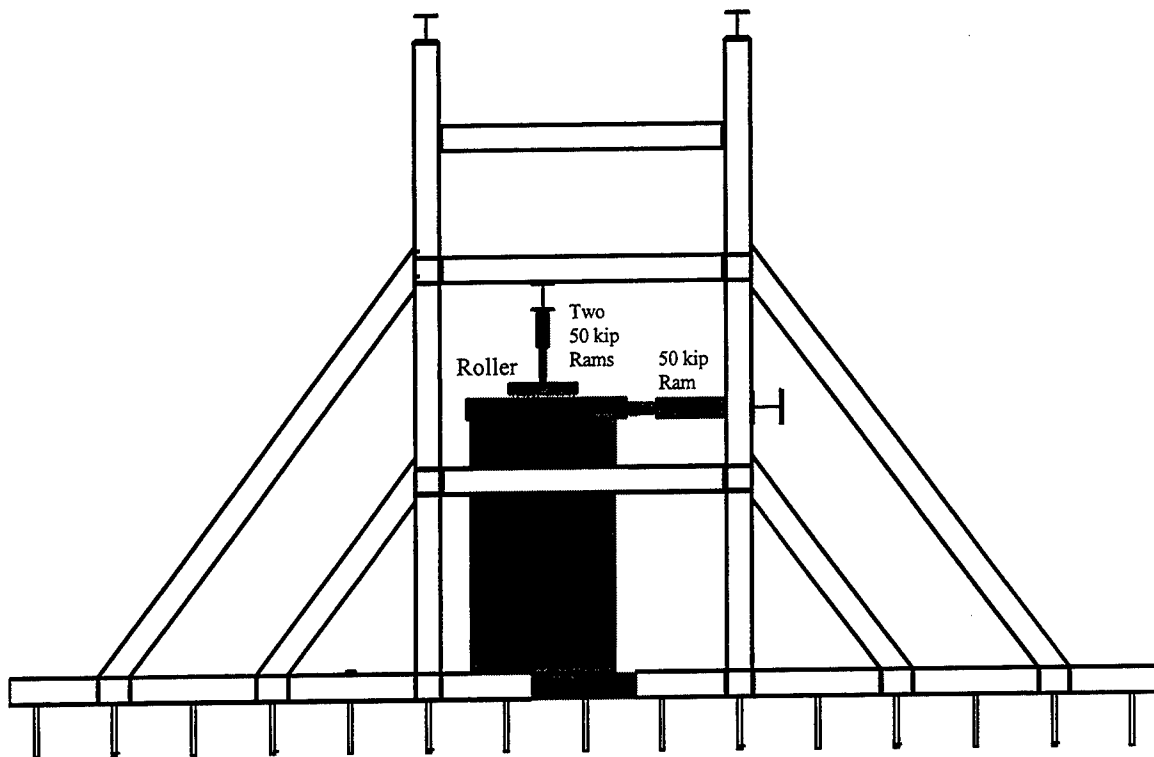


Figure 4. Overall experimental layout.

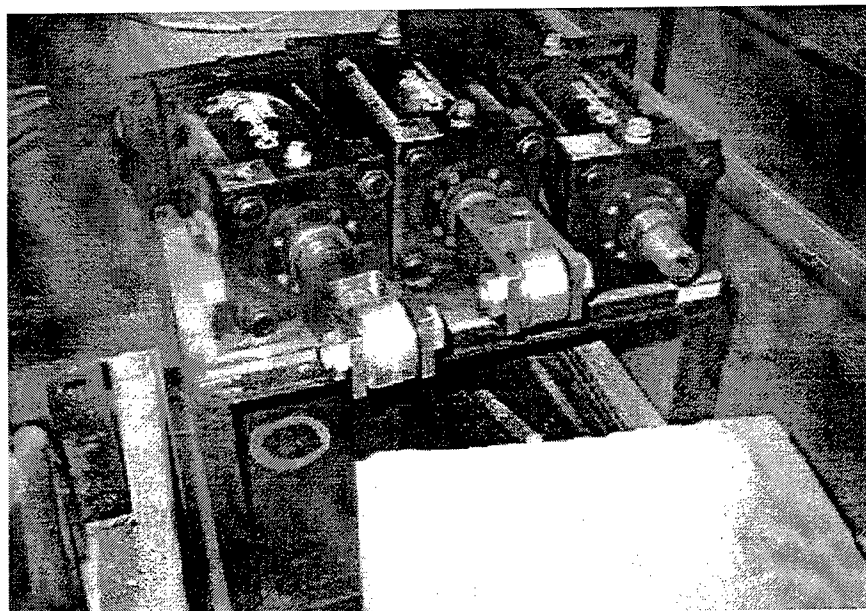


Figure 5. ITS-1 vertical load hydraulic ram and roller assemblies.

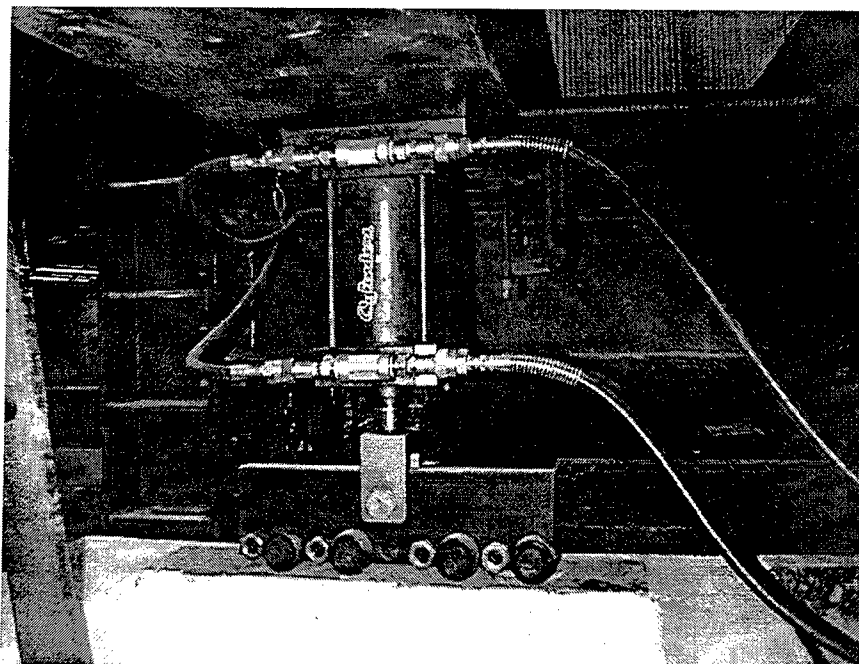


Figure 6. ITS-2 and ITS-3 vertical load hydraulic ram and roller assemblies.

The dimensions and configuration of the experimental components are shown in Figure 7. Each component consisted of an 18 in.-thick 9 ft- by 9-ft heavily reinforced concrete base that was bolted to the load floor, a 40-in. by 52-in., 10-ft tall tower section with 5-5/8-in.-thick walls, and a steel loading ring. Concrete properties for all three models can be found in Appendix B. A construction joint (cold joint) was located at the base of the tower sections for ease of construction and to simulate an almost universal existence of cold joints in critical sections of prototype structures. This cold joint was expected to have a significant impact on the response of the components, and each was carefully constructed.

The reinforcing layout of the tower section is shown in Figure 8. Reinforcing bar details are shown in Figure 9. The spacing and details for the reinforcing bars were the

same for all three experiments. For ITS-1 and ITS-2, the vertical reinforcement consisted of two layers of D1 deformed wire at a 2-in. center-to-center spacing. The horizontal reinforcement consisted of two layers of D1 deformed wire at a 1.5-in. center-to-center spacing. The area of a D1 wire is 0.01 in.² and, with the specified spacing, the vertical steel percentage (ρ_v) was 0.18 percent. The specified horizontal steel percentage (ρ_h) was 0.24 percent. The total steel percentage was thus 0.42 percent with a ρ_v to ρ_h ratio of 0.75. These values are representative of the lower midrange of those encountered in the population of existing Corps intake towers.

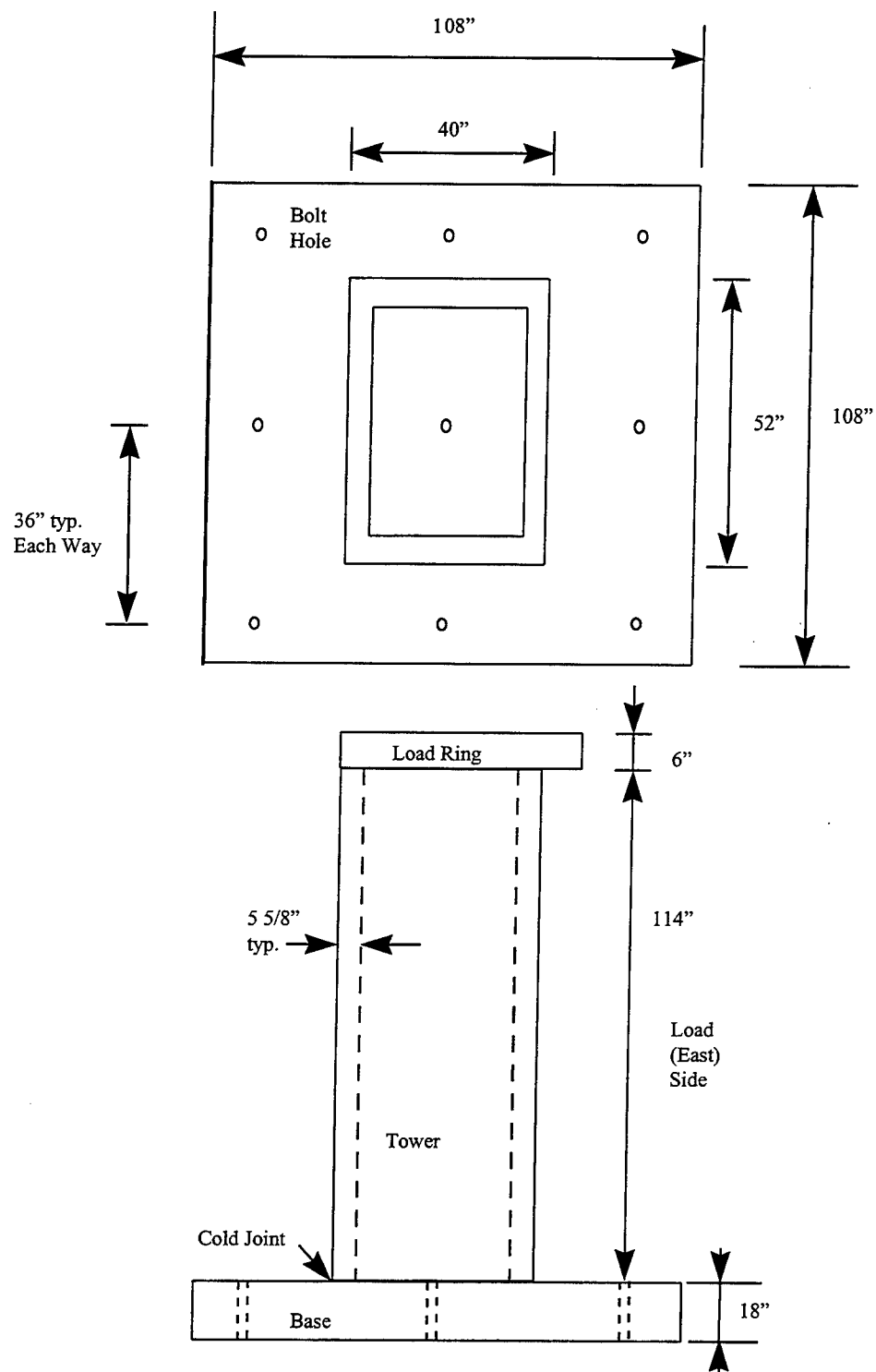


Figure 7. Model dimensions and configuration.

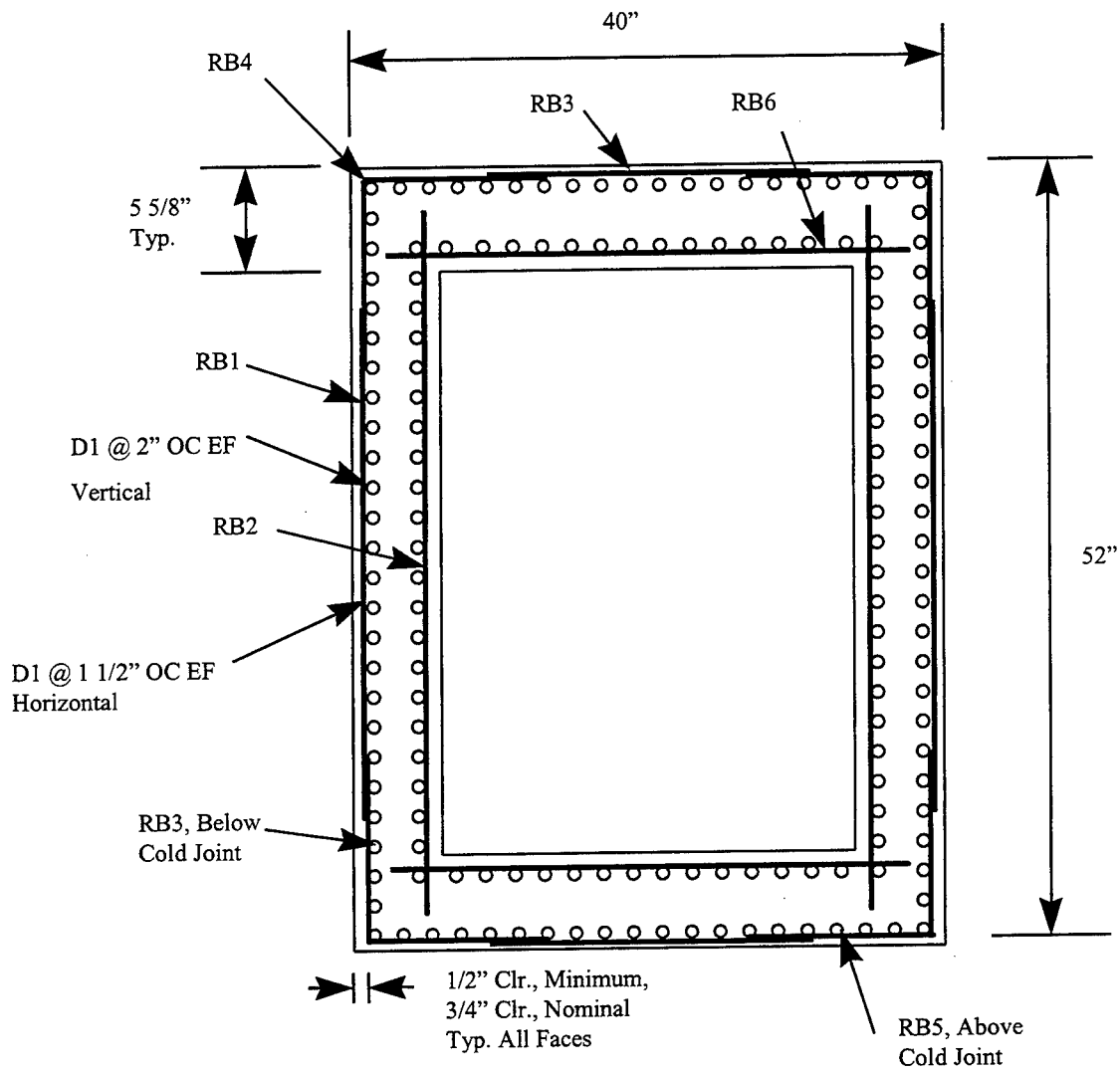


Figure 8. Tower section reinforcement layout.

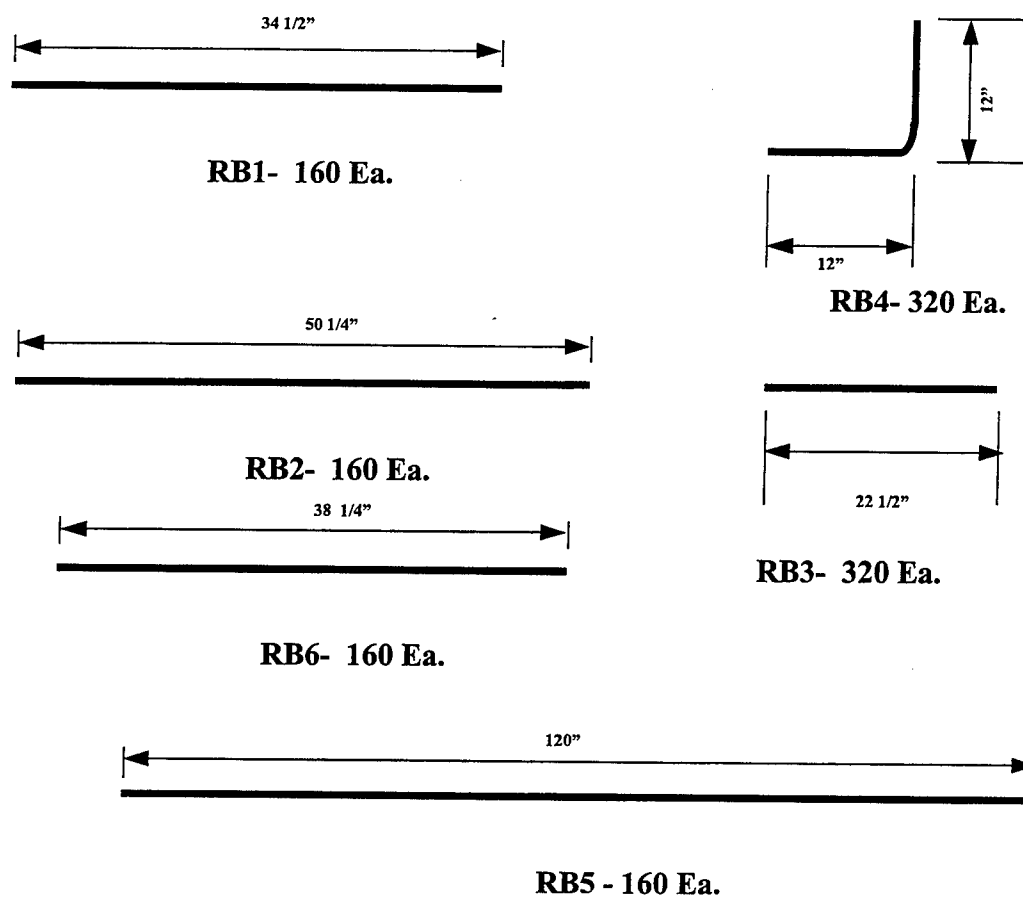


Figure 9. Reinforcing bar details.

For ITS-3, the vertical reinforcement consisted of two layers of D2 deformed wire at a 2-in. center-to-center spacing. The horizontal reinforcement consisted of two layers of D2 deformed wire at a 1.5-in. center-to-center spacing. The area of a D2 wire is 0.02 in.² and, with the specified spacing, the vertical steel percentage (ρ_v) was 0.36 percent. The specified horizontal steel percentage (ρ_h) was 0.48 percent. The total steel percentage was, thus, 0.84 percent, with a ρ_v -to- ρ_h ratio of 0.75. These values are representative of the upper midrange of those encountered in the population of existing Corps intake towers. For all models, the corner details were modeled after typical details

found in existing towers. A 4-in. lap/development length was specified for the corner details. The cold joint was modeled by casting vertical reinforcement (RB3) in the heavily reinforced base, allowing 4 in. to extend above the base. The resulting cold joint detail is typical of existing towers.

The 18-in.-thick base was reinforced with two layers of 60 ksi #6 reinforcing bar laid out in a 6-in. by 6-in. grid, with a vertical separation of 11 in. Hooks were bent at the ends of the bars, and the bars were tied to form a reinforcing bar cage approximately 12 in. in depth. The cage was set on standard chairs to create a bottom clearance of 1 in. and, hence, a top clearance of 5 in. This was done to minimize the influence this reinforcement might have on the cold joint response.

ITS-1 Instrumentation Configuration

At the time of the ITS-1 experiment, the data acquisition system used was capable of acquiring a total of 72 channels of data. Two of these channels were allocated to the measurement of load and deflection in the 50-kip horizontal hydraulic loader; deflection was measured at seven positions, and strain was measured at 63 positions.

Detailed locations of the strain gages can be seen in Figure 10 through Figure 14. On the west (compression) side of the structure (Figure 10), most of the strain gages were mounted so that the center of the gage was located 2 in. above the base of the tower section on the vertical reinforcing dowels. This allowed for the measurement of the magnitude and distribution of the compression strain in the concrete at this critical

section. Also shown in Figure 10 are strain gages located on the main vertical steel at intervals up the structure beginning at 6 in. from the base. In addition to providing a measurement of the magnitude and distribution of the strain, these measurements were expected to be used to calculate the rotational and deflection ductility of the structure. One horizontal strain measurement was also made. In addition to the internal strain gages, six external strain gages were mounted on the west (compression) wall at an elevation of 2 in. and 6 in. (Figure 11). These gages were attached to the bare concrete wall in an attempt to directly measure vertical concrete strains.

The strain gages located in the north side wall of the test component are shown in Figure 12. In the expected compression zone, strain gages were located 2 in. above the base, as they were in the compression wall. In the expected tension zone of the side wall, as well as all of the tension wall (Figure 13 and Figure 14), the lowest strain gages were mounted so that the center of each gage was located at the center of the cold joint. It was expected that the cold joint would act as an initial crack causing a concentration of the tensile stresses and initiating yielding in this region. It was intended that the location of gages at this point would allow for the measurement of the magnitude and distribution of the tensile strain in the reinforcement at this critical section. Additional strain gages were located on the main vertical and horizontal steel to measure the distribution of the strain in the plastic hinge zone. As in the compression wall, gages were located at intervals up the wall to provide a measurement of the magnitude and distribution of the strain, and for the calculation of the rotational and deflection ductility of the structure.

Figure 15 shows the location of the deflection gages. These gages were Celesco Model 101 PT-101 transducers, with a working range of 10 in. This type of gage contains a spring-motor that winds a cable around a drum attached to a linear rotary potentiometer. The output varies with the linear motion of the cable as translated to the rotation of the drum. These "yo-yo" type gages were used to back up the strain gage measurements of the rotational and deflection ductility of the structure.

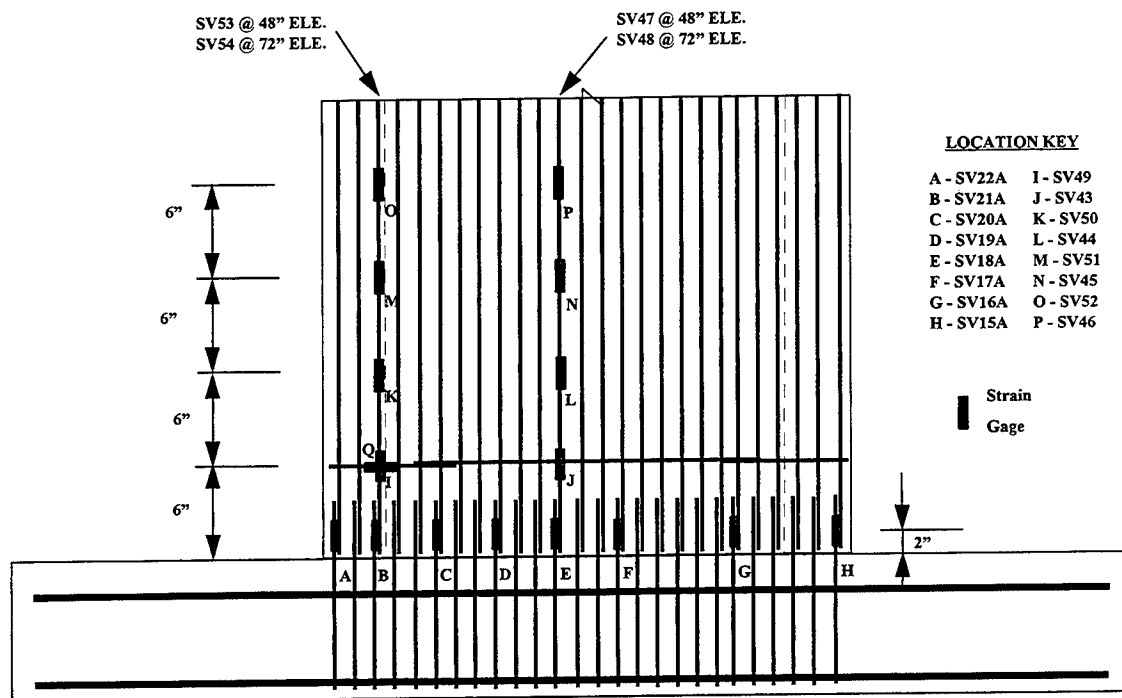


Figure 10. Location of strain gages mounted on exterior reinforcing layer, on west (compression) side of ITS-1 structure.

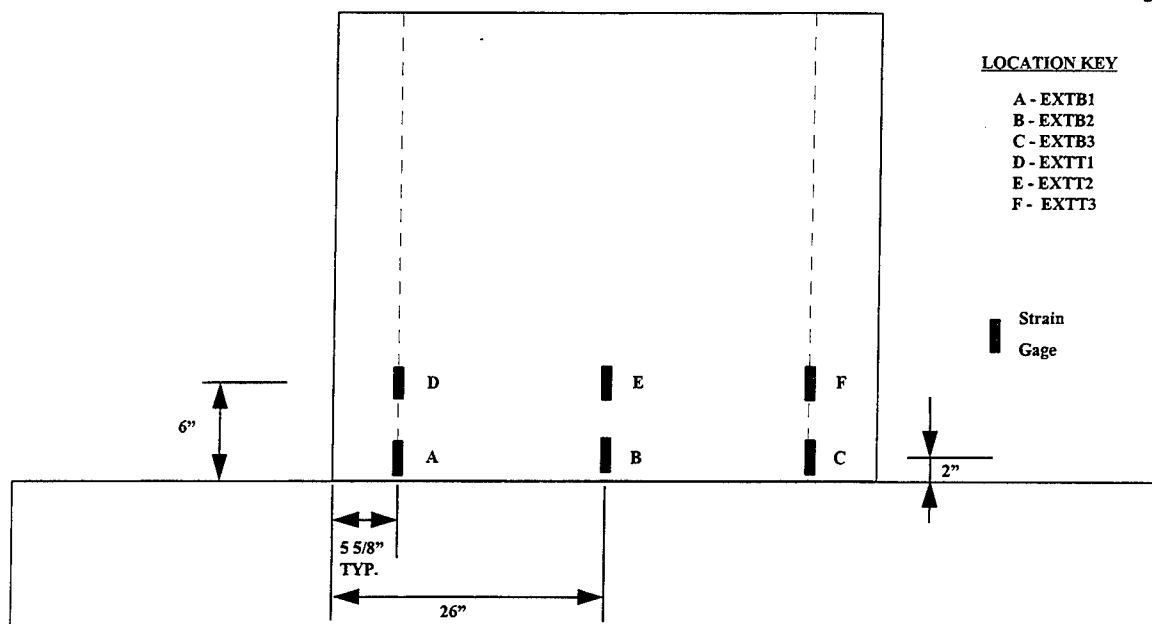


Figure 11. Location of strain gages mounted on exterior of wall, on west (compression) side of ITS-1 structure.

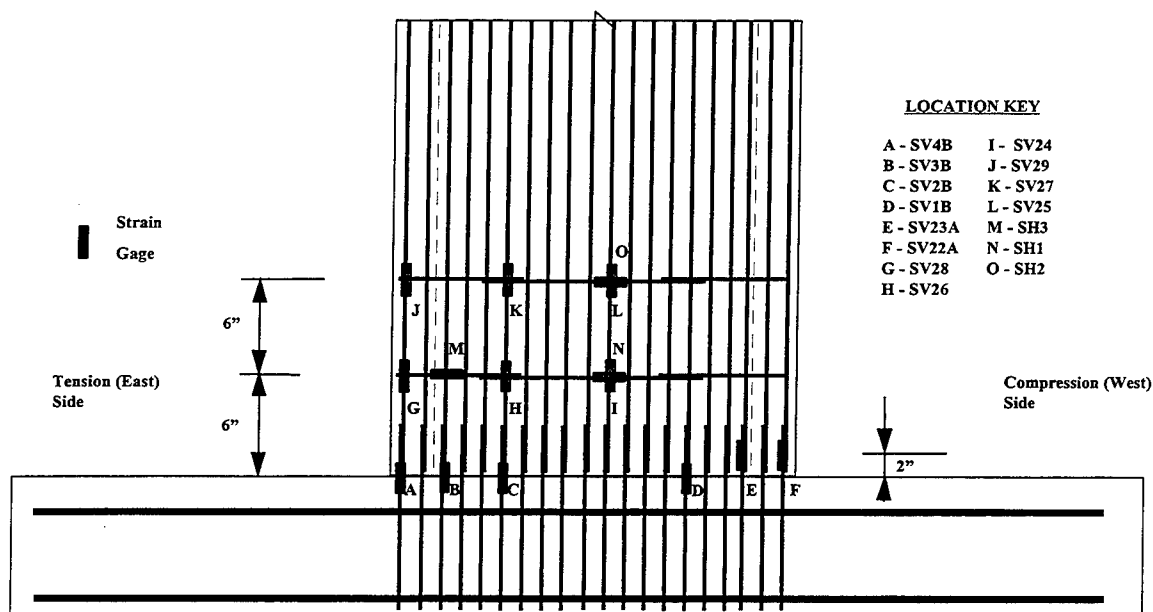


Figure 12. Location of strain gages mounted on exterior reinforcing layer, on north side of ITS-1 structure.

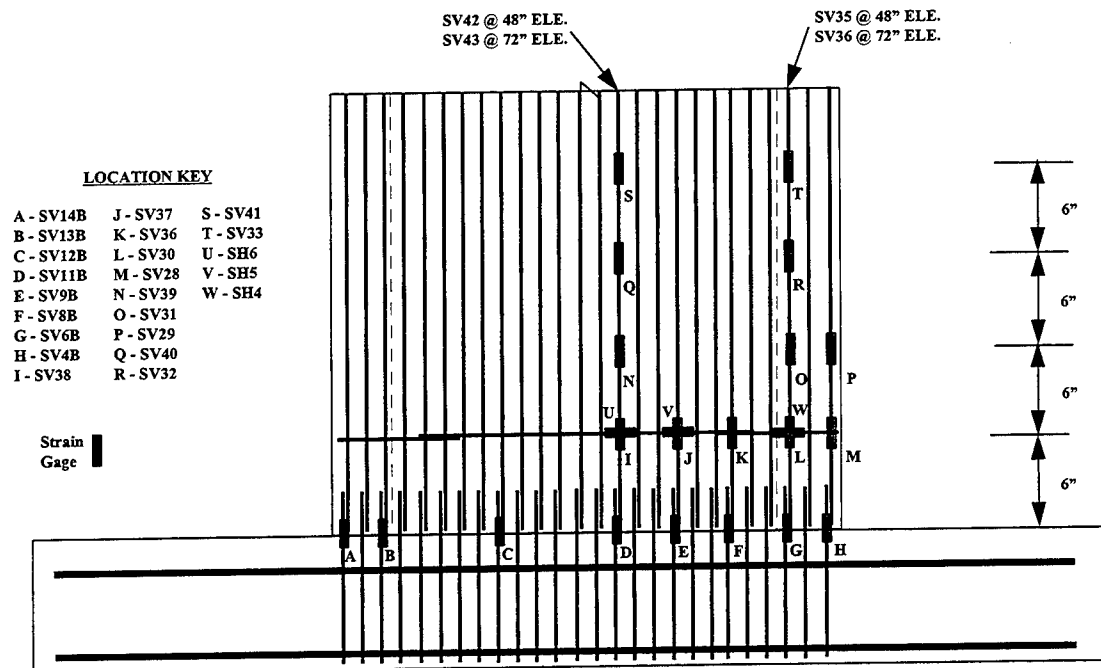


Figure 13. Location of strain gages mounted on exterior reinforcing layer, on east (tension) side of ITS-1 structure.

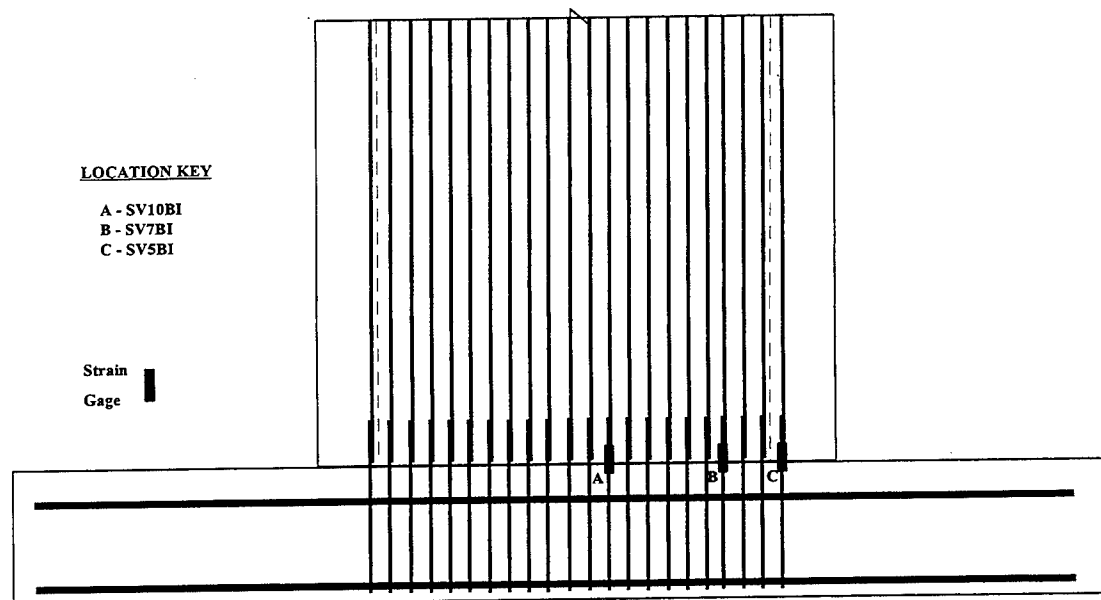


Figure 14. Location of strain gages mounted on inner reinforcing layer, on east (tension) side of ITS-1 structure.

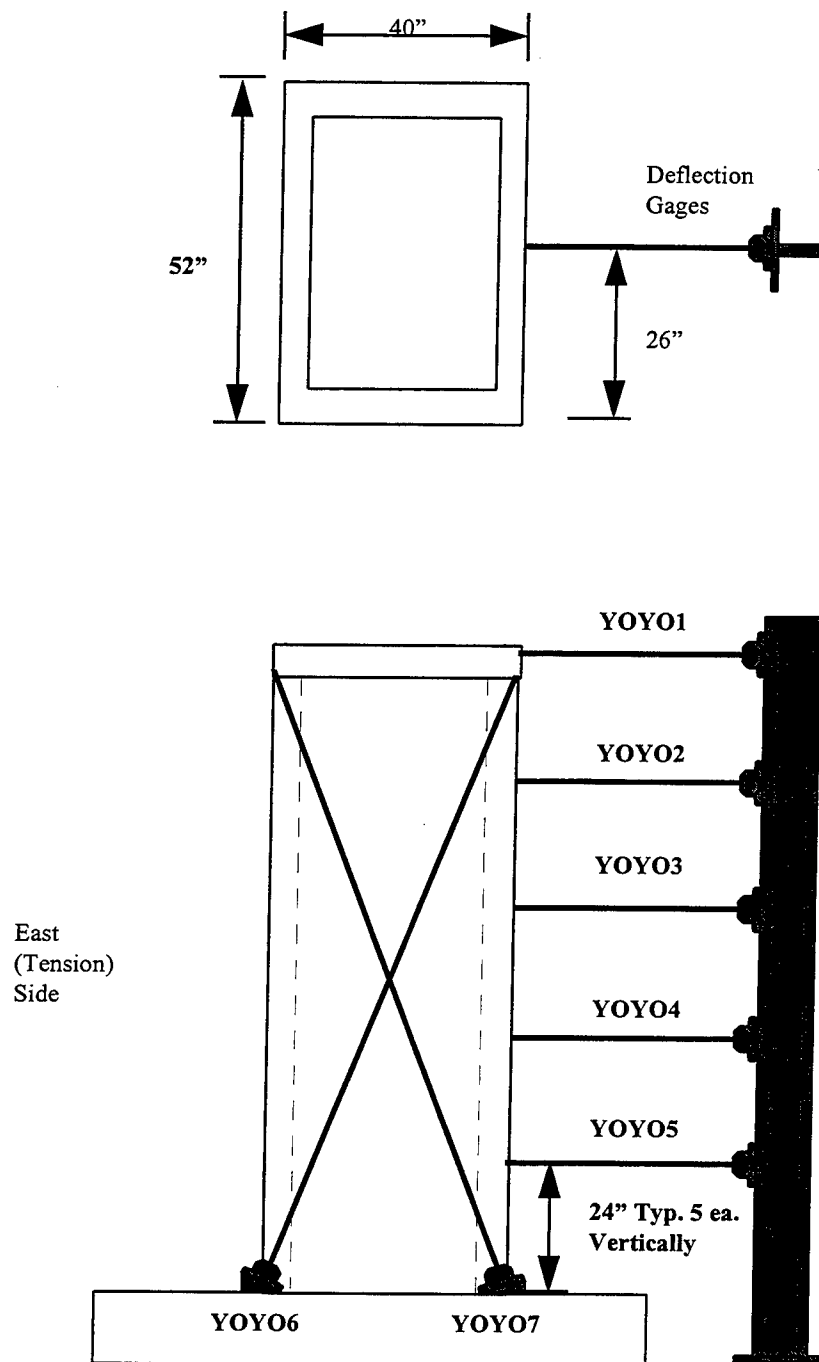


Figure 15. Plan view and elevation view of deflection gage locations on ITS-1 structure.

ITS-2 and ITS-3 Instrumentation Configuration

At the time of the ITS-2 and ITS-3 experiments, the data acquisition system used was capable of acquiring a total of 80 channels of data. The same instrumentation layout was used in both experiments. Two of the channels were allocated to the measurement of load and deflection in the 50-kip horizontal hydraulic loader, deflection was measured at 14 positions, and strain was measured at 66 positions.

Detailed locations of the strain gages can be seen in Figure 16 and Figure 17. Most of the strain gages were mounted at the base of the tower. These gages were mounted on the vertical reinforcing dowels so that the center of the gage was located at the cold joint at the base of the tower section or at 2 in. above the cold joint. This allowed for the measurement of the magnitude and distribution of the tensile and compressive strains in the concrete at this critical section. Strain gages were also located on the main vertical steel at intervals up the structure beginning at 6 in. from the base. In addition to providing a measurement of the magnitude and distribution of the strain, these measurements were expected to be used to calculate the rotational and deflection ductility of the structure.

Figure 18 and Figure 19 show the location of the deflection gages. These gages were Linearly Varying Deflection Transducers (LVDT), with working ranges that varied from 6 in. to 0.5 in. Ten of the gages were positioned to measure the horizontal deflection of the tower at various elevations at both the center and north edge of the west wall. Thus positioned, the gages were capable of obtaining information on both the

flexural and torsional responses of the structure. Four deflection gages were mounted vertically along the base of the north wall. These gages were expected to give a direct measurement of the rotation at this critical section.

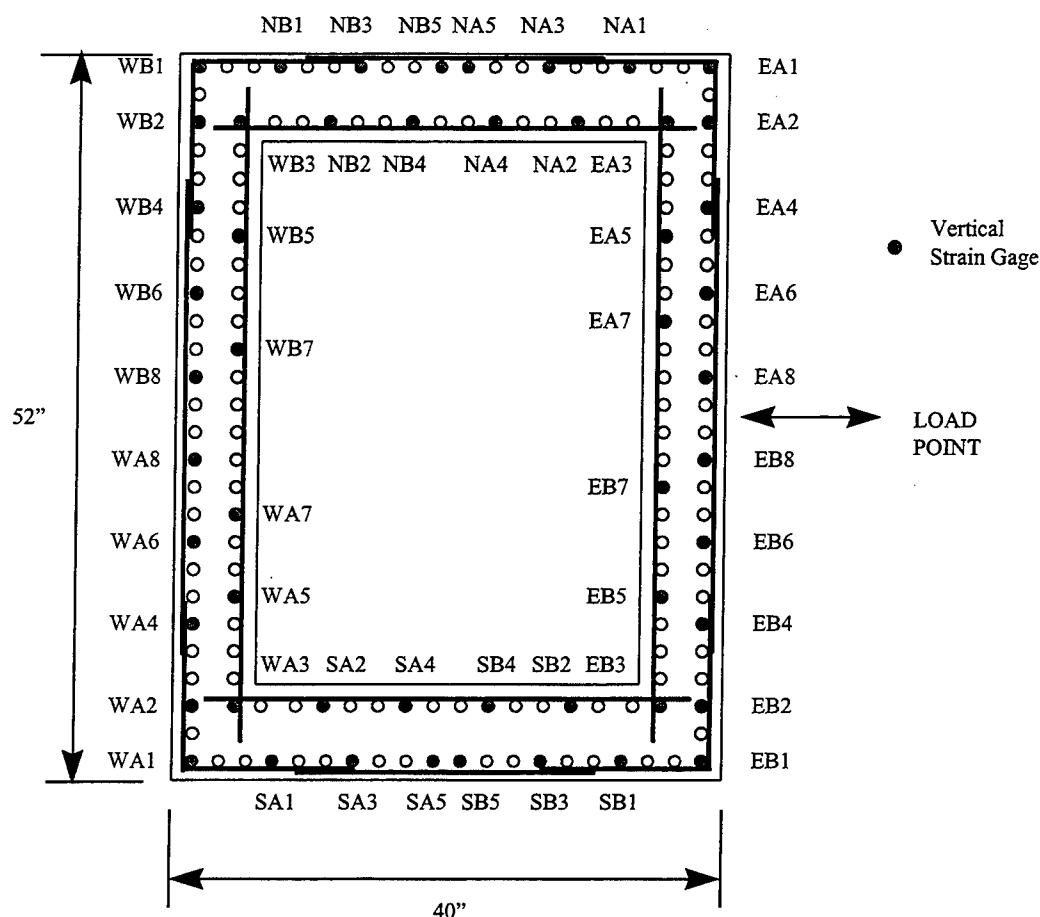


Figure 16. Location of strain gages placed on the vertical reinforcing at the base of the ITS-2 and ITS-3 structures. Gage designations containing the letter "B" were located at the base, those with "A" at 2 in. above the base.

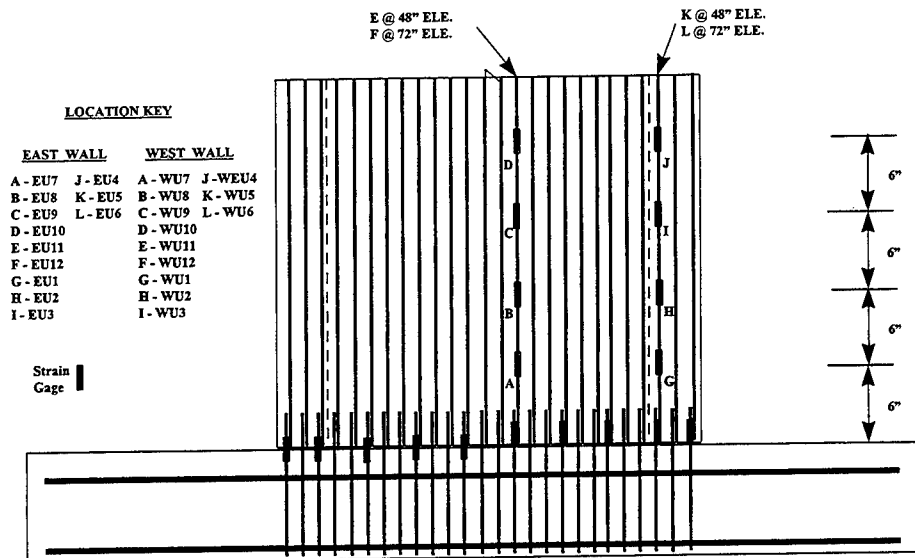


Figure 17. Location of strain gages mounted on exterior reinforcing layer, on east and west sides of the ITS-2 and ITS-3 structures.

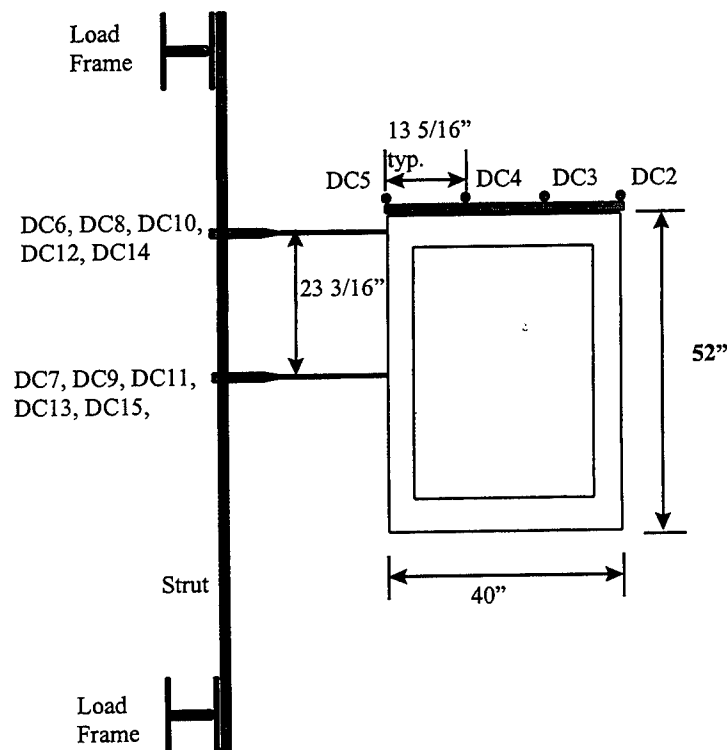


Figure 18. Plan view of deflection gage locations on ITS-2 and ITS-3 structures.

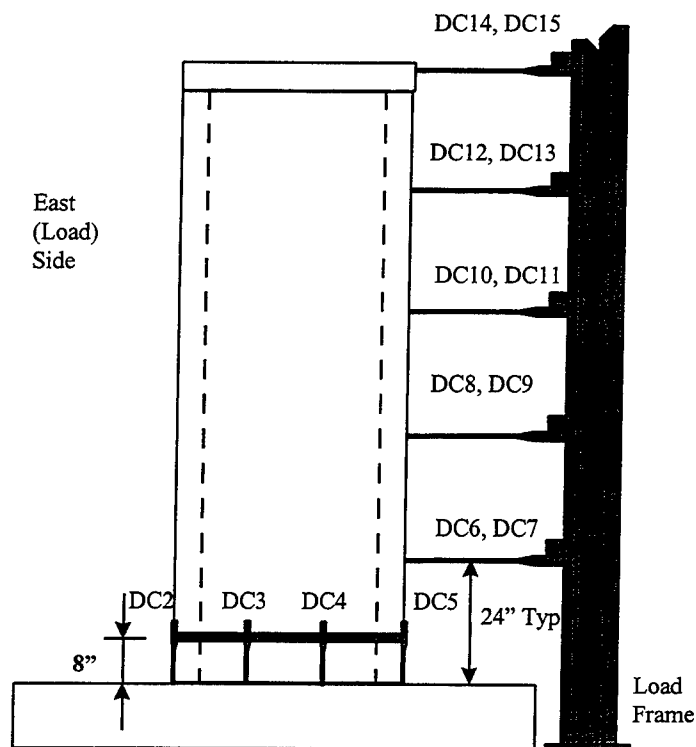


Figure 19. Side view of deflection gage locations on ITS-2 and ITS-3 structures.

Test Article Construction

The tower models were constructed within the Large-Scale Load Frame. The models were constructed within the frame to minimize the chance of damage to the models prior to experimentation. Construction in-place also allowed the use of a very close tolerance in the placement of hold-down bolts, minimizing this potential source of error in the experiment. These advantages out-weighed the disadvantage of occupying the frame for the entire construction process.

The 18-in.-thick bases were constructed first. The base reinforcing consisted of two layers of #6 bars laid out in a 6-in. by 6-in. grid tied to form a reinforcing bar cage

approximately 12 in. in depth. Figure 20 shows the ITS-2 cage placed in the base concrete forms. The vertical tower model reinforcement was placed in the base slab extending from the bottom of the slab to 4 in. above the base slab surface. Proper placement of the model reinforcement was assured by using a wooden template with holes drilled at the correct location for each bar. Figure 20 also shows the 2-in.-diameter steel conduit pipes used to form the hold-down bolt holes. These conduits extended 6 in. down into the load floor creating a very snug fit of the hold-down bolts. Concrete was placed in one lift in the base slab.

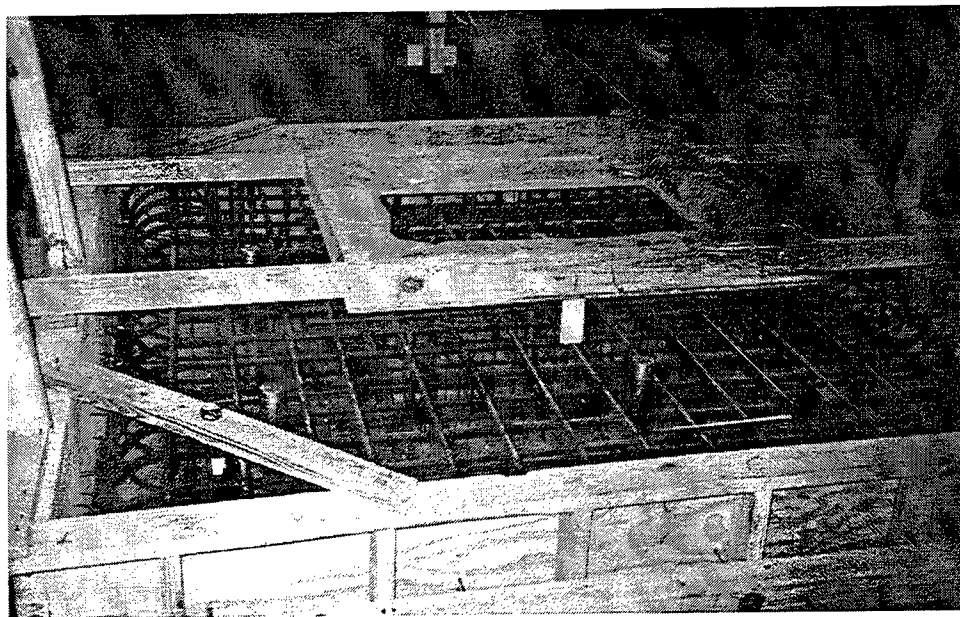


Figure 20. Base slab reinforcement, ITS-2.

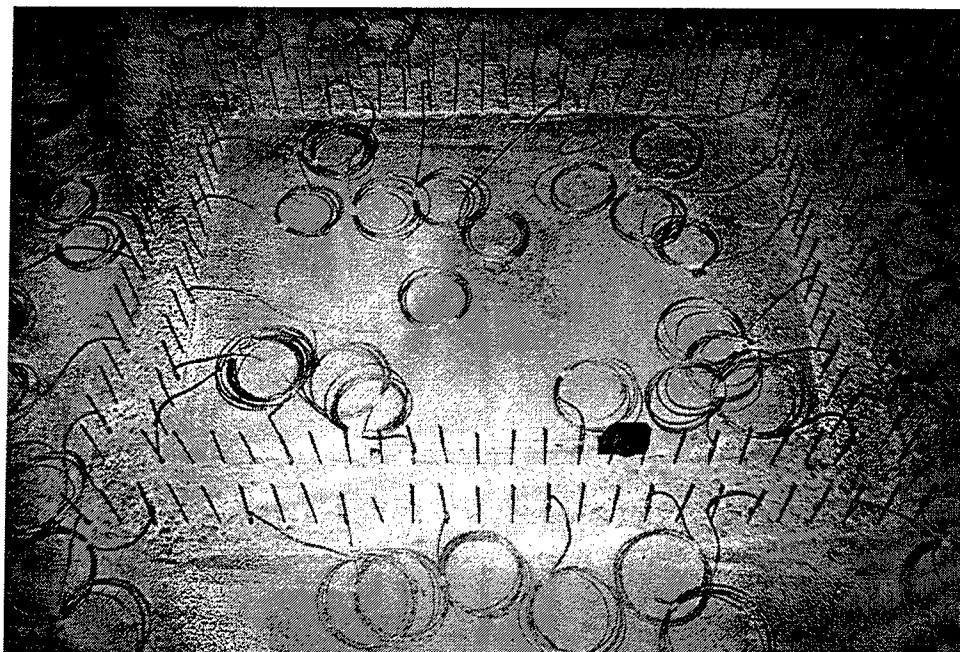


Figure 21. View of model reinforcement, after base slab concrete placement, ITS-2.

The tower section of each model was constructed on top of the base slabs. The intersection of the tower sections with the base slabs modeled the type of construction joint detail found in typical intake towers. A 4-in. length of tower reinforcing extended above the base slab to form a lap splice with the tower section vertical reinforcing. The base slab concrete in this area was sandblasted to remove laitance and promote proper adherence of the tower section concrete to the base slab. The inner forms were constructed, and tower section reinforcement was placed. Figure 21 shows a view of the construction joint at the base of the tower section for ITS-2. Figure 22, Figure 23, and Figure 24 show the completed tower section reinforcement cage for the ITS-1, ITS-2, and ITS-3 models, respectively.

For each model the tower section concrete was placed in two lifts to avoid excessive aggregate segregation during placement. First, the lower forms were constructed, and the concrete was placed. After a short curing time, the top surface of the bottom lift was sandblasted and the upper forms constructed. The top 8 in. of the outer form consisted of the horizontal load ring. After the upper lift was placed, the concrete was allowed to cure for one week, and the forms were stripped. The tower was painted flat white to increase crack visibility. The completed ITS-2 model can be seen in Figure 25 and Figure 26. The ITS-1 and ITS-3 models were virtually identical in appearance to the ITS-2 model. More pre-experiment photographs of each model will be presented in the experimental results chapter for each experiment.

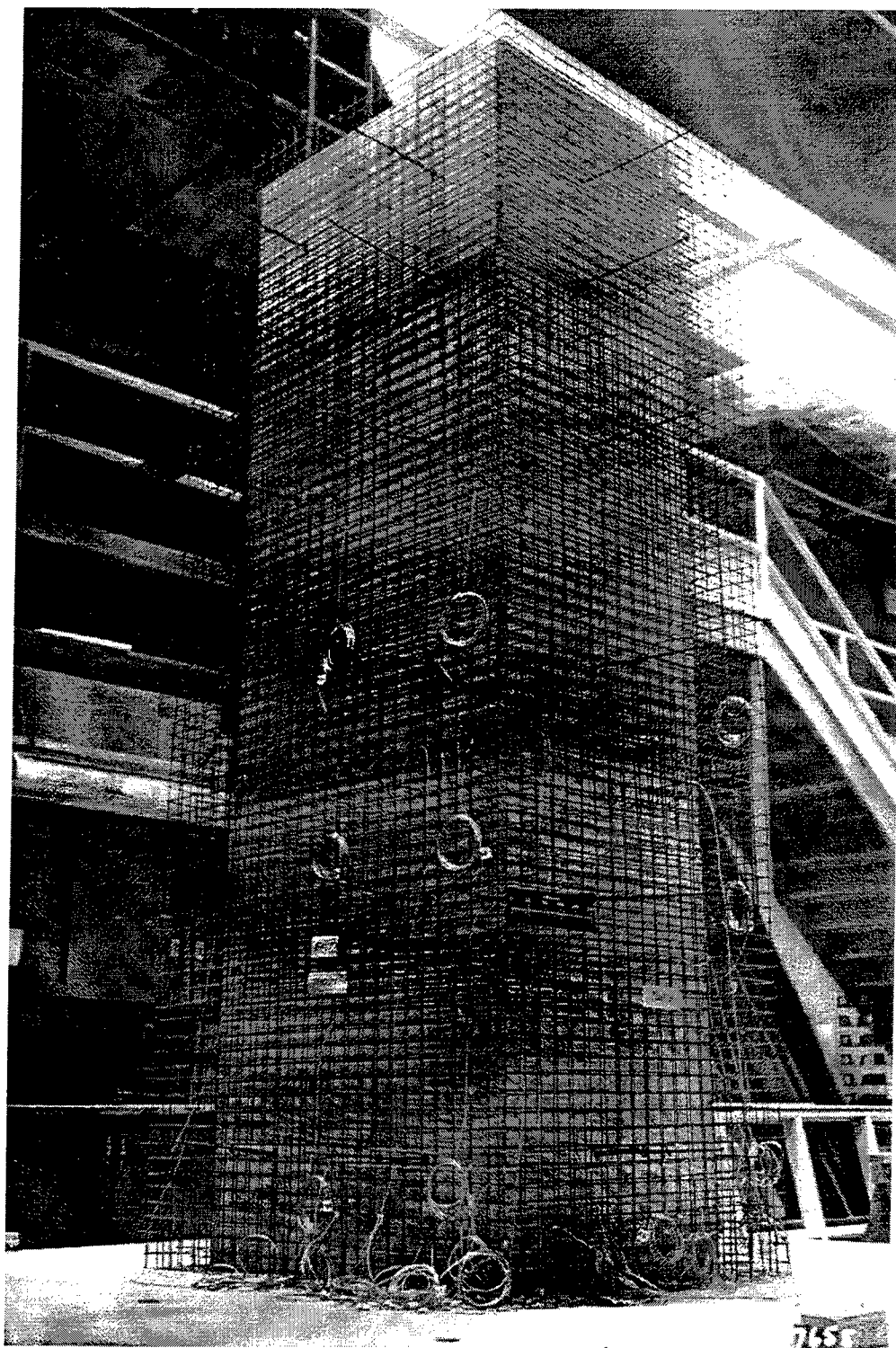


Figure 22. Completed reinforcing cage for ITS-1.

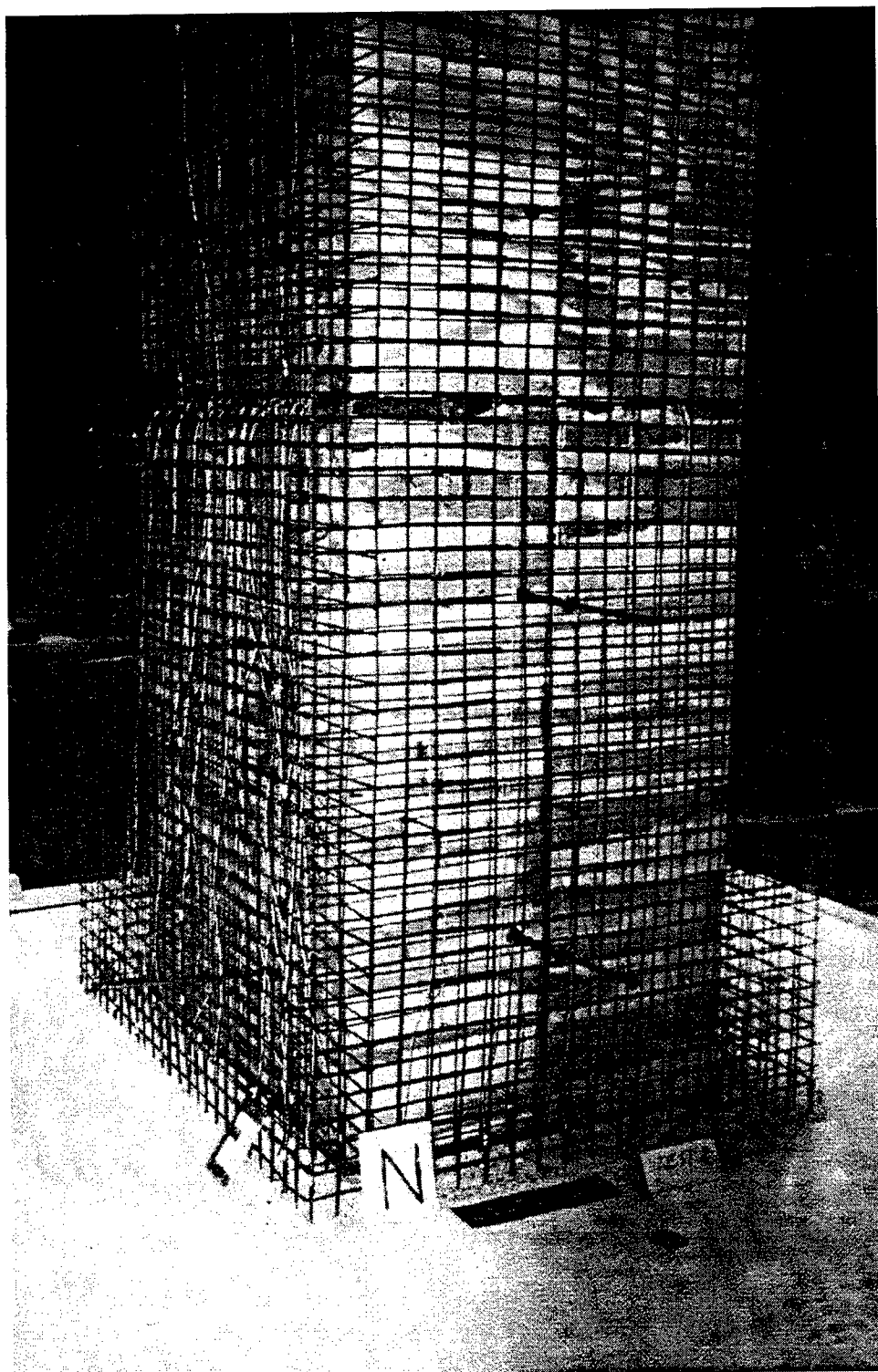


Figure 23. Completed reinforcing cage for ITS-2.

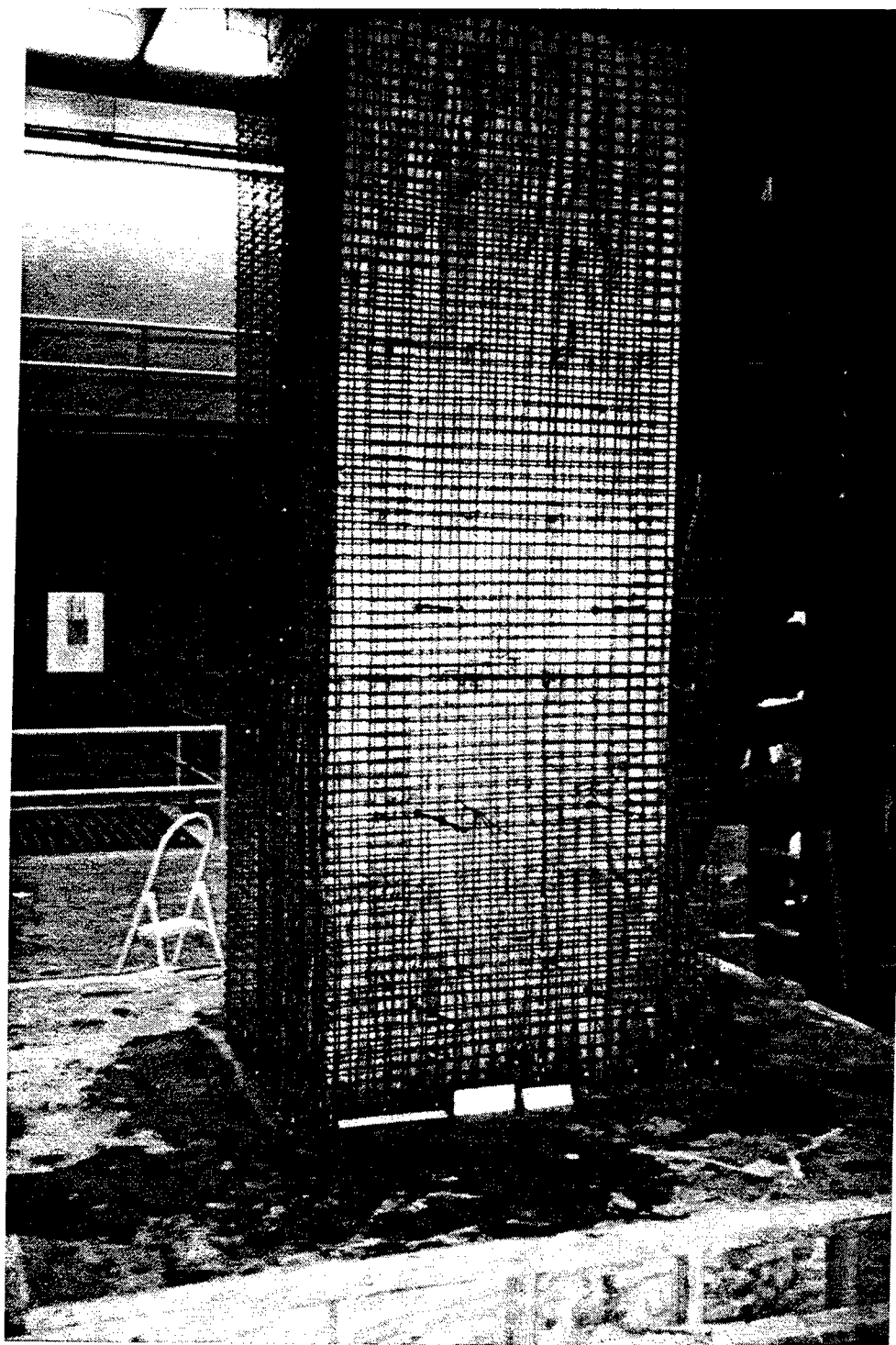


Figure 24. Completed reinforcing cage for ITS-3

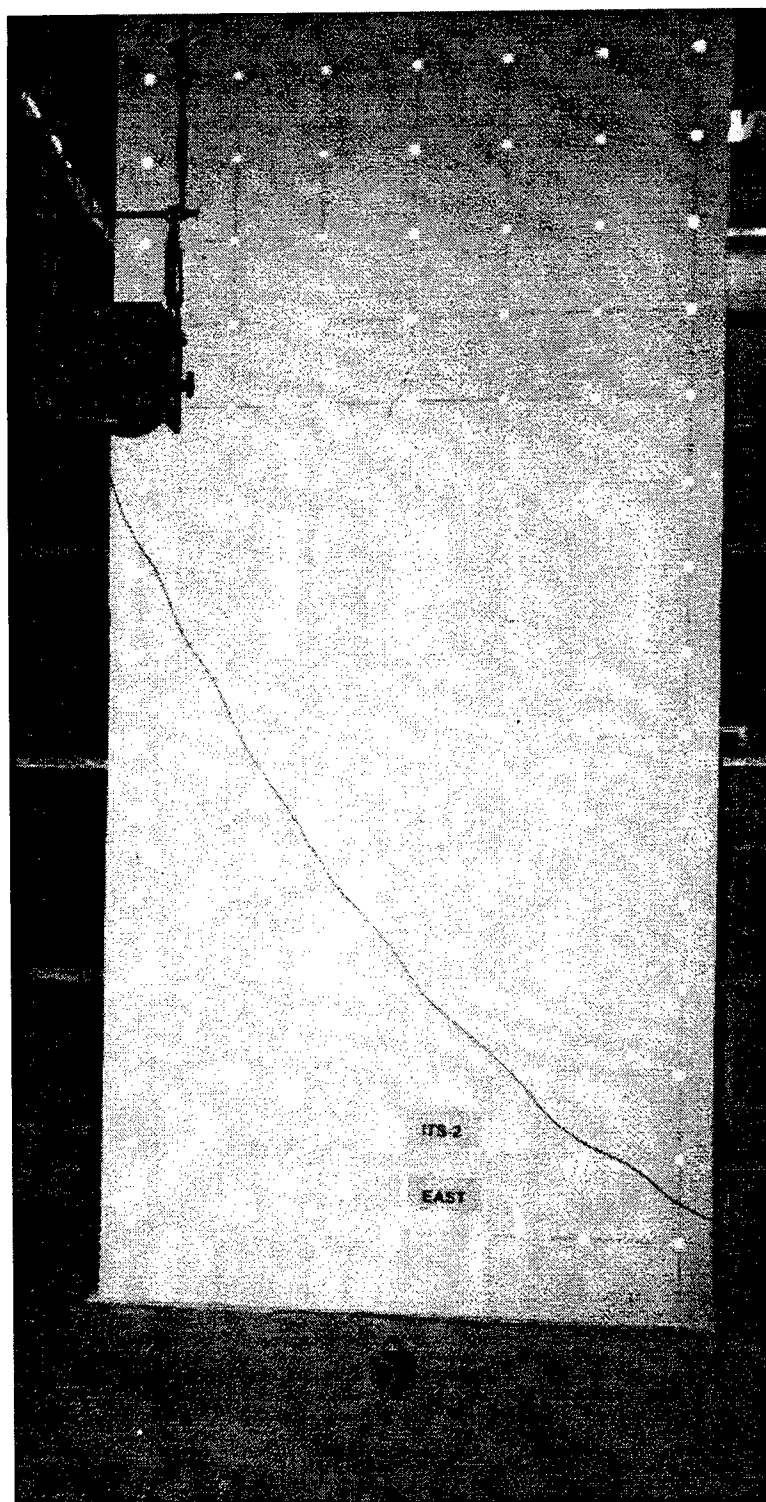


Figure 25. East side of complete ITS-2 structure.

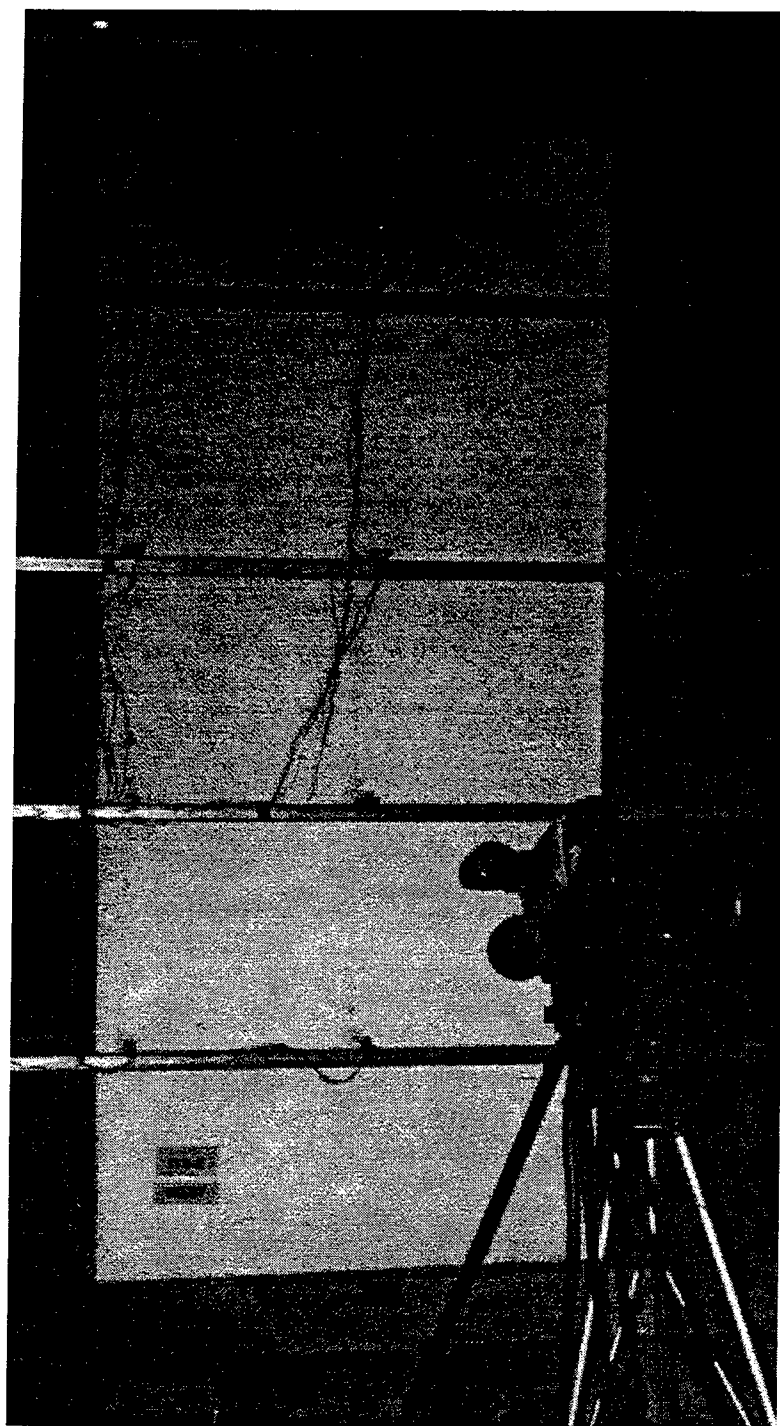


Figure 26. West side of complete ITS-2 structure.

ITS-1 and ITS-2 Material Properties

The properties of the concrete and steel used in the ITS-1 and ITS-2 structures are presented in Appendix B. The objective was to duplicate the materials as close as possible for these two models. The reinforcement used was D1 deformed wire. The yield strength of this wire, as delivered, was approximately 80,000 psi. In order to reduce this yield strength to the desired level, the steel was heated for 1-1/2 hr. at a temperature of 1,080° F, removed from the oven and allowed to air cool. This annealing process reduced the yield strength to approximately 41,000 psi, with a modulus of elasticity of 28,300,000 psi and a strain at yield of 0.0015 in./in. The approximate strain at rupture was 0.18 in./in. A sufficient quantity of steel was treated to construct two structures for use in the ITS-1 and ITS-2 experimentation.

Unconfined compressive tests were conducted on standard concrete cylinders on the day of the ITS-1 experiment. The concrete used in the ITS-1 reaction base had an average unconfined compressive strength of 4,920 psi. The first lift of the tower section had an average unconfined compressive strength of 3,820 psi and an average static modulus of 3,963,250 psi. The second lift of the tower section had an average unconfined compressive strength of 4,000 psi, and an average static modulus of 4,098,300 psi.

Unconfined compressive tests were also conducted on standard concrete cylinders on the day of ITS-2 experiment. The concrete used in the ITS-2 reaction base had an average unconfined compressive strength of 5,330 psi and an average static modulus of

4,942,100 psi. The first lift of the tower section had an average unconfined compressive strength of 4,010 psi and an average static modulus of 4,100,500 psi. The second lift of the tower section had an average unconfined compressive strength of 3,770 psi and an average static modulus of 4,029,225 psi.

ITS-3 Material Properties

The properties of the concrete and steel used in the ITS-3 structure are also presented in Appendix B. The objective was to increase the strength of the steel and decrease the strength of concrete from that used in the prior experiments. The reinforcement used was D2 deformed wire. The yield strength of this wire, as delivered, was approximately 73,000 psi. In order to reduce this yield strength to the desired level, the steel was heated for 2-1/2 hr. at a temperature of 1,050° F, removed from the oven and allowed to air cool. This annealing process reduced the yield strength to approximately 64,000 psi, with a modulus of elasticity of 28,500,000 psi and a strain at yield of 0.0023 in./in. The strain at rupture ranged from about 0.1 in./in. to 0.16 in./in.

Unconfined compressive tests were conducted on standard concrete cylinders on the day of the ITS-3 experiment. The concrete used in the ITS-3 reaction base had an average unconfined compressive strength of 2,040 psi and an average static modulus of 3,050,000 psi. The first lift of the tower section had an average unconfined compressive strength of 3,060 psi and an average static modulus of 4,180,000 psi. The second lift of the tower section had an average unconfined compressive strength of 2,660 psi and an average static modulus of 3,800,000 psi.

Experimental Procedure

As mentioned above, force was applied to the each model with servocontrolled hydraulic loaders. A vertical load was applied to the structure by two 50-kip loaders. A total load of 66 kips was applied throughout each experiment to simulate the dead load of an 80-ft-tall full-scale tower. Horizontal load was applied by a deflection-controlled loader at a rate of 0.01 in./sec. This horizontal deflection could be stopped and restarted at any time. In recording the motions, the negative excursions corresponded to a compression load in the ram and indicated an east to west motion. Positive excursions corresponded to tension loads in the ram and indicate a west to east motion. Each experiment was put on hold frequently to allow for modal surveys; vertical loads were maintained during these holds.

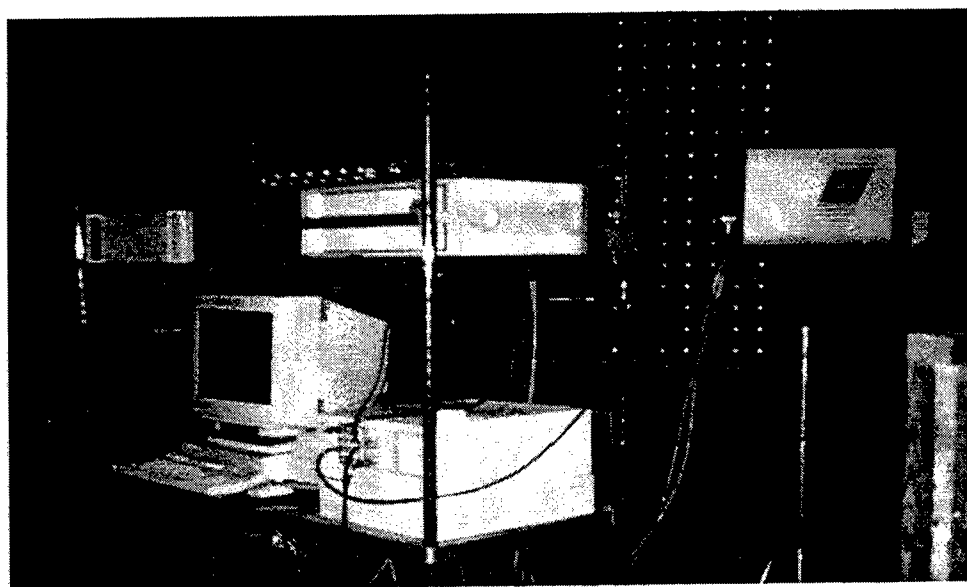


Figure 27. Lazon modal survey system.

Active data were digitally acquired at a rate of two samples per second. This sampling rate was maintained throughout each experiment, including when application of horizontal load was halted. It was felt that acquisition of data during these holds would be important to capture any relaxation and reloading that might occur.

Data were also acquired on the natural frequencies and mode shapes of the structure. Modal surveys of the model were conducted before, during, and after testing, using the LAZON 7000 system (Figure 27). Photographic support included video cameras, as well as black and white and color still photography. Photographic coverage included before, during, and after experimentation.

CHAPTER 4

ITS-1 EXPERIMENTAL RESULTS

Introduction

The ITS-1, one-way excursion experiment was completed on September 26th, 1995. The one-way excursion horizontal load was applied to induce a deflection in the east to west direction. The experiment was temporarily stopped six times to allow for the modal survey, measurement, and photography of the structure. The experiment required approximately 4 hrs to conduct. Seventy-two channels of active data were recorded, and 10 modal surveys were conducted. Also, passive measurements of structural response were recorded. Video and still photography were included.

Structural Response

Photographs of the response of ITS-1, at an imposed deflection of 2 in., are presented in Figure 28 through Figure 33. Visual inspection of the model during loading led to the following observations. Damage to the model was limited to the bottom of the tower section at the interface with the rigid base. The damage consisted of one tension crack that extended across the east (tension) wall and into both the north and south side walls. The tension crack did not appear to indicate simply a failure of the cold joint

located in this area. The crack did not follow the interface of the cold joint, but rather appeared to dip downward below the cold joint into the concrete base material before returning to the surface at the far side of the wall. No evidence of a crushing failure of the concrete in the west (compression) wall was observed. Figure 33 shows a close-up view of the south corner of the east wall at the maximum imposed deflection of 2 in. A ruptured reinforcing bar is clearly visible to the left with the necking and elongation that are typical of a ductile tension failure. Ruptured reinforcing bars were visible across the entire east wall as well as for a distance of approximately 21.5 in. along the north wall and 16.5 in. along the south wall, as measured from the east wall. The crack sloped downward into the experimental specimen and extended below the interface of the tower section and into the base slab.

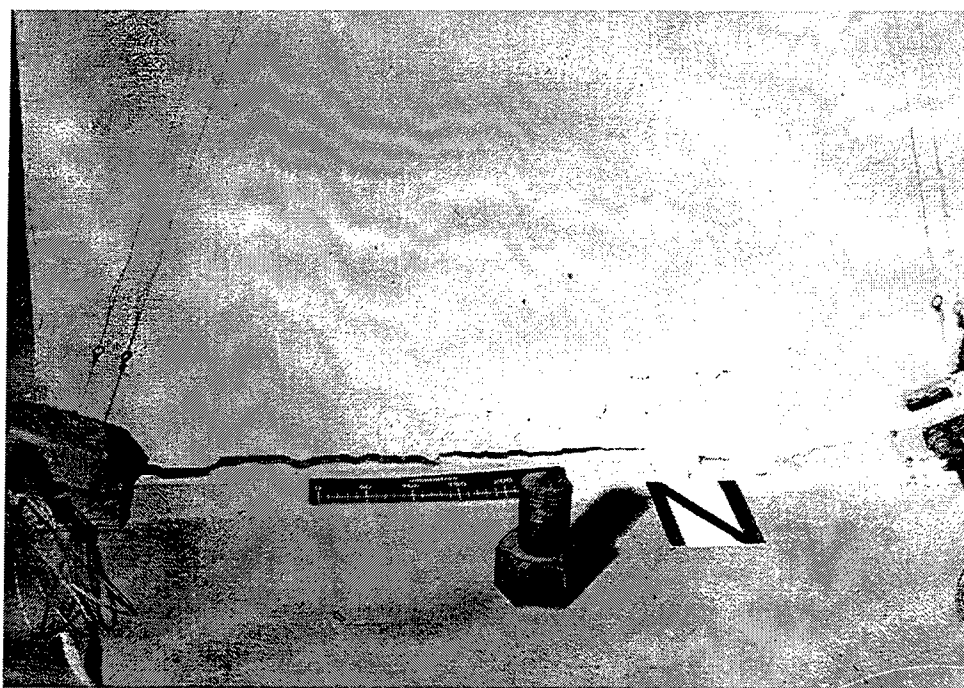


Figure 28. ITS-1, post-experiment view of north wall, imposed top deflection of 2 in.

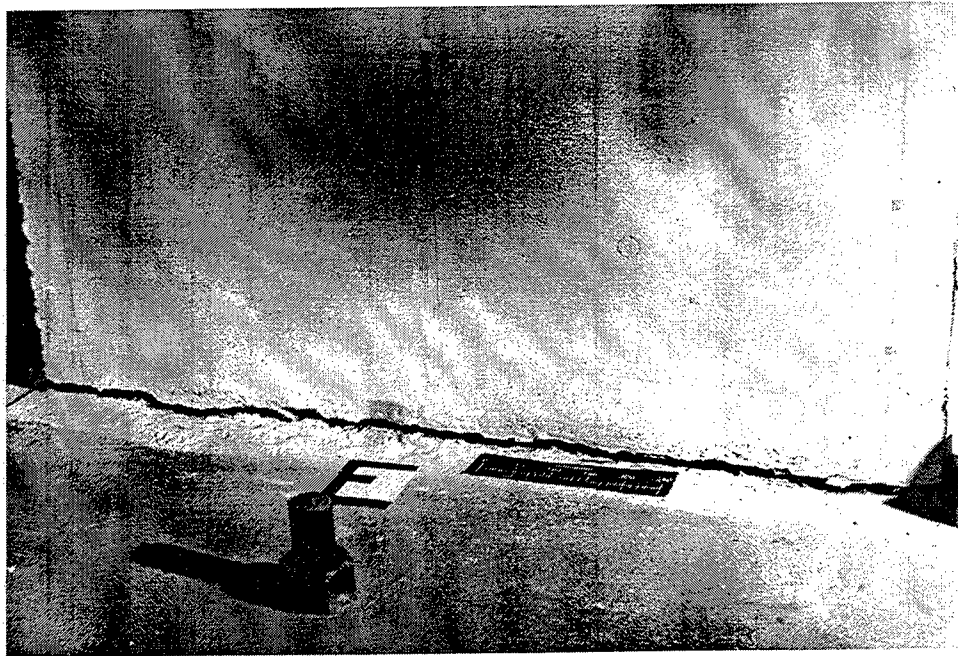


Figure 29. ITS-1, post-experiment view of east (tension) wall, imposed top deflection of 2 in.

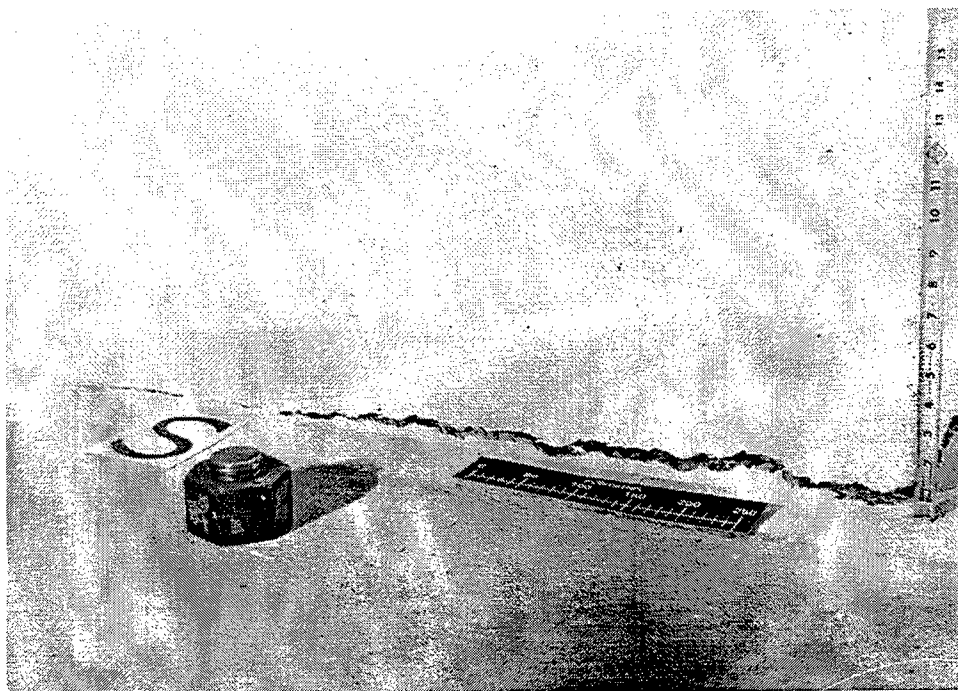


Figure 30. ITS-1, post-experiment view of south wall, imposed top deflection of 2 in.

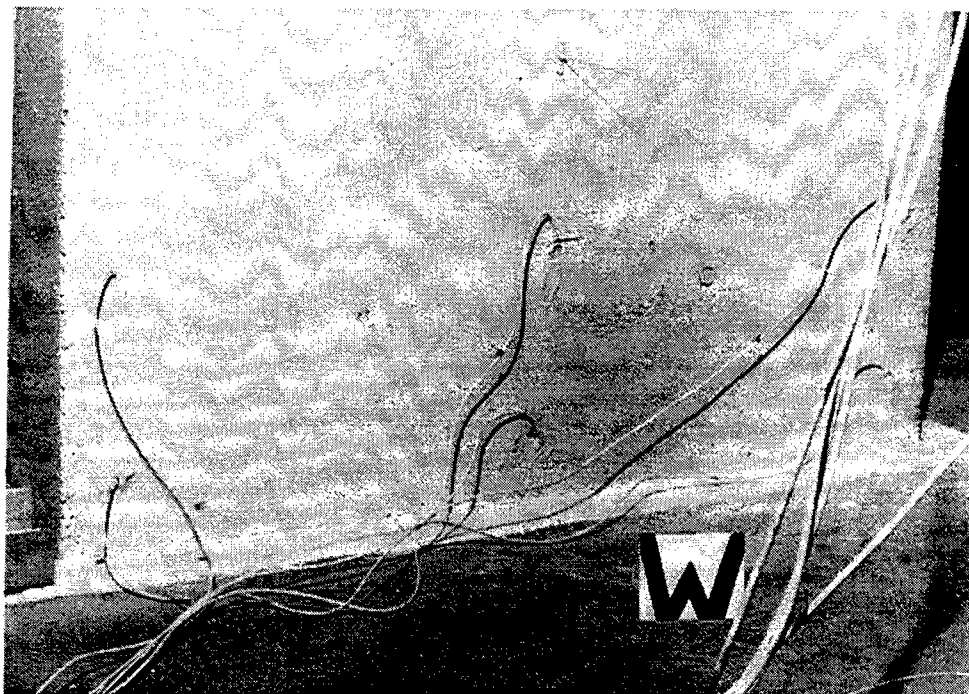


Figure 31. ITS-1, post-experiment view of west (compression) wall, imposed top deflection of 2 in.



Figure 32. ITS-1, close-up view of interior south-east corner , imposed top deflection of 2 in.

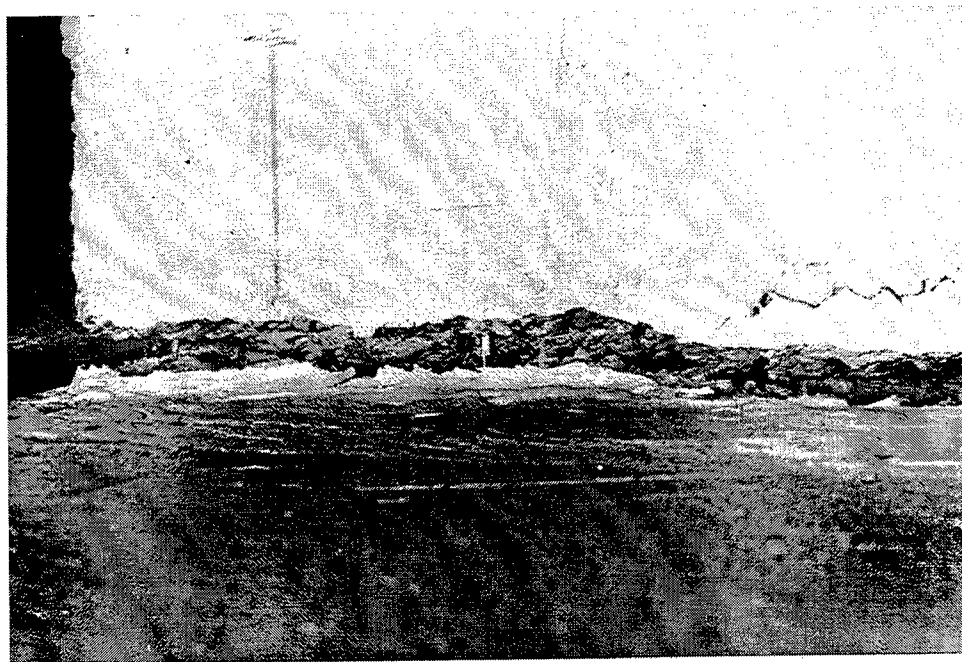


Figure 33. ITS-1, close-up view of south-east corner, imposed top deflection of 2 in.

Active Instrumentation Response

Seventy-two channels of active data were recorded during the experiment. Of these channels, 57 were strain measurements, 6 measured deflections of the model, and 2 measured deflection and load in the horizontal hydraulic loader. The constant vertical load applied to the top of the structure was monitored but not recorded. Recording took place at 10 samples per second and, thus, during the approximate 4 hours of the experiment, a total of about 1,000,000 samples were taken for the 72 channels. All plotting and data analyses for ITS-1 were conducted with the structural response plotted against the deflection imposed on the model by the horizontal loader, as measured by the loader LVDT gage.

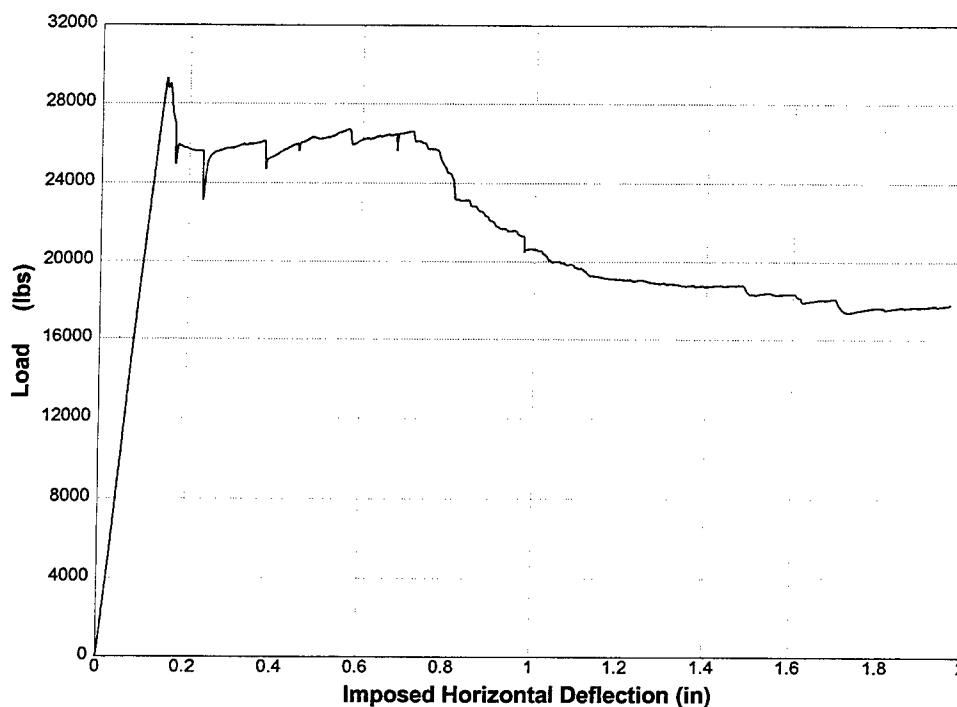


Figure 34. Horizontal load versus horizontal loader deflection.

Load Response

The most important response measured in this experiment is the relationship of the horizontal load imposed at the top of the structure to the horizontal deflection measured at the same location. This relationship is the most direct measurement of the deflection ductility of the structure and also relates indirectly to the curvature ductility. Figure 34 shows the force imparted by the horizontal loader versus the deflection of the loader. The force was measured by a load cell mounted on the loader; deflection was measured by the loader internal LVDT gage.

Examination of the load-deflection history shows a linear-elastic response up to a deflection of approximately 0.15 in. with a load of approximately 29,300 lb. At this point the section appears to crack, resulting in a 11.5-percent reduction in the load carried by

the structure to 25,900 lb at a deflection of approximately 0.175 in. The decrease in load capacity after cracking was expected as the cracking moment capacity of the section had been calculated to be greater than the yielding moment in this lightly reinforced member. An abrupt downward excursion of the load curve below the general trend of the curve at about 0.17 in. is due to the fact that the experiment was put on hold at this deflection so that a modal survey could be conducted. During the delay, and subsequent holds, the structure relaxed slightly causing a reduction of the load carried. When the experiment was restarted, the load curve rose back to approximately the pre-hold value and continued. Therefore, the modal survey holds conducted at the deflections of 0.17 in., 0.23 in., 0.38 in., 0.45 in., 0.68 in., 0.98 in., and 1.98 in. apparently had little effect on the overall response of the structure.

After the decrease in load to approximately 25,900 lb at 0.175 in., a gradual increase in load of about 2.3 percent of the peak value, to approximately 26,600 lb at a deflection of approximately 0.72 in. was experienced. The increase in load may reflect the redistribution of stress in the section as well as strain hardening of the reinforcing bars as yielding occurred. At about 0.72 in., a pronounced decrease in load began. There was a gradual reduction of approximately 30 percent of the peak value, resulting in a value of approximately 17,800 lb at a deflection of approximately 1.96 in. The decrease in load reflects the rupturing of steel as deflection continued. The load appears to be asymptotic to a value of approximately 17,800 lb, reflecting the diminishing contribution of the

reinforcing steel to the capacity of the section to the point where the simple restoring moment of the actual and imposed dead load contributed the majority of resistance.

The deflection ductility is readily apparent on further examination of the load deflection curve. Deflection ductility can be defined as the ratio of the deformation that a structure or element can undergo without a significant loss of initial yielding resistance to the initial yield deformation [4]. Using this definition, with the deflection at initial yielding of approximately 0.175 in., a maximum deflection before significant loss of initial yielding resistance of approximately 0.75 in., the deflection ductility is approximately 4.3.

A deflection ductility of 4.3 is a significant finding in that displacement ductilities of conventionally reinforced concrete members can be expected to be in a range of between 3 and 5. In accordance with current Corps criteria, a similar ductility allows load reduction factors in the range of between 1/2 and 1/3. However, load reduction is only allowed if it can be demonstrated that brittle failure mechanisms do not lead to an unacceptable strength reduction with cyclic loads. This was not a cyclic experiment and therefore can only be used to demonstrate that the experiment model has the potential for significant ductility. The ITS-2 and ITS-3 experiments examined how much of this ductility is available under cyclic loads.

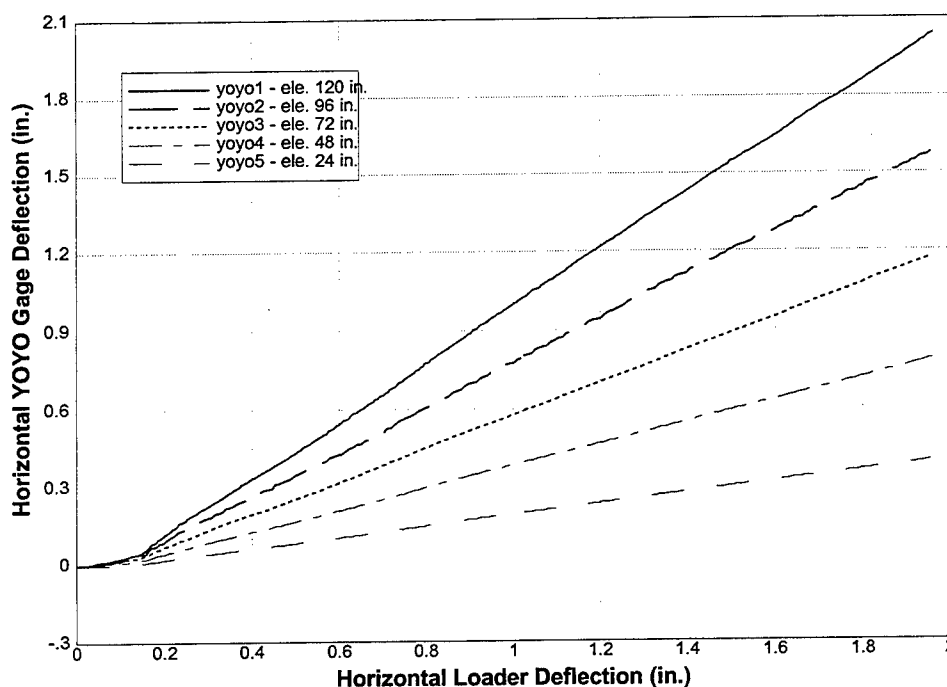


Figure 35. Horizontal deflection at various elevations, plotted against imposed loader deflection.

Deflection Response

Horizontal deflections were measured at 2-ft intervals along the height of the structure. These measured deflections are shown plotted against the recorded movement of the loader deflection (imposed horizontal loader deflection) in Figure 35. Two distinct regions can be seen in the plot. The curve changes shape and slope at the imposed deflection of approximately 0.15 in. This is the same deflection that corresponds to the onset of cracking, as observed in the load deflection curve discussed in the previous section.

Both the pre-cracking and post-cracking deflections were closely examined. The pre-cracking deflections were relatively small for accurate measurement with the gages

used; however, some trends were apparent. Curves were fit to the data and used to generate an approximate deflected shape of the structure just prior to cracking, as shown in Figure 36. The deformed shape of the structure does not appear to be that of a cantilever beam. A cantilever beam would be expected to exhibit a shape described by a second-order equation without an inflection point. The observed deflected shape appears to have an inflection point, or reversal in curvature, somewhere in the upper third of the structure. The observed shape implies that a restraining moment may have existed at the top of the structure. The apparent moment may have been the result of an inadvertent restraint of the top of the structure by the roller apparatus used to apply vertical load. The apparent restraining force does not appear to affect the post-cracking response. The pre-cracking deflections measured by these gages were close to the lower limit of accepted accuracy of the gages; thus, detailed conclusions as to the deflected shape based on these measurements should be viewed with some degree of skepticism. The vertical load applicator was redesigned to reduce any inadvertent restraint in the ITS-2 and ITS-3 experiments.

The horizontal deflections measured after cracking were very linear in nature, and first-degree curves fit to these data show a very high degree of correlation. The slopes of the curves corresponded to the relative heights at which the measurements were made, implying that a large part of the measured deflections was due to a rigid-body rotation of the tower. The deflected shapes of the structure generated from these data (Figure 37)

were also linear, and the nature of these curves tends to confirm that rigid-body rotation of the tower dominated its post-cracking deflection.

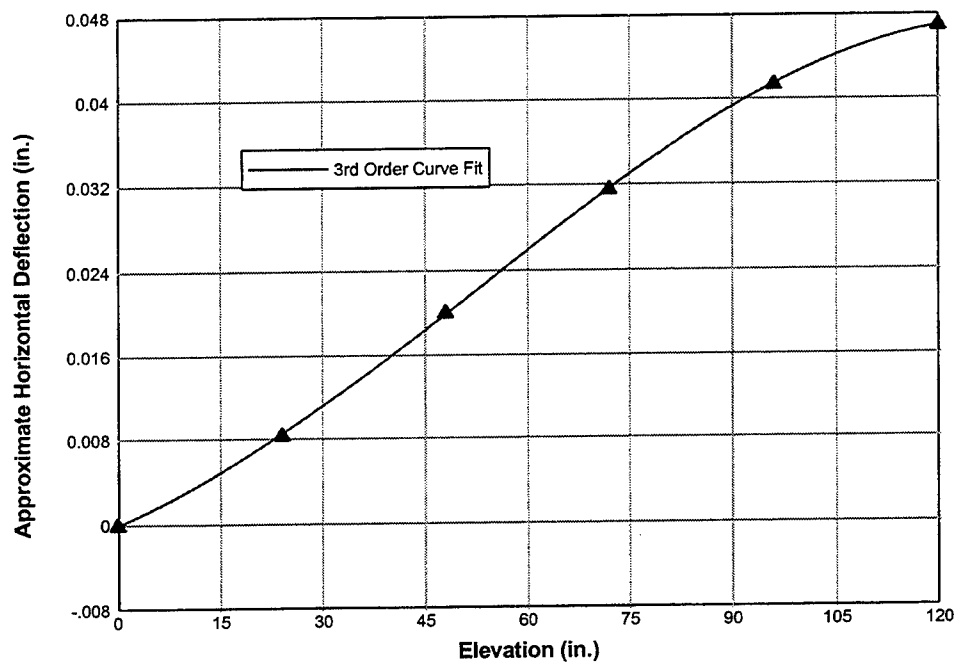


Figure 36. Approximate structure deflected shape just prior to cracking.

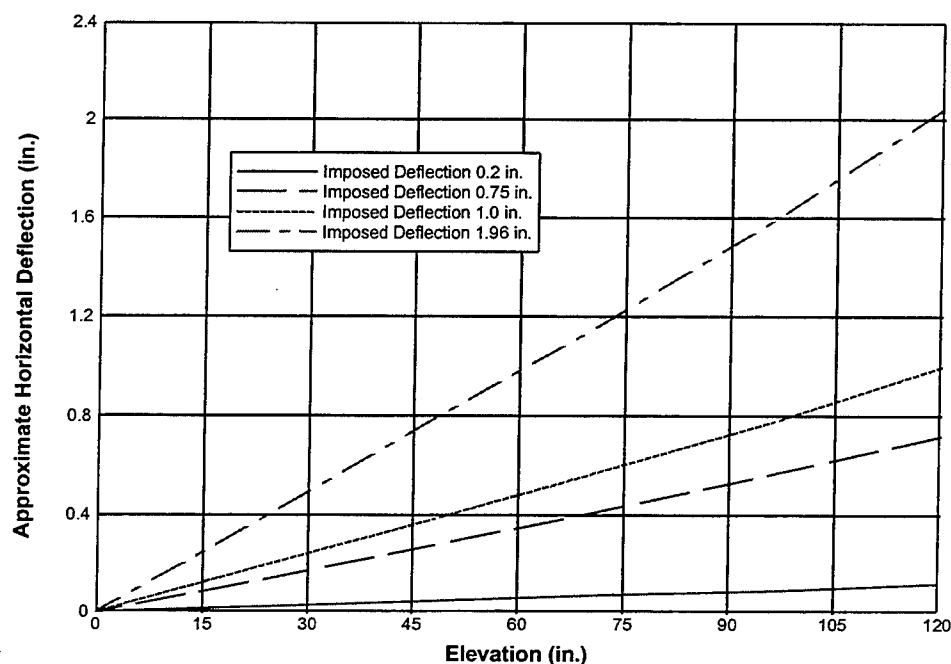


Figure 37. Structure deflected shapes after cracking.

Strain Response

Fifty-seven strain gage measurements were made during the ITS-1 experiment. Both vertical and horizontal gages were located throughout the model, with most of the gages located in the expected failure zone at the base of the tower. A personal computer mapping program, Surfer, was used to generate, from the recorded data, three-dimensional (3-D) representations of the distributions of the strains in the model. The generation of these 3-D representations required a considerable data reduction effort. However, the visualization of the results of the large number of measurements, in a cogent form, was well worth the effort.

Figure 38 shows the strain distribution for the outermost gages in the east (tension) wall up to an imposed horizontal loader deflection of about 0.17 in. It is evident

that the strains were maximum at the location of the side walls, as is to be expected due to the redistribution of load to the rigid side walls. The maximum strain at an imposed deflection of approximately 0.15 in. was approximately 300 microstrain. Shortly after the imposition of this deflection, the section apparently cracked. The post-cracking strains are not shown in Figure 38 because the post-cracking tensile strain measured by a gage is determined by whether or not the gage happens to fall exactly within the crack path. Given the low steel percentage in the model, it would be expected that the actual state of strain within the crack would quickly enter into the plastic regime. Reinforcement located just above or below the crack would likely remain in the elastic range. A strain distribution generated using data from gages within and outside the crack would be misleading.

Figure 39 shows the strain distribution for the outermost gages in the north wall up to a horizontal loader deflection of about 0.17 in. The east (tension) wall is to the left while the west (compression) wall is to the right of the graph. An initial compressive strain was present across the section due to the imposition of the model dead load by the vertical loaders. With the increase in imposed horizontal deflection, the strain distribution quickly resolves into well-defined compressive and tensile regions, with the neutral axis located at about 4 in. to the compressive side of the center of the wall. The maximum tensile strain, at an imposed deflection of approximately 0.15 in., was approximately 300 to 400 microstrain. Cracking occurred shortly after the imposition of this deflection. The beginning of plastic straining can be seen in the gage locations that

intersected the crack. As in the east (tension) wall plot, the post-cracking strains are not shown for the reasons cited above.

Figure 40 shows the strain distribution for the outermost gages in the west (compression) wall up to a horizontal loader deflection of about 2.0 in. As for the east (tension) wall, it is evident that the strains were maximum at the location of the side walls. The maximum compressive strain at an imposed deflection of 0.5 in. appears to have been approximately 700 microstrain. This relatively large number is based upon one gage and hence may be suspect. After an imposed deflection of about 1.6 in., Figure 40 indicates that the wall began to go into tension, implying that the neutral axis was located to the exterior of the outermost layer of steel. The maximum tensile strain was about 400 microstrain, a value that is close to the strain to be expected near the tensile capacity of concrete.

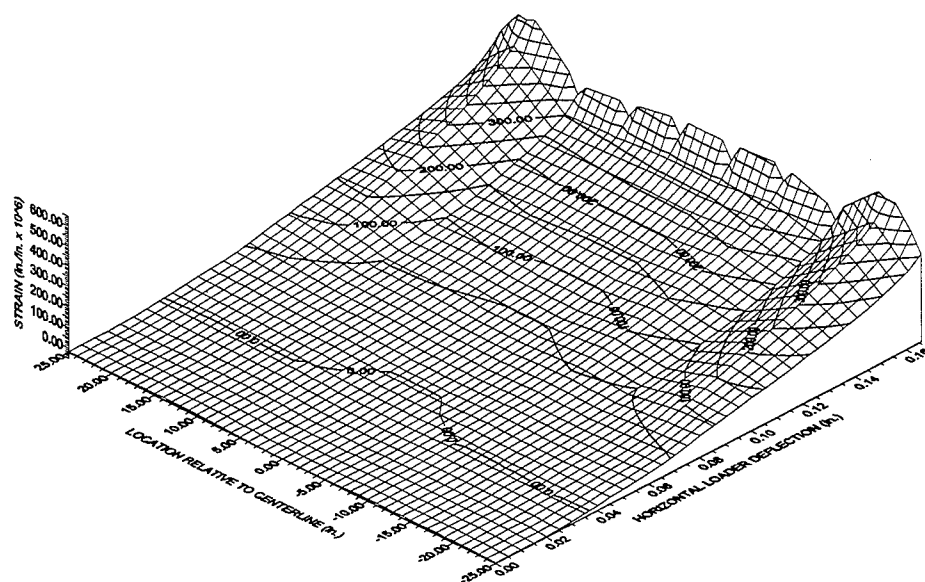


Figure 38. Distribution of vertical strain in outermost reinforcing bars in the east (tension) wall up to initial yielding.

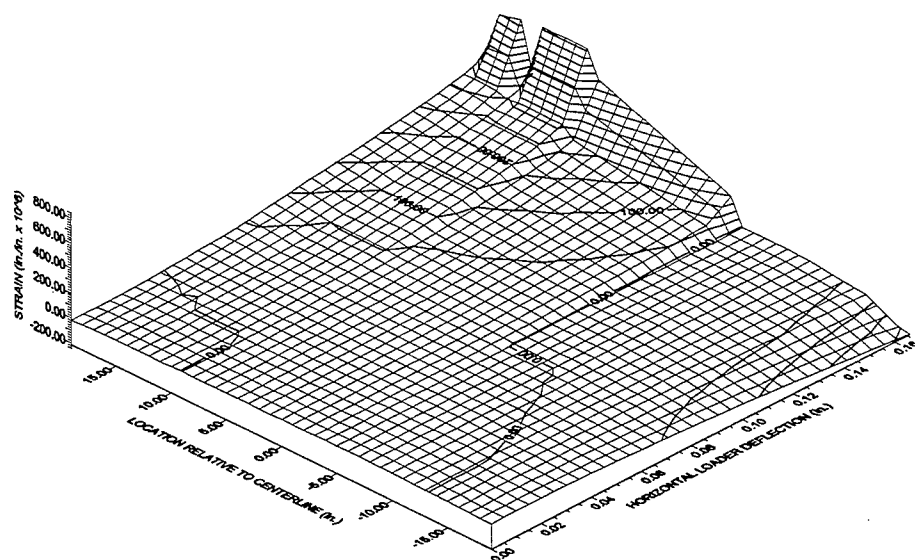


Figure 39. Distribution of vertical strain in outermost reinforcing bars in the north wall up to initial yielding.

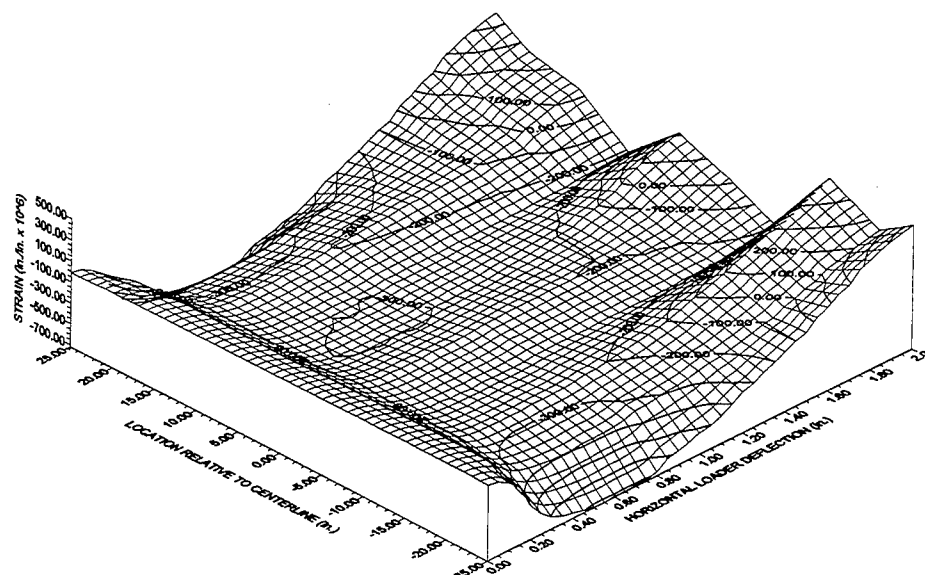


Figure 40. Distribution of vertical strain in outermost reinforcing bars in the west (compression) wall at 2 in. elevation, up to final deflection.

Figure 41 and Figure 42 show the strain distributions generated from the exterior gages mounted on the surface of the west (compression) wall at an elevation of 2 in. and 12 in. The fact that there were only three gages at each elevation limits what can be deduced about the detailed distribution of strains; however, general trends can be noted. The distribution of compressive strains appears to be reversed from that of the interior reinforcing bar gages discussed in the prior section. For the exterior gages, the maximum compressive strains are located in the center of the wall. This seems to be a real phenomenon, given that the exterior gages at both elevations reflect the same trend. The magnitudes of the strains were similar to those measured on the interior, but there was no reversal into tensile strains at large imposed horizontal deflections. The lack of tensile strains could be expected as the neutral axis could not extend beyond the boundary of the base of the structure without the system becoming unstable. The maximum compressive

strain at an imposed deflection of about 2.0 in. appears to have been approximately 1,500 microstrain, a value that is about half of the strain to be expected near the compressive capacity of concrete. This value is consistent with the fact that no crushing of the concrete was observed during the experiment.

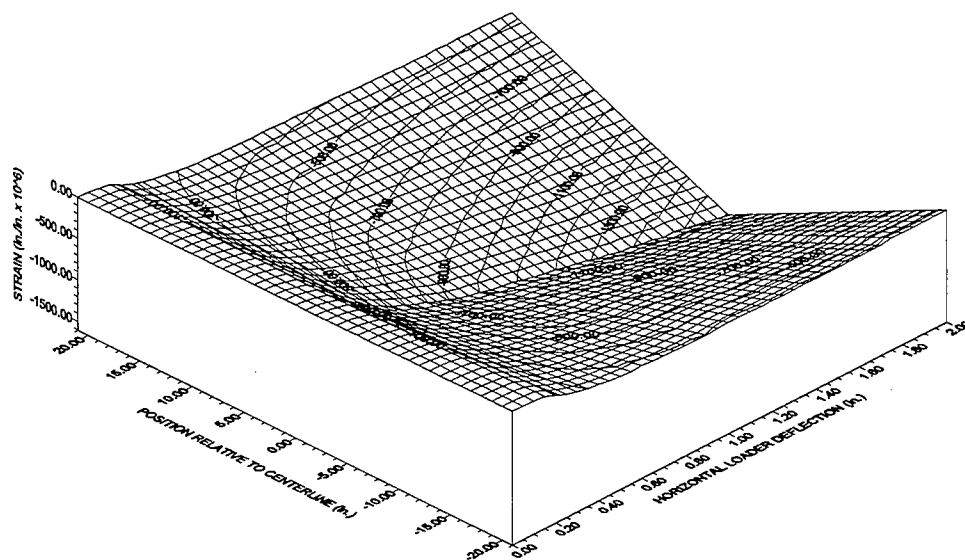


Figure 41. Vertical strain measured on outside of west (compression) wall at 2 in. elevation.

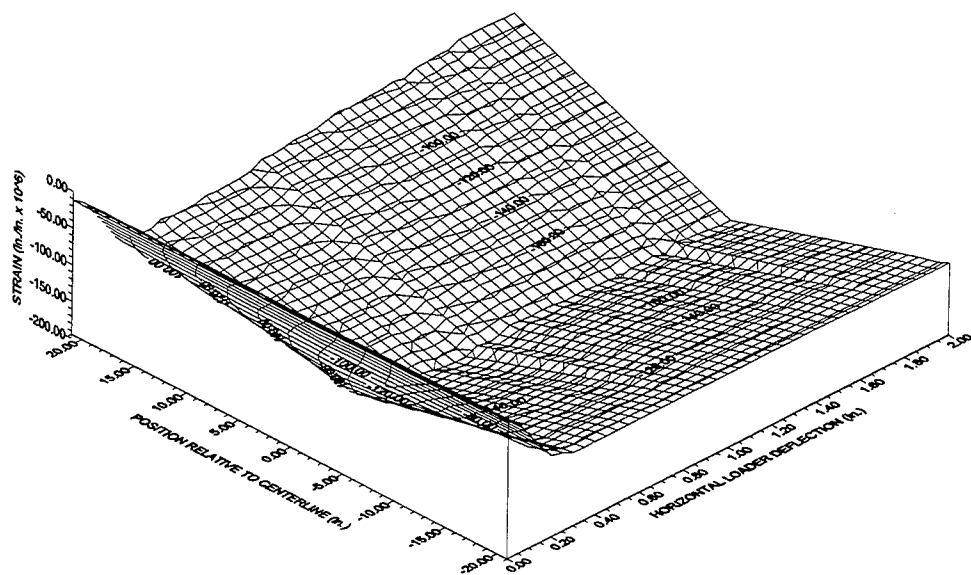


Figure 42. Vertical strain measured on outside of west (compression) wall at 12 in. elevation.

Vertical strain gages were mounted on the outer-most reinforcing bars at various elevations up the side of the structure, in both the east (tension) and west (compression) walls. In both walls, one vertical array was located at 3 in., and one at 21 in. from the center of the wall. Figure 43 through Figure 47 show the distribution of the measured strains plotted against height up the structure and also versus the imposed horizontal displacement.

Several observations can be made about the vertical distribution of strain in the model. In the east (tension) wall, the strain distribution was dominated by plastic strain in the base of the model (Figure 43). When the lowest gage response is deleted, Figure 44 and Figure 45, the strains in the upper part of the model exhibit an almost uniform distribution of strain. In fact, there appears to be a counterintuitive, slight increase in strain with increasing elevation. Considering the tower as a simple cantilever, one would expect a decrease in stress and, hence, strain with increasing height.

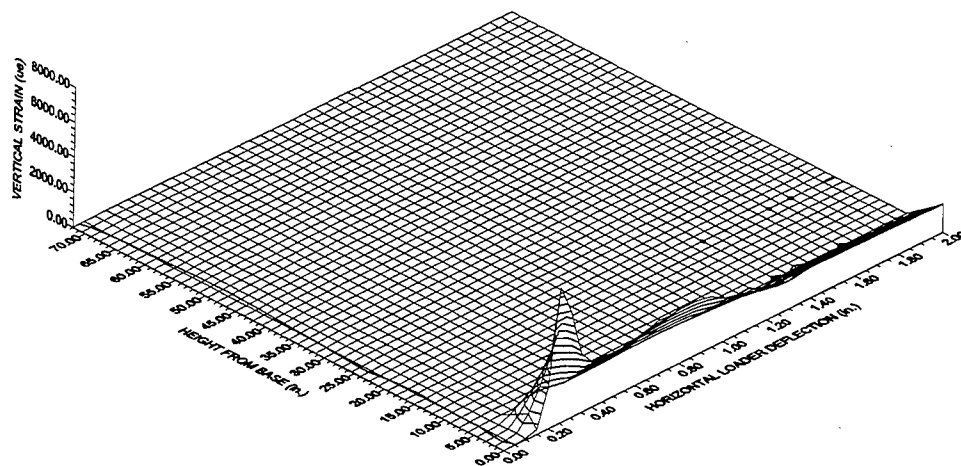


Figure 43. Vertical strain measured up side of structure, 3 in. from the center of east (tension) wall, including bottom gage.

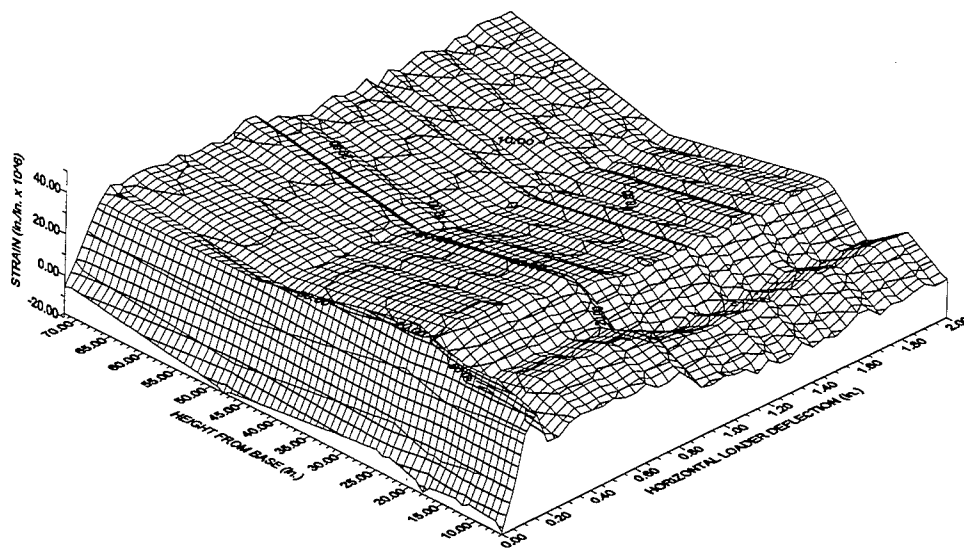


Figure 44. Vertical strain measured up side of structure, 3 in. from the center of east (tension) wall without the bottom gage.

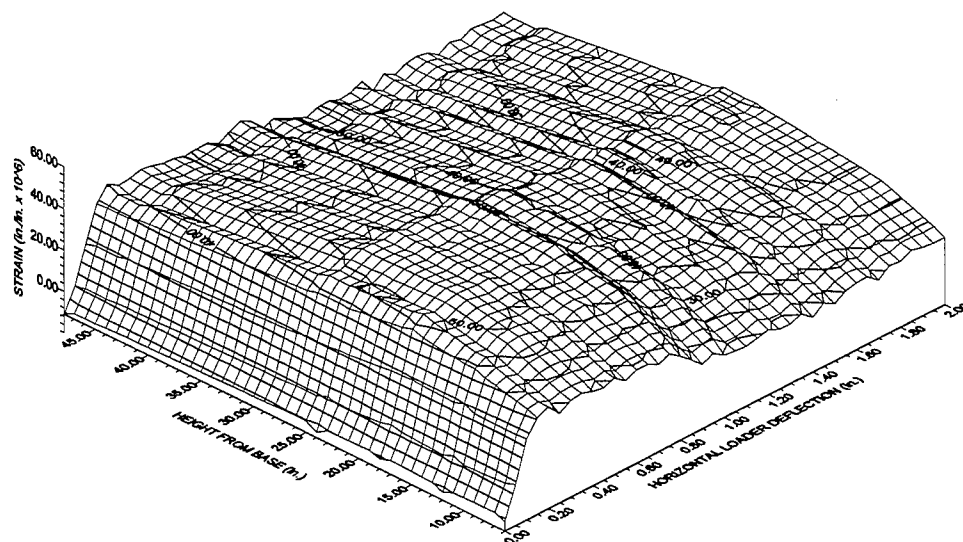


Figure 45. Vertical strain measured up side of structure, 21 in. from the center of east (tension) wall without the bottom gage.

In the west (compression) wall, the strain distributions shown in Figure 46 and Figure 47 were not dominated by plastic strain in the base of the model. The upper part of the model exhibits a decrease in compressive strains with increasing elevation. This is as one would expect in considering the tower as a simple cantilever. The only complication appears at the base of the model under large imposed deflections, where tensile strains are generated after the neutral axis moves to the exterior of the reinforcing layer.

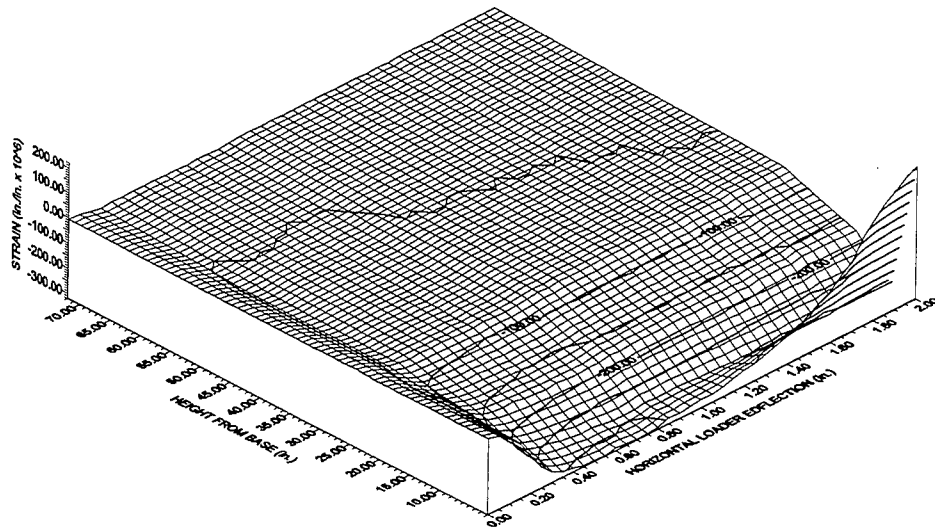


Figure 46. Vertical strain measured up side of structure, 3 in. from the center of west (compression) wall, including bottom gage.

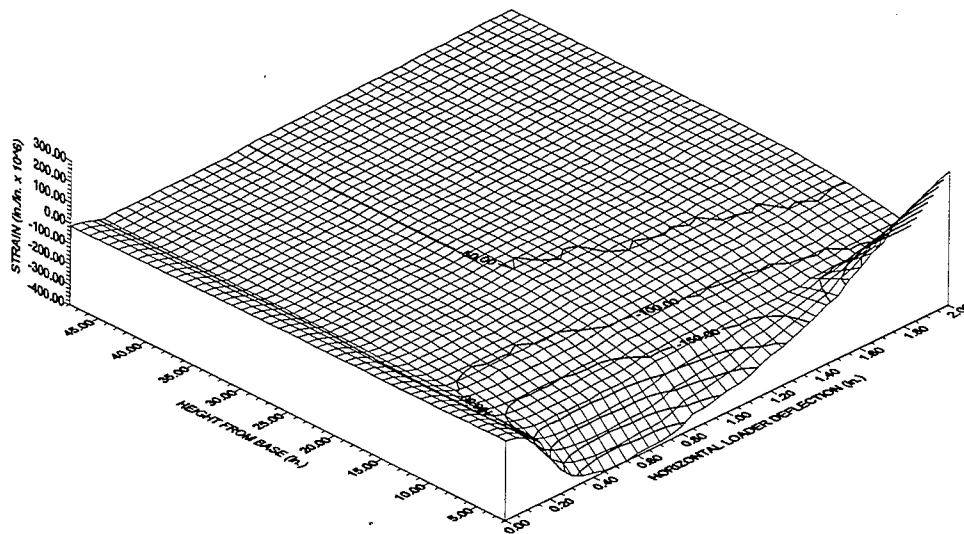


Figure 47. Vertical strain measured up side of structure, 21 in. from the center of west (compression) wall, including bottom gage.

The section strain distribution at an imposed deflection of approximately 0.15 in. is shown in Figure 48. This is the deflection just prior to the occurrence of cracking. A well-defined strain distribution is visible. Tensile strains are concentrated at the corners of the east (tension) wall, with a localized peak visible immediately across from the interior corner of the structure. This peak strain is 400 microstrain to 500 microstrain in tension, a range considered close to failure for concrete. The apparent location of the neutral axis remains at about 8 in. from the structure centerline, towards the compression wall.

The post-cracking section strain distribution, recorded at an imposed deflection of approximately 0.18 in., is shown in Figure 49. The post-cracking strain distribution is not as uniform as the pre-cracking distribution because the strains measured are dependent upon whether or not a crack intersects the location of the gage. After cracking, most of the strain is localized in the immediate vicinity of the crack and, hence, only gages in this vicinity will record these large strains. The large tensile strains that were recorded (25,000 microstrain to 38,000 microstrain) are values that exceed the yielding strain, approximately 1,750 microstrain, of the steel used in this model. The fact that this occurs immediately after cracking indicates that, due to the low reinforcement ratio in the structure, the cracking capacity of the section is greater than the elastic capacity of the reinforcement. This result was expected from the pre-experiment analysis. The apparent location of the neutral axis shifts well into the west (compression) wall.

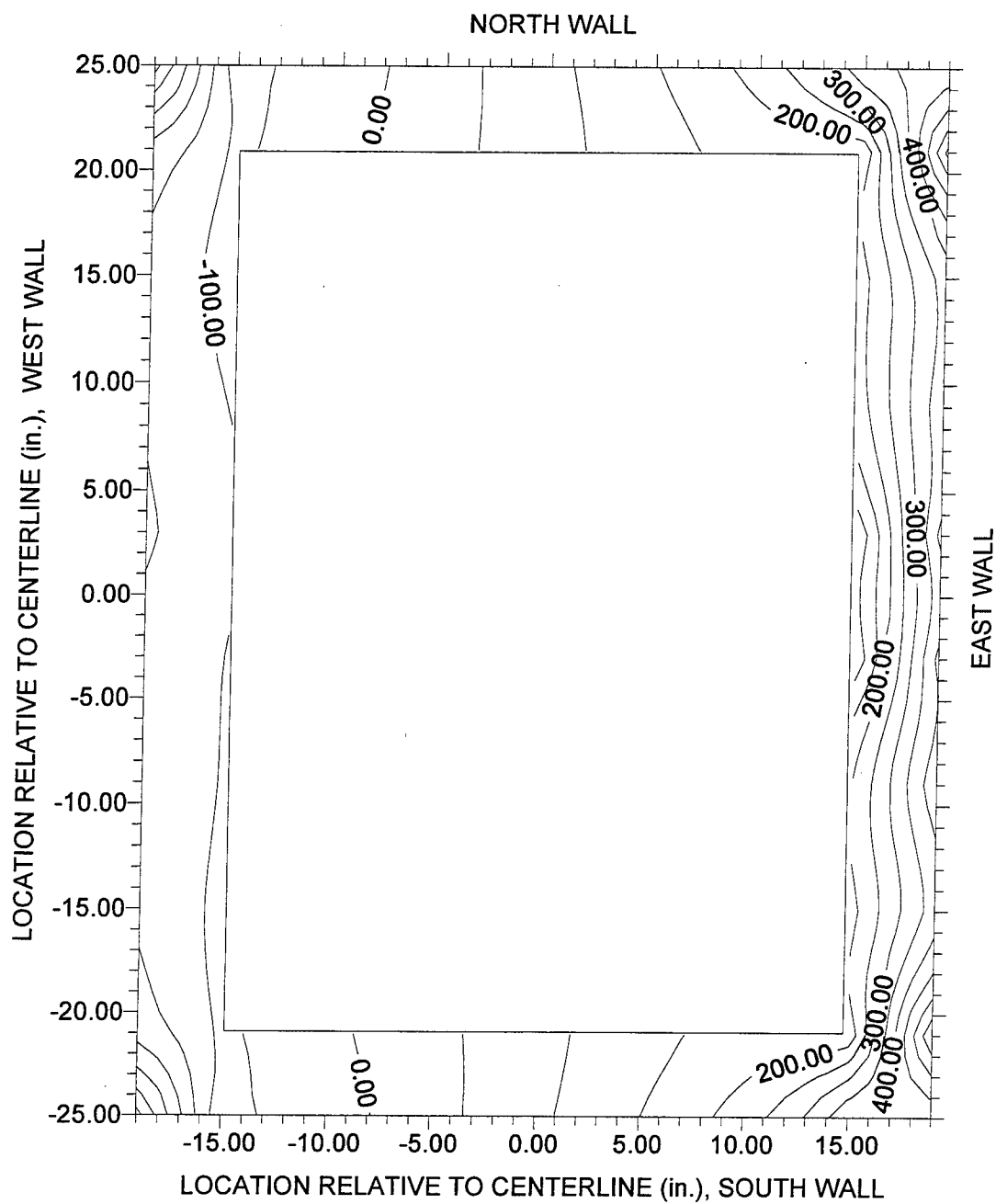


Figure 48. Vertical strain distribution at base of structure for a horizontal loader deflection of 0.15 in.

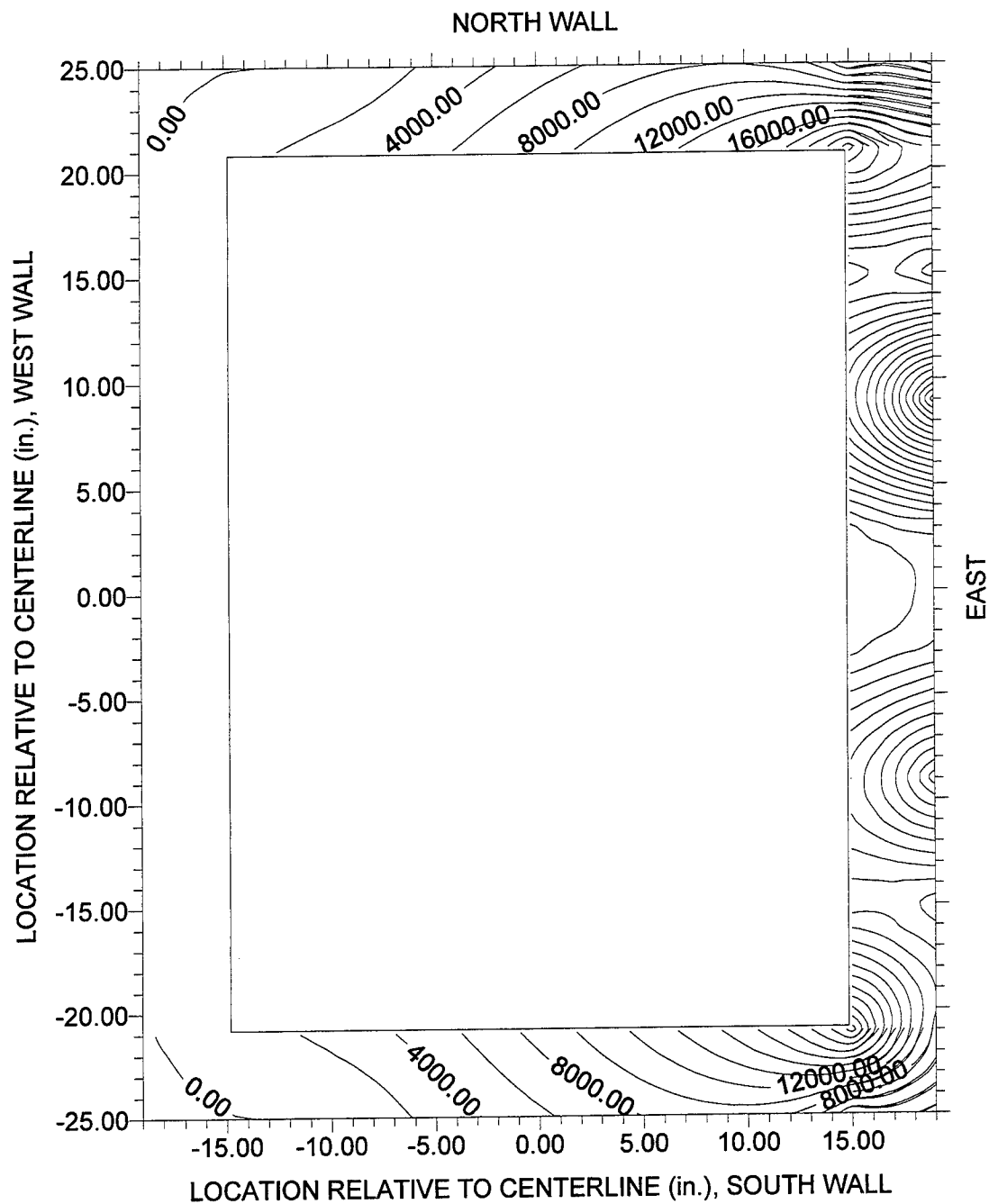


Figure 49. Vertical strain distribution at base of structure for a horizontal loader deflection of 0.18 in.

Modal Response

A substantial effort was expended to collect modal response data before, during, and after the experiment. The modal response data were acquired to assist in the estimation of the changes in the modal response of intake towers due to accumulation of damage during an earthquake. The shifting of the natural period of a tower may have the effect of reducing the load acquired from the earthquake, thus substantially increasing the effective capacity of the structure. The analysis of these data was conducted using the IDEAS computer program.

A first modal survey of the ITS-1 structure was conducted after the model was bolted to the floor, but before the vertical and horizontal rams were attached. This configuration is similar to a prototype tower in that it is a vertical cantilever, unrestrained at the top. The frequency response function of the model is shown in Figure 50. Clear peaks are visible in the range of 0 Hz to 450 Hz with corresponding coherence values of close to 1.0. Using the modal extraction capabilities of the IDEAS program, several modes of response were identified. Graphical representations of five of these modes are shown in Figure 51 to Figure 55. Figure 51 shows the shape of the lowest frequency mode at 46 Hz. This motion appears to be the fundamental frequency in the first bending mode. The second mode shape shown (Figure 52) appears to be a more complex response, consisting of torsional and bending components. This type of motion is consistent with an ovaling response of the model. A clearly torsional response, at a frequency of 121 Hz, is presented in Figure 53. The fourth mode, shown in Figure 54,

was a localized response at a frequency of 200 Hz. It appears that this response is associated with the cold joint located at mid-height of the tower model. This seems to indicate that the cold joint influenced the response of the wall, but the relatively coarse grid of measurement points used in the survey precludes any detailed conclusions from this response. The mode presented in Figure 55 was extracted at a frequency of 440 Hz. This appears to be the second bending mode of the undamaged structure, but the mode shape is not very clear. The lack of clarity may be due to the fact that the extraction occurred at a frequency very close to the upper end of the data range.

A modal survey of the ITS-1 structure was conducted after the experiment was completed, and the model had suffered a total top excursion of 2 in. As in the first modal survey, the model was bolted to the floor, but the vertical and horizontal rams were not attached. Again, this configuration is similar to a prototype tower in that it is a vertical cantilever, unrestrained at the top. The frequency response function of the model is shown in Figure 56. As in the undamaged model, clear peaks are visible in the range of 0 Hz to 450 Hz, with corresponding coherence values close to 1.0. A substantial difference is observed between the shape of the frequency response functions of the damaged and undamaged models. The first peak of the post-experiment (damaged model) plot appears to begin at a substantially lower frequency (longer period) than for the undamaged model. Such a trend can prove beneficial if it can be substantiated. The coherence in the post-experiment survey is quite low for many frequencies. The lower coherence may reflect

the nonlinear nature of the damaged structure and perhaps the elimination of some modes of response.

Again using the modal extraction capabilities of the IDEAS program, several modes of response were identified for the damaged model. Graphical representations of five of these modes are shown in Figure 57 to Figure 61. Figure 57 presents the shape of the lowest frequency mode at 14 Hz. This motion appears to be a bending and rocking mode. Another bending and rocking mode (Figure 58) appears at a frequency of 20 Hz. This second mode is very similar to the first mode, appearing to differ only in that there is a small rotational component about the south corner of the wall in the first mode, but about the north corner in the second mode. The two modes of response at 14 Hz and 20 Hz for the damaged model appear to replace the fundamental bending mode of the undamaged model at 46 Hz. A clearly torsional response, at a frequency of 34 Hz, can be seen in Figure 59. This seems to correlate to the first torsional mode of the undamaged model at a frequency of 121 Hz. A fourth mode, shown in Figure 60, was a response unique to the damaged model and occurred at a frequency of 81 Hz. It appears that this response may be associated with a rocking of the model about the center of gravity of the model. It is interesting to note that the mode of response associated with the cold joint in the middle of the undamaged tower model did not appear in the damaged model. The low coherence of the frequency response function in the 200-Hz range probably explains the lack of a cold joint response. An alternative explanation is that the apparent cold joint response in the undamaged model was an artifact of some unknown problem with the

survey data, and did not really exist. The final mode discussed is presented in Figure 61 and was extracted at a frequency of 429 Hz. This shape is very clearly the second bending mode of the damaged structure. The modal survey for the damaged structure had a frequency range of about twice that of the undamaged structure; hence, the extraction process resulted in a much clearer mode shape. The second bending mode frequencies did not change much due to damage, only decreasing 2.5 percent from 440 Hz to 429 Hz.

It is interesting to compare the measured modal frequencies to those calculated for a simple cantilever beam. An approximate formulation is found in the literature [5]:

$$\omega_n = k_n^2 \sqrt{\frac{EIg}{A\gamma}} \quad (3)$$

where ω_n is the nth natural rotational frequency (radians/sec), and where for the first frequency $k_1L=1.875$, and for the second frequency $k_2L=4.694$, where L is the length (120 in.). Also, where E is the stiffness modulus (3.0×10^6 lb/in.²); I , the gross section modulus (1.966×10^5 in.⁴); g , the gravity constant (386.4 in./sec.²); A , the area (908 in.²), and γ , the material density (8.68×10^{-2} lb/in.³). Recalling that:

$$f = \frac{\omega}{2\pi} \quad (4)$$

the first bending and second mode natural frequencies are calculated to be 66 Hz and 415 Hz, respectively. These calculated values compare well to the measured values of 46 Hz and 440 Hz for the first and second bending modes of the undamaged structure. The calculation seems to validate the selection of the 440-Hz mode as the second bending

mode. As mentioned above, the selection of this mode as the second bending mode was questionable due to the lack of data just above this frequency.

In addition to the pre-experiment and post-experiment modal surveys, modal surveys were conducted during the loading of the ITS-1 structure. During these surveys, the tower model was restrained at the top by the horizontal and vertical loaders and, thus, the configuration of the model did not represent a free-standing tower. The surveys were conducted to examine the shift of modal response of the model, under the experimental loads and constraints, with increasing damage. This objective was met with mixed success. The main difficulty encountered was a lack of coherence in the frequency response of the structure. It is hypothesized that the vibration of the hydraulic loaders imparted sufficient energy into the model to degrade the response measurement. Modes could not be extracted from these data due to insufficient coherence. However, several peaks are identifiable on the frequency response function measured at the drive point. Comparisons of the shift in frequency of these peaks should give an indication of change in modal response of the model with increasing damage. The four peaks that occurred at the lowest frequencies appear to correspond to important modes. The value of the frequency corresponding to each of these peaks was read from the frequency response function for each survey conducted. This value was paired with the input horizontal deflection at which the survey was conducted. The result is presented in Figure 62, which shows the change of the peak frequencies with increasing input deflection.

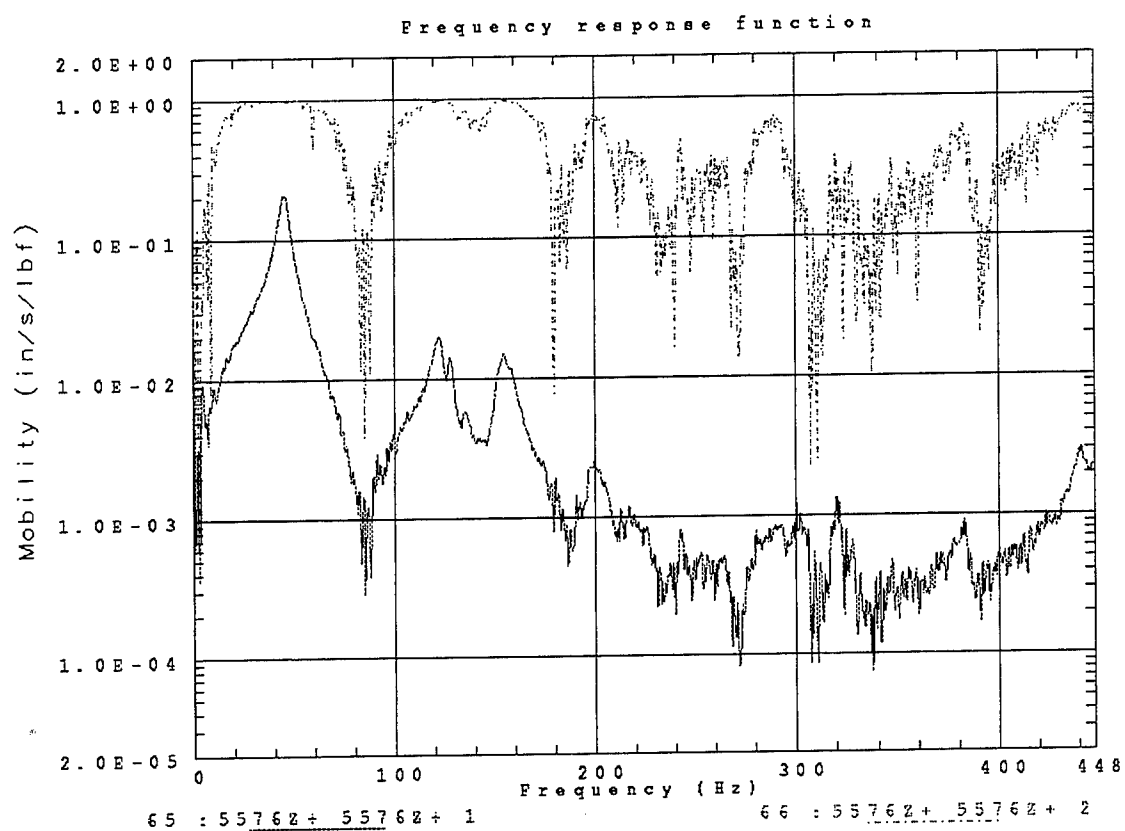


Figure 50. Frequency response function for undamaged ITS-1 structure.

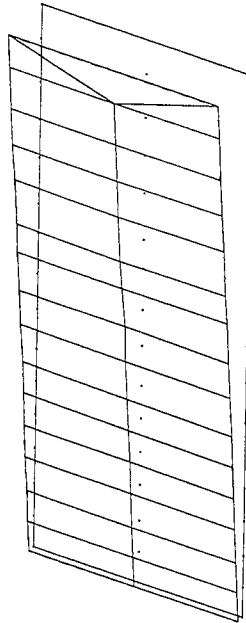


Figure 51. Bending mode for undamaged ITS-1 structure at 46 Hz.

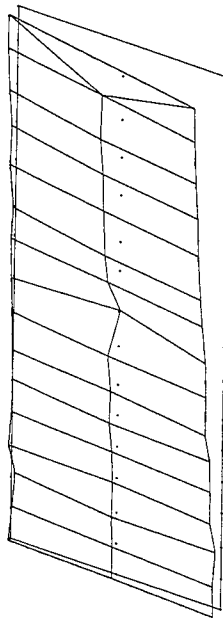


Figure 52. Ovaling mode for undamaged ITS-1 structure at 69 Hz.

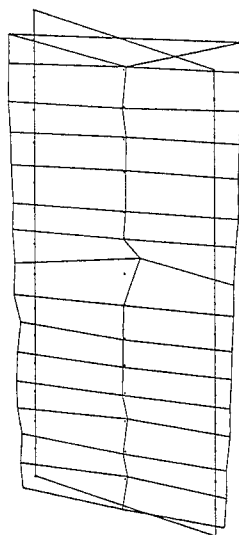


Figure 53. Torsional mode for undamaged ITS-1 structure at 121 Hz.

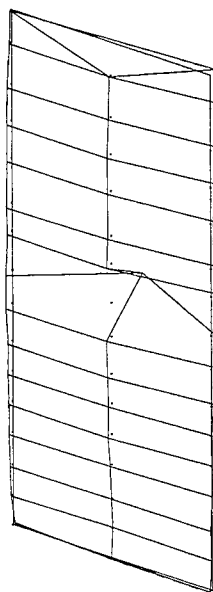


Figure 54. Localized response associated with cold joint for undamaged ITS-1 structure at 200 Hz.

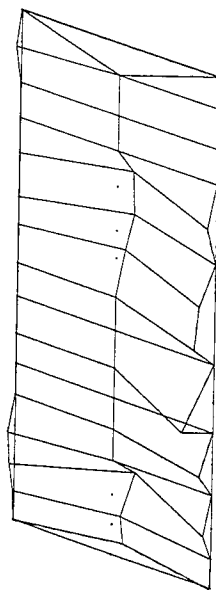


Figure 55. Second bending mode for undamaged ITS-1 structure at 440 Hz.

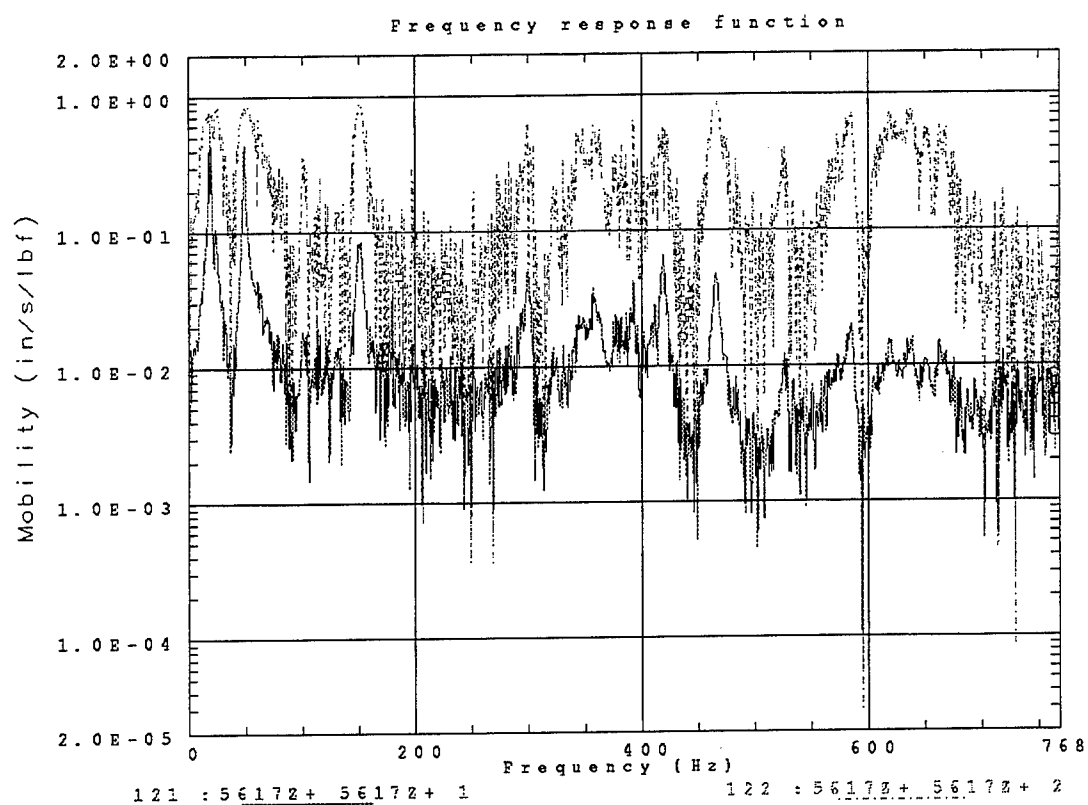


Figure 56. Frequency response function for damaged ITS-1 structure.

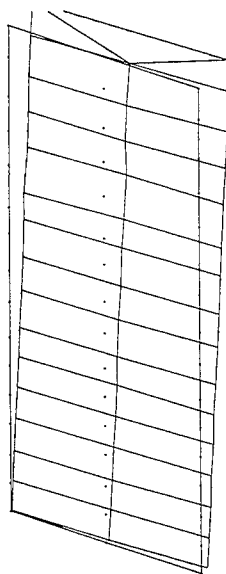


Figure 57. Bending and rocking mode for damaged ITS-1 structure at 14 Hz.

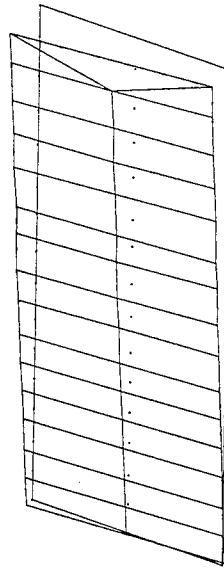


Figure 58. Bending and rocking mode for damaged ITS-1 structure at 20 Hz.

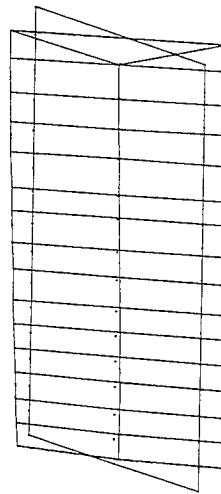


Figure 59. Torsional mode for damaged ITS-1 structure at 34 Hz.

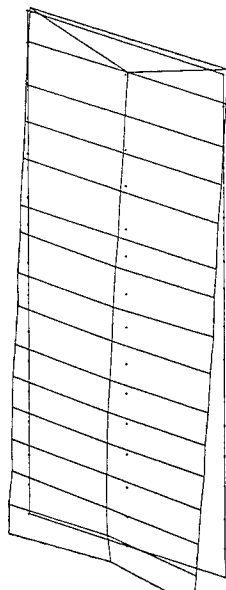


Figure 60. Rocking about center of gravity for damaged ITS-1 structure at 81 Hz.

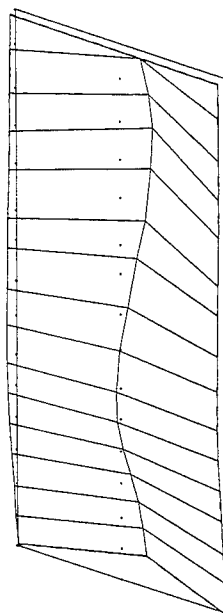


Figure 61. Second bending mode for damaged ITS-1 structure at 429 Hz.

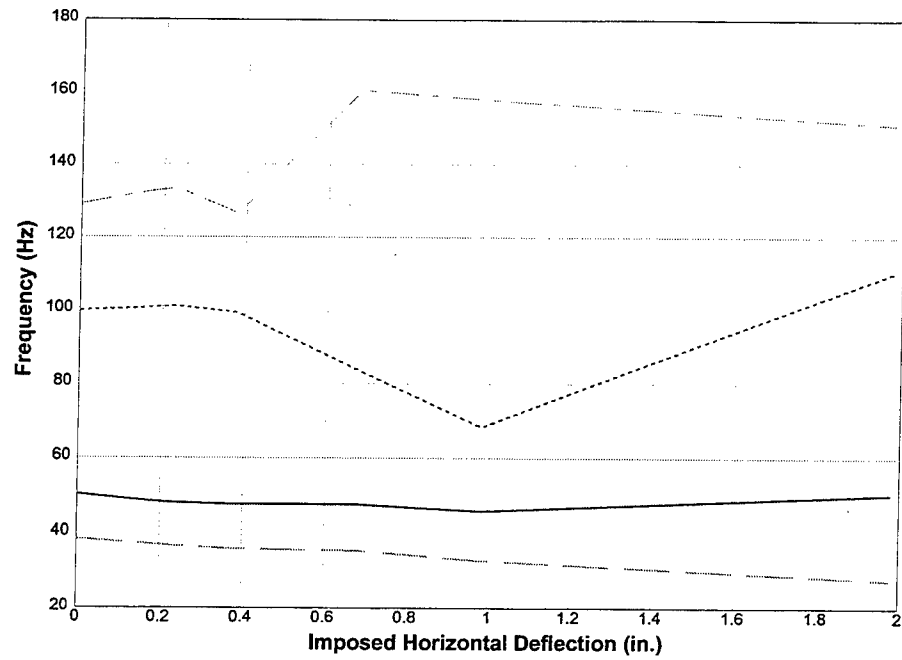


Figure 62. Variation of first four modes of vibration during loading of ITS-1 structure.

CHAPTER 5

ITS-2 EXPERIMENTAL RESULTS

Introduction

The cyclic excursion experiment ITS-2 was completed on May 31, 1996. A vertical load was applied to the structure and held constant throughout the experiment to simulate dead load. The horizontal load was applied by a deflection controlled loader at a rate of 0.01 in./sec. Each cycle consisted of one excursion in both the east and west directions, beginning with a 0.1-in. excursion and increasing by 0.1 in. for each subsequent cycle. The experiment was temporarily stopped eight times to allow for the modal survey, measurement, and photography of the structure. The experiment required approximately 6 hours to conduct. Seventy-two channels of active data were recorded, 10 modal surveys were conducted, and passive measurements of structural response were recorded. Video and still photography were included.

Structural Response

Photographs of the response of ITS-2 can be seen in Figure 63 to Figure 74.

Visual inspection of the model during loading led to several observations. Damage to the model was limited to the bottom of the tower section at the interface with the rigid base. The damage consisted of one tension crack that extended across the base of the model. The tension crack did not follow the interface of the cold joint located in this region but dipped downward below the cold joint into the concrete base material before returning to the surface at the far side of the wall (Figure 75 to Figure 81). Crushing and/or degradation of the concrete was not evident as the load cycles were repeated. The ultimate failure of the structure appeared to be controlled by the response of the reinforcing bars. Figure 80 shows a close-up view of a ruptured reinforcing bar, with the necking and elongation that are typical of a tension failure. Ruptured reinforcing bars were visible across the entire base of the structure.

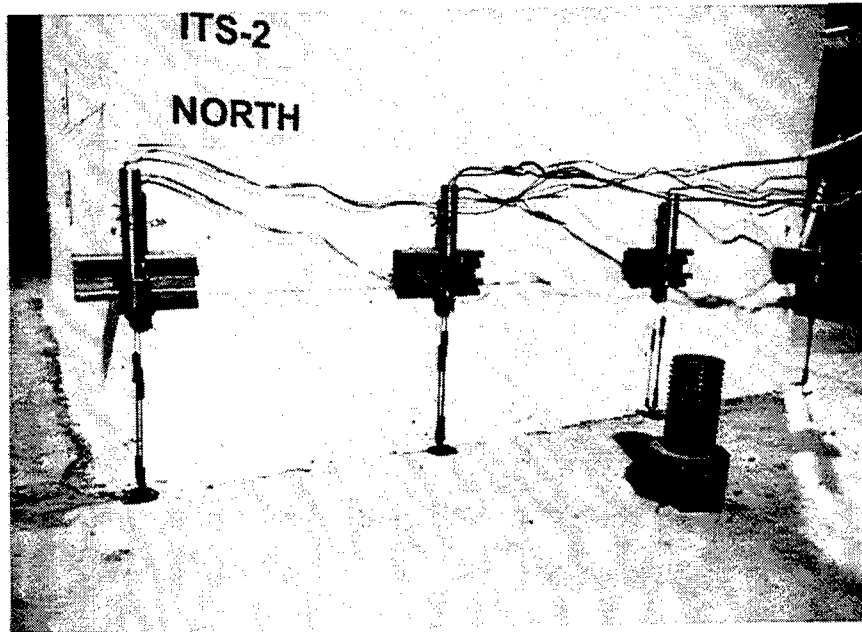


Figure 63. ITS-2 pre-experiment view of north wall.

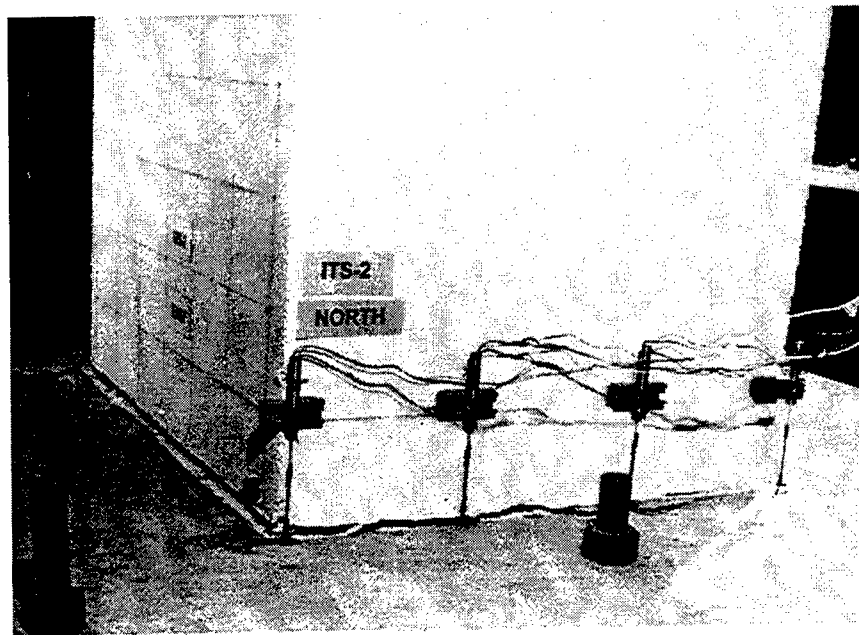


Figure 64. ITS-2 view of north wall, imposed top deflection of 2 in. towards the west.

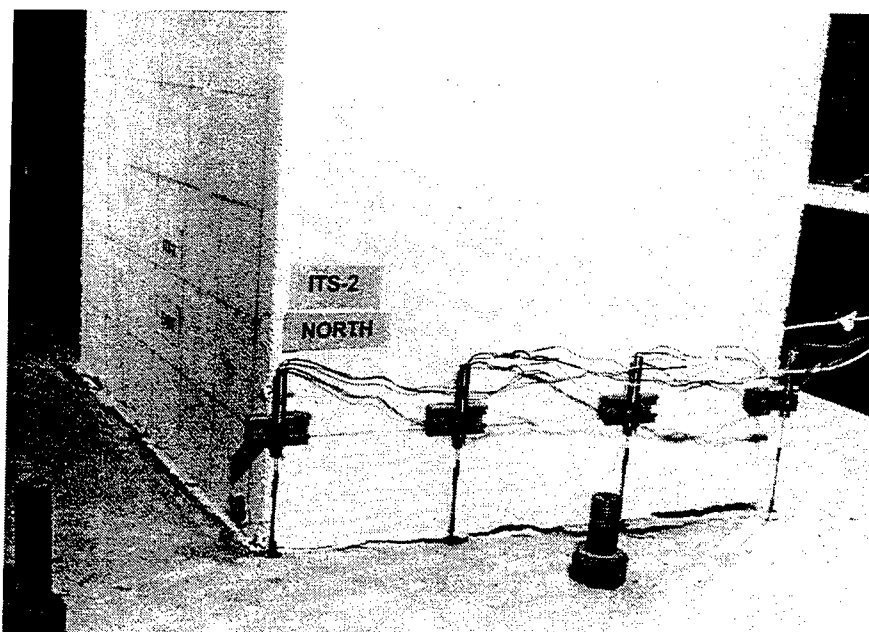


Figure 65. ITS-2 view of north wall, imposed top deflection of 2 in. towards the east.

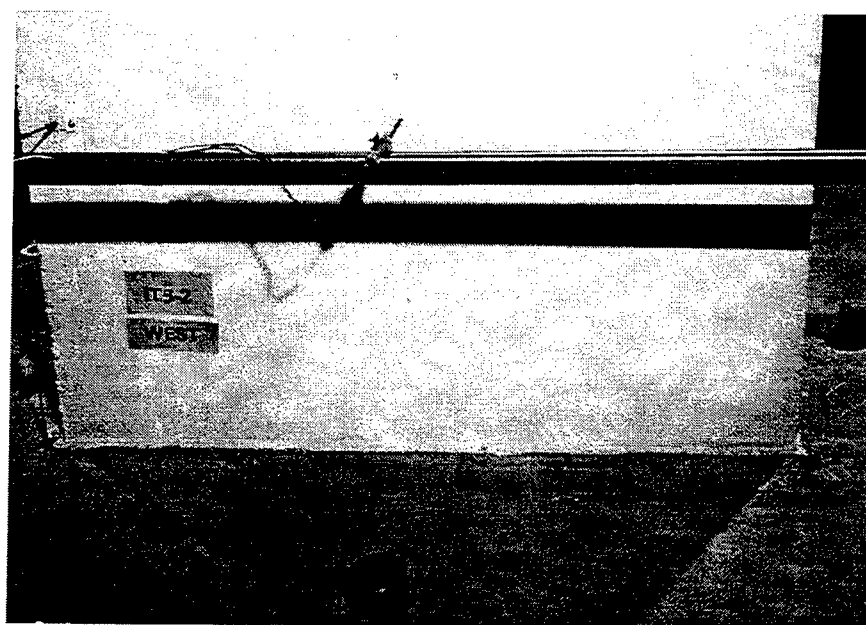


Figure 66. ITS-2 pre-experiment view of west wall.

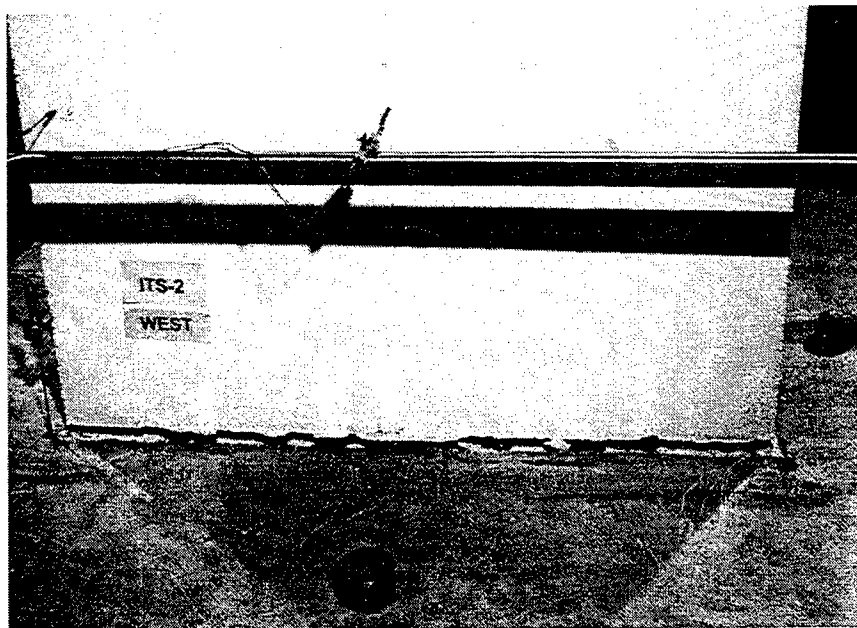


Figure 67. ITS-2 view of west wall, imposed top deflection of 2 in. towards the west.

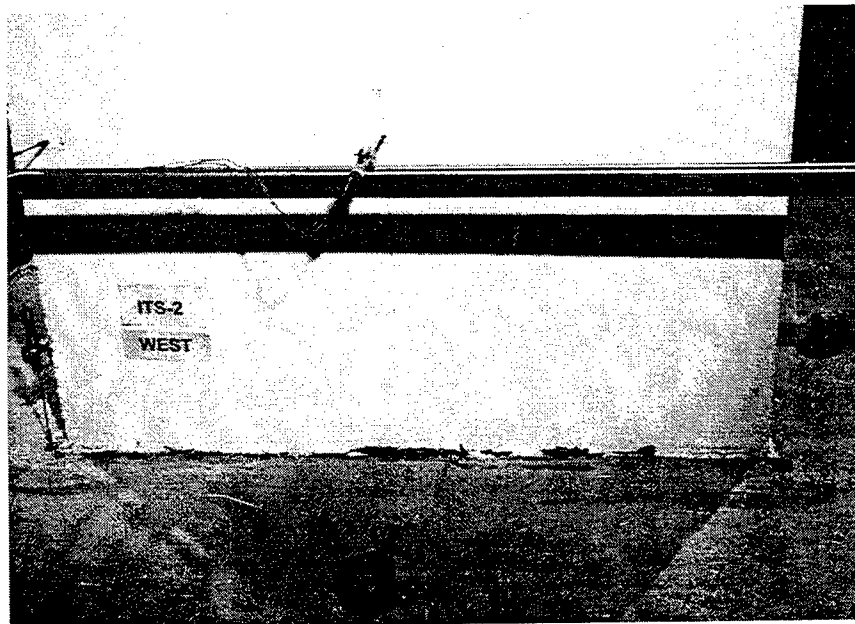


Figure 68. ITS-2 view of west wall, imposed top deflection of 2 in. towards the east.

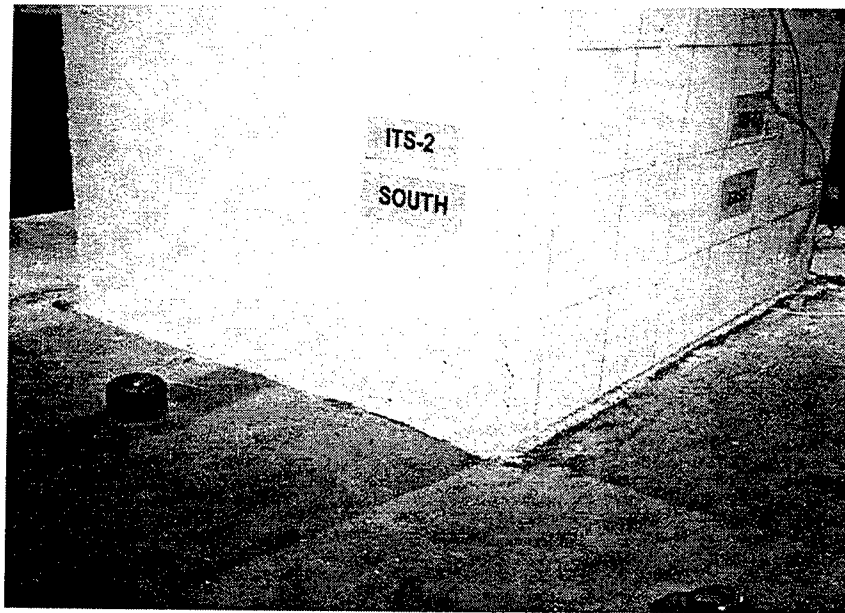


Figure 69. ITS-2 pre-experiment view of south and east walls. .



Figure 70. ITS-2 view of south and east walls, imposed top deflection of 2 in. west.



Figure 71. ITS-2 view of south and east walls, imposed top deflection of 2 in. east.

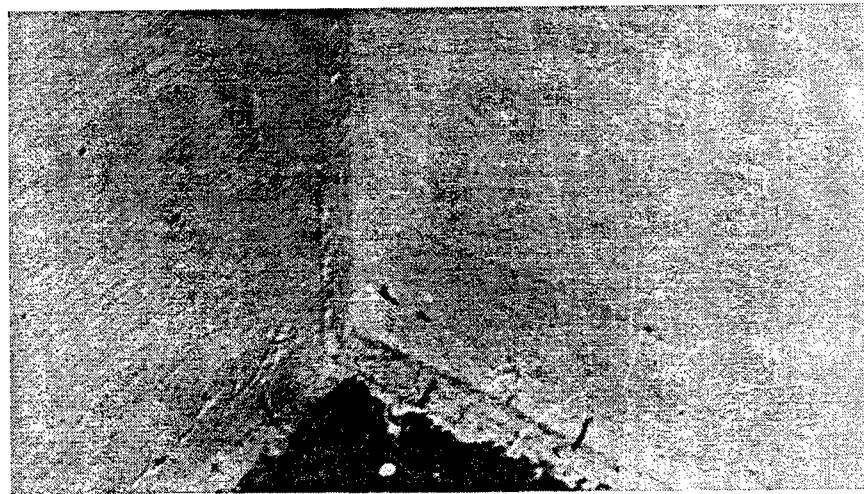


Figure 72. ITS-2 pre-experiment close-up view of interior south-east corner.

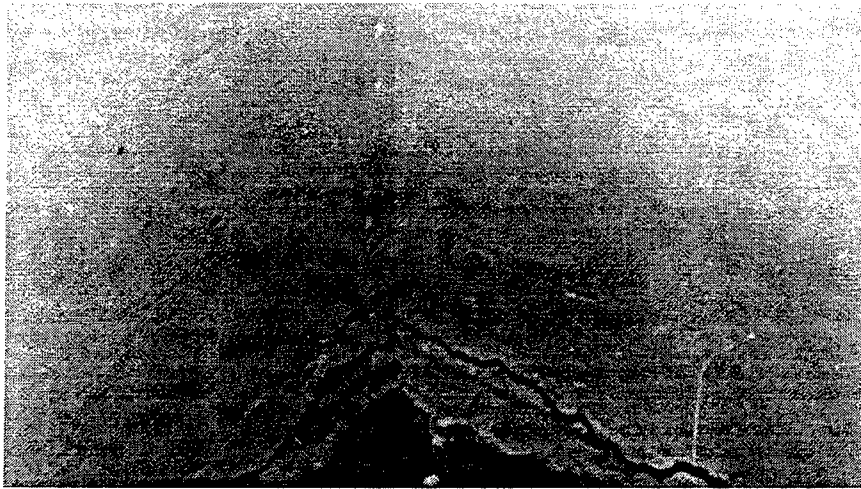


Figure 73. ITS-2 close-up view of interior south-east corner, imposed top deflection of 2 in. towards the west.

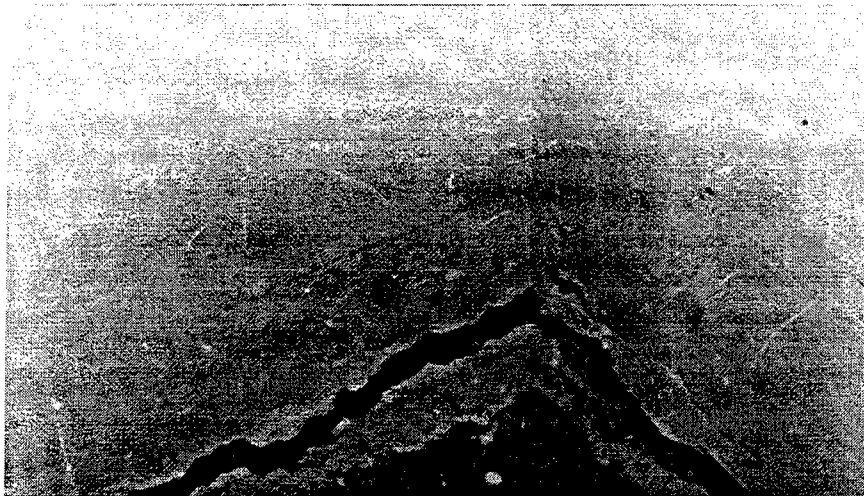


Figure 74. ITS-2 close-up view of interior south-east corner, imposed top deflection of 2 in. towards the east.

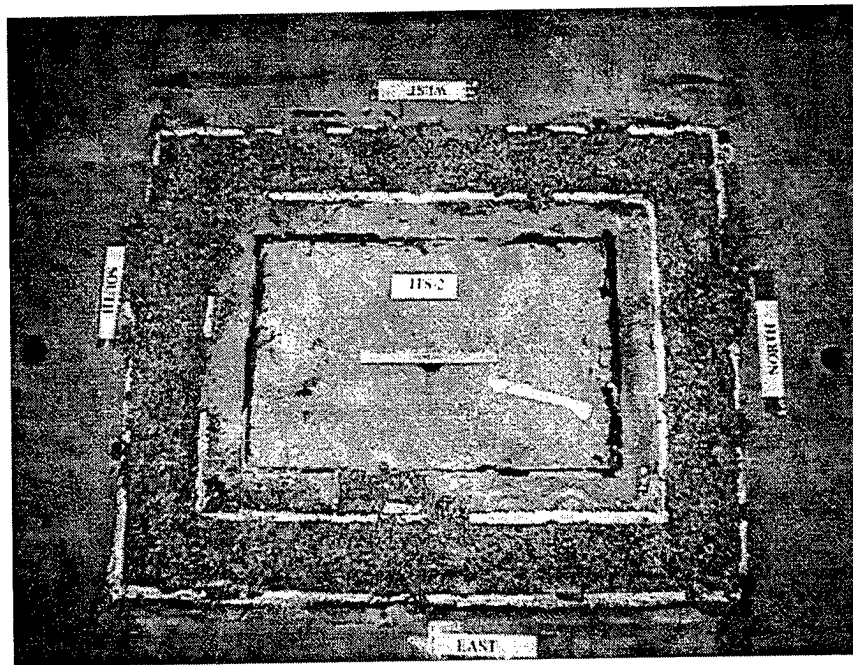


Figure 75. Base of ITS-2 model with tower section removed.



Figure 76. Close-up view of failure plane under east wall of ITS-2.



Figure 77. Close-up view of failure plane under north wall of ITS-2.

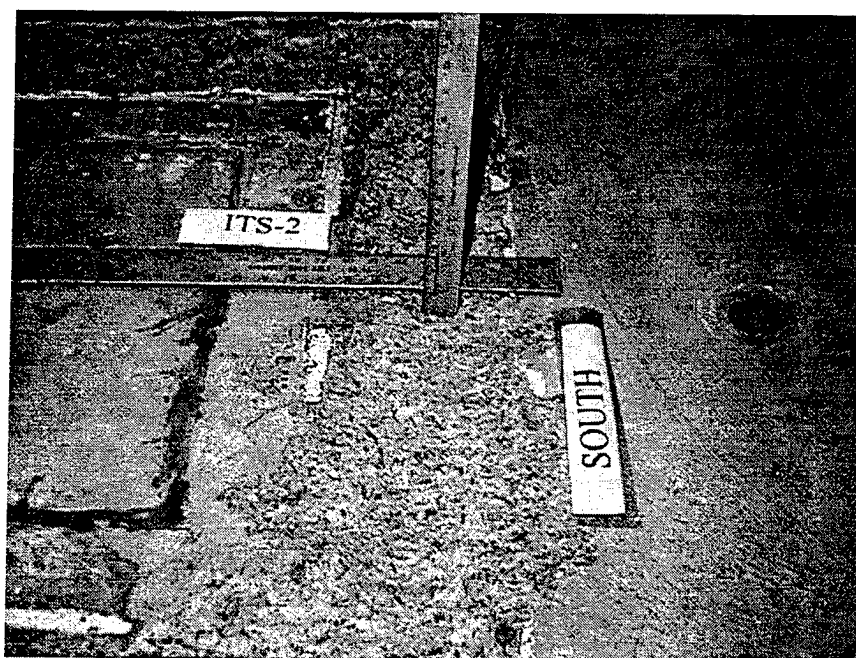


Figure 78. Close-up view of failure plane under south wall of ITS-2.



Figure 79. Close-up view of failure plane under west wall of ITS-2.



Figure 80. ITS-2, typical failed reinforcing bar.

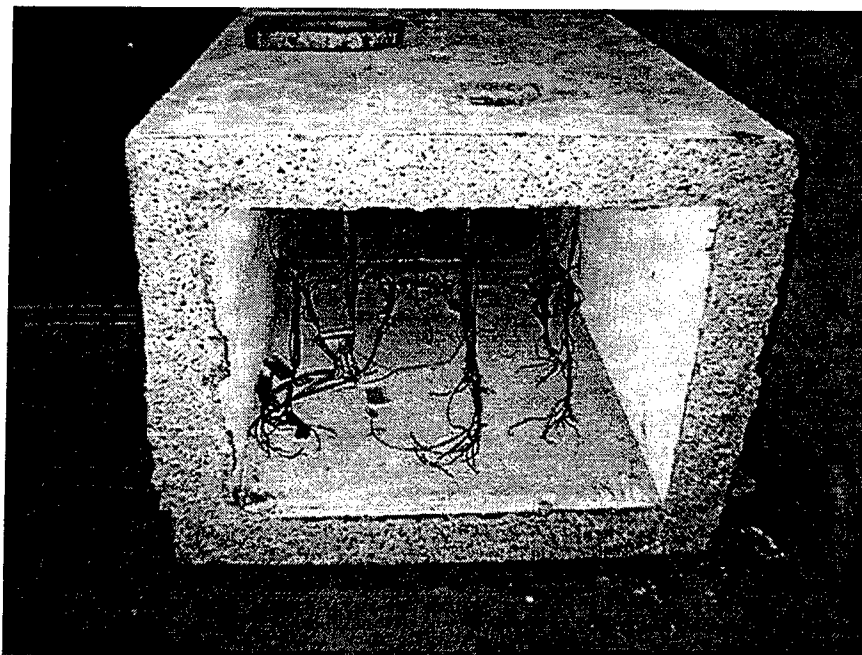


Figure 81. Failure surface at bottom of ITS-2 tower section.

Active Instrumentation Response

Eighty channels of active data were recorded during the experiment. Two of these channels were allocated to the measurement of load and deflection in the 50-kip horizontal hydraulic loader. Deflection was measured at 14 positions, and strain was measured at 66 positions. The constant vertical load applied to the top of the structure was monitored but not recorded. Recording occurred at 2 samples per second and thus, during the approximate 6 hours of the experiment, a total of about 3,500,000 samples were acquired for the 80 channels. The majority of data plotting and analyses were conducted with the structural response plotted against the deflection imposed on the model by the horizontal loader as measured by the loader LVDT gage. The horizontal loader deflection (ram movement) was the controlled input parameter in this experiment.

Some analyses were conducted based on the horizontal deflection response of the top of the model measured by LVDT gages.

Load Response

An important response measured in this experiment is the relationship of the horizontal load imposed at the top of the structure to the horizontal deflection measured at the same location. Figure 82 shows the force imparted by the horizontal loader versus the deflection of the loader. The force was measured by a load cell mounted on the loader, and deflection was measured by the loader internal LVDT gage. It is from this plot that the yield and ultimate deflections are most easily identified. The yield and ultimate deflections are directly related to the deflection ductility of the structure and also relate indirectly to the curvature ductility.

The initial direction of the loader was from east to west, imparting a compression (negative) load to the load cell and negative deflection measurements. Examination of the load-deflection history indicates a linear-elastic response for the first four excursions (two complete cycles) of the loader. The first excursion, from 0 to -0.1 resulted in a measured load of -18,590 lb. The second excursion, from 0 to 0.1, resulted in a measured load of 16,070 lb. The third excursion, from 0 to -0.2 resulted in a measured load of -38,750 lb. The fourth excursion, from 0 to 0.2, resulted in a measured load of 34,520. During the fifth excursion, cracking appears to have occurred upon the ram returning to an imposed deflection of -0.2 in., at a load of -37,334 lb. The magnitude of the measured load decreased abruptly to a level -30,060 lb, at a deflection of about -0.23 in. The

decrease in load capacity after cracking was expected as the cracking moment capacity of the section had been calculated to be greater than the yielding moment in this lightly reinforced member. There were no further abrupt changes with increasing load cycles, rather some strain hardening and subsequent degradation was witnessed.

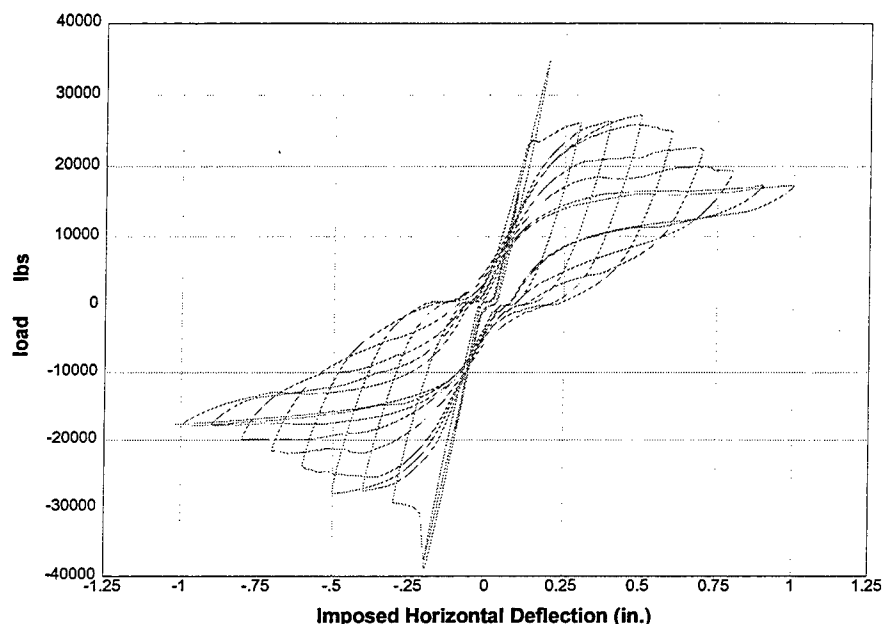


Figure 82. Horizontal load versus horizontal loader deflection.

In order to determine the deflection ductility of the model, one must determine the yield and ultimate deflections of the structure. The deflection ductility is defined as the ratio of these two values. From examining the load deflection curve, it appears that the ultimate deflection occurred during the fifth cycle at the ninth and tenth excursion, at deflection of approximately -0.50 in. and a load of -27,750 lb, and a deflection of about 0.50 in. and a load of 27,240 lb, respectively. Another method of determining the point of substantial degradation is to find the point at which the amount of energy absorbed by

the structure begins to decrease with further cycles. The area within a hysteresis loop is a measure of the amount of energy lost. Thus, the area within the load-deflection curve for each complete cycle measures the energy absorbed by the structure during that cycle. Figure 83 shows the energy absorbed in each cycle of the ITS-2 experiment using this approach. It appears that the substantial degradation takes place after the sixth cycle. Utilization of the values from the fifth cycle should be a conservative estimate.

As discussed, cracking first occurred at an imposed deflection of a -0.2 in., at a load of -37334 lb. Because the yielding moment is less than the cracking moment for this lightly reinforced structure, the yield deflection can be taken as the same as the cracking deflection. Given the identification of both the yield deflection (0.2 in.) and ultimate deflection (0.5 in.), the deflection ductility is 2.5. Figure 84 shows the deflection ductility of both the ITS-1 and ITS-2 experiments. Recalling that the ITS-1 and ITS-2 structures were identical, there appears to be a 50-percent reduction in ductility due to the cyclic loading of ITS-2. A deflection ductility of 2.5, under cyclic loads, is a significant finding. This value is only slightly lower than ductilities expected of conventionally reinforced concrete members. Therefore, this cyclic experiment seems to demonstrate that the experimental model has significant ductility.

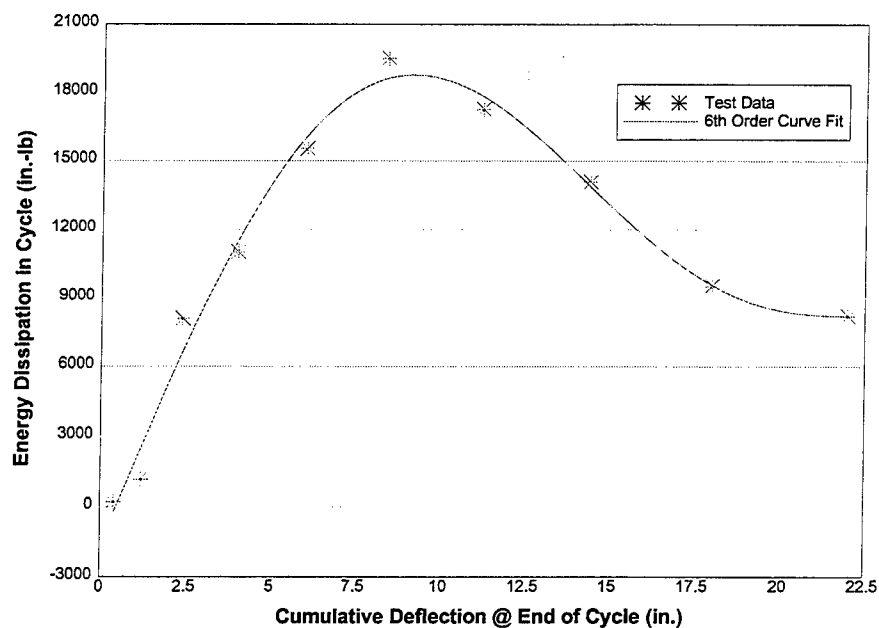


Figure 83. ITS-2 energy dissipation per load cycle, as measured by area inside of load-deflection curve.

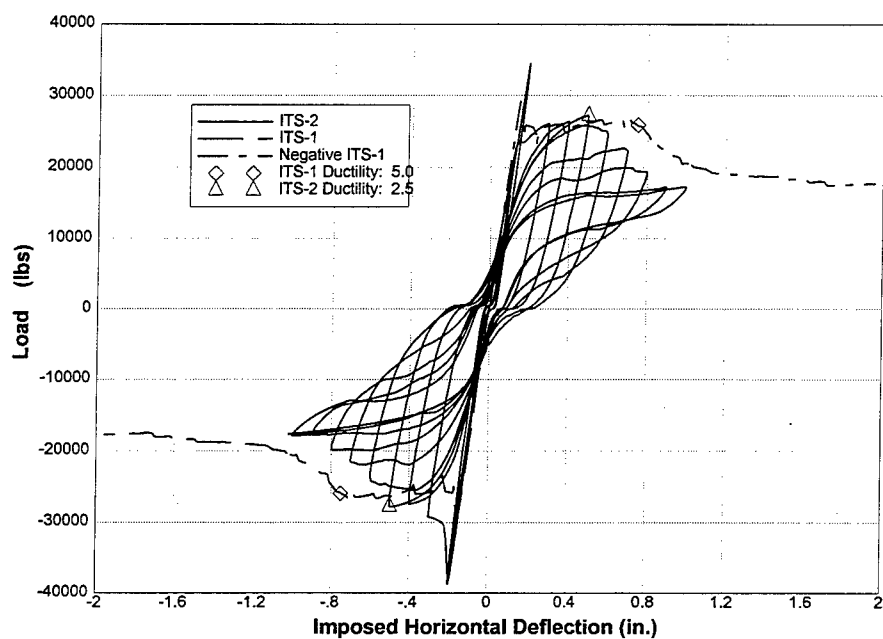


Figure 84. Observed ductility for ITS-1 and ITS-2 as related to the imposed deflection.

Further analysis indicates that even more ductility may be available. Figure 85 presents the load-deflection history of the ITS-2 experiment, with the deflection being the measured deflection at the top of the structure on the side opposite the loader (Gage DC15). Using this measurement has the advantage of eliminating any effects of the stiffness of the reaction frame, or any slack in the loader system. This measurement has the slight disadvantage that it may confound some of the structural response with the controlled parameter. That is, the effects of shear lag may cause the model to appear stiffer than it really is. A substantial increase in initial stiffness was witnessed when the measured deflection is considered instead of the imposed deflection. As a result, the yield deflection is reduced substantially, increasing the measured ductility from 2.5 to 5.1. Close examination of the load-deflection curve indicates that this increase in stiffness is, at least partially, a real response. The elastic portion of the load-deflection curve is much more linear at the load reversal point, indicating the elimination of slack in the loader device. Ductility of the ITS-2 model is, thus, somewhere between 2.5 and 5.1.

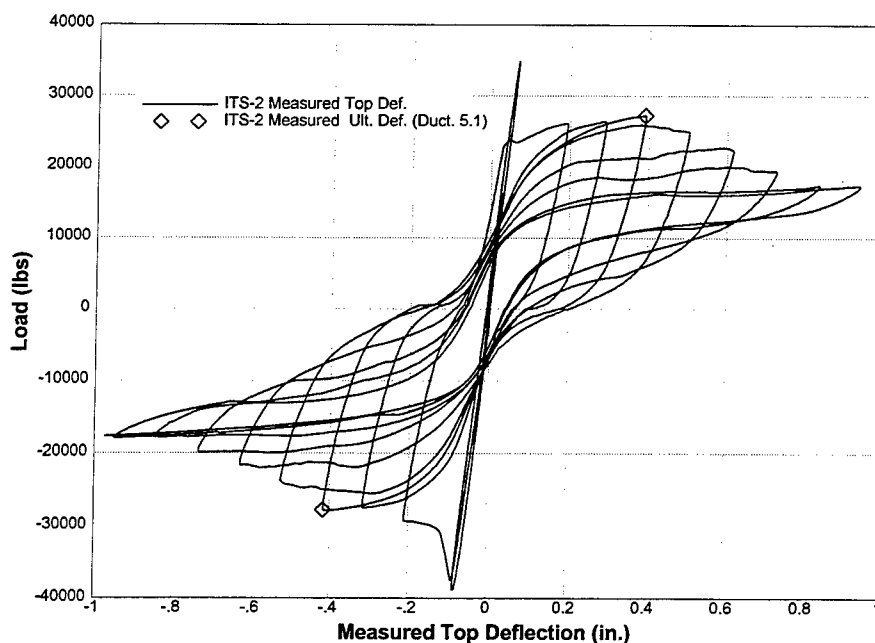


Figure 85. Observed ductility for ITS-2 as related to the measured top deflection.

Deflection Response

Horizontal deflections were measured at 2-ft intervals along the height of the structure. These measured deflections are shown plotted against the cumulative deflection imposed on the structure by the horizontal loader in Figure 86. The cumulative imposed horizontal deflection shown is a running sum of the travel of the horizontal loader. This has the effect of unfolding the data for ease of visualization. This technique was used extensively in the analysis and presentation of the results of this experiment. Presented in this manner, first yield occurred at 0.6 in., second yield at 1.0 in., first ultimate at 2.8 in., and second ultimate at 3.6 in. These points correspond to the top of the third excursion, top of the fourth excursion, top of the seventh excursion, and top of the eighth excursion, respectively.

Close examination of Figure 86 shows that there appears to be very little torsional response. The two gages at each elevation, located at the center and edge of the model give essentially the same values. It is also interesting to see the pattern that emerges when the deflections are normalized to the height of the gage (Figure 87); that is, when the deflection at each elevation is divided by the fraction of its location up the total height. The deflection curves collapse into one curve. This implies that the deflection at any given elevation is a linear function of height. In other words, the structure has a linear deflected shape.

The deflected shape of the model can be directly determined by plotting the horizontal deflections measured at each elevation against height (Figure 88). Included in this figure is a second-order curve fit to the data. Both a linear and second-order curve fit were developed for each set of measured deflections at the top of the first eight excursions. The correlation coefficients for the curve fits are shown in Figure 89. The second-order fits are slightly better for the first four excursions, after which a linear fit is essentially as good. Yielding occurs at the fourth excursion. A cantilever beam would be expected to exhibit a shape described by a second-order equation. This implies that the response of the ITS-2 model is dominated by rigid-body rotation after first yield, a fact that has important implications to the analysis of the response of the structure.

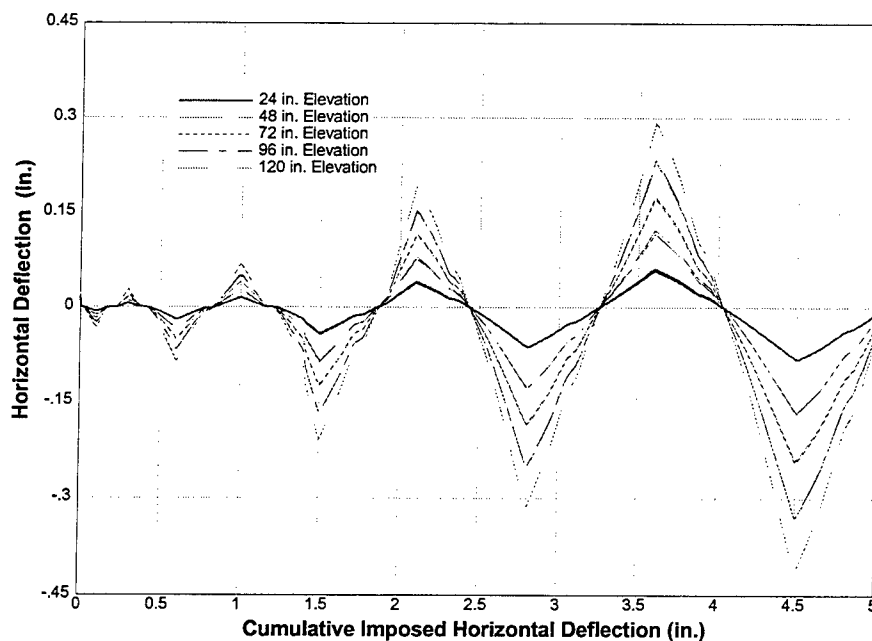


Figure 86. ITS-2 measured horizontal deflection at various elevations.

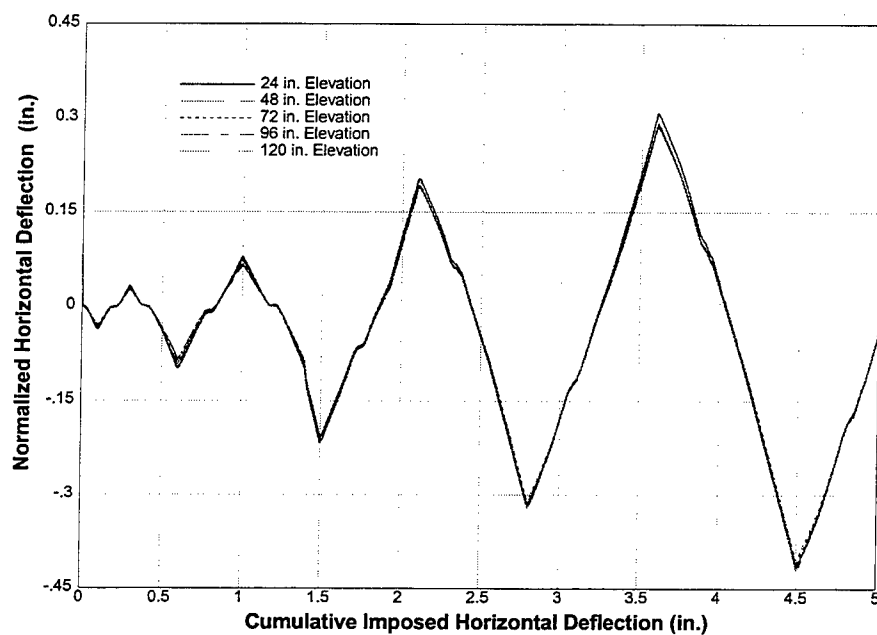


Figure 87. ITS-2 measured horizontal deflection at various elevations, normalized by height on the structure.

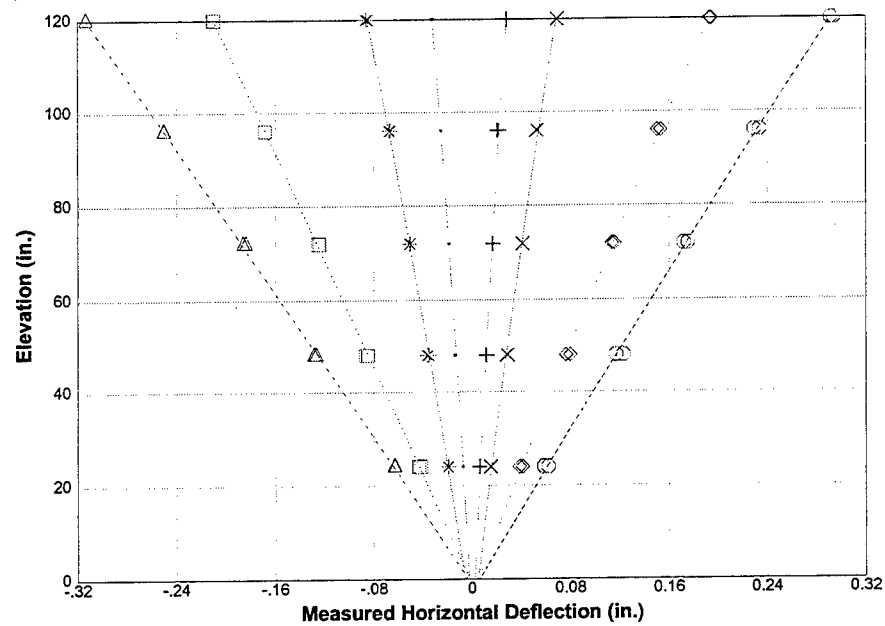


Figure 88. Deflected shape of ITS-2 at the top of the first eight excursions, as measured by the horizontal deflection gages.

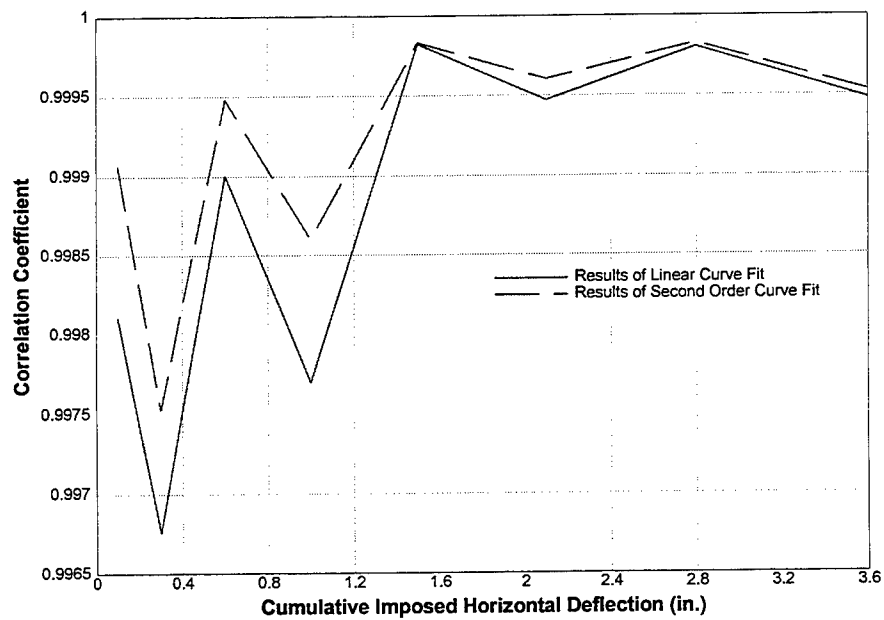


Figure 89. Correlation coefficients for linear and second-order curve fits to the deflected shape of ITS-2 at the top of the first eight excursions.

Strain Response

Strain gage measurements were made at 66 positions during the experiment.

Vertical gages were located throughout the model, with most of the gages located in the expected failure zone at the base of the tower. A personal computer mapping program, Surfer, was used to generate contour plots of the distributions of the strains, in the base of the model, from the recorded data. Contour plots of the distribution of the vertical strain at the base and at 2 in. above the base of the ITS-2 model can be found in Appendix C. Plots were generated at the top of each leg of each load cycle, as well as at the zero deflection point for each cycle. North is towards the top of the page in all plots.

Contours of vertical strain at the base of the ITS-2 tower for an imposed top deflection of -0.1 in. can be seen in Figure C1. This is the top of the first load cycle, and cracking has not yet occurred. A well-defined strain distribution is visible. Tensile strains are concentrated at the corners of the east wall with a localized peak of about 120 microstrain. This peak tensile strain is below the range considered close to failure for concrete. A similar plot can be seen in Figure C3 at the peak of the next excursion at an imposed top deflection of 0.1 in., as well as in Figure C5 and Figure C7 at the top of each leg of the 0.2-in. cycles.

The post-cracking section strain distribution, recorded at the base of the ITS-2 tower for an imposed top deflection of -0.3 in. and a cumulative imposed travel of 1.5 in., that is, the top of the first leg of the third load cycle, is shown in Figure C9. The post-cracking strain distribution is not as uniform as the pre-cracking distribution because the

strains measured are dependent upon whether or not a crack intersects the location of the gage. The large tensile strains that were recorded (25,000 microstrain to 35,000 microstrain) are values that exceed the yielding strain, approximately 1,750 microstrain, of the steel used in this model. The fact that this occurs immediately after cracking shows that due to the low reinforcement ratio in the structure, the cracking capacity of the section is greater than the elastic capacity of the reinforcement. This result was expected from the pre-experiment analysis. The apparent location of the neutral axis shifts well into the west wall. Figure C11, for an imposed top deflection of 0.3 in. and a cumulative imposed travel of 2.1 in., that is, the top of the second leg of the third load cycle, shows that these tensile strains are not recovered and, hence, are permanent plastic deformations. Also, Figure C20, Figure C21, and Figure C22 show that only a very small amount of this plastic deformation extends up into the model at an elevation of 2 in. This confirms the very localized failure mode of the model.

Modal Response

A substantial effort was expended to collect modal response data before, during, and after the experiment. Surveys were conducted with and without the loading rams attached. Surveys without rams attached (non-loaded surveys) were conducted prior to experimentation and after the experiment was completed. Eight surveys were conducted during the experiment with the rams attached and with the vertical model dead load applied (loaded surveys). These data were acquired to assist in the estimation of the changes in the modal response of intake towers due to accumulation of damage during an

earthquake. Graphical representation of the modes extracted using the IDEAS program can be found in Appendix D.

As in ITS-1, the first modal survey of the ITS-2 structure was conducted after the model was bolted to the floor but before the vertical and horizontal rams were attached. There were 112 survey points for this survey. The frequency response function of the model is shown in Figure 90. Clear peaks are visible in the range of 0 Hz to 600 Hz, with corresponding coherence values close to 1.0. Using the modal extraction capabilities of the IDEAS program, several modes of response were identified. Graphical representations of three of these modes are shown Appendix D. Figure D1 shows the shape of the lowest frequency mode at about 44 Hz. This motion appears to be the fundamental frequency in the first bending mode. The first torsional mode (Figure D2) occurs at approximately 121 Hz. Also, a second torsional mode shape (Figure D3) is observed at a frequency of about 157 Hz. The second bending mode of the undamaged structure is shown in Figure D4 and was extracted at a frequency of about 457 Hz.

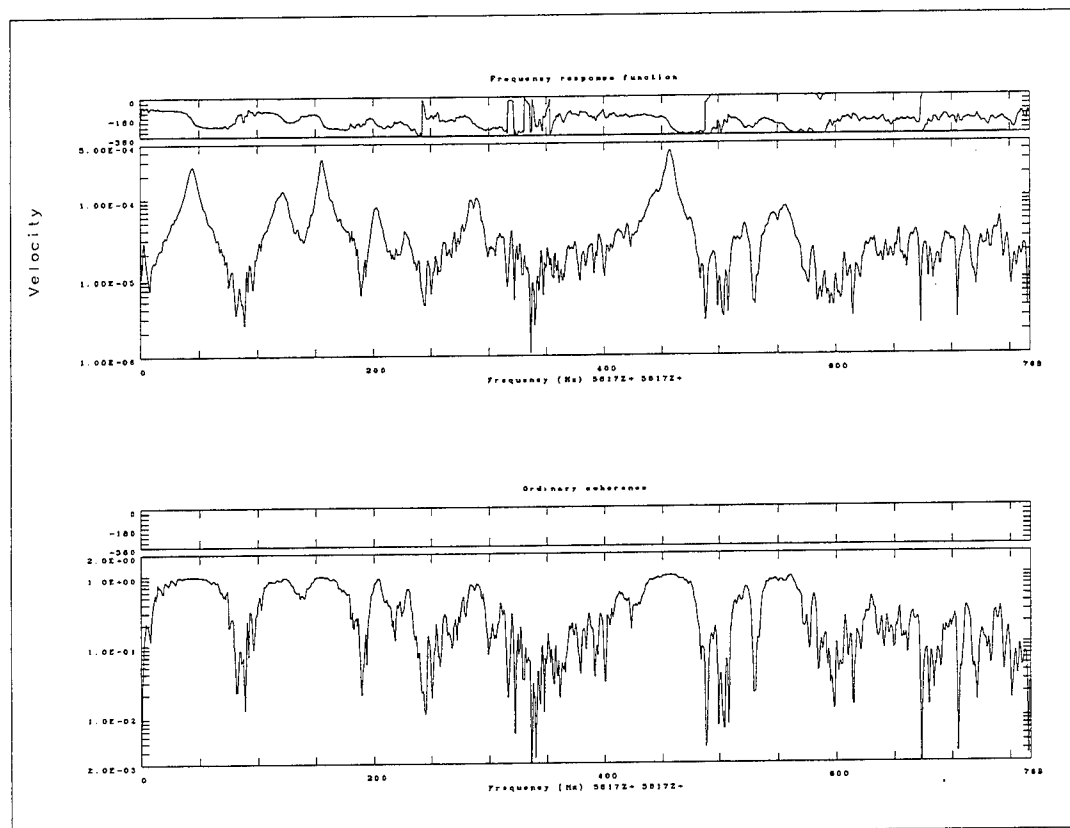


Figure 90. ITS-2 frequency response function from pre-experiment survey.

A modal survey of the ITS-2 structure was conducted after the experiment was conducted and the model had suffered a maximum top excursion of 2.0 in. As in the pre-experiment surveys, the model was bolted to the floor but the vertical and horizontal rams were not attached. The frequency response function of the model is shown in Figure 91. As in the pre-experiment model clear peaks are visible. A substantial difference between the shape of the frequency response functions of the damaged and undamaged models can be observed.

Graphical representations of four of the modes extracted are shown Figure D5 through Figure D8. Figure D5 shows the shape of the lowest frequency mode at

approximately 23 Hz. This motion appears to be the first bending mode and indicates a reduction from the pre-experiment natural frequency of 49 percent. The first torsional mode of response in the damaged model appears in Figure D6 at about 94 Hz, a reduction of 23 percent from the pre-experiment natural frequency. The second torsional mode appears in Figure D7 at 157 Hz, virtually unchanged from the pre-experiment value. The second bending mode of response in the damaged model appears in Figure D8 at 340 Hz. This corresponds to a reduction from the pre-experiment natural frequency of 26 percent. The second bending response of the damaged model appears to be more complex due to the freedom of the bottom of the model to move relative to the base.

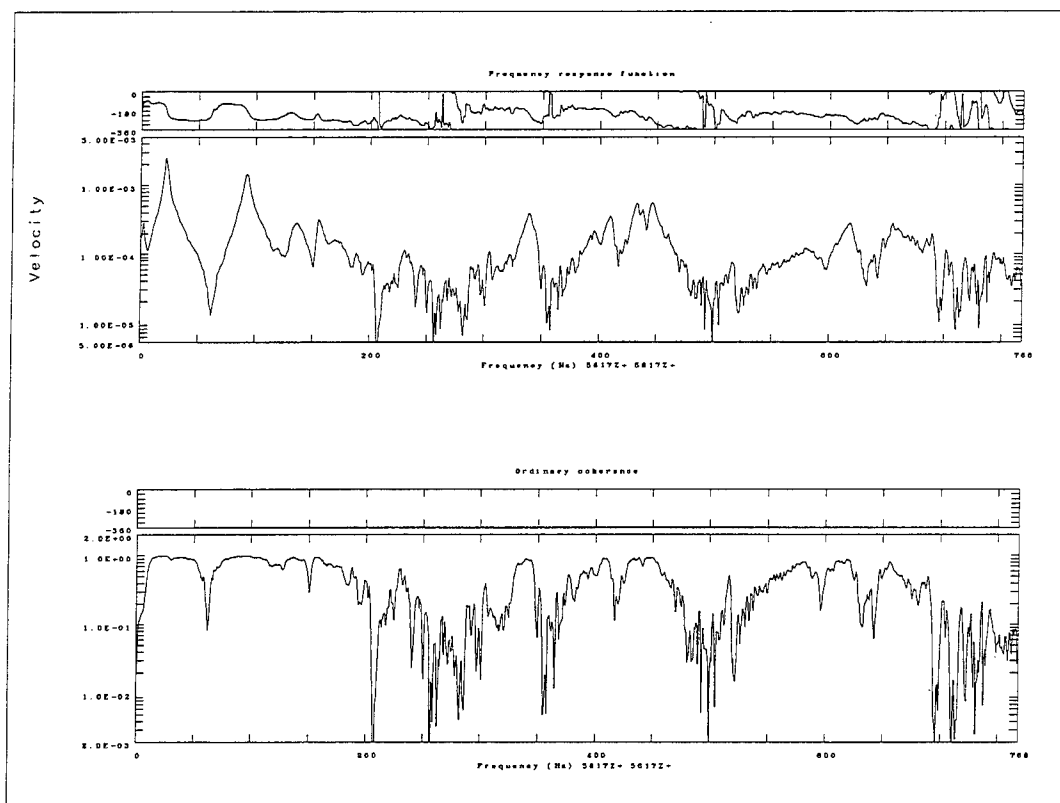


Figure 91. ITS-2 frequency response function from post-experiment survey.

In addition to the two non-loaded surveys, eight surveys were conducted during the experiment with the rams attached and with the vertical model dead load applied (loaded surveys). Due to the fact that these surveys had to be conducted while the experiment was on hold, the time spent on each survey had to be minimized. The number of survey points was reduced to 9 from the 112 points surveyed in the non-loaded surveys. In spite of this reduction, the first bending, torsional, and second bending modes were clearly visible when extracted. It was apparent that the application of the vertical load and the attachment of the horizontal loader did not restrain the top of the tower so as to preclude these modes from being active. In fact, the pre-experimental loaded and non-loaded surveys showed very similar natural frequencies for these modes. The loaded first bending mode was 55 Hz compared to the non-loaded 44 Hz. The loaded torsional mode was 138 Hz compared to the non-loaded 121 Hz. The loaded second bending mode was 455 Hz compared to the non-loaded 457 Hz.

Of greater interest is the variation of the modal response of the model with increasing damage. One way of determining this relationship is to plot the natural frequencies of the models against the maximum excursion experienced. The plot can be further simplified by normalizing the frequency to the undamaged model frequency. Figure 92 shows this relationship for the first bending mode, Figure 93 for the first torsional mode, and Figure 94 for the second bending mode. It is immediately apparent that there is a well-defined reduction for both the first bending and first torsional modes

for the ITS-2 model. It is also apparent that there is little consistent change in the frequency of response for the second bending mode. It is interesting to note that the reduction in all three modes was much greater for the non-loaded models. The lesser reduction for the loaded models perhaps reflects the fact that the applied vertical loads tend to close flexural cracks, reducing their influence on the model response. The loaded values may be the most realistic, given that the vertical loads were applied in order to simulate the prototype state of stress at the crack. It can be concluded that for the ITS-2 model, the first bending and first torsional modes were reduced by about 15 percent, and that the second bending mode was not significantly reduced.

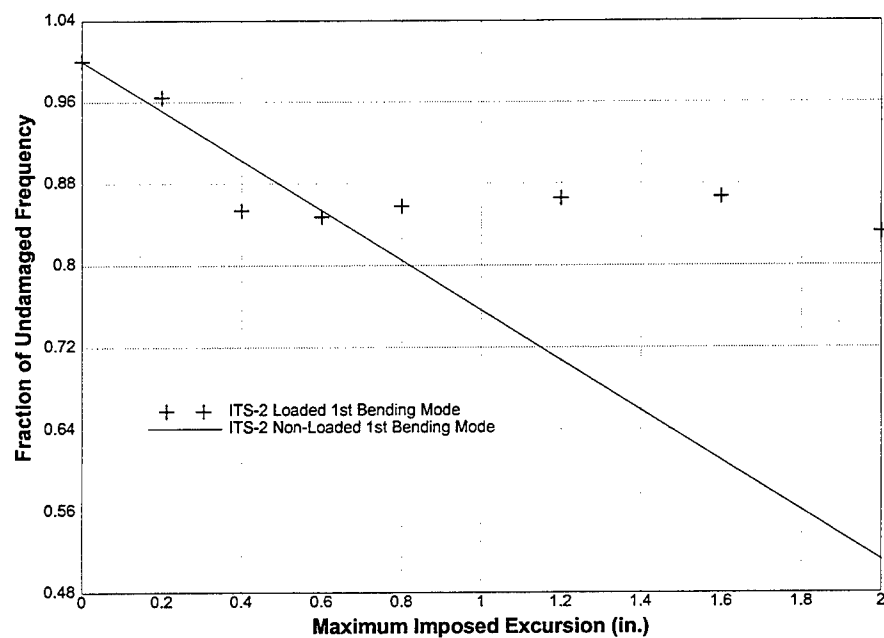


Figure 92. Change of first bending mode with increasing damage for ITS-2 model.

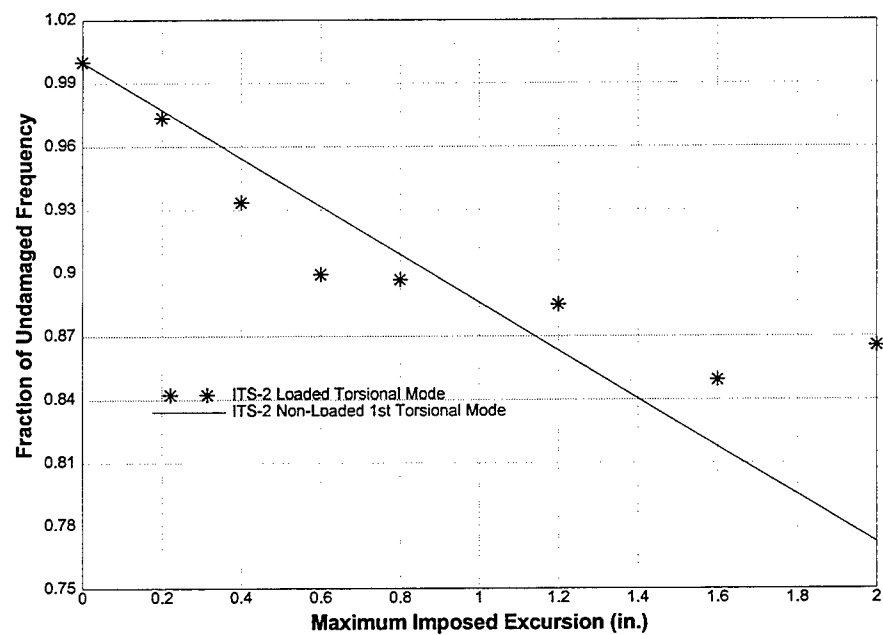


Figure 93. Change of first torsional mode with increasing damage for ITS-2 model.

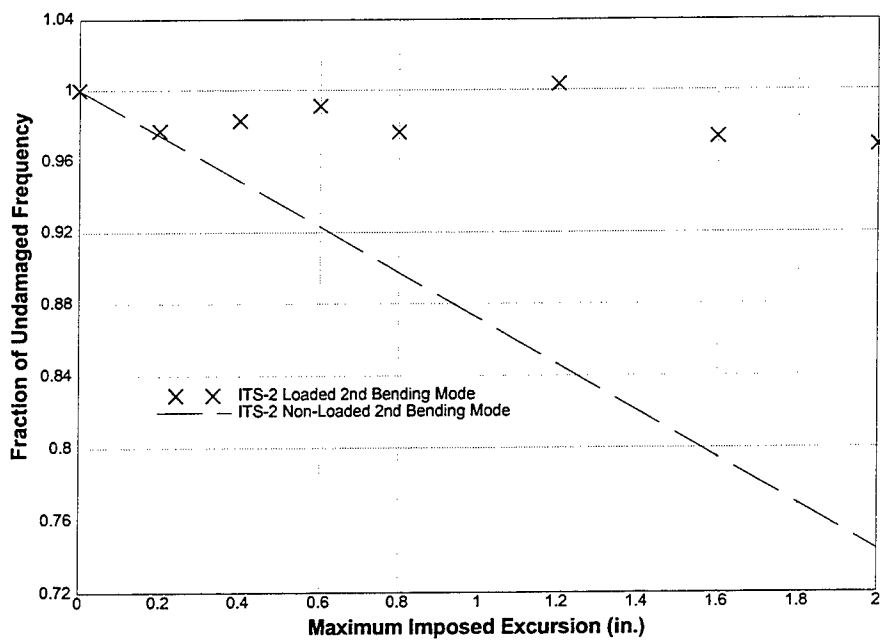


Figure 94. Change of second bending mode with increasing damage for ITS-2 model.

CHAPTER 6

ITS-3 EXPERIMENTAL RESULTS

Introduction

The cyclic excursion experiment ITS-3 was completed on October 28, 1996. A vertical load was applied to the structure and held constant throughout the experiment to simulate dead load. The horizontal load was applied by a deflection-controlled loader at a rate of 0.01 in./sec. Each cycle consisted of one excursion in both the east and west directions, beginning with a 0.1-in. excursion and increasing by 0.1 in. for each subsequent cycle. The experiment was temporarily stopped seven times to allow for the modal survey, measurement, and photography of the structure. The experiment required approximately 6 hours to conduct. Seventy-two channels of active data recorded and 10 modal surveys were conducted. Video and still photography were included.

Structural Response

The structural response of the ITS-3 structure was very similar to that of the ITS-1 and ITS-2 models. Photographs of the response of ITS-3 are presented in Figure 95 to Figure 104. Visual inspection of the model during loading led to several observations. As in the prior experiments, damage to the model was limited to the bottom of the tower section at the interface with the rigid base. The damage consisted of one tension crack that extended across the base of the model. The tension crack did not follow the interface of the cold joint located in this region but dipped downward below the cold joint into the concrete base material before returning to the surface at the far side of the wall. In spite of the increased vertical steel percentage and decreased concrete strength, there was no evidence of crushing of the concrete and there was no apparent degradation of the concrete as the load cycles were repeated. As in ITS-1 and ITS-2, the ultimate failure of the ITS-3 structure appeared to be controlled by the response of the reinforcing bars. Ruptured reinforcing bars were visible across the entire base of the structure.

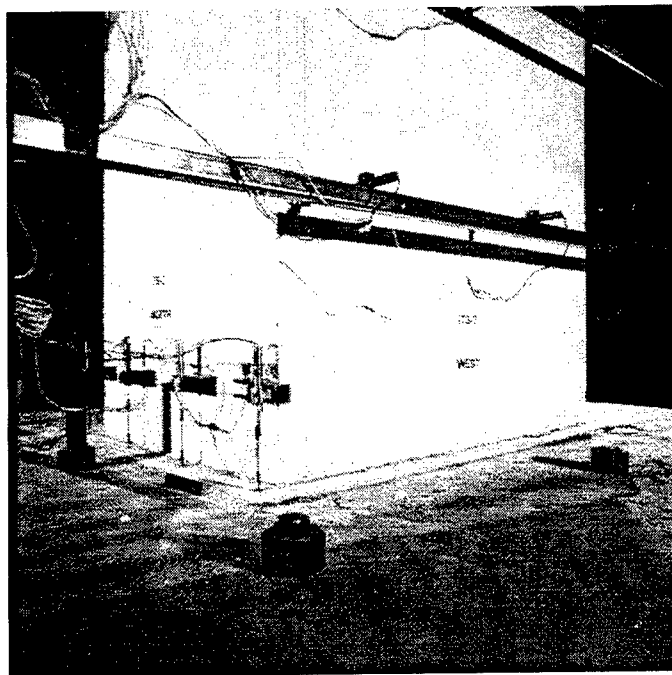


Figure 95. ITS-3 pre-experiment view of north and west walls.

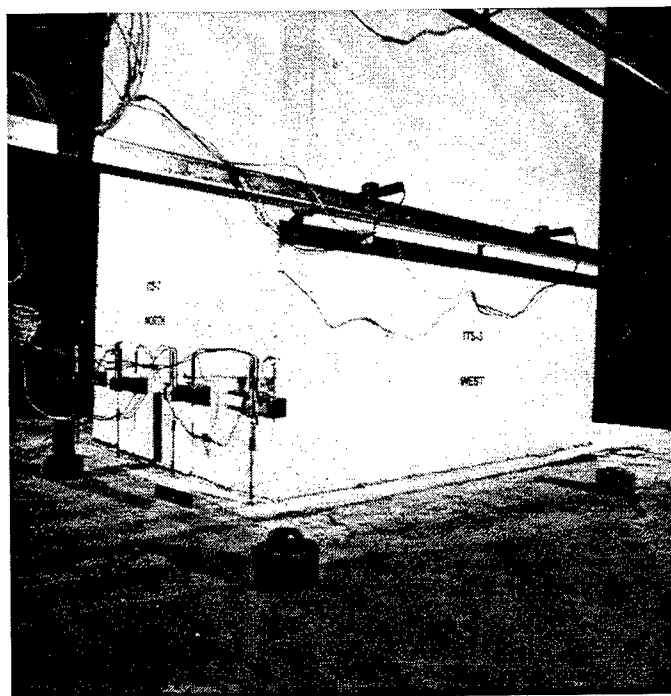


Figure 96. ITS-3 view of north and west walls, imposed top deflection of 1.6 in. towards the west.

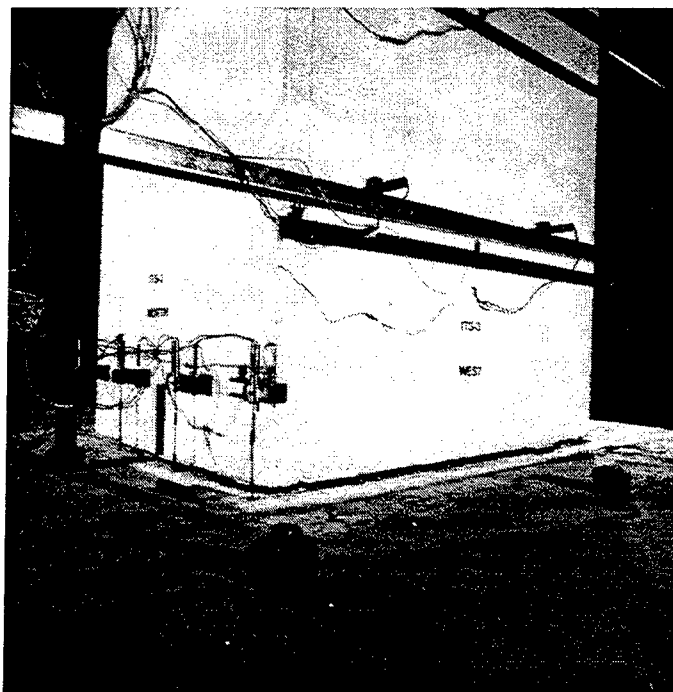


Figure 97. ITS-3 view of north and west walls, imposed top deflection of 1.6 in. towards the east.

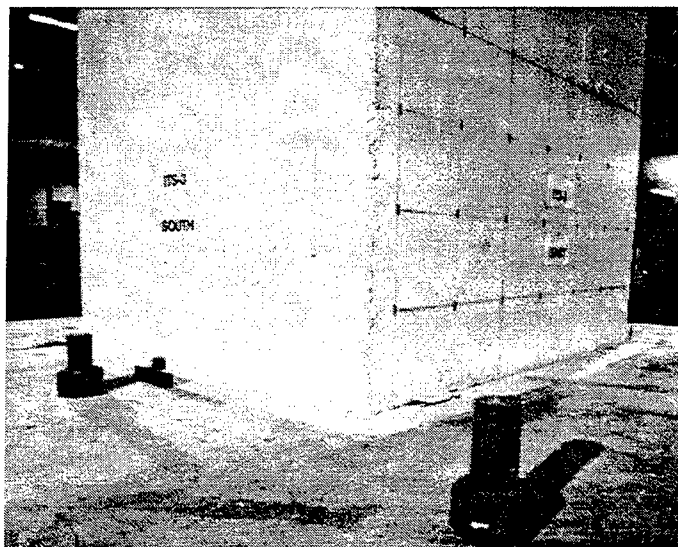


Figure 98. ITS-3 pre-experiment view of south and east walls.

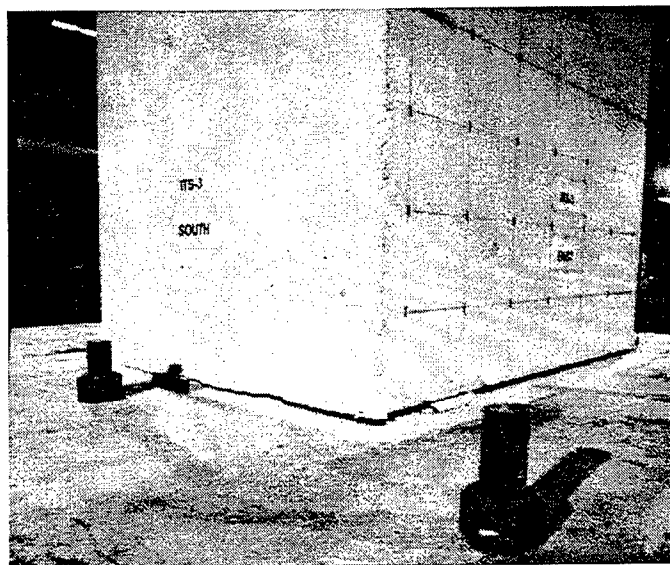


Figure 99. ITS-3 view of south and east walls, imposed top deflection of 1.6 in. towards the west.

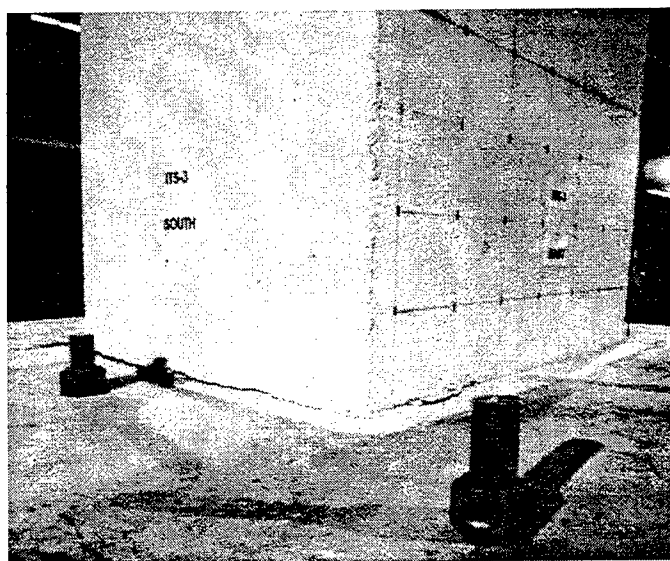


Figure 100. ITS-3 view of south and east walls, imposed top deflection of 1.6 in. towards the east.



Figure 101. ITS-3 pre-experiment close-up view of interior south-east corner.

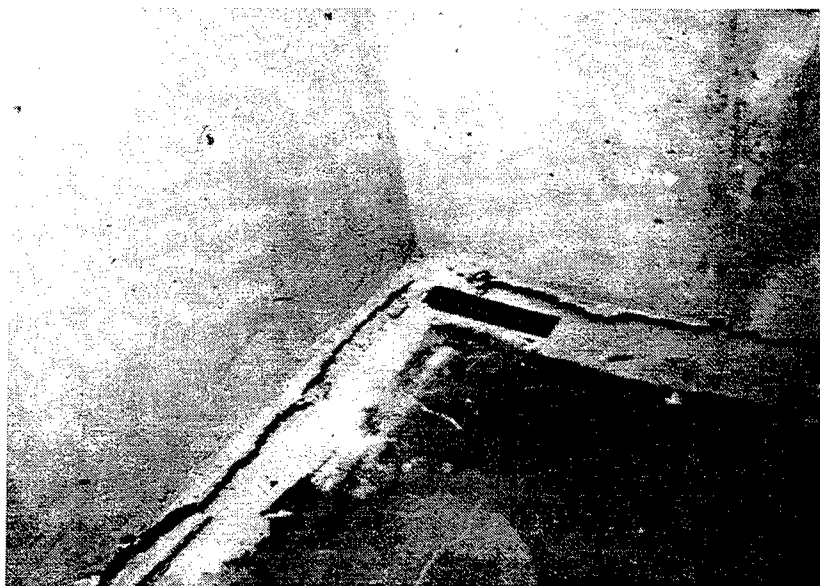


Figure 102. ITS-3 close-up view of interior south-east corner, imposed top deflection of 1.6 in. towards the west.

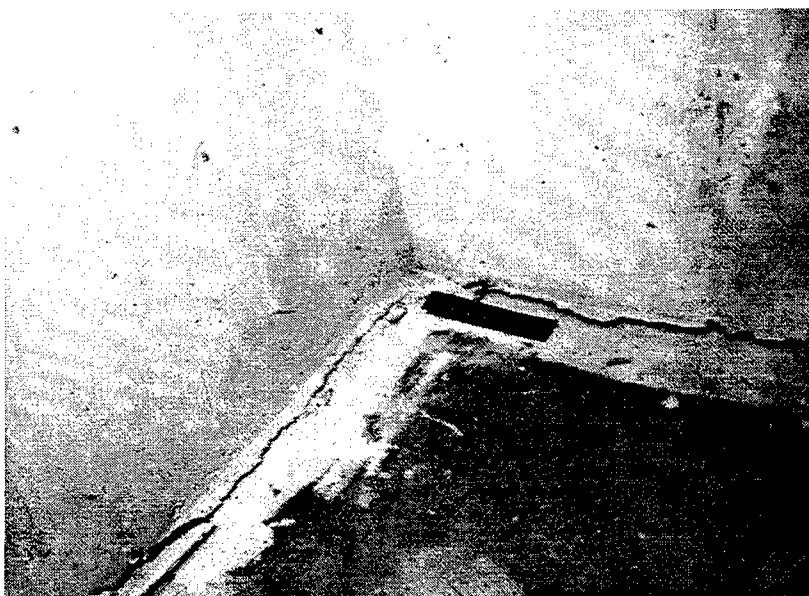


Figure 103. ITS-3 close-up view of interior south-east corner, imposed top deflection of 1.6 in. towards the east.

Active Instrumentation Response

Eighty channels of active data were recorded during the experiment. Two of these channels were allocated to the measurement of load and deflection in the 50-kip horizontal hydraulic loader. Deflection was measured at 14 positions, and strain was measured at 66 positions. The constant vertical load applied to the top of the structure was monitored but not recorded. Recording was performed at 2 samples per second and thus, during the approximate 6 hours of the experiment, a total of about 3,500,000 samples were taken for the 80 channels. Based on the experience gained in analyzing the ITS-2 experiment, the majority of plotting and data analyses were conducted with the structural response plotted against the deflection measured by the LVDT gage located at the top of the model. As discussed in the prior chapter, the horizontal loader deflection

was the controlled input parameter in these experiments; however, the inevitable existence of slack in the loader as well as load frame flexibility led to the realization that the measured response was the best response parameter to focus on during experimental analysis.

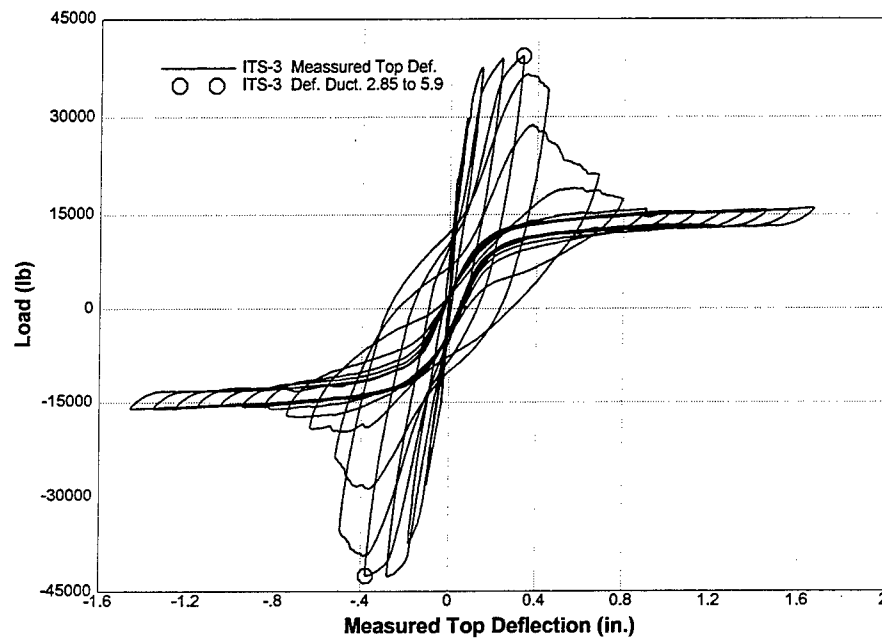


Figure 104. Horizontal load versus measured horizontal deflection.

Load Response

Figure 104 shows the force imparted by the horizontal loader versus the deflection of the top of the ITS-3 structure. The force was measured by a load cell mounted on the loader, and deflection was measured by the external LVDT gage DC15. The initial direction of the loader was from east to west, imparting a compression (negative) load to the load cell and negative deflection measurement. Examination of the load-deflection history shows a linear-elastic response for the first four excursions (two complete cycles)

of the loader. The first excursion, from a loader excursion of 0 to -0.1 in., resulted in a measured deflection of -0.034 in. and a load of about -15,500 lb. The second excursion, from 0 to 0.1 in., resulted in a measured deflection of 0.022 in. and a load of 15,000 lb. The third excursion, from 0 to -0.2, resulted in a measured deflection of -0.099 and a load of -28,200 lb. The fourth excursion, from 0 to 0.2 resulted in a measured deflection of 0.077 and a load of 29,800 lb. During the fifth excursion, yielding of the entire section appears to have occurred at about a measured deflection of -0.135 in., at a load of -34,300 lb. Unlike ITS-1 and ITS-2, the measured load did not decrease at this point. As expected, the cracking moment did not exceed the ultimate moment for this more highly reinforced structure with weaker concrete. There were no abrupt changes with increasing load cycles, rather some strain hardening and then degradation was witnessed. It appears that the ultimate deflection occurred during the fifth cycle at the peak of the ninth and tenth excursions, at a measured deflection of -0.376 in. and a load of -42,600 lb, and a deflection of 0.336 in. and a load of 39,300 lb, respectively.

As was done for ITS-1 and ITS-2, the deflection ductility of the model was determined from the yield and ultimate deflections of the structure. Given the values of yield and ultimate measured deflections, the calculated deflection ductility for the ITS-3 model is 2.85. This value is less than the deflection ductility of 5.1 calculated for the ITS-2 model based on measured deflections. That the ductility of ITS-3 should be less than that of ITS-2 appears to be counter intuitive, given that the ITS-3 model has twice the vertical steel. However, close examination of the strain data measured at the base of

the ITS-3 model shows that the actual initial yield occurred during the first leg of the second excursion, at a much smaller measured deflection of about 0.06 in. This value gives a ductility ratio of about 5.9. The sensitivity of the ductility ratio to the exact definition of the yield point reflects the fact that the yield deflection for these lightly reinforced sections is a very small number. Thus, small changes in the yield deflection, relative to the ultimate deflection, have a large impact on the apparent ductility.

Deflection Response

Horizontal deflections were measured at 2-ft intervals along the height of the structure. These measured deflections are shown plotted against the cumulative deflection imposed on the structure by the horizontal loader in Figure 105. As in the ITS-2 analysis, the cumulative imposed horizontal deflection was used to unfold the data for ease of visualization. Presented in this manner, first yield occurred at 0.6 in., second yield at 1.0 in., first ultimate at 2.8 in., and second ultimate at 3.6 in. These points correspond to the top of the third excursion, top of the fourth excursion, top of the seventh excursion, and top of the eighth excursion, respectively.

Close examination of Figure 105 shows that there appears to be very little torsional response. As was also true in ITS-2, the two gages at each elevation of ITS-3, located at the center and edge of the model, gave essentially the same values. Again, the deflection curves collapse into one curve when the deflections are normalized to the height of the gage (Figure 106), that is, when the deflection at each elevation is divided

by the fraction of its location up the total height. The deflection at any given elevation is a linear function of height. In other words the structure has a linear deflected shape.

The deflected shape of the ITS-3 model was directly determined by plotting the horizontal deflections measured at each elevation against height (Figure 107). Included in this figure is a second-order curve fit to the data. Both a linear and second-order curve fit were done for each measured deflections at the top of the first eight excursions. The correlation coefficients for the curve fits are shown in Figure 108. The second-order fits are slightly better for the first four excursions, after which a linear fit is essentially as good. Yielding of the entire base section occurs in the fourth excursion. A cantilever beam would be expected to exhibit a shape described by a second-order equation. This implies that the response of the ITS-3 model, like the ITS-2 model, is dominated by rigid-body rotation after the first yield, a fact that has important implications to the analysis of the response of these structures.

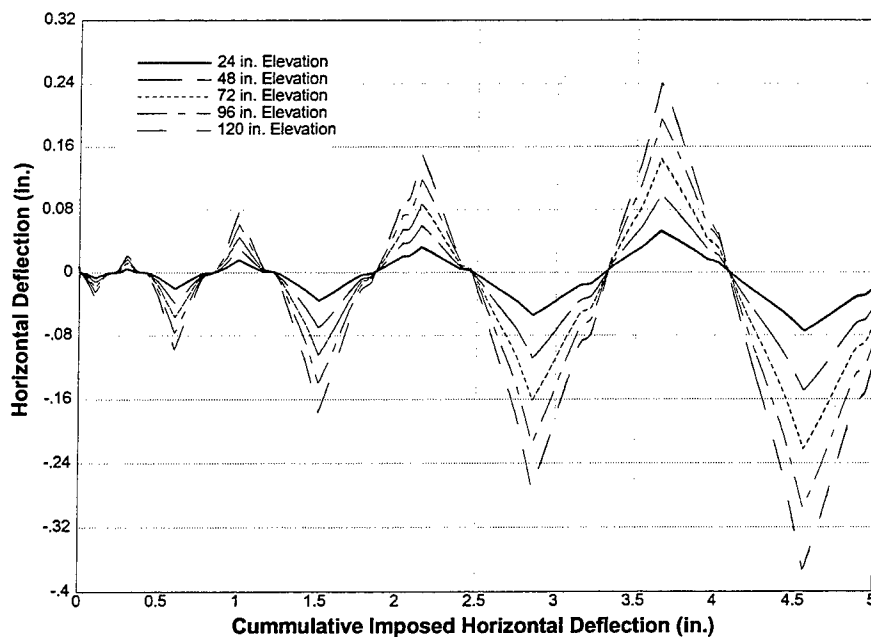


Figure 105. ITS-3 measured horizontal deflection at various elevations.

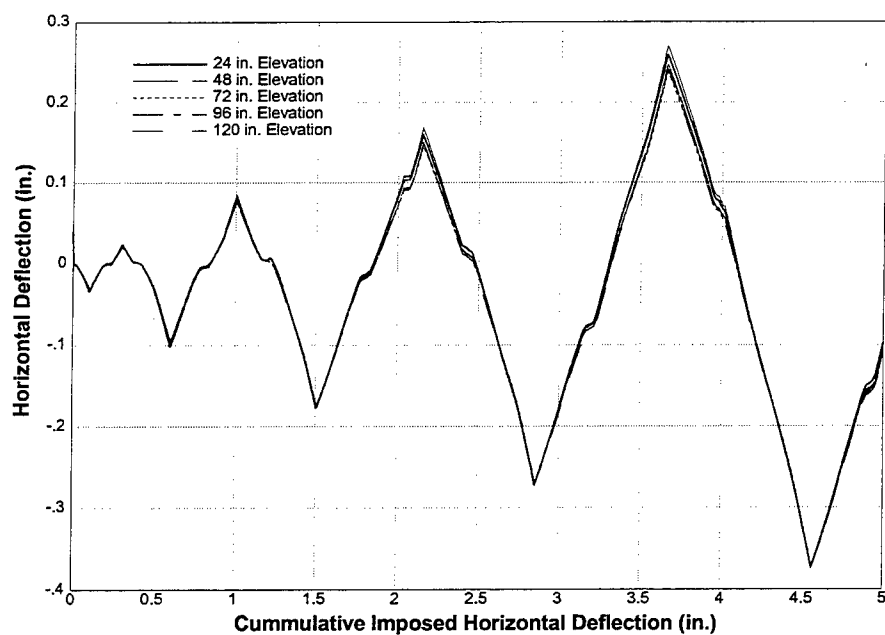


Figure 106. ITS-3 measured horizontal deflection at various elevations, normalized by height on the structure.

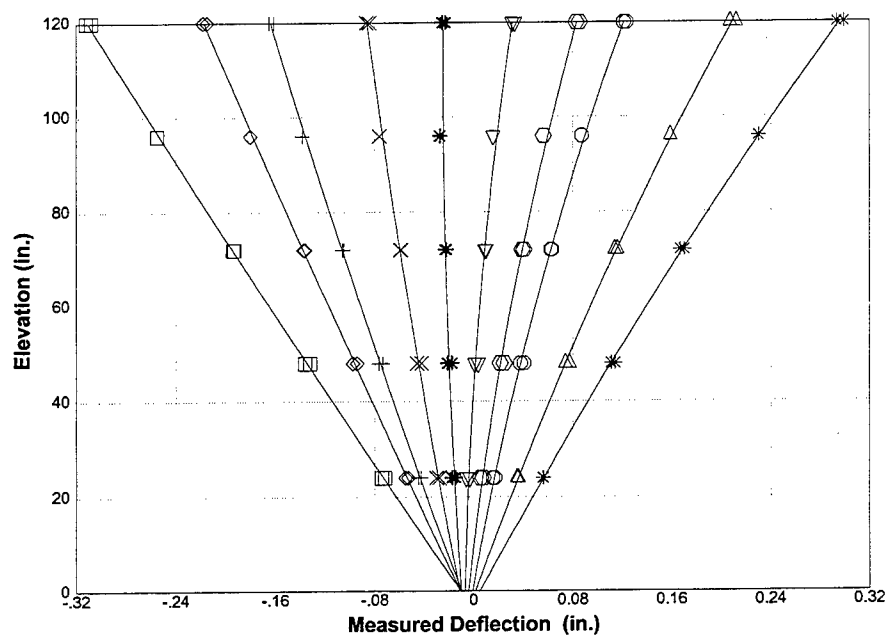


Figure 107. Deflected shape of ITS-3 at the top of the first ten excursions, as measured by the horizontal deflection gages.

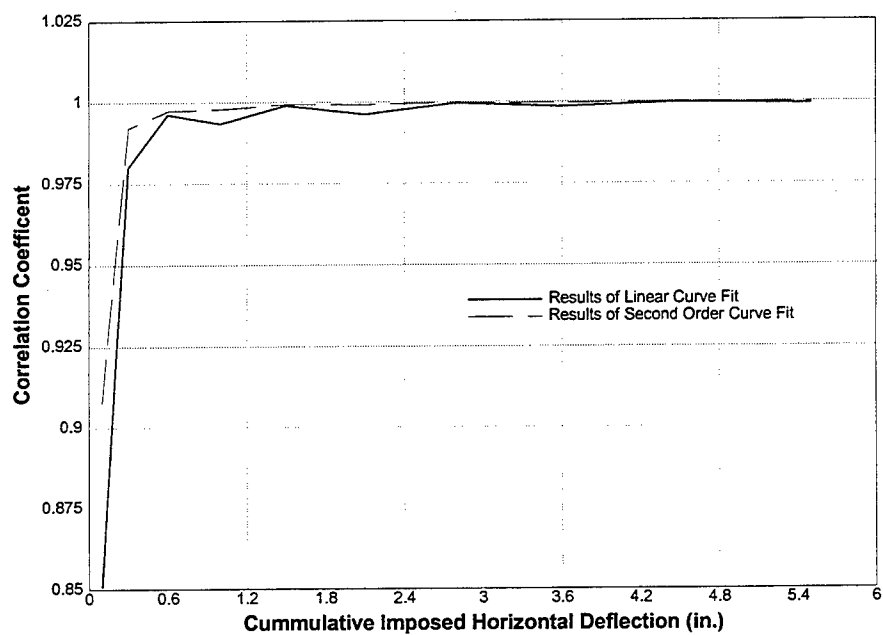


Figure 108. Correlation coefficients for linear and second-order curve fits to the deflected shape of ITS-3 at the top of the first ten excursions.

Strain Response

Strain gage measurements were made at 66 positions during the experiment. Vertical gages were located throughout the model, with most of the gages located in the expected failure zone at the base of the tower. As with prior experiments, contour plots of the distributions of the strains in the base of the model were generated from the recorded data. Contour plots of the distribution of the vertical strain at the base and at 2 in. above the base of the ITS-3 model can be found in Appendix C. Plots were generated at the top of each leg of each load cycle, as well as at the zero deflection point for each cycle. North is towards the top of the page in all plots.

Contours of vertical strain at the base of the ITS-3 tower for an imposed top deflection of -0.1 in. can be seen in Figure C23. This deflection is the top of the first load cycle and cracking has not yet occurred. A well-defined strain distribution is visible. Tensile strains are more uniform than those observed in the ITS-2 model at this deflection. At a maximum of about 200 microstrain, the peak tensile strain is just below the range considered close to failure for concrete. A similar plot can be seen in Figure C25 at the peak of the next excursion at an imposed top deflection of 0.1 in.; however, the strain levels are lower.

The post-cracking section strain distribution, recorded at the base of the ITS-3 tower for an imposed top deflection of -0.2 in. and a cumulative imposed travel of 0.6 in., that is, the top of the first leg of the third load cycle, is shown in Figure C27. The post-cracking strain distribution is not as uniform as the pre-cracking distribution because the

strains measured are dependent upon whether or not a crack intersects the location of the gage. This distribution differs substantially from that witnessed in the ITS-2 experiment. The post-cracking strains in the ITS-2 experiment immediately rose to exceed the yield strains of the steel used in that model, due to the fact that the cracking capacity of the section was greater than the elastic capacity of the reinforcement. In the ITS-3 model, the post-cracking strains remained below the expected yield strain of 2,287 microstrain until an excursion of -0.2 in. (Figure C27). The accumulation of yield strains with continued cycles was generally more graceful than witnessed in ITS-2. The yielding of the entire section occurred before the top of the first leg of the third cycle (Figure C31). Examination of the strain distributions at 2 in. above the base of the ITS-3 model, shown in Figure C36 to Figure C48, indicates a greater degree of spreading of the strain up into the structure than was witnessed in the ITS-2 model. The degree of spreading of the strain is very important. As will be discussed in the next chapter, the analysis of these lightly reinforced structures seems to be very dependent on the proper estimation of the strain penetration, or strain spreading, in the failure zone.

Modal Response

As in ITS-1 and ITS-2, a substantial effort was expended to collect modal response data before, during, and after the ITS-3 experiment. Surveys were conducted with and without the loading rams attached. The three surveys without rams attached (non-loaded surveys) were conducted prior to experimentation, post failure, and after the experiment was completed. Seven surveys were conducted during the experiment, with

the rams attached and with the vertical model dead load applied (loaded surveys).

Graphical representation of the modes extracted using the IDEAS program can be found in Appendix D.

A first modal survey of the ITS-3 structure was conducted after the model was bolted to the floor but before the vertical and horizontal rams were attached. The frequency response function of the model is shown in Figure 109. Clear peaks are visible in the range of 0 Hz to 600 Hz with corresponding coherence values of close to 1.0. Using the modal extraction capabilities of the IDEAS program, several modes of response were identified. Graphical representations of three of these modes are shown in Appendix D. Figure D9 shows the shape of the lowest frequency mode at 51 Hz. This motion appears to be the fundamental frequency in the first bending mode. The second mode shape shown (Figure D10) appears to be a clearly torsional response, at a frequency of 143 Hz. The third mode is shown in Figure D11 and was extracted at a frequency of 440 Hz. This response appears to be the second bending mode of the undamaged structure. It is interesting to note that the pre-experimental modes are similar to that seen in ITS-2.

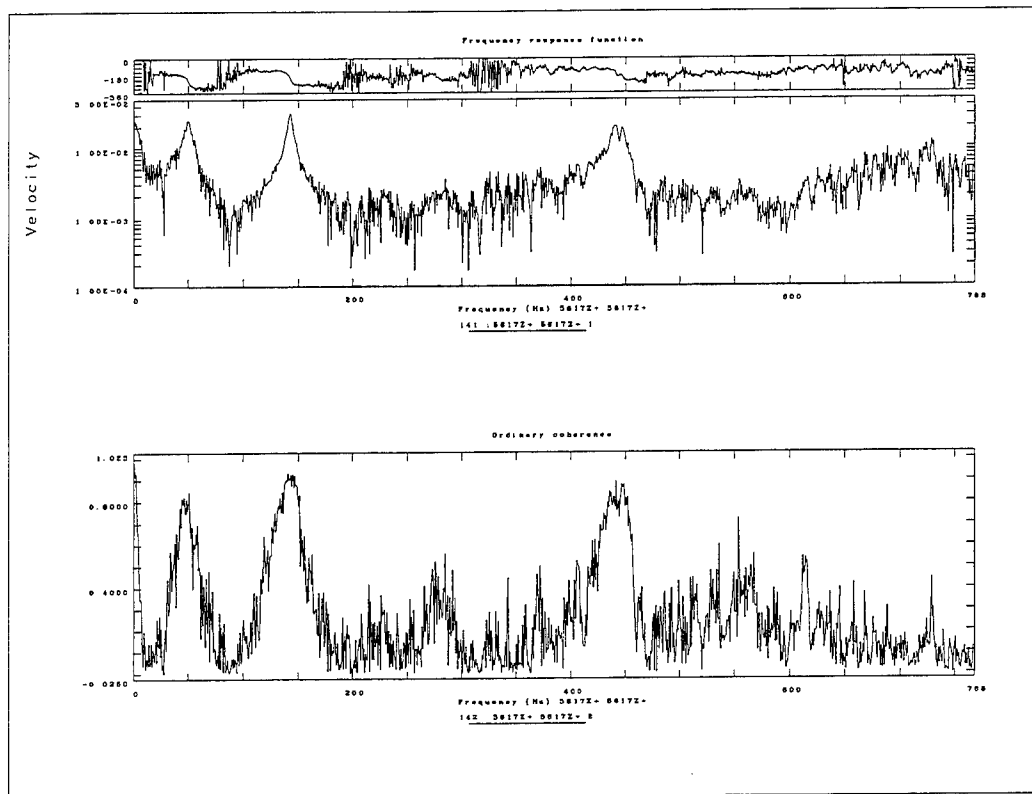


Figure 109. ITS-3 frequency response function from pre-experiment survey.

A non-loaded modal survey of the ITS-3 structure was conducted during the experiment in an attempt to capture the post-failure response. After the model had suffered an imposed top excursion of 0.6 in., the load capacity of the model appeared to have been reduced and the structure was deemed to have failed. The vertical and horizontal rams were detached for this modal survey. Again, this configuration is similar to a prototype tower in that it is a vertical cantilever unrestrained at the top. The frequency response function of the model is shown in Figure 110. As in the undamaged model, there are clear peaks visible. A substantial difference between the shape of the frequency response functions of the damaged and undamaged models can be observed.

The first peak of the post-failure (damaged model) plot appears to begin at a substantially lower frequency (longer period) than for the undamaged model.

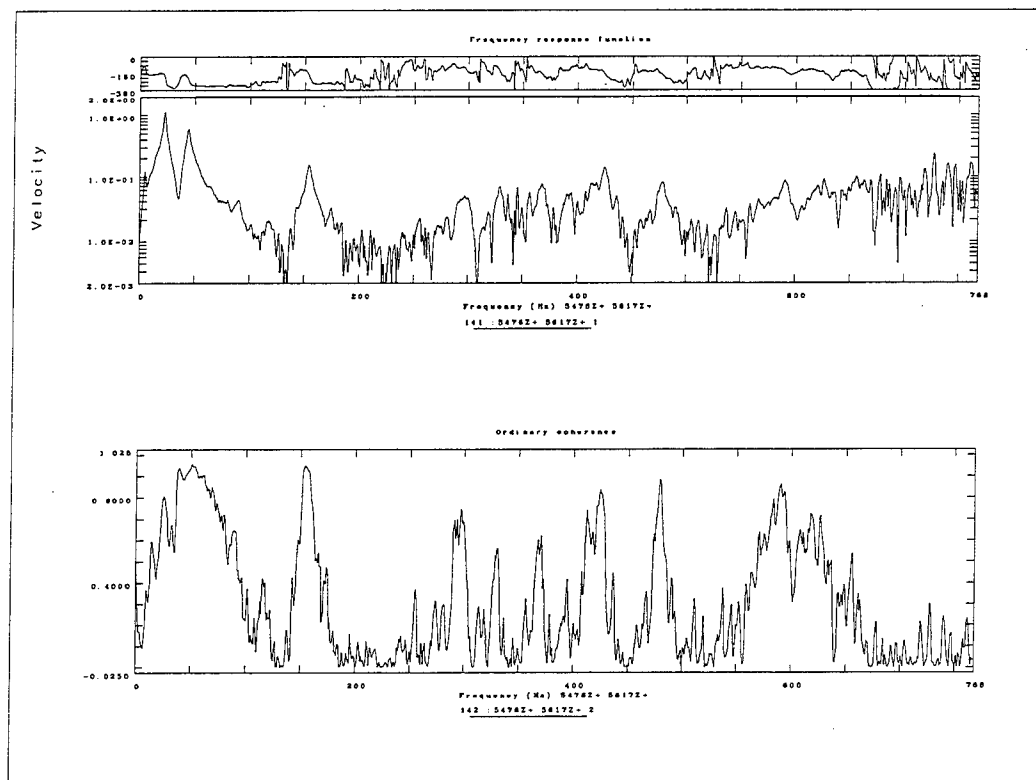


Figure 110. ITS-3 frequency response function from post-failure survey.

Several modes of response were identified for the damaged model. Graphical representations of four of these modes are shown in Figure D12 through Figure D15. Figure D12 shows the shape of the lowest frequency mode at 23 Hz. This motion appears to be the first bending mode. The first torsional mode of response in the damaged model (Figure D13) is at a natural frequency of 45 Hz, and the second torsion response (Figure D14) at 155 Hz. The second bending mode (Figure D15) is at 426 Hz.

A modal survey of the ITS-3 structure was conducted after the experiment was conducted, and the model had suffered a maximum top excursion of 1.6 in. As in the pre-experiment and post-failure modal surveys, the model was bolted to the floor; however the vertical and horizontal rams were not attached. The frequency response function of the model is shown in Figure 111. The response was very similar to the post-failure survey. The extracted modes of response had almost identical shapes (Figure D16 through Figure D19), with a slight decrease in the natural frequency for each of the major modes. Any damage that occurred after the post-failure survey did not appear to have greatly changed the modal response of the model.

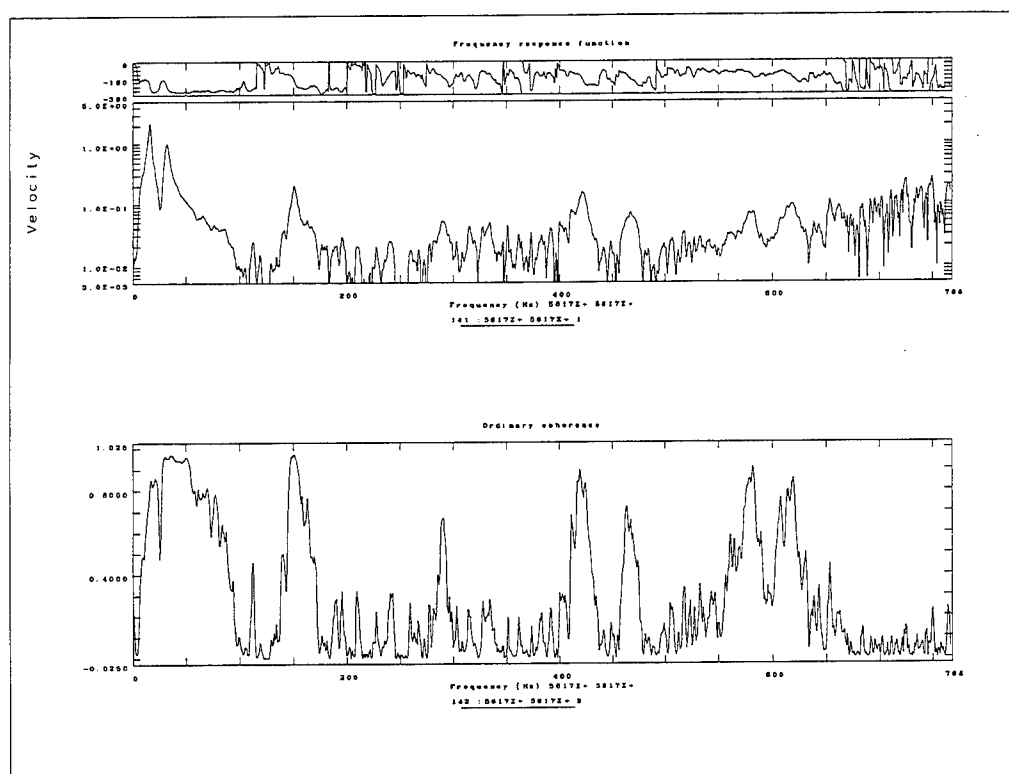


Figure 111. ITS-3 frequency response function from post-experiment survey

In addition to the three non-loaded surveys, seven surveys were conducted during the ITS-3 experiment, with the rams attached and with the vertical dead load applied (loaded surveys). Due to the fact that these surveys had to be conducted while the experiment was on hold, the time spent on each survey had to be minimized. The number of survey points was reduced to nine from 112 points surveyed in the non-loaded surveys. In spite of this reduction the first bending, torsional, and second bending modes were clearly visible when extracted. It was apparent that the application of the vertical load and the attachment of the horizontal loader did not restrain the top of the tower so as to preclude these modes from being active. In fact, the pre-experimental loaded and non-loaded surveys showed very similar natural frequencies for these modes. The loaded first bending mode was 55 Hz compared to the non-loaded 51 Hz. The loaded torsional mode was 138 Hz compared to the non-loaded 143 Hz. The loaded second bending mode was 455 Hz compared to the non-loaded 440 Hz.

As in ITS-2, the natural frequencies of the ITS-3 models were plotted against the maximum excursion experienced. The plot was further simplified by normalizing the frequency to the undamaged model frequency. Figure 112, Figure 113, and Figure 114 show this relationship for the first bending mode, the first torsional mode, and the second bending mode, respectively. For both the ITS-2 and ITS-3 models there appears to be a well-defined reduction for both the first bending and first torsional modes. It is also apparent that there is little substantial change in the frequency of response for the second bending mode. As in ITS-2, the ITS-3 reduction is greater for the non-loaded models,

reflecting the closing of the flexural cracks by the vertical load. The loaded models may be the most realistic, given that the vertical loads were applied to simulate the prototype state of stress at the crack. It can be concluded that, for both ITS-2 and ITS-3, the first bending and first torsional modes were reduced by between 10 and 15 percent, and that the second bending mode was not substantially reduced.

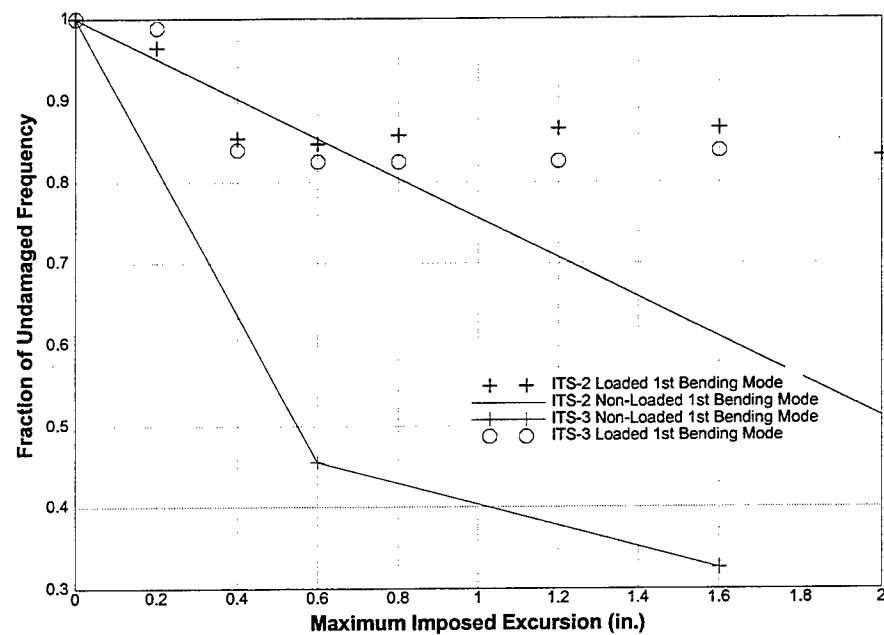


Figure 112. Change of first bending mode with increasing damage for ITS-2 and ITS-3 models.

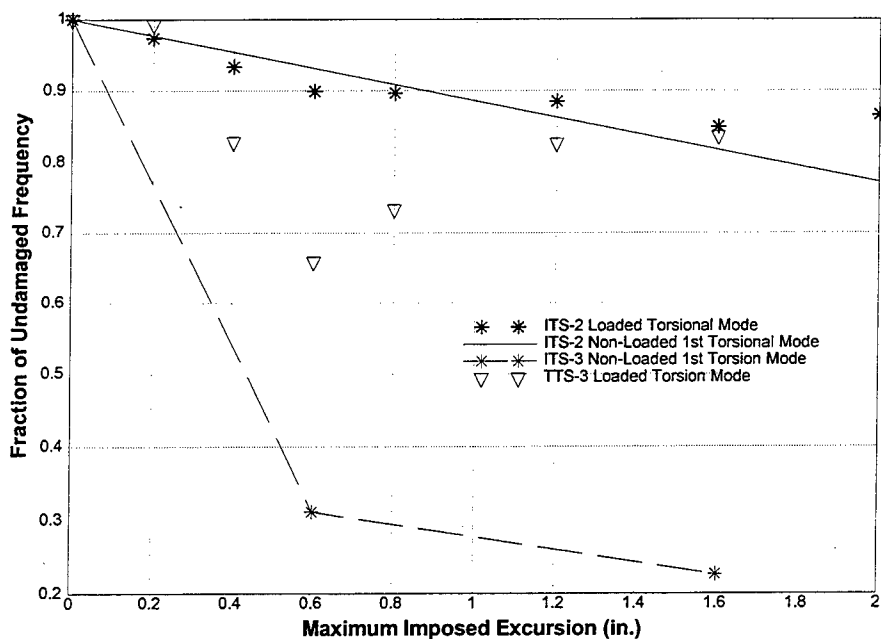


Figure 113. Change of first torsional mode with increasing damage for ITS-2 and ITS-3 models.

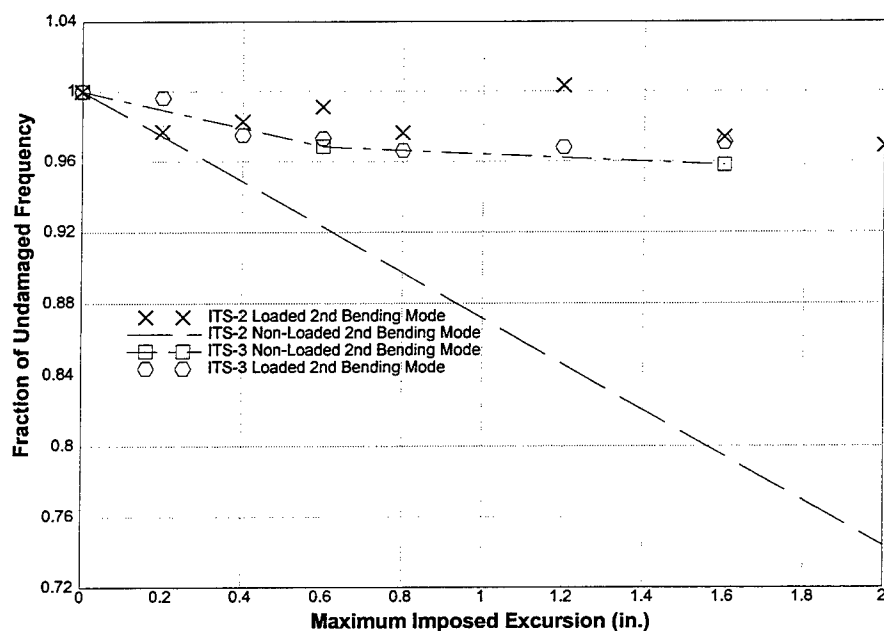


Figure 114. Change of second bending mode with increasing damage for ITS-2 and ITS-3 models.

CHAPTER 7

EXPERIMENTAL ANALYSIS

One objective of this research effort is the evaluation of the displacement-based analysis of intake towers. The fundamental premise of this method is the explicit consideration of the earthquake-induced displacements of a structure. The displacement-based analysis method is used as part of a response spectrum analysis of a tower. It attempts, in a simplified manner, to account for the shift of the structure's fundamental frequencies with formation of plastic regions in the structure. As cracking and yielding occur, the structure softens and the period of the structure increases. Often, this shifts the period out to a region of lower magnitude in the response spectrum, decreasing the loads on the structure.

The displacement-based analysis is presented as an alternative method of analysis in the current Corps of Engineers design and analysis guidance on intake towers, EC 1110-2-285, "Structural Analysis and Design of Intake Structures for Outlet Works." It is designated as being applicable to towers with vertical steel percentages of 1 percent

or less. As can be seen in Figure 115, almost all the critical sections identified in the analysis of the existing intake tower inventory have less than 1 percent vertical steel.

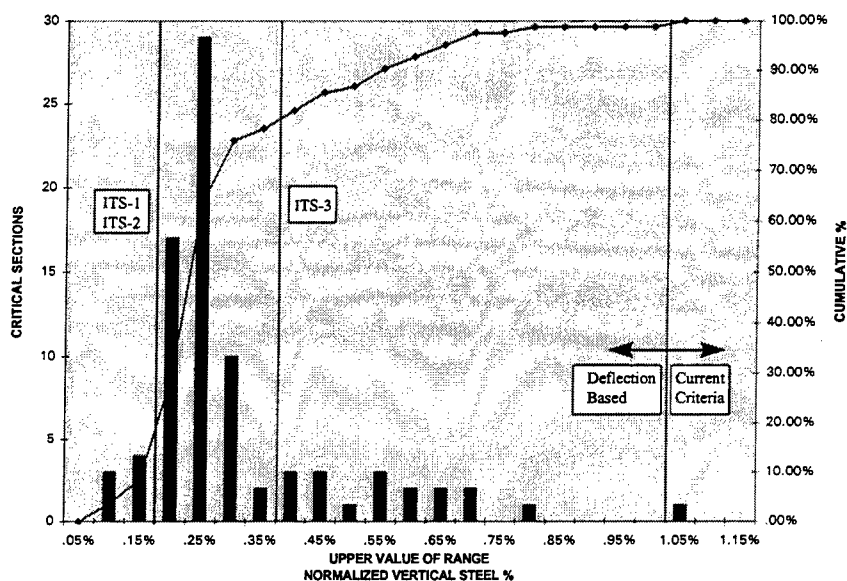


Figure 115. Suggested applicability of the displacement-based analysis technique.

The displacement-based analysis procedure follows three steps. In the first step, the displacement demand is calculated by response spectrum analysis assuming an effective stiffness for the section. This effective stiffness is an empirical parameter dependent on the loading and structural properties of the section. In the simplest case, it can be approximated by using half of the section moment of inertia (I) or half of the Young's modulus (E) for the material. Given the uniquely localized nature of the failure of these lightly reinforced intake towers, it may also be possible to model the response of the failure zone as a series of vertical springs or as a rotational spring.

In the second step of the displacement-based method, the displacement capacity of the structure is calculated. First, the moment-curvature relationship (m-phi diagram) of the section is calculated using stress block factors or a layer-by-layer approach. The curvatures calculated are used to calculate the displacement capacity of the structure using the following equation:

$$\delta_u = \frac{\phi_y l^2}{3} + (\phi_u - \phi_y) l_p \left(l - \frac{l_p}{2} \right) \quad (5)$$

where δ_u is the ultimate displacement at the elevation of interest; ϕ_y is the equivalent yield curvature at the base of the tower; ϕ_u is the ultimate curvature at the base of the tower; l_p is the plastic hinge length over which the ultimate curvature acts, and l is the structure height to the elevation of interest. Figure 116 shows the flexural response assumed in this equation. The yield curvature is assumed to form a triangular distribution up the structure. This is a significant assumption that can be very misleading. For slender, heavily reinforced structures, such as columns, the assumption of this distribution leads to the accurate prediction of yield displacements [6]. The extension of this assumption to intake towers must be carefully evaluated.

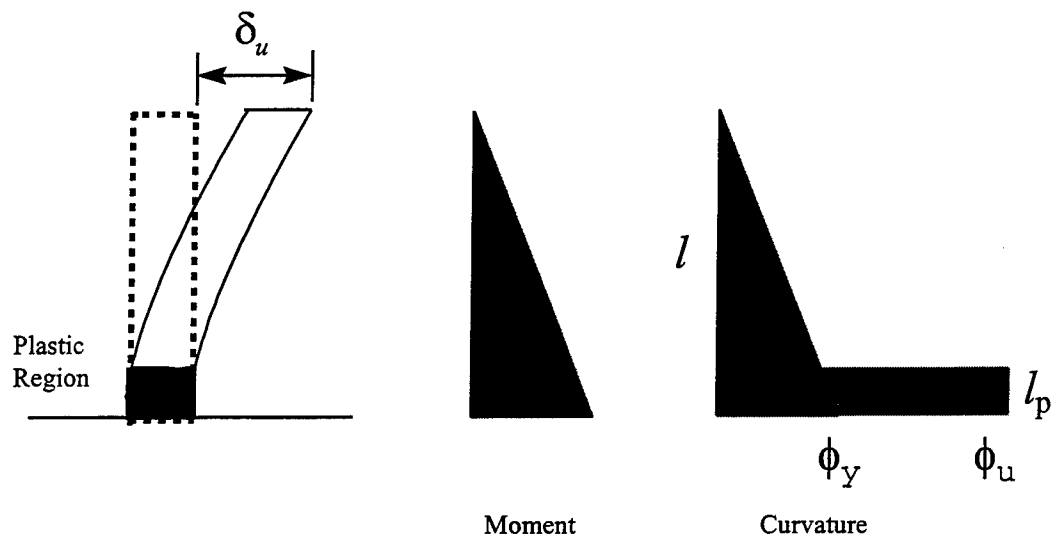


Figure 116. Assumed flexural response.

The value assumed for the plastic hinge length has a major influence on the results of this calculation. Determination of the plastic hinge length for reinforced concrete sections is a complex and poorly understood problem that depends on section shape, structure aspect ratio, reinforcing diameter and strength, and shear and axial load magnitudes. Two equations [7] used to estimate plastic hinge length, in the units of in., are:

$$l_p = 0.08l + 0.15d_b F_y \quad (6)$$

or

$$l_p = 0.3d_b F_y \quad (7)$$

where l is the structure height (in.), d_b is the reinforcing bar diameter (in.), and F_y is the reinforcing steel yield strength (ksi). Both equations attempt to include the influence of reinforcement variation and are defined as being applicable to ductile and brittle structures, respectively. It was suggested that structures be designated as brittle if 1.2 times the calculated cracking moment is greater than the ultimate moment of the section. Structures were to be designated as ductile if 2.0 times the calculated cracking moment, was less than the ultimate moment of the section. Numerous similar empirical equations for approximation of the plastic hinge length for various conditions also exist in the literature [6], [7], [8].

The demand-to-capacity ratio is calculated in the final step of the displacement-based method:

$$\frac{\delta_{Demand}}{\delta_u} < 1 \rightarrow OK \quad (8)$$

$$\frac{\delta_{Demand}}{\delta_u} > 1 \rightarrow Not - OK \quad (9)$$

where δ_{Demand} is the displacement demand calculated in the first step, and δ_u is the ultimate displacement capacity calculated in the second step. If the demand-to-capacity ratio is less than unity, the structure has sufficient capacity. If the ratio is greater than unity, the structure does not have sufficient capacity.

ITS-1 Analysis

The displacement-based analysis concept was used to predict the response of the ITS-1 model. The moment-curvature relationship was calculated using the RESPONSE [10] computer program. Assuming a triangular distribution of the yield curvature as discussed in the prior section, the yield displacement can be calculated as:

$$\delta_y = \frac{\phi_y l^2}{3} \quad (10)$$

and was calculated to be 0.016 in. Because 1.2 times the calculated cracking moment was greater than the ultimate moment, the structure was classified as a “brittle” structure, and the single crack assumption should apply. The plastic hinge length of 1.32 in. was calculated based on this single crack assumption (Equation 7). Applying the calculated values of the yield curvature, ultimate curvature, and hinge length in Equation 5, the ultimate calculated displacement was 0.35 in. The ratio of the ultimate to the yield deflection is the ductility ratio and is hence 1.84. A multi-crack assumption resulted in a hinge length of 10.26 in., with a calculated displacement ductility ratio of 7.25. The multi-crack assumption was considered an upper limit of predicted response.

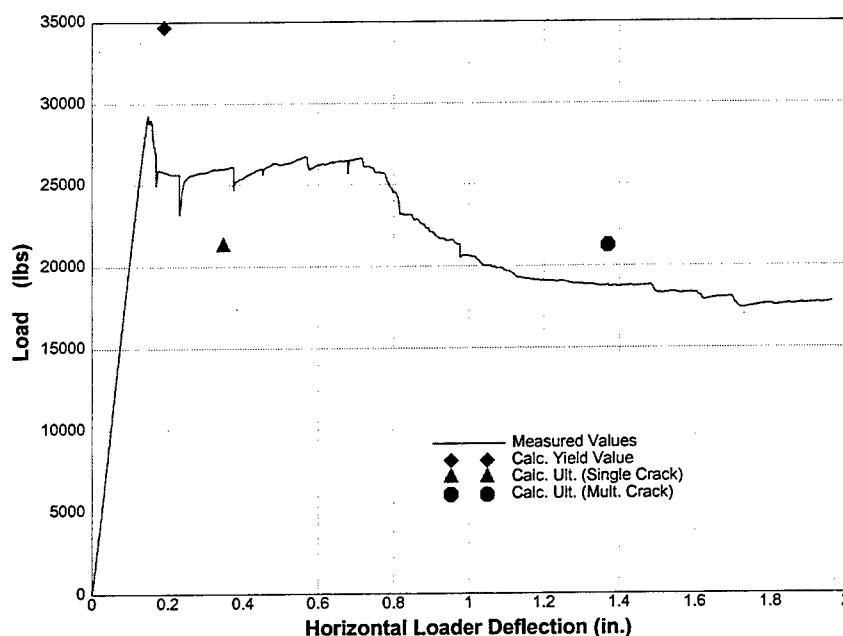


Figure 117. Observed and calculated ITS-1 response as related to imposed horizontal deflections.

Figure 117 shows these predicted values plotted against the experimental response. Overall, the analysis concept showed considerable promise. It appears that the cracking moment was over-predicted and the ultimate moment under-predicted by the RESPONSE program. The discrepancies are not due to any shortcoming of the displacement-based analysis concept but rather may be a result of the simplifying assumptions inherent in the formulation of the program, or the definition of the material properties. It can be expected that the definition of cracking strain of the concrete and the ultimate strain of the steel will have a direct relationship to the calculated cracking and ultimate moments. As will be discussed later, definition of these key parameters is not a trivial effort.

Of great interest is a comparison of the calculated and measured displacement ductility ratios and the plastic hinge length. The calculated displacement ductility ratio of 1.84 may be reasonable when compared to the measured value of 5.06, if consideration is given to the fact that the measured value is only due to a one-way excursion. ITS-1 was not a cyclic experiment and, therefore, can only be used to demonstrate that the experimental model has the potential for significant ductility. The cyclic experiments ITS-2 and ITS-3 were expected to show how much of this ductility can be safely utilized. Later experimentation also showed that significant error may be introduced by considering the imposed ram deflection as the structure deflection. The utilization of YOYO-type gages in ITS-1 placed severe constraints on the accuracy of the measured deflections. For this reason, all ITS-1 analyses were conducted based on the imposed ram deflection values.

Comparison of the calculated to experimental plastic hinge length is not a straightforward process. The plastic hinge length is not a directly measurable quantity, rather it is a parameter that relates the plastic curvature at the base of the structure to the plastic displacement at the top of the structure. It can be thought of as the distance over which the plastic curvature must act to result in the plastic displacement measured. The total displacement is equal to the sum of the yield and plastic displacements. Using the measured yield and ultimate displacements, the measured concrete strains, and estimated ultimate steel strains from reinforcing bar tests, the required plastic hinge length can be

calculated. The plastic hinge length calculated for this experiment was 1.1 in., which is close to the single crack estimate of 1.32 in.

For under-reinforced structures, such as intake towers, ductility is largely dependent on the ultimate steel strain. For such structures, failure occurs when the reinforcing bars rupture, not when concrete crushes. Figure 118 shows the relationship of ultimate steel strain and plastic hinge length on the displacement ductility ratio of the tower model. The relationship was defined by combining Equations 5 and 7 with the definition of deflection ductility and rearranging:

$$\mu = 1 + \left[\frac{(\epsilon_c + \epsilon_s)}{d} - \phi_y \right] l_p \left(l - \frac{l_p}{2} \right) \left(\frac{1}{\delta_y} \right) \quad (11)$$

Figure 118 was generated by assuming the measured yield deflection of 0.15 in. (δ_y), the calculated section yield curvature (ϕ_y) of 0.0000395 1/in., a constant concrete strain (ϵ_c) of 0.0003 in./in., the model depth (d) and length (l), and varying the ultimate steel strain (ϵ_s) and plastic hinge length (l_p) to calculate the deflection ductility (μ). Note that this assumes a triangular distribution of the section yield curvature. The relationship between ultimate strain and plastic hinge length is fairly direct, the larger the ultimate strain the smaller the plastic hinge calculated for a given ductility level. Accurate information on the ultimate steel strain capacity of the reinforcing bars in existing structures, of varying ages, is difficult to obtain. The strain capacity of the reinforcing bars is also influenced

by cyclic loading effects as well as construction details. This is clearly an area needing further consideration.

This analysis of the ITS-1 experiment indicates that this lightly reinforced structure possessed substantial ductility. The displacement-based analysis concept has been shown to be useable for the prediction of this response, and the needed parameters can be calculated from the experimental results. The fact that the loading was a one-way excursion, not cyclic, somewhat limits the applicability of these parameters. The ITS-2 and ITS-3 experiments did not have this limitation. The results of the ITS-1 experiment were very useful in designing the instrumentation and loading plan for these later cyclic experiments.

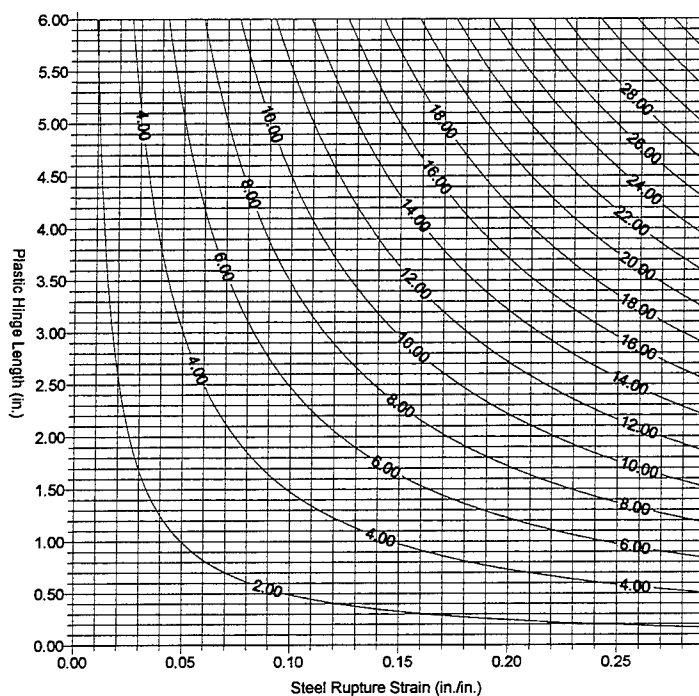


Figure 118. Relationship of ductility ratio to reinforcing steel ultimate strain and plastic hinge length, for ITS-1 model with invariant yield response.

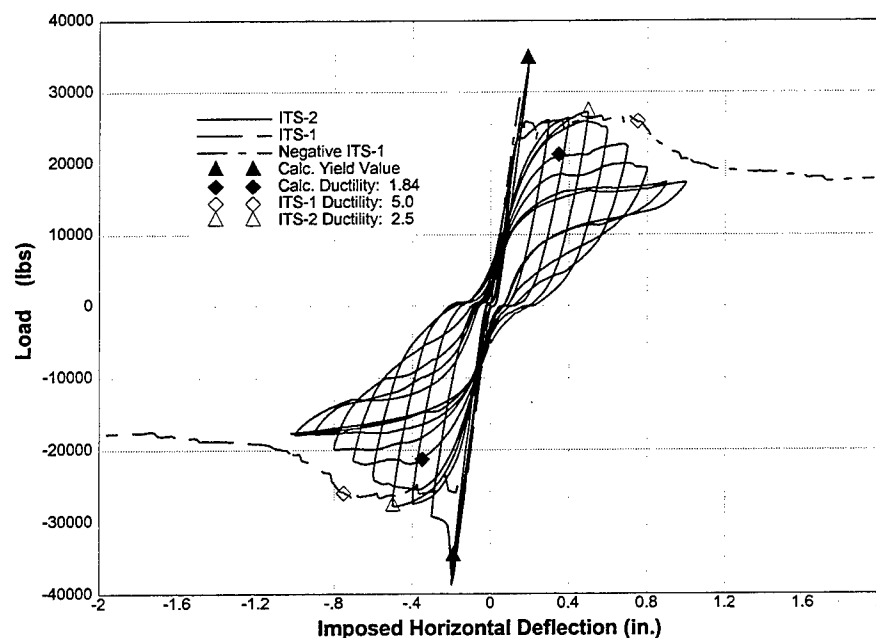


Figure 119. Observed and calculated ductility for ITS-1 and ITS-2 as related to the imposed deflection

ITS-2 Analysis

The ITS-1 and ITS-2 models were constructed to be as close to identical as possible. For this reason, the pre-experiment calculated response for ITS-1 also applies to ITS-2. The cyclic loading of ITS-2 can be expected to give a more realistic estimation of the earthquake response of a prototype intake tower. Figure 119 shows the observed and calculated ductilities for ITS-1 and ITS-2 as related to the deflection imposed by the horizontal loader. The ITS-2 measured ductility of 2.5 is much closer to the calculated ductility of 1.84 than was the ITS-1 ductility of 5.0. However, when based on the measured deflection of the structure, the ITS-2 measured ductility was 5.1, more than twice the calculated value (Figure 120). As discussed in Chapter 5, the ductility of 5.1 is thought to be a more realistic value. It appears that the yield deflection is overestimated

in the calculation. The technique appears to give a conservative estimation of the cyclic deflection ductility, but a closer examination of the actual response of the model is warranted.

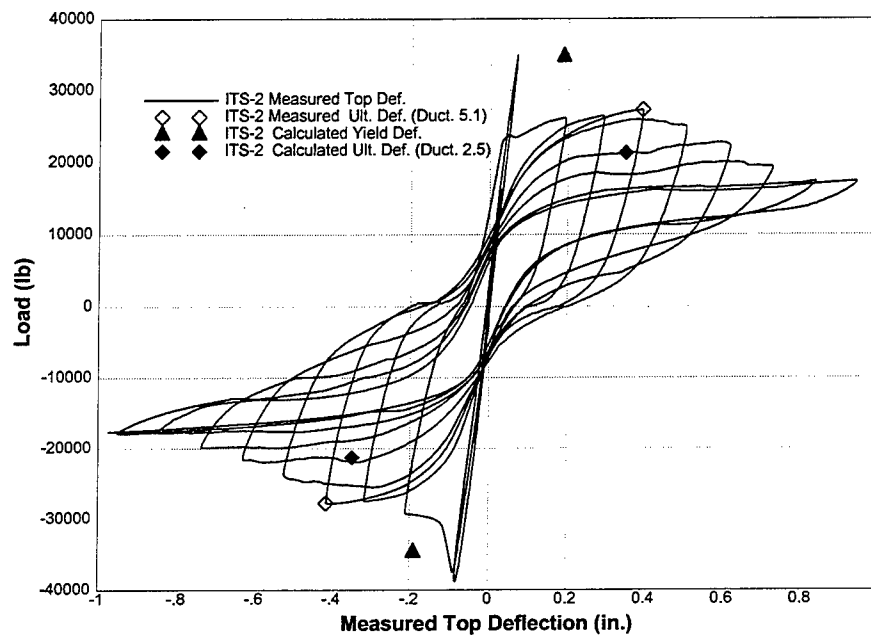


Figure 120. ITS-2 measured and calculated ductility as related to measured top deflection.

In order to understand how the response of the ITS-2 model relates to the deflection-based analysis technique, you must be able to determine several important parameters. One needs to be able to determine: the ultimate displacement at the elevation of interest (δ_u), the equivalent yield curvature at the base of the tower (ϕ_y), the ultimate curvature at the base of the tower (ϕ_u), and the plastic hinge length over which the ultimate curvature acts (l_p). As a first step, one must be able to separate the elastic deflection of the model from the plastic deflection. The elastic response can be estimated

by determining the initial stiffness of the structure and applying the measured load. The initial stiffness of the ITS-2 model was determined to be approximately 180,000 lb/in. of applied deflection (Figure E1). Multiplying this value by the measured load to give an approximate elastic deflection history, then subtracting this from the measured deflection, produces a plastic deflection history (Figure E2).

The next step is to determine the curvature at the base of the tower. Initially it was hoped that the strain gages located at the base could provide this information.

Curvature in a reinforced concrete member can be defined as:

$$\phi = \left[\frac{(\epsilon_c + \epsilon_s)}{d} \right] \quad (12)$$

where (ϵ_c) is concrete strain, (ϵ_s) is steel strain, and (d) is the section depth [8].

Unfortunately, strain gages lack the ability to elongate much beyond the elastic limit of the reinforcing steel and, thus, failed shortly after cracking occurred at the base of the model. Fortunately, the vertical deflection gages mounted at the front and the back of the model (DC2 and DC5) gave a direct measurement of the rotation of the base of the model. Subtracting the vertical deflection measured by DC5 from DC2 and dividing by the distance between the gages, and assuming a 1-in. gage length, a curvature history can be plotted (Figure E3 and Figure E4). This curvature relationship compares favorably with the curvatures generated from the strain gages before they failed. Using the parameters generated so far, and assuming a triangular distribution of the yield curvature as before, one can calculate the plastic hinge length as being about 1.0 in. (Figure E5).

However, it was soon realized that assuming a triangular distribution of the yield curvature may not be realistic for these lightly reinforced towers.

To quantify the difference between the actual and assumed curvature distribution, one can use the vertical strain gages mounted in the body of the model. These gages were mounted well above the damage zone at the base of the tower and returned good data for the entire experiment. Using Equation 12, and the average vertical strains measured at each elevation, curvature plots were generated (Figure E8 to Figure E11). Taking the curvature at each elevation and dividing by the distance from the top of the model to the gage, one can determine the slope of the curvature triangle. Overlaying each of these plots (Figure E12) reveals that the slopes are virtually identical for all the elevations above 6 in. These curves can be averaged to arrive at a good estimate of the slope of the curvature triangle in the body of the model (Figure E13). The curvature at the base of the model is simply the slope of the curvature triangle multiplied by the total height of the model.

The first indication that the assumption of a triangular distribution of the yield curvature was problematic was seen when the base curvature calculated from the body strains was compared to that generated from the initial stiffness. As mentioned above, the initial stiffness of the model was used to approximate the elastic portion of the model response. Assuming a triangular distribution of the curvature, the base curvature was calculated from this elastic motion and plotted against the measured load (Figure E14). When this same process was repeated with the base curvatures generated from the body

strains (Figure E15), the curvatures from the body strains were almost exactly one order of magnitude smaller. At first this was thought to be an instrumentation problem. Careful examination of the strain data and the testing of a known steel sample with the same instrumentation setup revealed that this was not the case. The strain data were correct and the difference was real.

To further clarify the situation, the body strain base curvature history was used to calculate the top deflection that would result from just this curvature (Figure E16). The deflections that resulted were very much smaller than those measured at the top of the model, even before yielding occurred. If the yield curvature in the model was indeed distributed as a triangle, these deflections should have been at least reasonably close. This issue will be considered further by examining the results of the ITS-3 experiment.

ITS-3 Analysis

The ITS-3 model was substantially different from the ITS-1 and ITS-2 models in that it had twice the reinforcing steel, and material properties were different. The overall dimensions were the same. The vertical steel percentage was selected in order to represent the upper part of the distribution of existing intake towers (Figure 115); thus, the model had a greater vertical steel percentage than about 80 percent of the existing rectangular towers. The concrete strength was lowered, and the steel strength increased in order to try to force the failure mode toward crushing of the concrete. Pre-experimental calculations were performed using the same methods as for prior experiments. The ultimate moment was about 1.34 times the calculated cracking

moment. Unlike the ITS-1/ITS-2 analyses this is a value greater than 1.2. An ultimate moment that falls between 1.2 and 2.0 times the cracking moment indicates a structure that has expected response intermediate between brittle and ductile [7]. This intermediate value of cracking moment was an intended consequence of the design of the ITS-3 experiment.

The definition of a brittle failure, in this context, is one in which there is little spreading of the plastic zone. The ITS-3 model failed with only one crack, and with no evidence of spreading and, hence, appeared to be a brittle failure. Knowing this, the plastic hinge length is calculated to be 2.86 in. long, by using Equation 7, a steel yield strength of 60 ksi, and a bar diameter of 0.159 in. Again assuming a triangular distribution of the yield curvature, one can calculate the yield and ultimate deflections and, hence, the expected ductility ratio (Figure 121). The calculated ductility of 2.43 is reasonably close to the lower limit of the measured ductility range. Recall that the lower limit value of ductility, 2.85, was calculated by assuming that yielding occurred when the entire section yielded. Further examination of Figure 121 indicates that the calculated ultimate and yield deflections are substantially overestimated by the calculation, and it may only be happenstance that their ratio is similar to the experimental value of ductility. Note that the calculated yield and ultimate loads are very close to the experimental value.

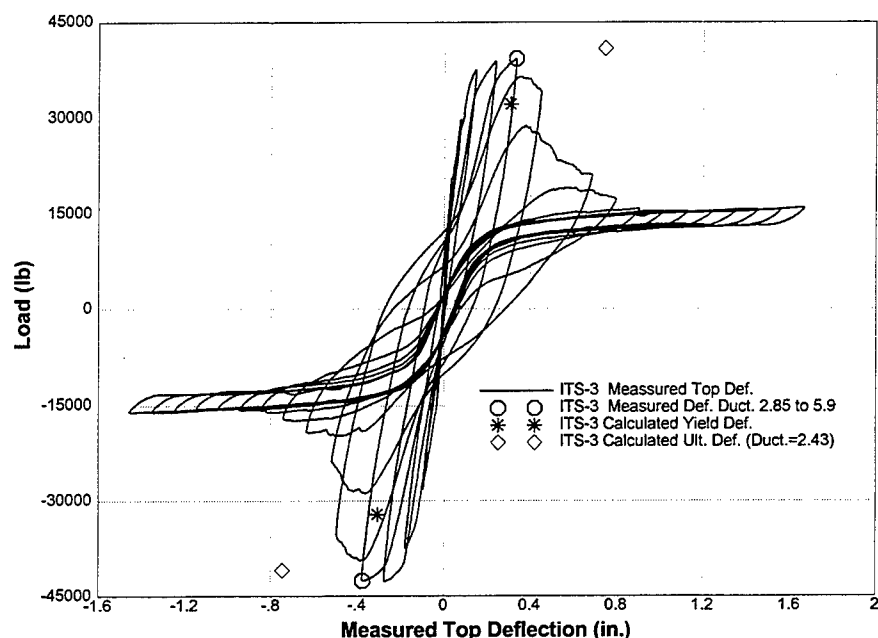


Figure 121. ITS-3 measured and calculated ductility as related to measured top deflection.

The fact that the calculations overestimated the deflections but correctly estimated the loads confirms that the assumed distributions of the yield and/or ultimate curvatures may be incorrect. Using the same methods as in ITS-2, the body strains in the model were used to estimate the curvature triangle of the model (Figure E17 to Figure E19). Again, the curvature triangle was used to estimate the top deflections (Figure E20). The top deflections estimated in the manner were about seven times lower than the measured response. This disparity was smaller than the tenfold error seen in ITS-2, but is still a very large discrepancy. It was abundantly clear at this point that the simplifying assumptions used in the analysis do not reflect the actual response of the model in both the ITS-2 and ITS-3 experiments. The difference, no doubt, reflects the relatively unique nature of these very lightly reinforced structures. The tower failure modes differ

substantially from the majority of the structures for which the deflection-based analysis technique was originally developed. A closer look at the underlying assumptions should lead to the modifications to account for these differences.

Modification of Deflection-Based Analysis

The deflection-based analysis technique has some relatively subtle features that can be easily misunderstood. Foremost of these features is the definition of the relationship between the yield curvature, ϕ_y , at the base of the tower and the yield deflection, δ_y , at the point of interest on the structure (Equation 10). Embedded in this relationship are assumptions of both the distribution of the yield curvature and the effective stiffness of the structure. The yield curvature is defined by the following relationship [7]:

$$\phi_y = \frac{M_y}{E_c I_c} \quad (13)$$

where M_y is the yield moment, E_c is the concrete modulus of elasticity, and I_c is the cracked-section moment of inertia. The cracked-section moment of inertia included in this equation can be considered as the effective stiffness of the structure. The effective stiffness is a complex parameter, dependent on the material properties, reinforcement ratios, and axial loads [6]. This parameter makes inherent assumptions about the distribution of cracking along the height of the structure so that it can be taken as an average value to be applied to the entire member. Thus, when applying Equation 13 to calculate the yield curvature, one must first calculate an effective stiffness that relates the

response of the entire structure to the yield curvature and moment at the base of the structure. The calculation of the effective stiffness is not a trivial task. After calculating the yield curvature, one must then apply Equation 10 to calculate the yield deflection. This calculation assumes a triangular distribution of the curvature, a distribution that the experimentation has shown is not realistic for the localized response of the lightly reinforced intake tower models. It is apparent that the deflection-based analysis technique should be modified to better reflect the relatively unique, localized response of the existing intake towers.

Any modification of the deflection-based analysis method should have as its basis an accurate model of the response of the intake tower. This response is characterized by three phases of response. The first phase is an elastic beam response of the entire tower up to the initial cracking at the base. This response is easily calculated based on the gross section properties and an assumption of a triangular distribution of moments and curvature. The second phase is a localized response of the elastic straining of the reinforcement in the crack up to yielding. This localized elastic straining bears a striking resemblance to the third phase, the localized response of the plastic straining of the reinforcement in the crack up to ultimate deflection. In both the second and third phases, a localized rotation takes place at the base of the tower. One method of incorporating this response is to consider each phase separately by assuming a triangular distribution of the elastic curvature, and separate hinge lengths over which the yield and ultimate curvatures act (Figure 122).

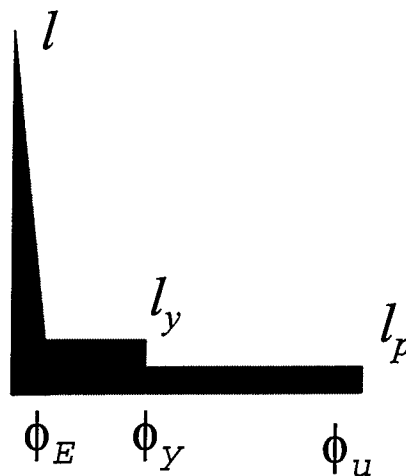


Figure 122. Proposed curvature relationship.

Using the curvature relationships shown in Figure 122, one can write an equation for the ultimate deflection of the tower:

$$\delta_u = \frac{\phi_E l^2}{3} + (\phi_y - \phi_E) l_y \left(l - \frac{l_y}{2}\right) + (\phi_u - \phi_y) l_p \left(l - \frac{l_p}{2}\right) \quad (14)$$

where δ_u is the ultimate displacement at the elevation of interest, ϕ_E is the elastic curvature at the base of the tower just before cracking, ϕ_y is the curvature in the cracked section at the base of the tower at first yield, ϕ_u is the ultimate curvature at the base of the tower, l_y is the yield hinge length over which the yield curvature acts, l_p is the plastic hinge length over which the ultimate curvature acts, and l is the structure height to the elevation of interest. This formulation introduces the additional parameter of the yield hinge length which must be empirically quantified; however, it has several advantages. The formulation of Equation 14 uses a realistic distribution of section yield curvature.

Also, the elastic section stiffness is used for elastic deflection, and the structural response is largely controlled by localized rebar response as was witnessed in the experimentation.

Equation 14 can be simplified by observing that the total height of the structure to the point of interest (l) can be expected to be considerably larger than elastic and plastic hinge lengths. This assumption has the effect of centering the elastic and plastic rotations at the center of the single crack formed in these lightly reinforced structures, a reasonable approximation of the actual response. Hence, Equation 14 can be simplified to:

$$\delta_u = \frac{\phi_E l^2}{3} + (\phi_y - \phi_E) l_y l + (\phi_u - \phi_y) l_p l \quad (15)$$

Equation 15 is simply the summation of elastic deflection of the uncracked tower at the yield moment (δ_E), the deflection at the elevation of interest due to the rotation of the cracked section at the yield moment, and the deflection at the elevation of interest due to the rotation of the cracked section during the plastic deformation up to the failure (δ_p):

$$\delta_E = \frac{\phi_E l^2}{3} \quad (16)$$

$$\delta_y = \delta_E + (\phi_y - \phi_E) l_y l \quad (17)$$

$$\delta_p = (\phi_u - \phi_y) l_p l \quad (18)$$

$$\delta_u = \delta_y + \delta_p \quad (19)$$

The total deflection at yield (δ_y) is equal to the summation of elastic deflection of the uncracked tower at the yield moment (δ_E) and the deflection at the elevation of interest due to the rotation of the cracked section at the yield moment. This total deflection at yield (δ_y) is needed in order to calculate the deflection ductility μ :

$$\mu = \frac{\delta_y}{\delta_u} \quad (20)$$

One can calculate values for the yield and plastic hinge lengths in terms of measured deflections and curvatures by simply rearranging Equations 17, 18, and 19:

$$l_y = \frac{\delta_y - \delta_E}{l(\phi_y - \phi_E)} \quad (21)$$

$$l_p = \frac{\delta_u - \delta_y}{l(\phi_u - \phi_y)} \quad (22)$$

The values of l_y and l_p calculated from the experimental data from ITS-2 and ITS-3 can be presented in Table 2 and Table 3, respectively. In all cases, the elastic deflection (δ_E) and elastic curvature (ϕ_E) are taken from the values calculated from the strain gage measurements in the body of the tower. The yield and ultimate deflections are the measured deflections at the top of the tower at the yield and ultimate responses. Two values of the yield curvature were used, the first was calculated from the measured strains at the base of the tower, and the second was calculated from the yield strains measured in static tensile tests of the reinforcing bars (Table B3 and Table B4). Three values of

ultimate curvature were calculated, the first from an assumed ultimate strain of 5 percent, the second from the ultimate strains measured in static tensile tests of the reinforcing bars, and the third from the vertical deflection gages at the base of the tower.

In both experiments, the yield hinge length (l_y) is larger for the base measured yield curvature than for the yield curvature estimated from the yield strains measured in static tensile tests of the reinforcing bars. This difference reflects a reduction in yield capacity, due to cyclic loading, for the base measured yield curvature. This reduction was not a single ratio, as there was a 24-percent reduction for ITS-2 and a 49-percent reduction for ITS-3. The numerical values of l_y for the two experiments differed considerably, reflecting the difference in material characteristics and the size of the reinforcing bars. The best estimates of the yield hinge length (l_y) were 20.9 in. for ITS-2 and 5.5 in. for ITS-3.

The determination of the plastic hinge length l_p was not greatly influenced by different values of the assumed yield curvature. There was a large difference between the values calculated based on ultimate curvature from the static tensile test strains and the values based on both the assumed strain of 5 percent and the measured vertical deflection curvature. This difference is due to the reduction in the ultimate capacity induced by the cyclic loading. The selection of the 5-percent strain value was intended to model just this reduction, and it seemed to perform well. The best values for the plastic hinge lengths are thought to be 1.6 in. for ITS-2 and 2.2 for ITS-3. Both of these values compare very

favorably to the pre-experimental calculated (Equation 7) plastic hinge lengths of 1.32 in. and 2.85, respectively.

It is evident that it is possible to find a yield length that can reproduce the ITS-2 and ITS-3 experimental results. The greater question is whether or not a realistic value of this parameter can be estimated for use in analysis of existing intake towers. Assuming a relationship similar to Equation 7, where the plastic hinge length is a function of bar diameter and steel yield strength, one can write:

$$l_y = C_y d_b F_y \quad (23)$$

where C_y is some constant. Using the experimental values of l_y , the known values of the bar diameter (d_b) in in., and the steel yield strengths (F_y) in ksi, the constant C_y is 4.62 for ITS-2 and 0.57 for ITS-3. Obviously, this is not the proper relationship, and it is probably unrealistic to base this relationship on only two samples. This relationship can probably be determined by a well-designed series of cyclic reinforcing bar pull-out experiments.

Table 2. ITS-2 yield and plastic hinge lengths.

	Elastic	Yield	Yield				
	Curvature	Curvature	Hinge				
Yield	From Body	From Base	Length				
Deflection	Strains	Strains	l_y (in.)				
-8.51E-02	-4.48E-06	-2.98E-05	20.923				
	Elastic	Yield	Yield				
	Curvature	Curvature	Hinge				
Yield	From Body	Rebar Tests	Length				
Deflection	Strains	0.15% Strain	l_y (in.)				
-8.51E-02	-4.48E-06	-3.78E-05	15.923				
	Yield	Ultimate	Plastic	Ultimate	Plastic	Ultimate	Plastic
	Curvature	Curvature	Hinge	Curvature	Hinge	Curvature	Hinge
Ultimate	From Base	Assumed	Length	Rebar Tests	Length	Deflection	Length
Deflection	Strains	5% Strain	L_p (in.)	18% Strain	L_p (in.)	Gages	L_p (in.)
-0.41498	-2.98E-05	-1.30E-03	2.1643	-4.68E-03	0.591	-3.06E-03	1.558
	Yield	Ultimate	Plastic	Ultimate	Plastic	Ultimate	Plastic
	Curvature	Curvature	Hinge	Curvature	Hinge	Curvature	Hinge
Ultimate	From Rebar	Assumed	Length	Rebar Test	Length	Deflection	Length
Deflection	Tests	5% Strain	L_p (in.)	18% Strain	L_p (in.)	Gages	L_p (in.)
-0.41498	-3.78E-05	-1.30E-03	2.1779	-4.68E-03	0.592	-3.06E-03	1.558

Table 3. ITS-3 yield and plastic hinge lengths.

	Elastic	Yield	Yield				
	Curvature	Curvature	Hinge				
Yield	From Body	From Base	Length				
Deflection	Strains	Strains	l_y (in.)				
-5.95E-02	-3.47E-06	-6.87E-05	5.479				
	Elastic	Yield	Yield				
	Curvature	Curvature	Hinge				
Yield	From Body	Rebar Tests	Length				
Deflection	Strains	0.23% Strain	l_y (in.)				
-5.95E-02	-3.47E-06	-1.32E-04	2.775				
	Yield	Ultimate	Plastic	Ultimate	Plastic	Ultimate	Plastic
	Curvature	Curvature	Hinge	Curvature	Hinge	Curvature	Hinge
Ultimate	From Base	Assumed	Length	Rebar Tests	Length	Deflection	Length
Deflection	Strains	5% Strain	L_p (in.)	12% Strain	L_p (in.)	Gages	L_p (in.)
-0.35406	-6.87E-05	-1.30E-03	1.993	-3.07E-03	0.8178	-2.40E-03	2.231
	Yield	Ultimate	Plastic	Ultimate	Plastic	Ultimate	Plastic
	Curvature	Curvature	Hinge	Curvature	Hinge	Curvature	Hinge
Ultimate	From Rebar	Assumed	Length	Rebar Test	Length	Deflection	Length
Deflection	Tests	5% Strain	L_p (in.)	12% Strain	L_p (in.)	Gages	L_p (in.)
-0.35406	-1.32E-04	-1.30E-03	2.102	-3.07E-03	0.8355	-2.40E-03	2.231

Utilization of the procedure outlined above is a relatively complicated affair that requires the estimation of both the yield and plastic hinge lengths during the calculation of the deflection capacity of the tower. In a conversation with Dr. Jack Moehle of the University of California about this procedure, he pointed out that it may be possible to further simplify the assumed response of the structure by eliminating the explicit calculation of the yield response. A primary reason for explicitly calculating the yield response is to calculate the deflection ductility, the ratio of the yield to the ultimate deflection. It is possible to define a second parameter as the elastic ductility, the ratio of the elastic deflection response of the uncracked tower at the yielding moment and the ultimate deflection. This definition allows one to combine the total post-cracking response of the failure zone into a single parameter, the plastic rotation (θ_p), assuming a mode of response as shown in Figure 123. This mode of response reflects the localized, single crack, response of the lightly reinforced intake tower by assuming that all post-cracking rotation occurs within this single crack.

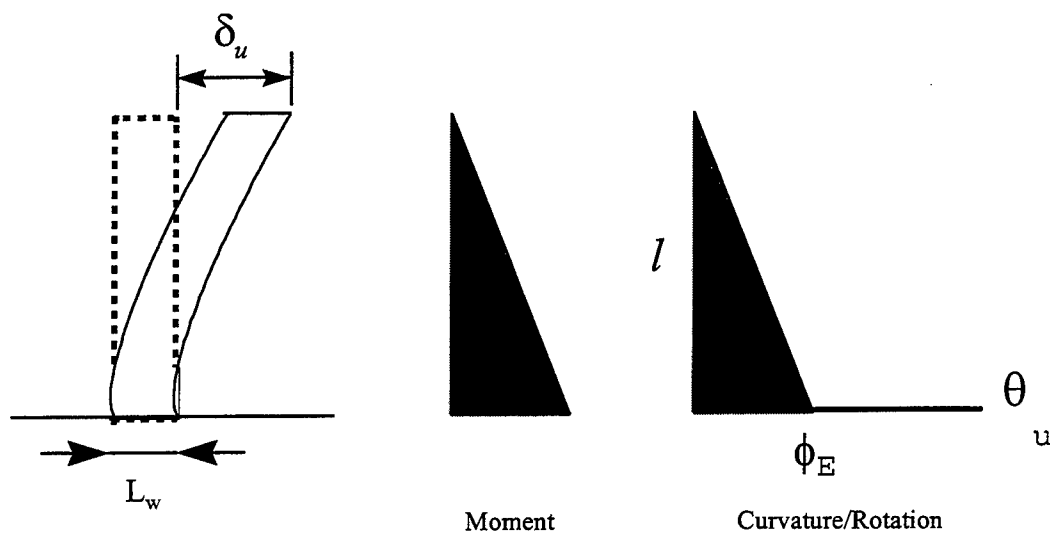


Figure 123. Assumed flexural response.

By assuming that all post-cracking rotation occurs within a single crack the formulation of the deflection equations can be simplified to:

$$\delta_u = \frac{\phi_E l^2}{3} + \theta_p l \quad (24)$$

where the elastic curvature is defined as the base curvature of the uncracked tower under the yielding moment:

$$\phi_E = \frac{M}{EI_g} \quad (25)$$

and the plastic rotation is defined as the total rotation in the crack. This plastic rotation can be written in terms of the ultimate strain capacity of the reinforcing steel (ϵ_u), the

width of the tower in the direction of loading (l_w), and a strain penetration length (l_s) for the reinforcing steel:

$$\theta_p = \frac{\varepsilon_u l_s}{l_w} \quad (26)$$

The definition of the strain penetration length (l_s) can be problematic. As with the definition of the yield lengths, a well-designed series of cyclic reinforcing bar pull-out experiments may be needed to properly define this parameter. In fact, the same experiments could be conducted to determine both parameters. For the ITS-2 and the ITS-3 experiments, the strain penetration length (l_s) can be directly calculated from the elastic deflection at yield as determined from the body strain gages, the measured ultimate deflection, and an assumed ultimate steel strain. For ITS-2, the strain penetration length (l_s) was calculated to be 2.59 in. (Table 4) for an assumed ultimate strain of 5 percent, and 0.72 in. for the ultimate strain of 18 percent. For ITS-3, the strain penetration length (l_s) was calculated to be 2.22 in. (Table 5) for an assumed ultimate strain of 5 percent, and 0.92 in. for the ultimate strain of 12 percent. The first values given are assumed to reflect the cyclic degradation, and the second are based on the ultimate strain from reinforcing bar tension tests. As with the yield hinge length, it is probably unrealistic to base the relationship of the strain penetration length (l_s) to the other controlling parameters on only two samples. Further experimentation is required.

Table 4. ITS-2 strain penetration length determination.

Cumulative Stroke @ Yield	Yield Deflection	Elastic Curvature From Body Strains	Elastic Deflection From Body Strains		
0.6	-8.51E-02	-4.48E-06	-2.15E-02		

Cumulative Stroke @ Ultimate	Ultimate Deflection	Elastic Deflection From Body Strains	Plastic Rotation	Strain Penetration Assumed 5% Strain	Strain Penetration Rebar Tests 18% Strain
4.5	-0.41498	-2.15E-02	-3.28E-03	2.59E+00	0.719520614

Table 5. ITS-3 strain penetration length determination.

Cumulative Stroke @ Yield	Yield Deflection	Elastic Curvature From Body Strains	Elastic Deflection From Body Strains		
0.554219	-5.95E-02	-3.47E-06	-1.67E-02		

Cumulative Stroke @ Ultimate	Ultimate Deflection	Elastic Deflection From Body Strains	Plastic Rotation	Strain Penetration Assumed 5% Strain	Strain Penetration Rebar Tests 12% Strain
4.52	-0.35406	-1.67E-02	-2.81E-03	2.22E+00	0.92549807

The analysis of the ITS-1, ITS-2, and ITS-3 experiments has demonstrated that the deflection-based analysis technique can be applied to the existing intake towers. It has been shown, however, that the assumptions used for application of this technique to more heavily reinforced structures must be reconsidered when the technique is applied to these very lightly reinforced towers. It appears that the assumption of the triangular distribution of the yield curvature is an unrealistic model of the actual distribution when failure is concentrated at a single crack across the critical section. The two suggested modifications of the technique successfully address this concern.

CHAPTER 8

SUMMARY, CONCLUSIONS, AND RECOMMENDATIONS

Summary

The overall objective of this research was to understand the nonlinear response of existing, lightly reinforced intake towers. The ultimate objective was the evaluation and/or development of approximate or simplified analysis procedures for the evaluation of the ductility of existing intake towers. There were two phases in the fulfillment of this ultimate objective. The first phase was a statistical analysis of the inventory of existing intake towers. The specific objective of the tower inventory analysis was to quantify the distribution and variation of the structural characteristics of the U.S. Army Corps of Engineers inventory of existing intake towers as related to their earthquake location hazard. This analysis was used to assist in the identification of possible failure mechanisms and to help quantify the extent of the problem of the seismic response of existing towers. The information generated was used in planning the second phase of

this research effort, the Intake Tower Substructure (ITS) experimentation series. These experiments were successful in demonstrating that the scale models of typical intake towers had significant ductility available. Information on the specific response of these models was used to suggest modifications of the deflection-based analysis procedure for application to the evaluation of the ductility of existing intake towers, hence fulfilling the overall objective of the entire research program.

Conclusions

A primary finding of this work is that the lightly reinforced intake towers modeled exhibited significant ductility under the static application of one-way and cyclic bending loads. The failure mechanism consisted of the formation of a single crack without crushing or degradation of the concrete. The ductility exhibited was largely dependent upon the ultimate strain capacity of the reinforcement. Hence, the response of reinforcement in this crack determined the ultimate response of the entire structure. The ductility observed in the experimentation should be available in the majority of existing intake towers. An extensive effort was made to ensure that the experimental models reflected the properties of the existing intake tower inventory of the U.S. Army Corps of Engineers. It should be noted that the utility of this ductility in an earthquake may be dependent on the impact of dynamic effects.

Modal surveys conducted before, during, and after the experiments indicated that there was a substantial decrease in the natural frequencies of the first two modes of the models due to structural damage. The surveys also demonstrated that the first bending

mode was the primary mode of response, and the first torsional mode was the second mode of response. This result seems to validate the design of the experiments for the application of bending loads. It can be concluded that a dynamic analysis of an existing intake tower should include the decrease in the natural frequency of the models with damage.

A final conclusion of this research is that the deflection-based analysis technique can be applied to the existing intake towers. It was shown, however, that the assumptions used for application of this technique to more heavily reinforced structures must be reconsidered when the technique is applied to these very lightly reinforced towers. It appears that the assumption of the triangular distribution of the yield curvature is an unrealistic model of the actual distribution when failure is concentrated at a single crack across the critical section. Two suggested modifications of the technique successfully address this concern. Both modifications require the introduction of additional parameters that model the geometry and the localized strain response of the sections.

Recommendations

It is recommended that the deflection analysis technique be pursued as the primary simplified analysis procedure for the evaluation of the ductility of existing intake towers. The technique should be modified to reflect the unique nature of the response of these towers. The two suggested modifications of the technique require an additional experimental and analytical effort. This effort will be needed to quantify the parameters introduced to model the geometry and the localized strain response of the towers. It is

suggested that a series of cyclic reinforcing bar pull out experiments be conducted to address this need.

REFERENCES

- 1 Uniform Building Code, 1991 Edition, International Conference of Building Officials, Whittier, CA.
- 2 Wood, S.L., "Performance of reinforced concrete buildings during the 1985 Chile earthquake: Implications for design of structural walls," Earthquake Spectra, EERI, Vol. 7, No. 4, November 1991.
- 3 Wang, C., and Salmon, C.G, Reinforced Concrete Design. Third Edition, Harper & Row, New York, NY.
- 4 Bertero, V.V., "Design Guidelines for Ductility and Drift Limits," UCB/EERC-91/15, July 1991.
- 5 Harris, C., Shock and Vibration Handbook, McGraw-Hill Book Company, New York, 1988.
- 6 U.S. Department of Transportation, Federal Highway Administration, Seismic Retrofitting Manual for Highway Bridges, Publication No. FHWA-RD-94-052, May 1995.
- 7 Nicoletti, J.P., and Priestly, M.J.N., Review Comments of Draft Appendix B, "Seismic Design and Evaluation of Free-Standing Intake Towers," Letter from URS Consultants to Commander, U.S. Army Corps of Engineers, Huntsville, AL, 1995.
- 8 Moehle, J.P., "Displacement Based Design of RC Structures Subjected to Earthquakes," Earthquake Spectra, Vol. 8, No. 3, 1992.
- 9 Park, R., and Paulay, T, Reinforced Concrete Structures, John Wiley and Sons, Inc., New York, 1975.
- 10 Felber, A.J., "RESPONSE: A Program to Determine the Load-Deformation Response of Reinforced Concrete Sections," M.A.Sc. thesis, Department of Civil Engineering, University of Toronto, 1990.

APPENDIX A

INVENTORY ANALYSIS RESULTS

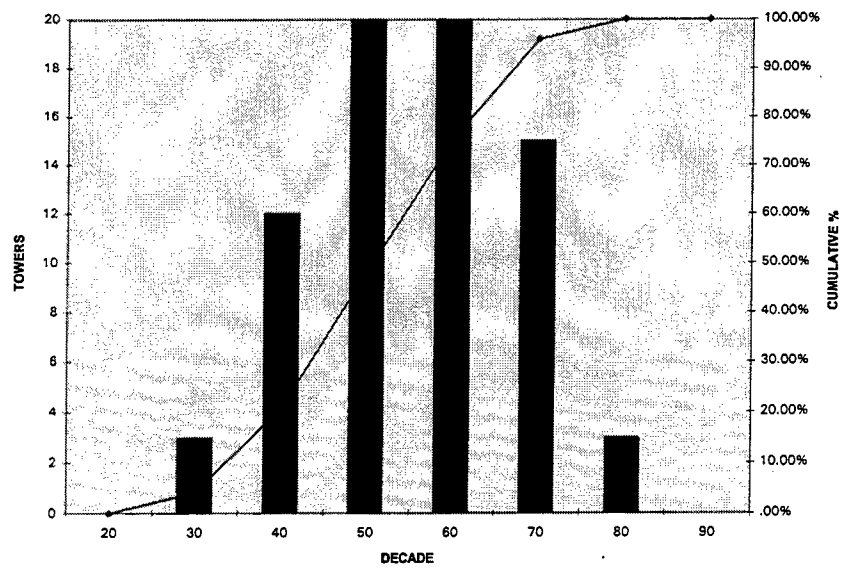


Figure A1. Distribution of towers by decade of design/construction.

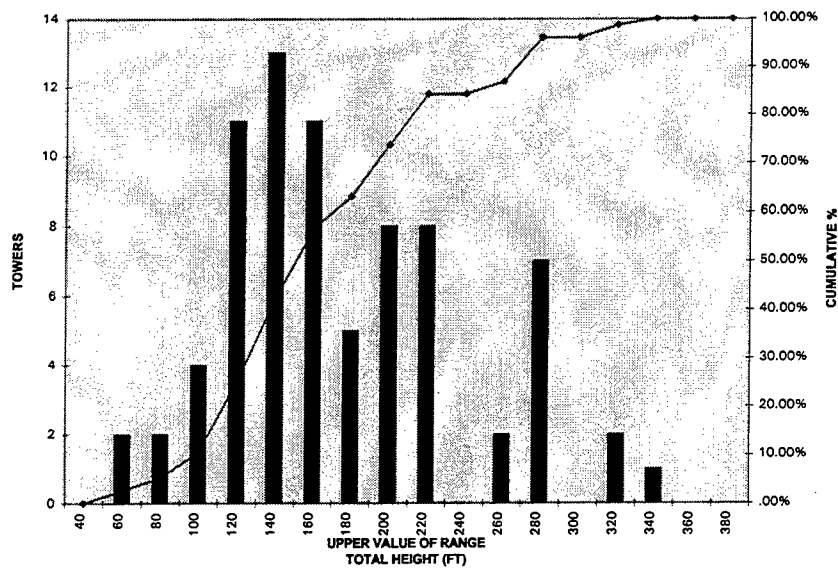


Figure A2. Distribution of towers by total height.

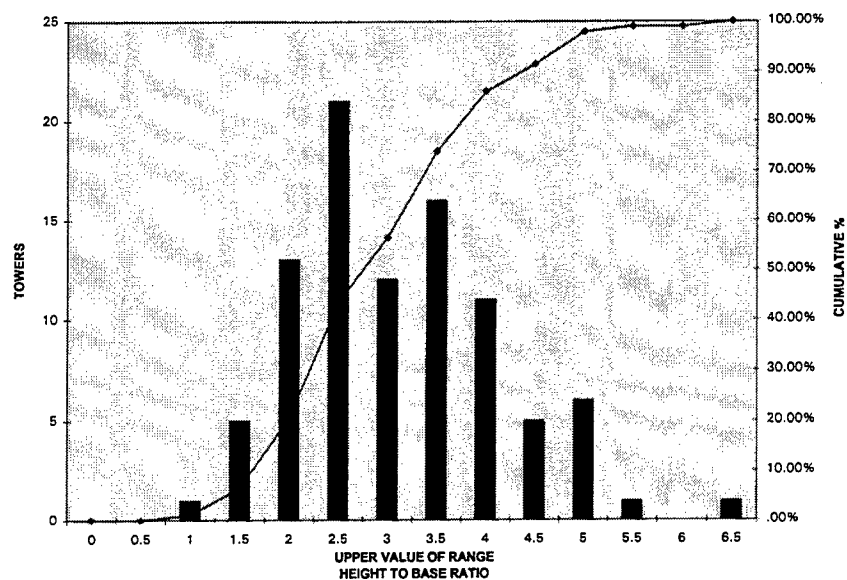


Figure A3. Distribution of rectangular towers by ratio of total height to base width.

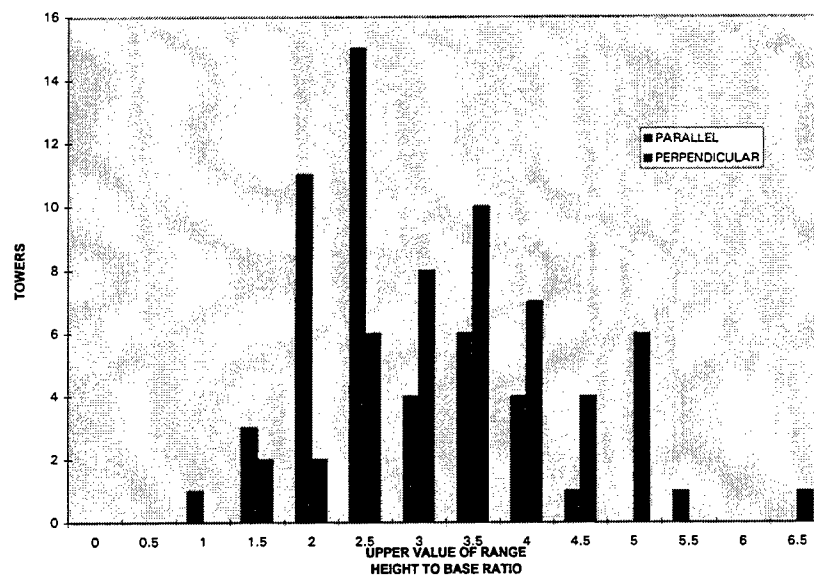


Figure A4. Distribution of rectangular towers by ratio of height to base width for parallel and perpendicular axis directions.

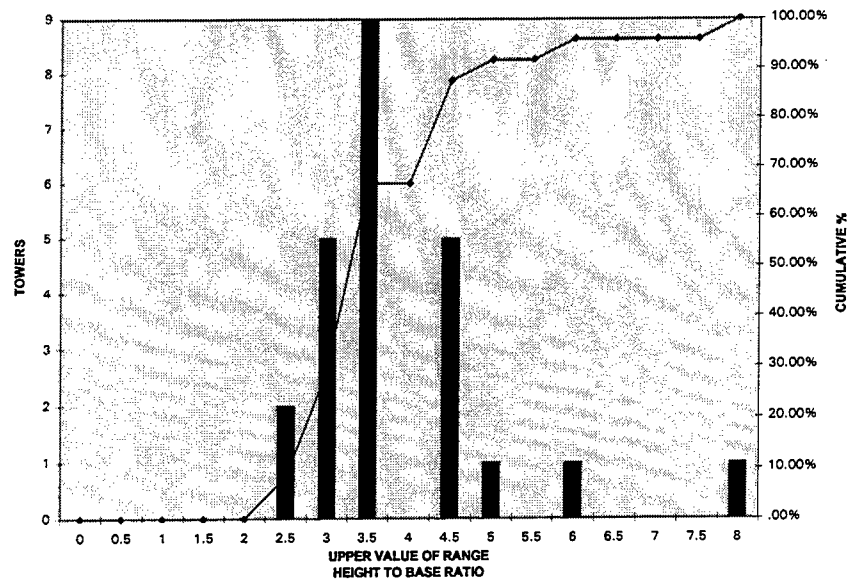


Figure A5. Distribution of nonrectangular towers by ratio of total height to base width.

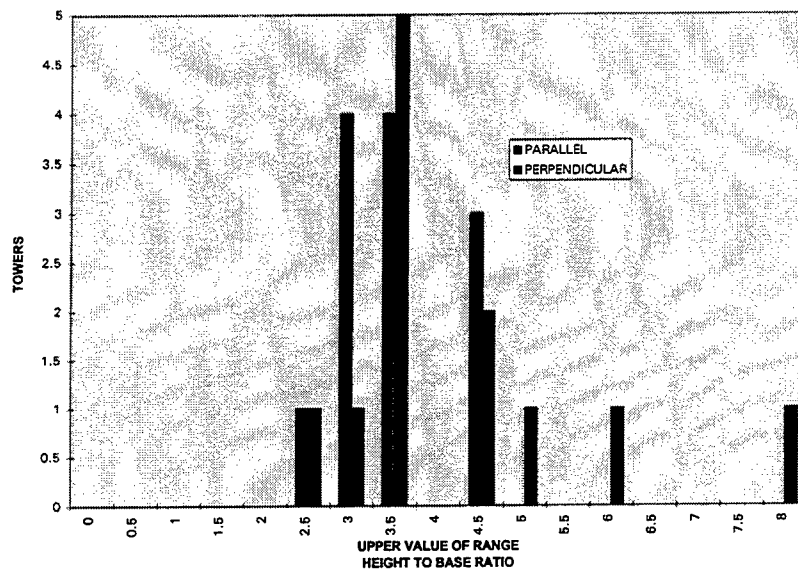


Figure A6. Distribution of nonrectangular towers by ratio of height to base width for parallel and perpendicular axis directions.

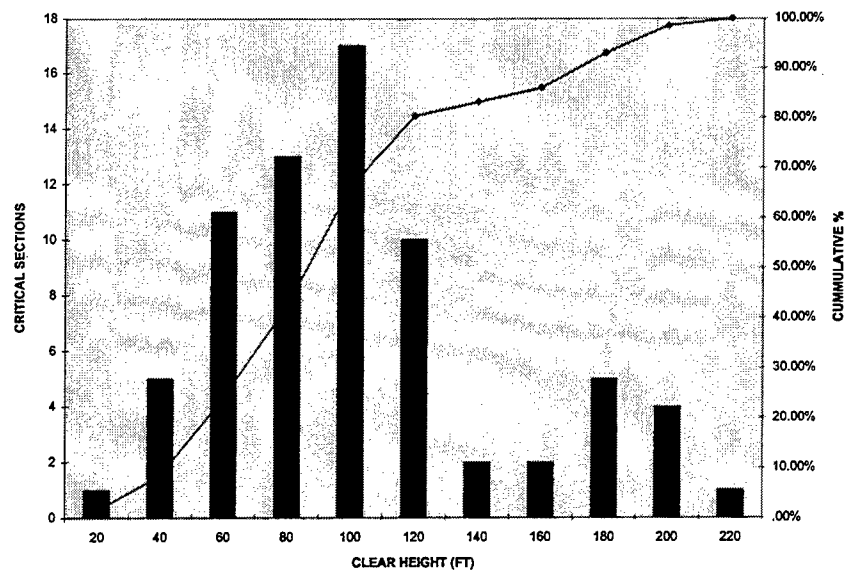


Figure A7. Distribution of critical sections by height above critical section.

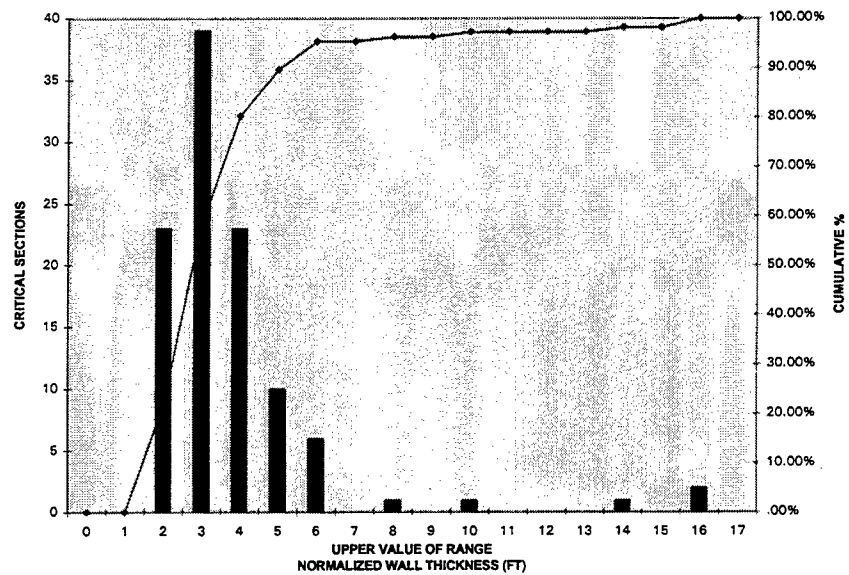


Figure A8. Distribution of rectangular tower critical sections by normalized wall thickness.

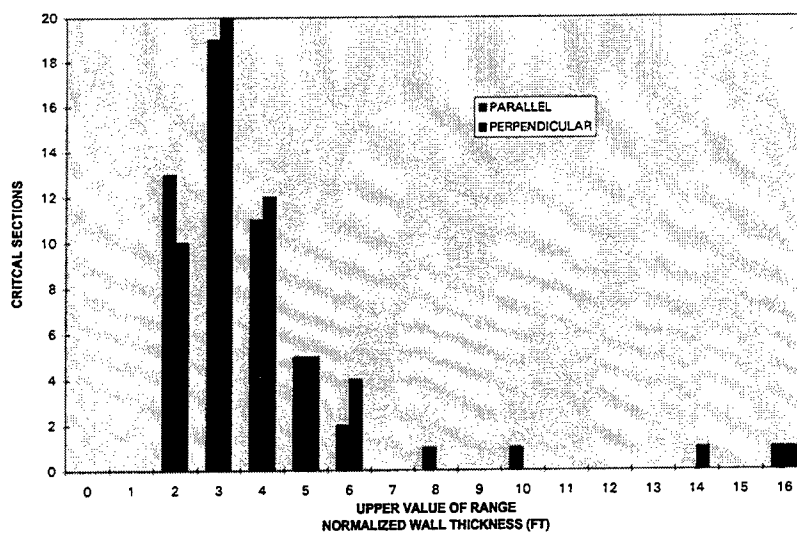


Figure A9. Distribution of rectangular tower critical sections by normalized wall thickness for parallel and perpendicular axis directions.

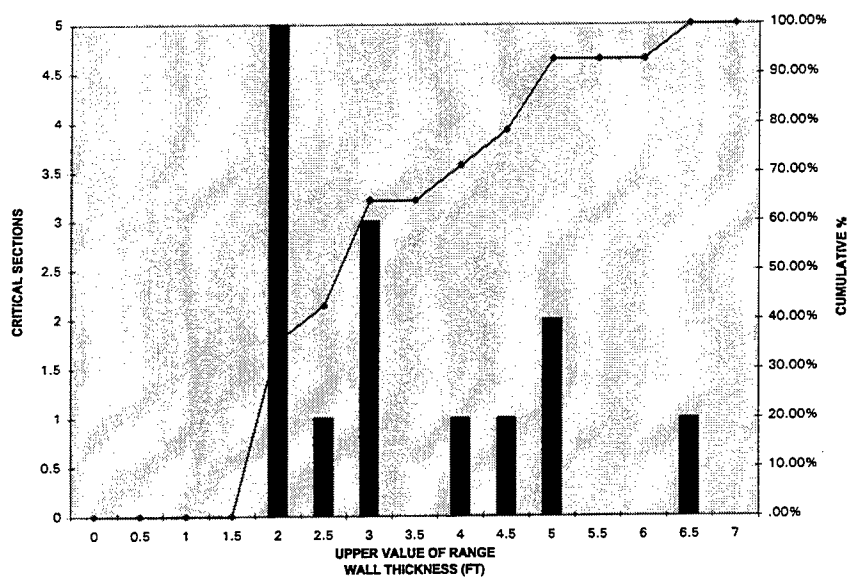


Figure A10. Distribution of nonrectangular tower critical sections by wall thickness.

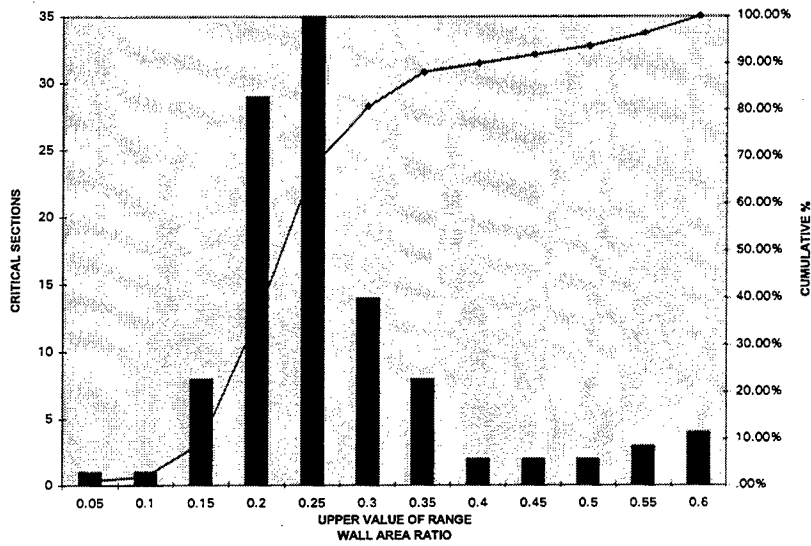


Figure A11. Distribution of rectangular tower critical sections by wall area to gross area ratio.

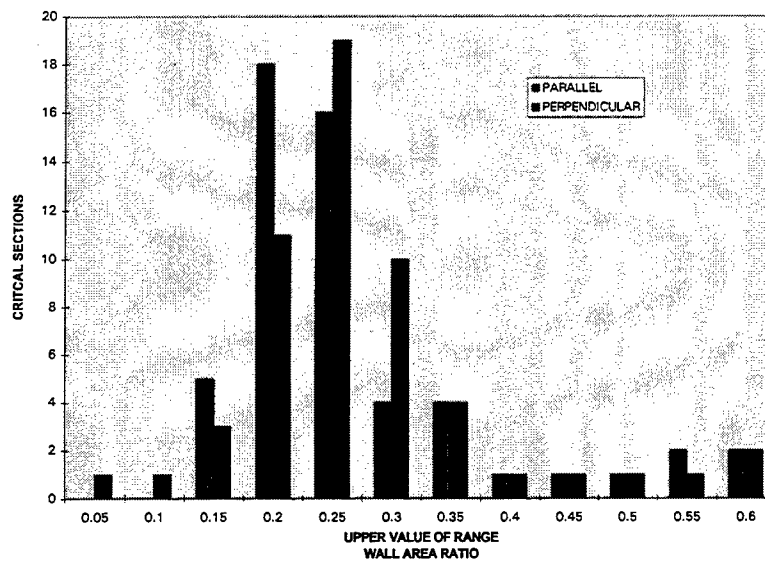


Figure A12. Distribution of rectangular tower critical sections by wall area to gross area ratio for parallel and perpendicular axis directions.

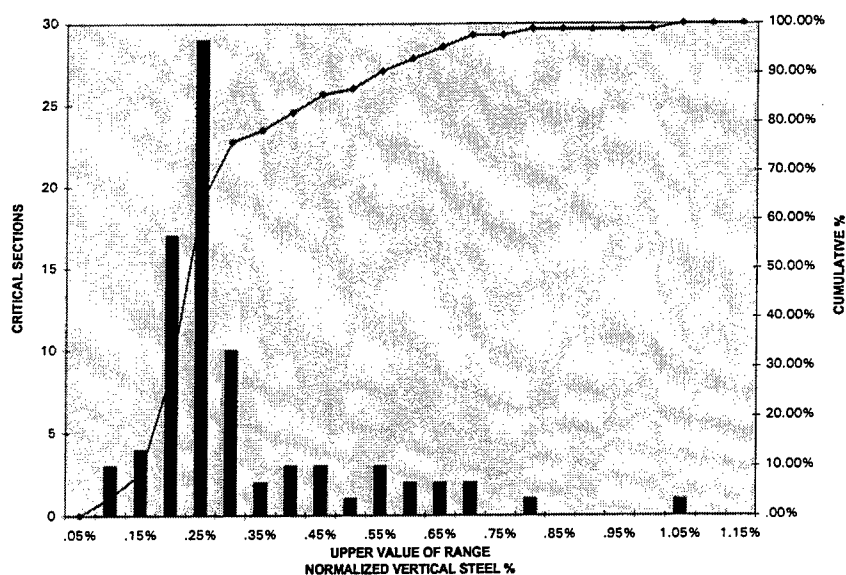


Figure A13. Distribution of rectangular tower critical sections by normalized vertical steel percentage of walls.

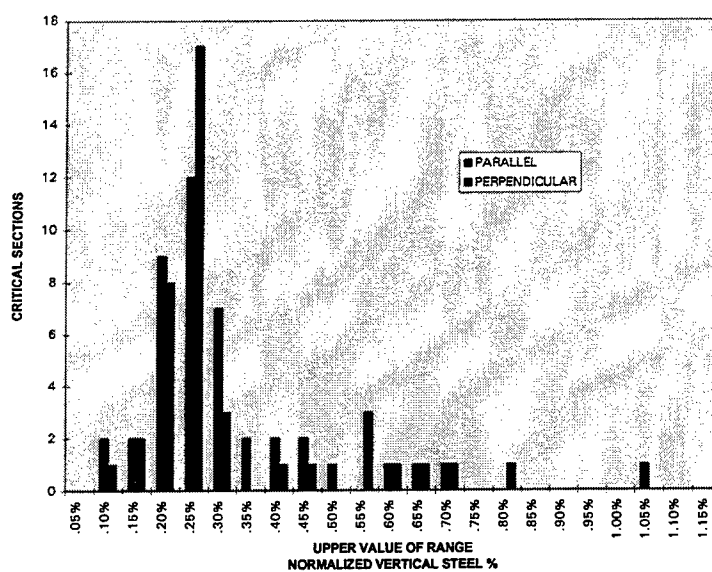


Figure A14. Distribution of rectangular tower critical sections by normalized vertical steel percentage of walls for parallel and perpendicular axis directions.

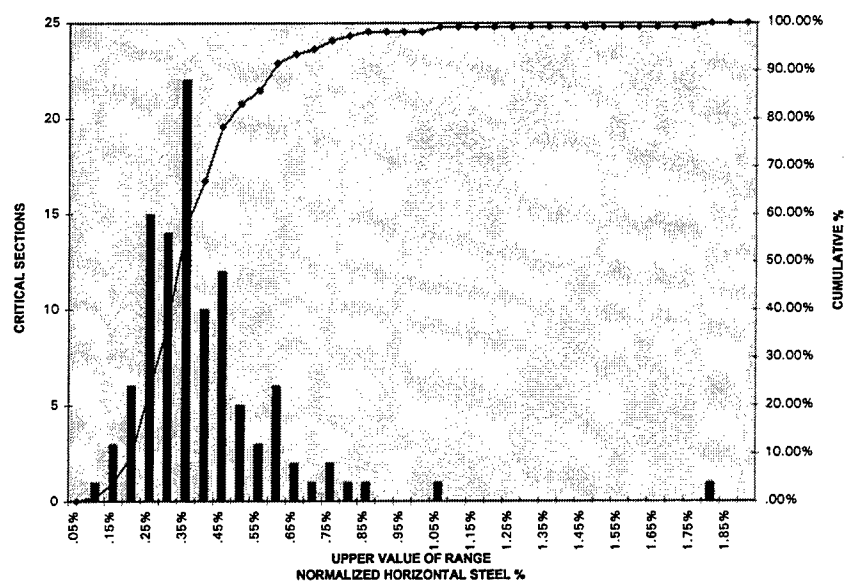


Figure A15. Distribution of rectangular tower critical sections by normalized horizontal steel percentage of walls.

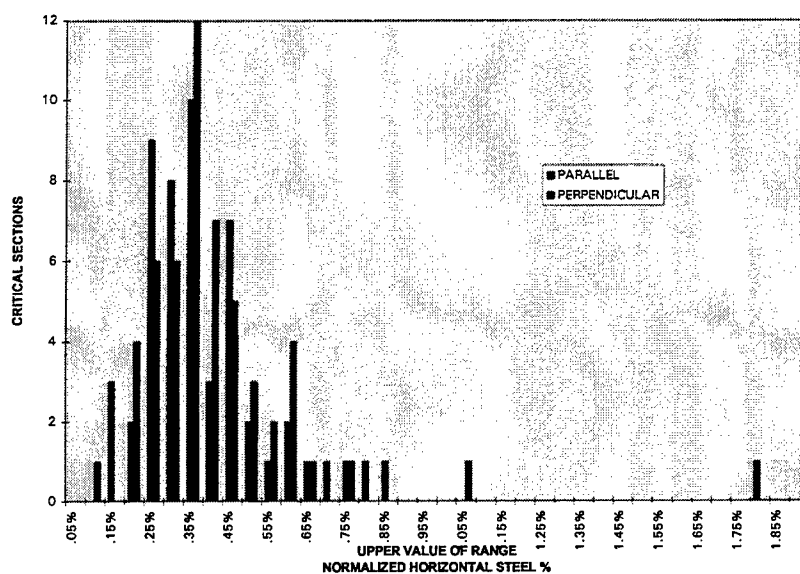


Figure A16. Distribution of rectangular tower critical sections by normalized horizontal steel percentage of walls for parallel and perpendicular axis directions.

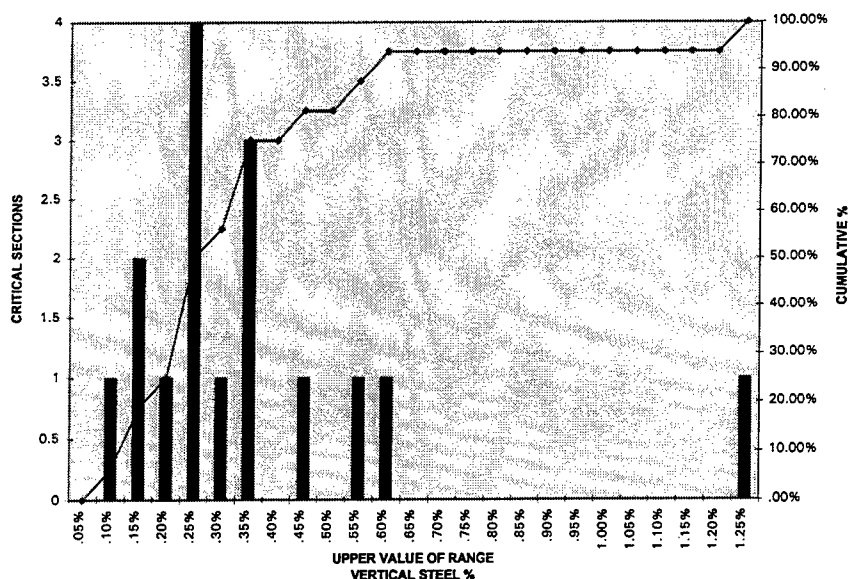


Figure A17. Distribution of nonrectangular tower critical sections by vertical steel percentage of walls.

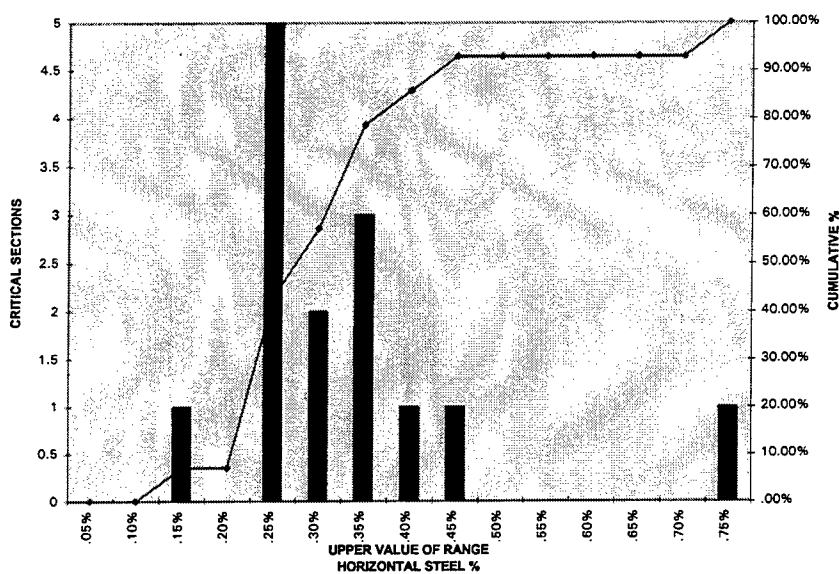


Figure A18. Distribution of nonrectangular tower critical sections by horizontal steel percentage of walls.

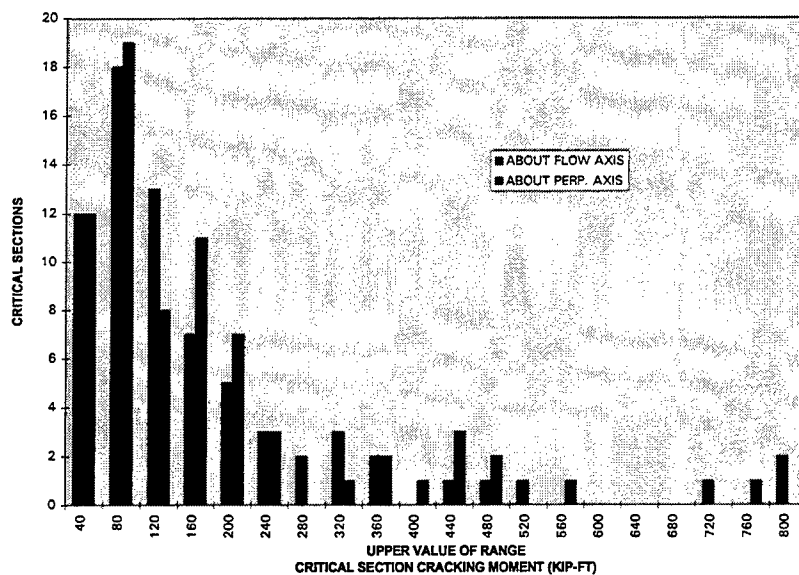


Figure A19. Distribution of all critical sections by moment required to initiate cracking of section.

APPENDIX B

MATERIAL PROPERTIES

Table B1. Tensile test results for reinforcement steel used in ITS-1 and ITS-2.

	Diameter (in.)	Peak Stress (ksi)	Break Stress (ksi)	Yield Stress (ksi)	Yield Strain (in./in.)	Elasticity Modulus (ksi)
Sample 1	0.114	44.280	39.287	40.423	0.001349	28247.89
Sample 2	0.114	44.609	40.214	41.858	0.001649	27161.34
Sample 3	0.114	43.443	39.018	40.573	0.001536	29430.70
Mean	0.114	44.111	39.506	40.951	0.001511	28279.98
Minimum	0.114	43.443	39.018	40.423	0.001349	27161.34
Maximum	0.114	44.609	40.214	41.858	0.001649	29430.70
Standard Dev.	0.0	0.601	0.627	0.789	0.000151	1135.02
Percent Covariance	0.0	1.363	1.588	1.9727	10.0142	4.014

Table B2. Concrete properties of ITS-1.

Batch		Slump	Age	Uncon.	Static	
Number	Location	(in.)	(days)	Comp. Str.	Modulus	
				(psi)	(psi)	
1	Foundation	4	7	2,920	-	
			28	4,300	-	
			28	4,280	-	
			28	3,890	-	
			55	4,940	-	Test Day
			55	4,920	-	Test Day
			55	4,930	-	Test Day
1	1st Lift, Walls	9.5	7	2,039	-	
			7	2,050	-	
			28	3,640	-	
			40	4,050	-	Test Day
			40	3,930	-	Test Day
			40	3,590	3,939,000	Test Day
2	1st Lift, Walls	9.5	7	missed	-	
			28	3,270	-	
			40	3,710	3,987,500	Test Day
1	2nd Lift, Walls	7.75	7	2,370	-	
			28	3,720	-	
			28	3,760	-	
			28	3,820	-	
			35	4,040	4,125,700	Test Day
			35	4,060	-	Test Day
2	2nd Lift, Walls	8	7	2,360	-	
			28	3,670	-	
			28	3,730	-	
			28	3,740	-	
			35	3,905	4,070,900	Test Day
			35	3,980	-	Test Day

Table B3. Concrete properties of ITS-2.

Batch		Slump	Age	Uncon.	Static	
Number	Location	(in.)	(days)	Comp. Str.	Modulus	
				(psi)	(psi)	
1	Foundation		28	5,080	4,836,700	
			28	5,070	5,106,600	
			28	4,910	-	
			84	5,430	4,307,200	Test Day
			84	5,170	5,195,700	Test Day
			84	5,380	5,323,400	Test Day
1	1st Lift, Walls	5	28	3,950	-	
			28	3,860	-	
			31	3,790	-	
			56	4,160	4,440,100	Test Day
			56	4,170	3,791,400	Test Day
			56	4,470	-	Test Day
2	1st Lift, Walls	5	28	3,510	-	
			28	3,160	-	
			31	3,420	-	
			56	3,800	4,095,000	Test Day
			56	3,630	4,075,500	Test Day
			56	3,820	-	Test Day
1	2nd Lift, Walls	7.5	29	3,550	-	
			29	3,510	-	
			29	3,550	-	
			52	3,630	4,030,100	Test Day
			52	3,820	4,126,100	Test Day
			52	4,020	-	Test Day
2	2nd Lift, Walls	8	29	3,450	-	
			29	3,340	-	
			29	3,560	-	
			52	3,700	3,949,800	Test Day
			52	3,740	4,010,900	Test Day
			52	3,730	-	Test Day

Table B4. Tensile test results for reinforcement steel used in ITS-3.

	Diameter (in.)	Peak Stress (ksi)	Break Stress (ksi)	Yield Stress (ksi)	Yield Strain (in./in.)	Elasticity Modulus (ksi)
Sample 1	0.157	73.113	67.107	70.386	0.002641	28319.678
Sample 2	0.157	72.766	70.512	70.307	0.002537	28761.867
Sample 3	0.157	64.096	60.991	57.885	0.002185	26995.843
Sample 4	0.157	67.785	60.786	64.411	0.002253	29176.568
Sample 5	0.157	62.315	59.745	57.191	0.002081	27863.386
Sample 6	0.157	65.026	58.673	60.675	0.002029	30042.96
Mean	0.157	67.51683333	62.969	63.47583333	0.002287667	28526.717
Minimum	0.157	62.315	58.673	57.191	0.002029	26995.843
Maximum	0.157	44.609	40.214	41.858	0.001649	29430.7
Standard Dev.	0	0.601	0.627	0.789	0.000151	1135.02

Table B5. Concrete properties of ITS-3.

Batch		Slump	Age	Uncon.	Static
Number	Location	(in.)	(days)	Comp. Str.	Modulus
				(psi)	(psi)
1	Foundation	9	7	920	--
			23	1600	--
			105	2,040	3.05 x E6
			105	2,130	3.05 x E6
			105	1,980	--
			105	2,010	--
1	1st Lift, Walls	8.5	7	1,160	--
			28	2,260	--
			28	2,280	--
			28	2,240	--
			77	3,290	4.15 x E6
			77	3,090	--
			77	2,930	--
			77	3,050	--
2	1st Lift, Walls	8.25	7	1,200	--
			28	2,260	--
			28	2,140	--
			28	2,290	--
			77	3,170	4.21 x E6
			77	2,910	--
			77	3,040	--
			77	2,990	--
1	2nd Lift, Walls	9	7	1,080	--
			29	2,080	--
			29	2,080	--
			29	2,080	--
			57	2,850	3.9 x E6
			57	2,670	--
			57	2,420	--
			57	2,550	--
2	2nd Lift, Walls	9.5	7	1,110	--
			29	2,110	--
			29	2,160	--
			29	2,150	--
			57	2,950	3.70 x E6
			57	2,650	--
			57	2,550	--
			57	2,660	--

APPENDIX C

STRAIN CONTOURS

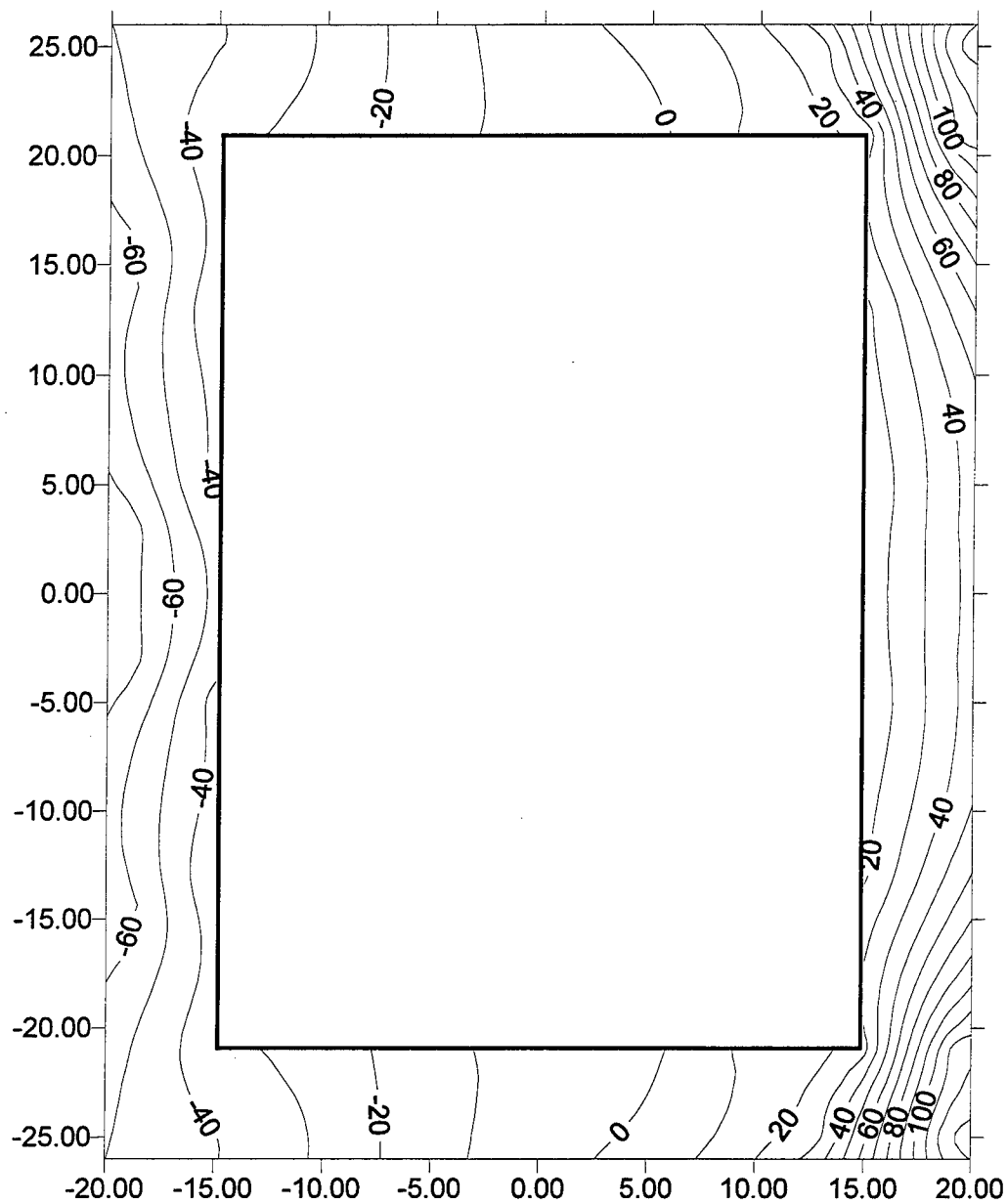


Figure C1. ITS-2 base strains, imposed deflection -0.1 in., cumulative travel of 0.1 in., that is, the top of the first leg of the first load cycle.

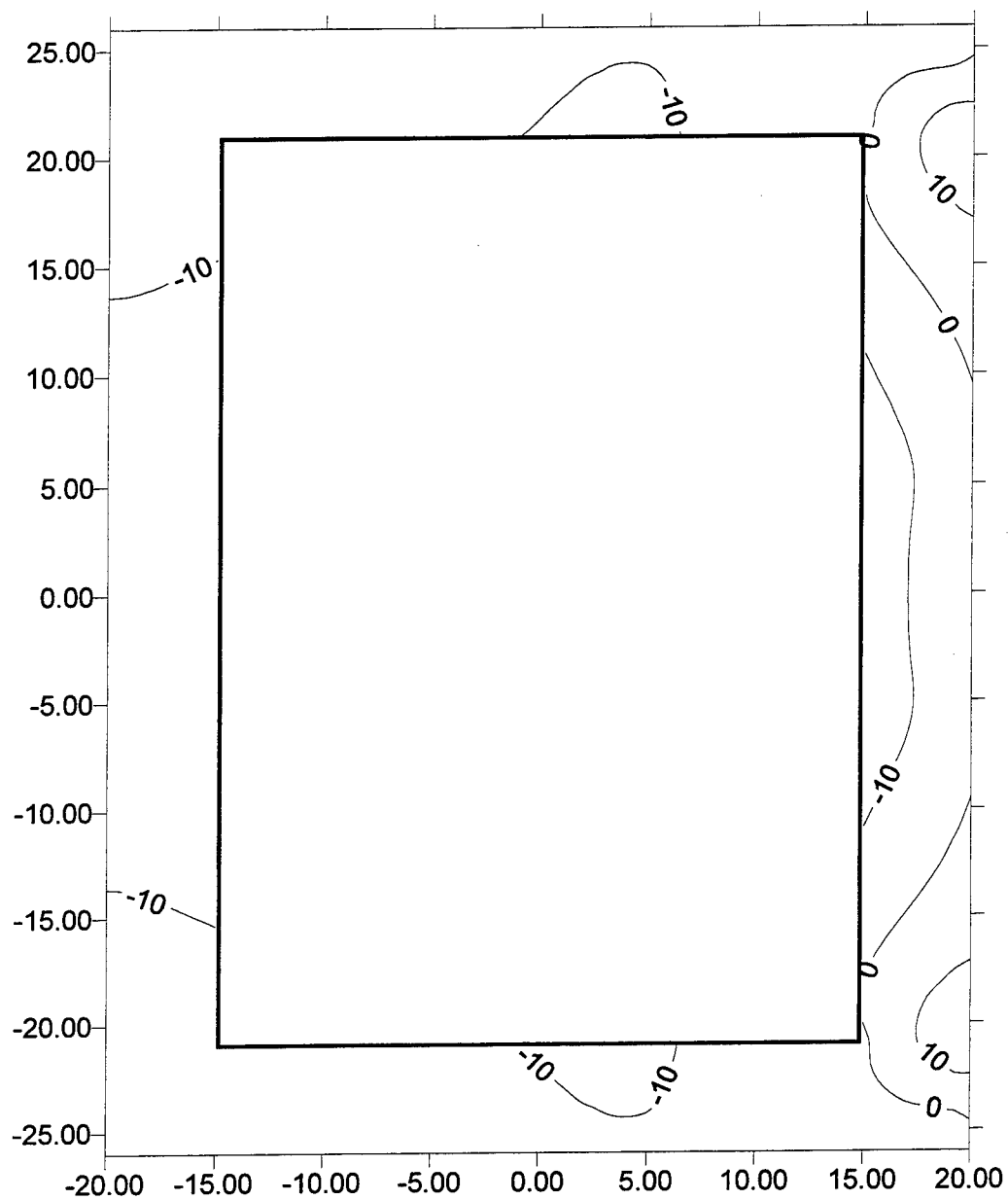


Figure C2. ITS-2 base strains, imposed deflection 0.0 in., cumulative travel of 0.2 in., that is, the bottom of the first leg of the first load cycle.

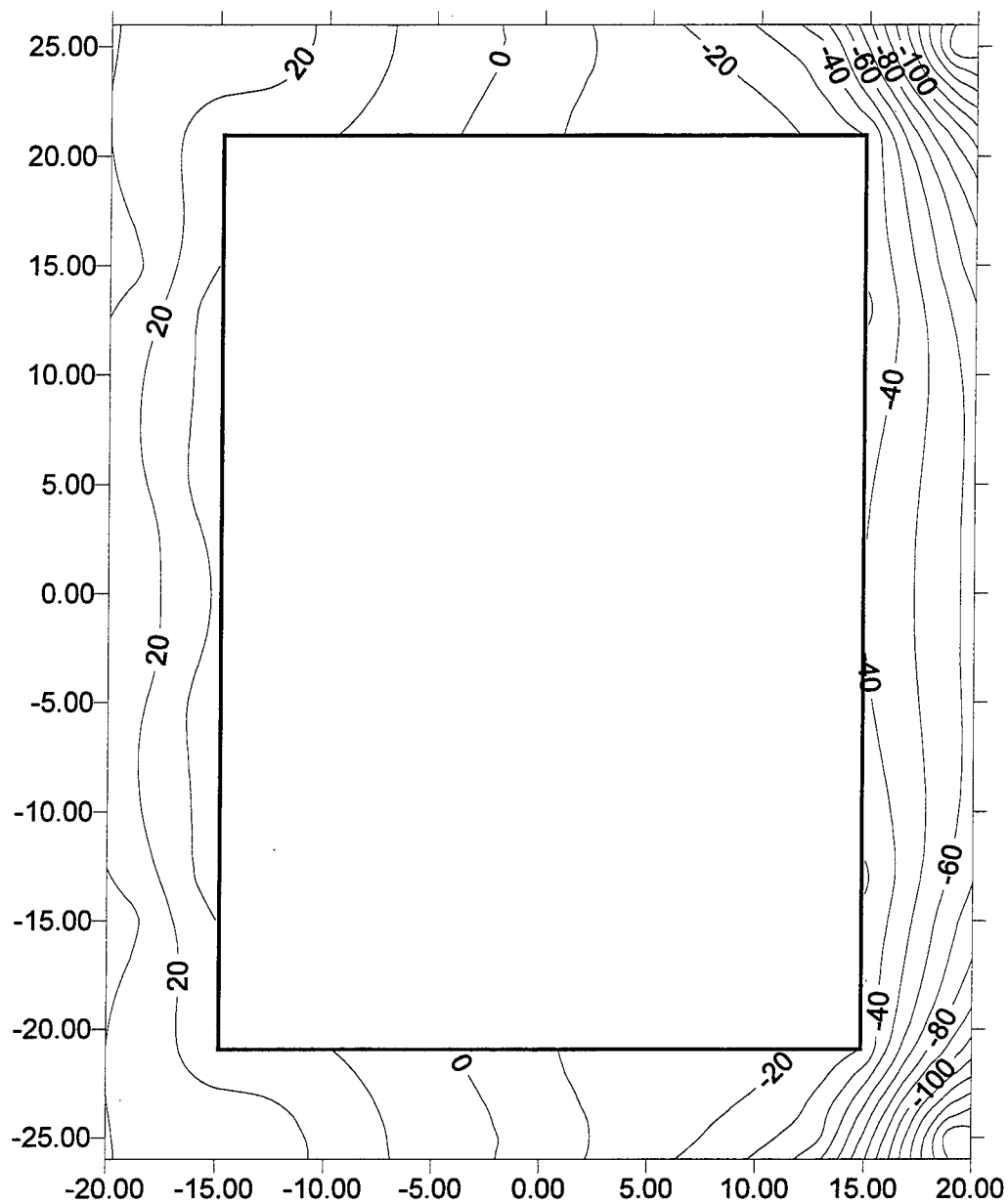


Figure C3. ITS-2 base strains, imposed deflection 0.1 in. and a cumulative imposed travel of 0.3 in., that is, the top of the second leg of the first load cycle.

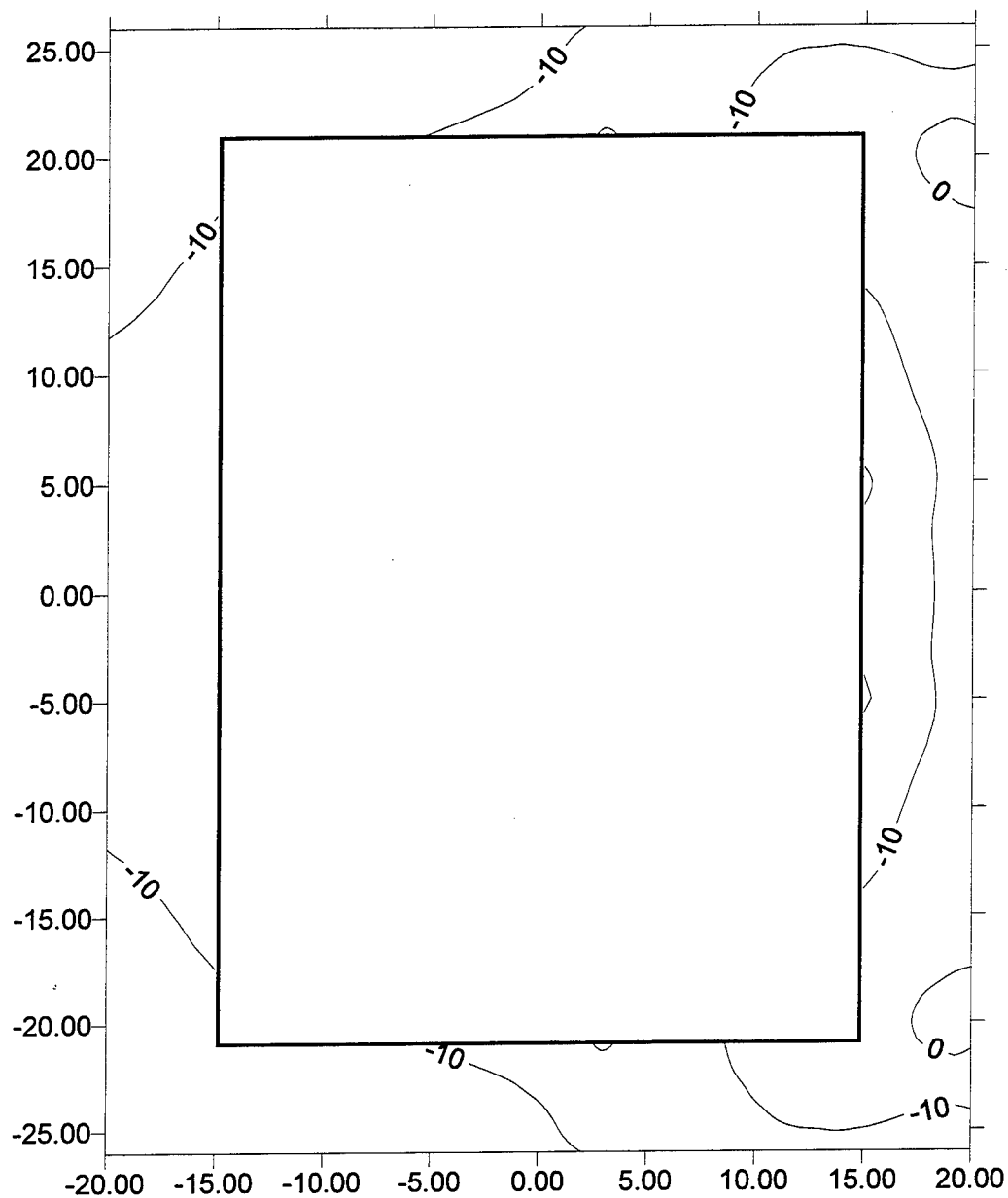


Figure C4. ITS-2 base strains, imposed deflection 0.0 in., cumulative travel of 0.4 in., that is, the bottom of the second leg of the first load cycle.

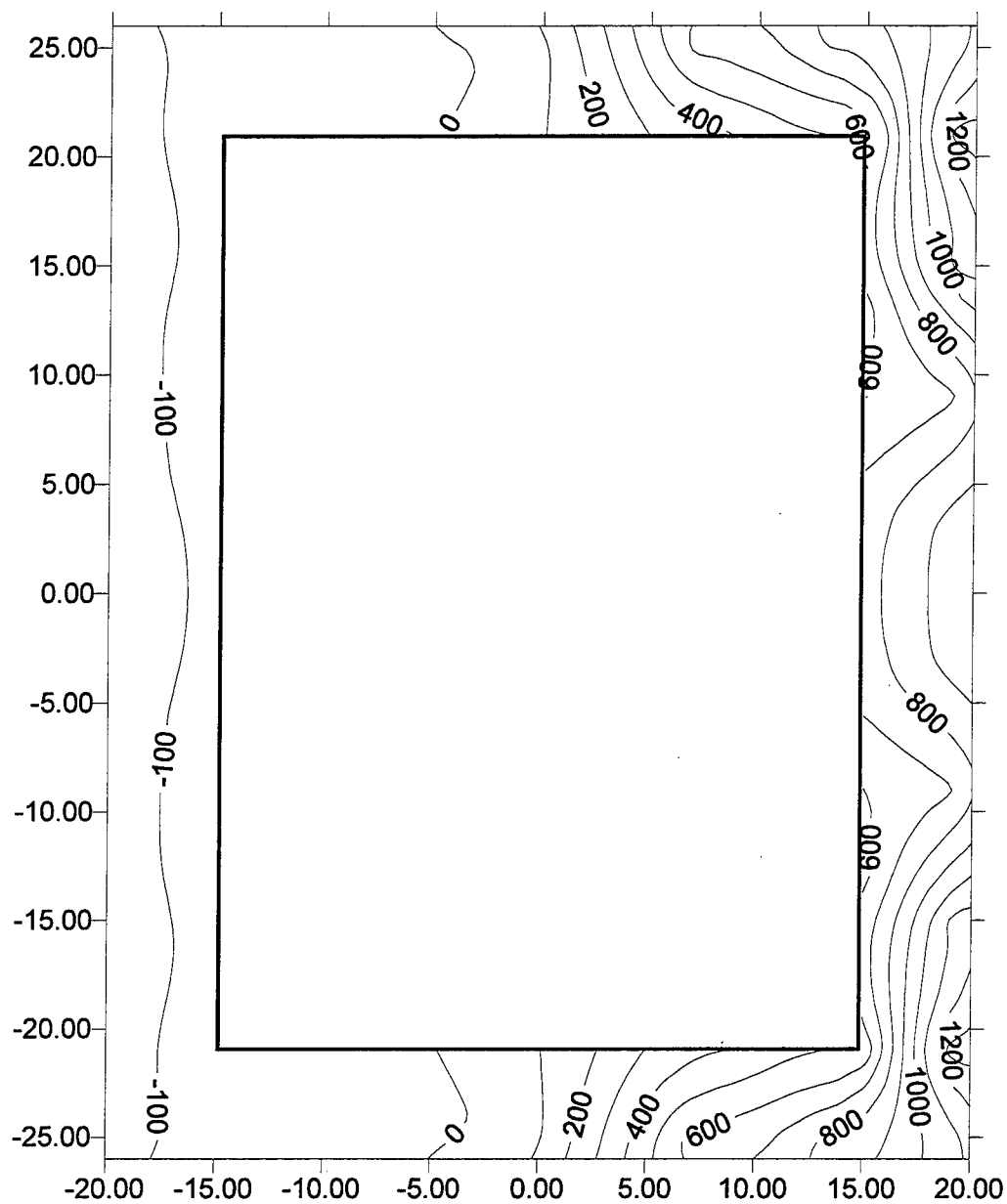


Figure C5. ITS-2 base strains, imposed deflection -0.2 in., cumulative travel of 0.6 in., that is, the top of the first leg of the second load cycle.

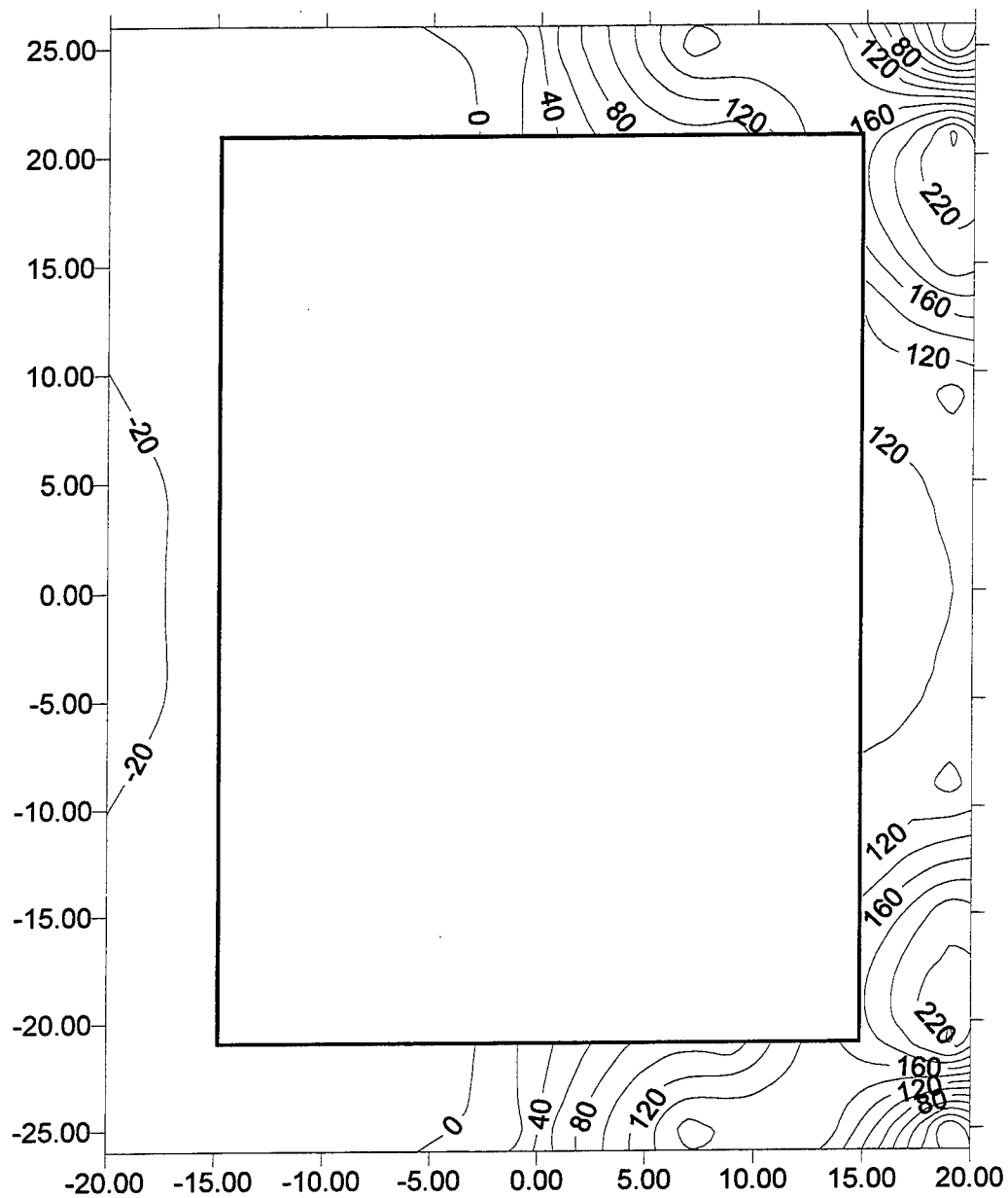


Figure C6. ITS-2 base strains, imposed deflection 0.0 in., cumulative travel of 0.8 in., that is, the bottom of the first leg of the second load cycle.

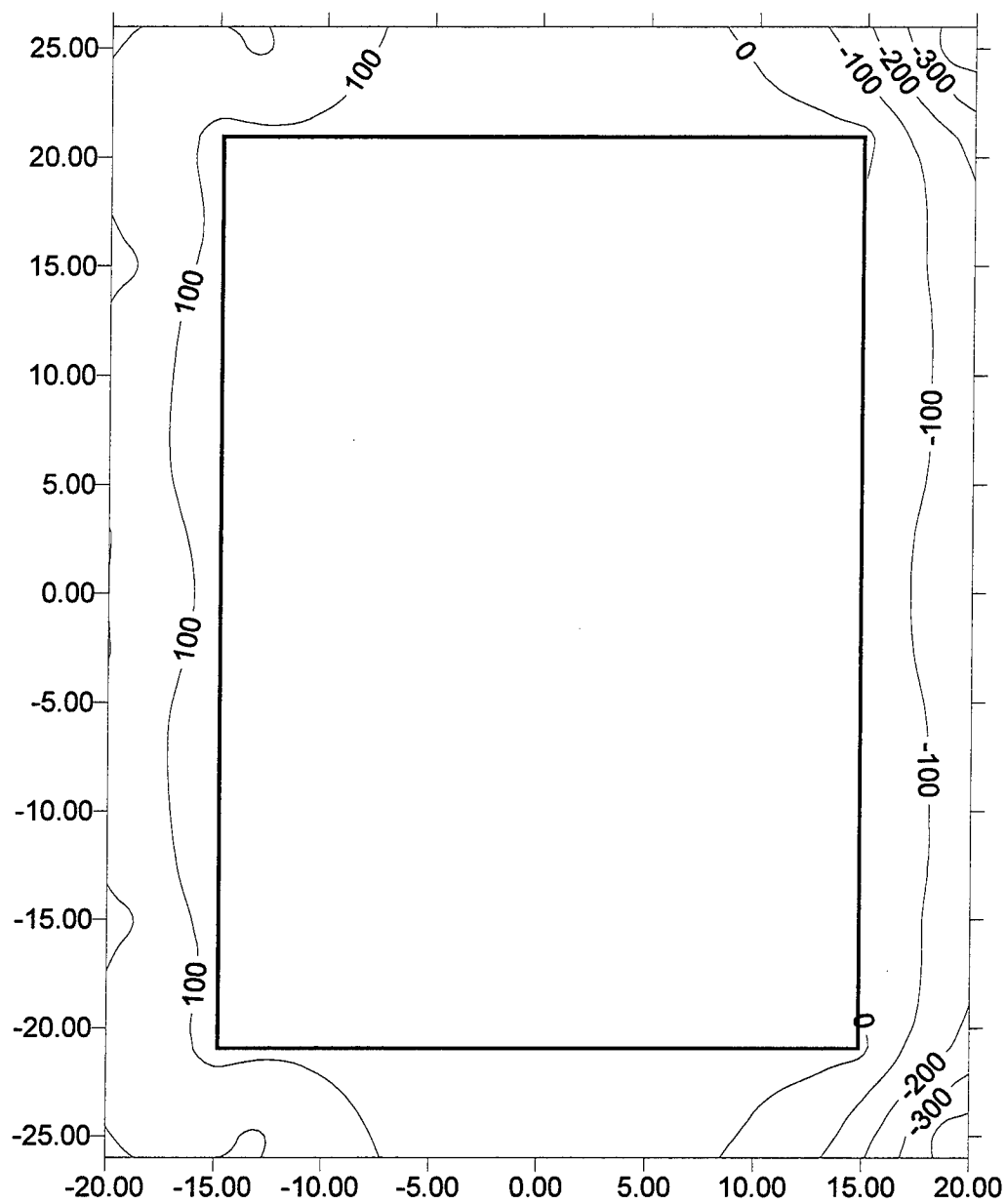


Figure C7. ITS-2 base strains, imposed deflection 0.2 in., cumulative travel of 1.0 in., that is, the top of the second leg of the second load cycle.

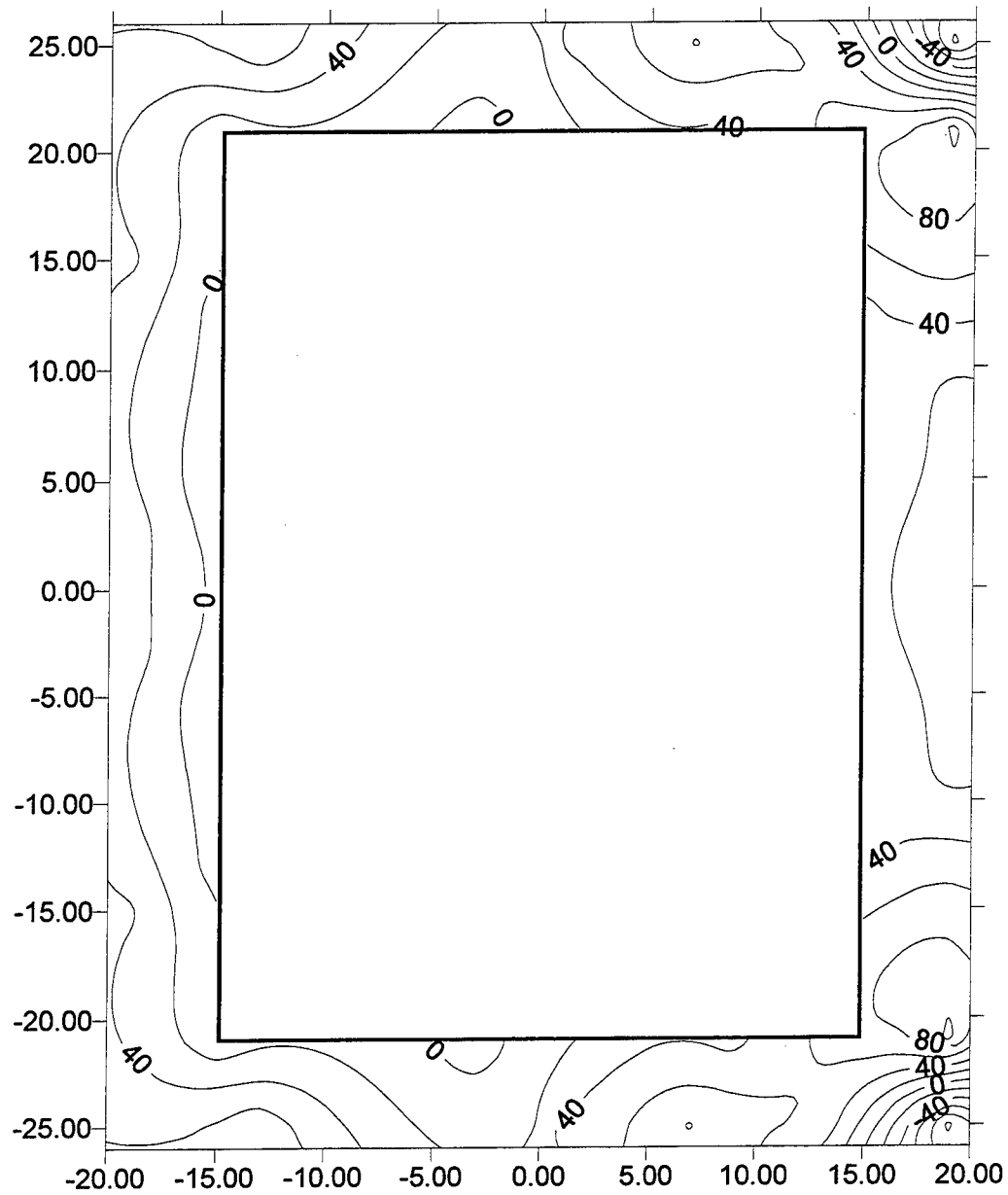


Figure C8. ITS-2 base strains, imposed deflection 0.0 in., cumulative travel of 1.2 in., that is, the bottom of the second leg of the second load cycle.

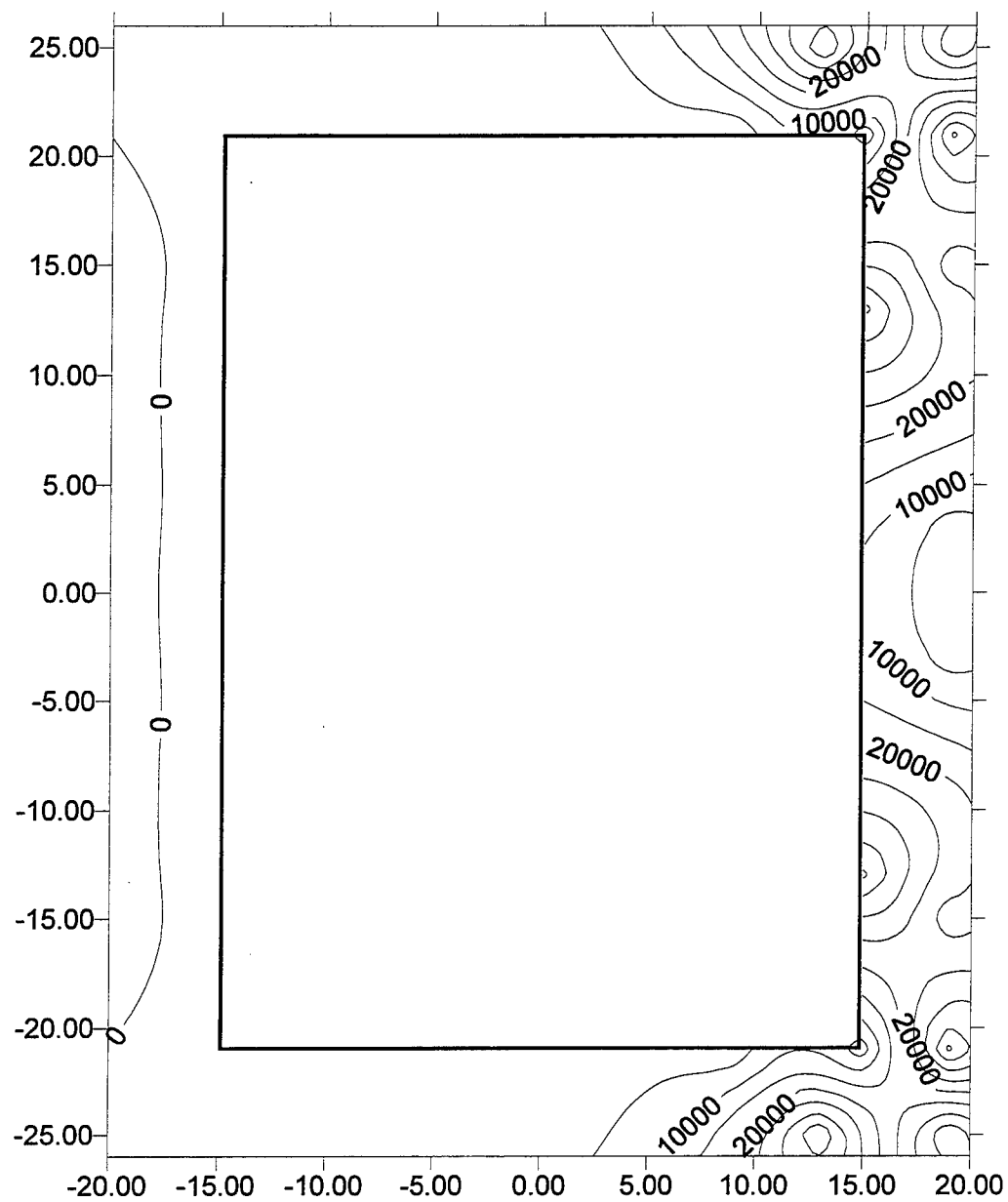


Figure C9. ITS-2 base strains, imposed deflection -0.3 in., cumulative travel of 1.5 in., that is, the top of the first leg of the third load cycle.

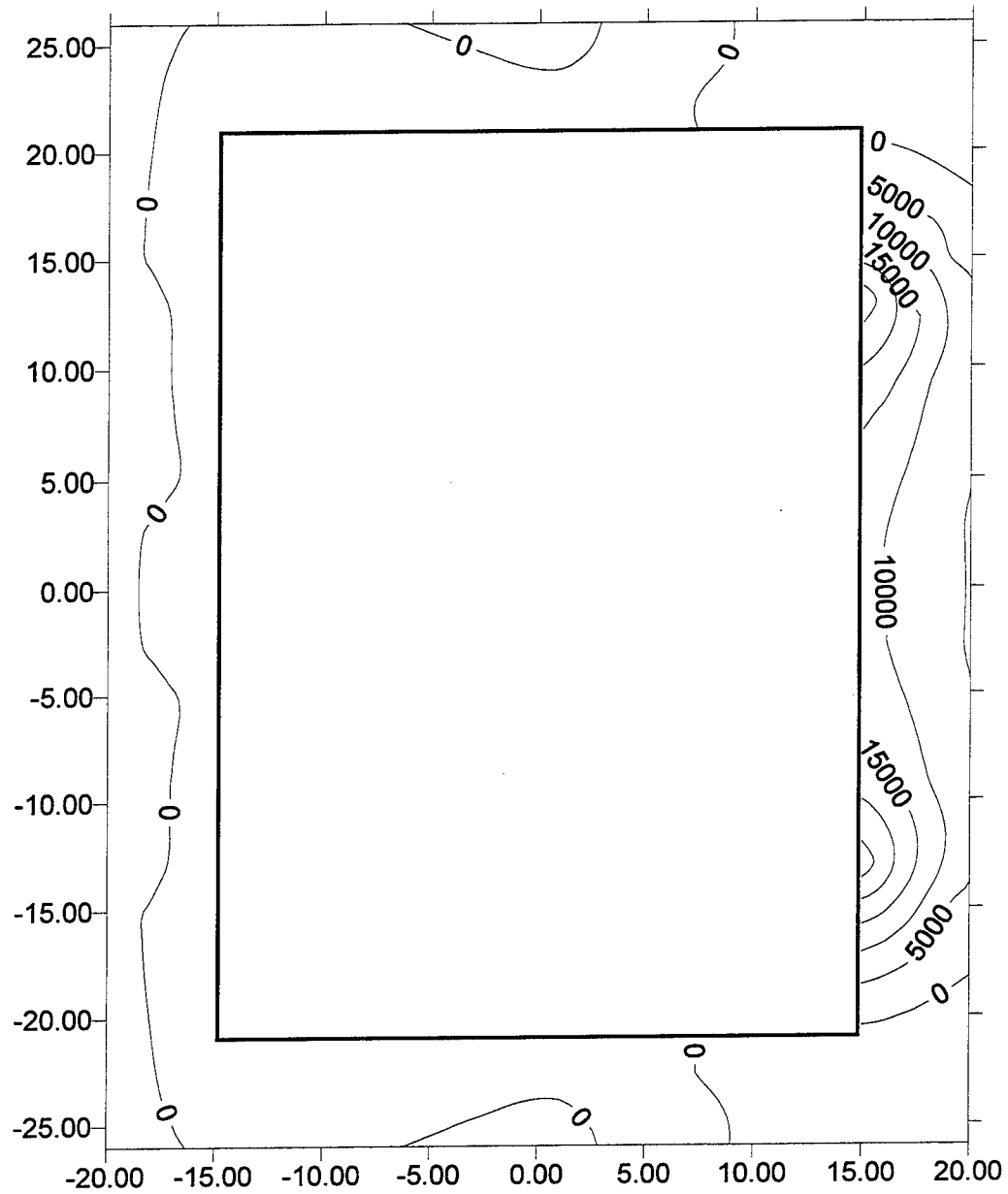


Figure C10. ITS-2 base strains, imposed deflection 0.0 in., cumulative travel of 1.8 in., that is, the bottom of the first leg of the third load cycle.

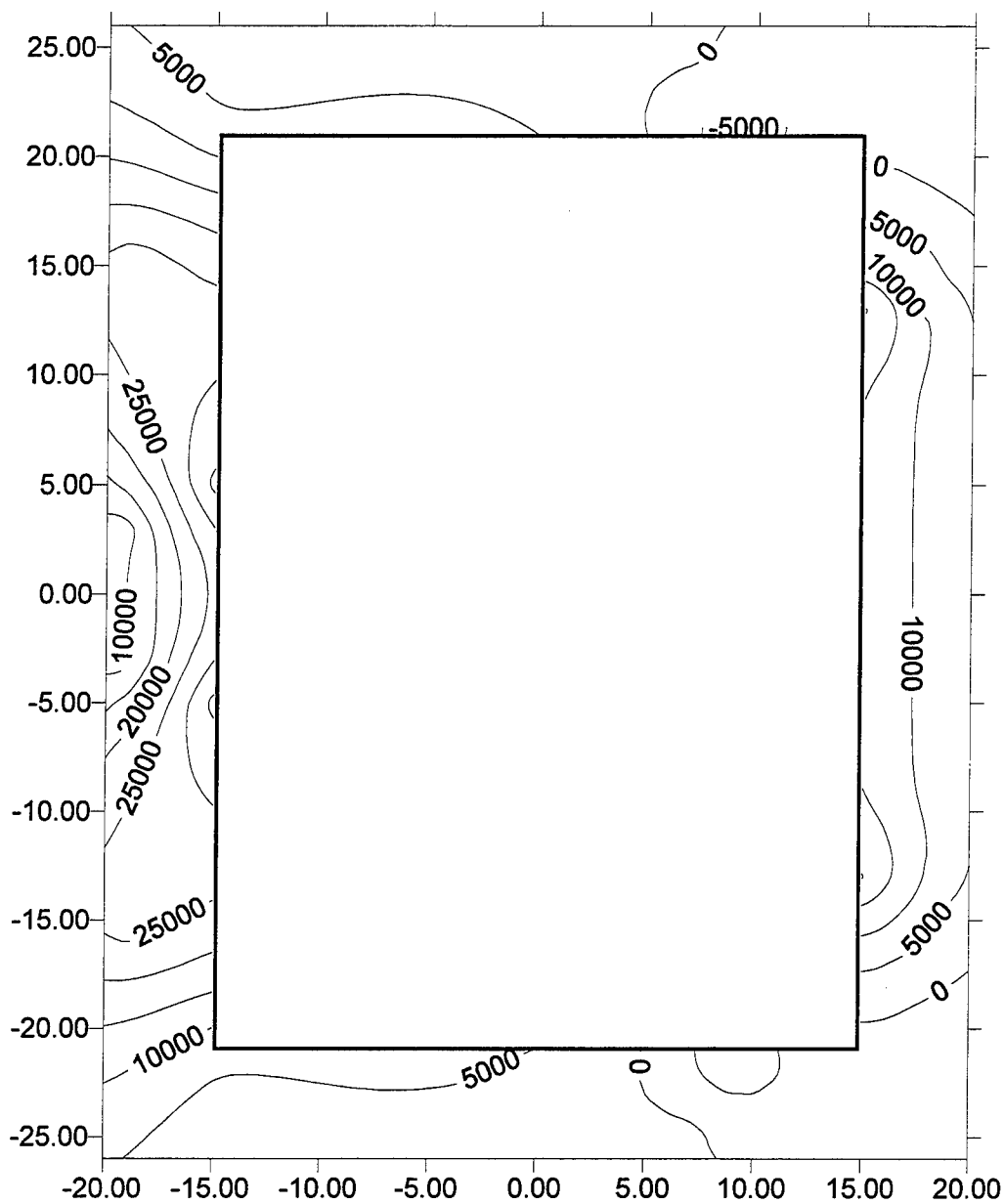


Figure C11. ITS-2 base strains, imposed deflection 0.3 in., cumulative travel of 2.1 in., that is, the top of the second leg of the third load cycle.

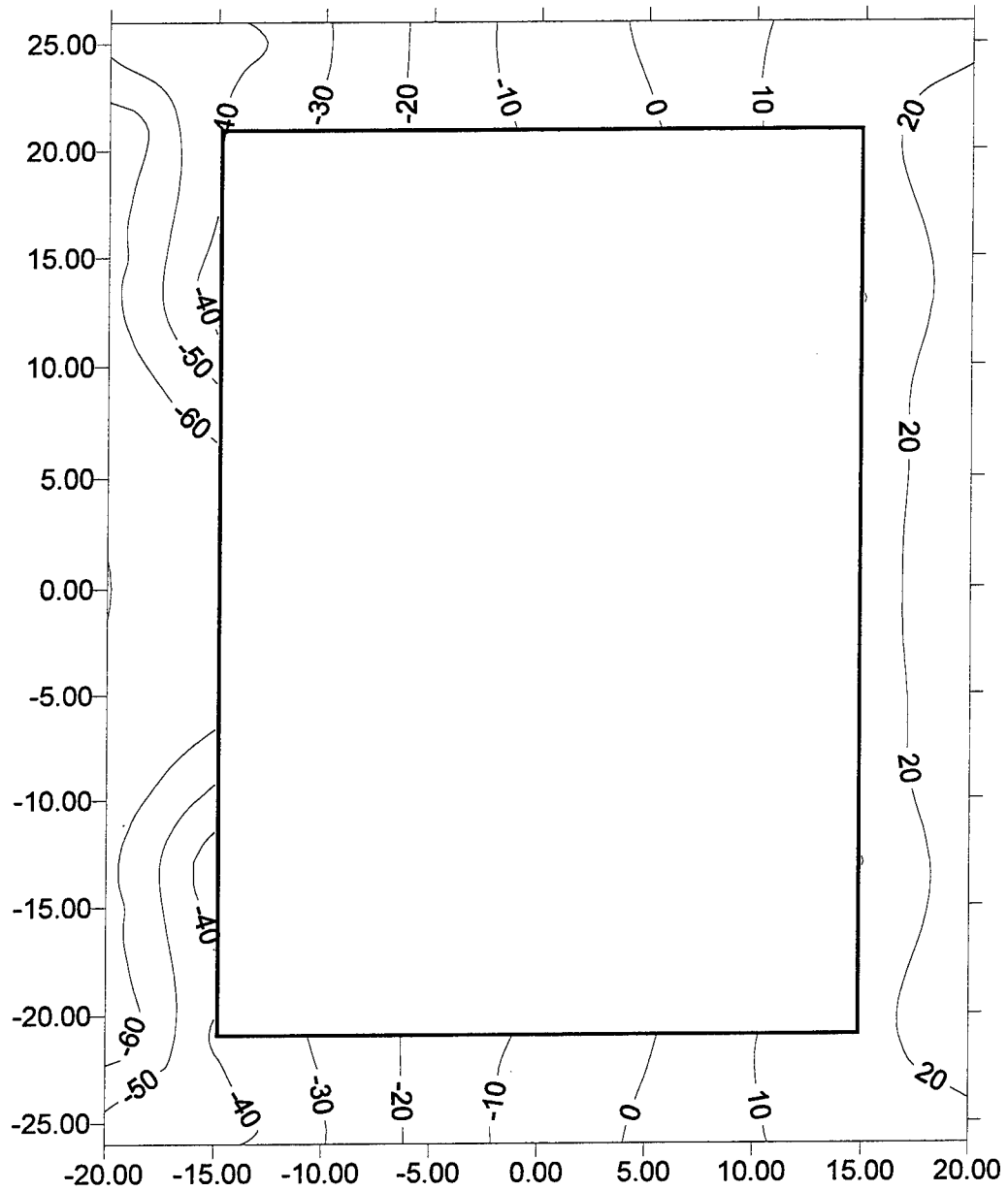


Figure C12. ITS-2 strains at 2 in. elevation, imposed deflection -0.1 in., cumulative travel of 0.1 in., that is, the top of the first leg of the first load cycle.

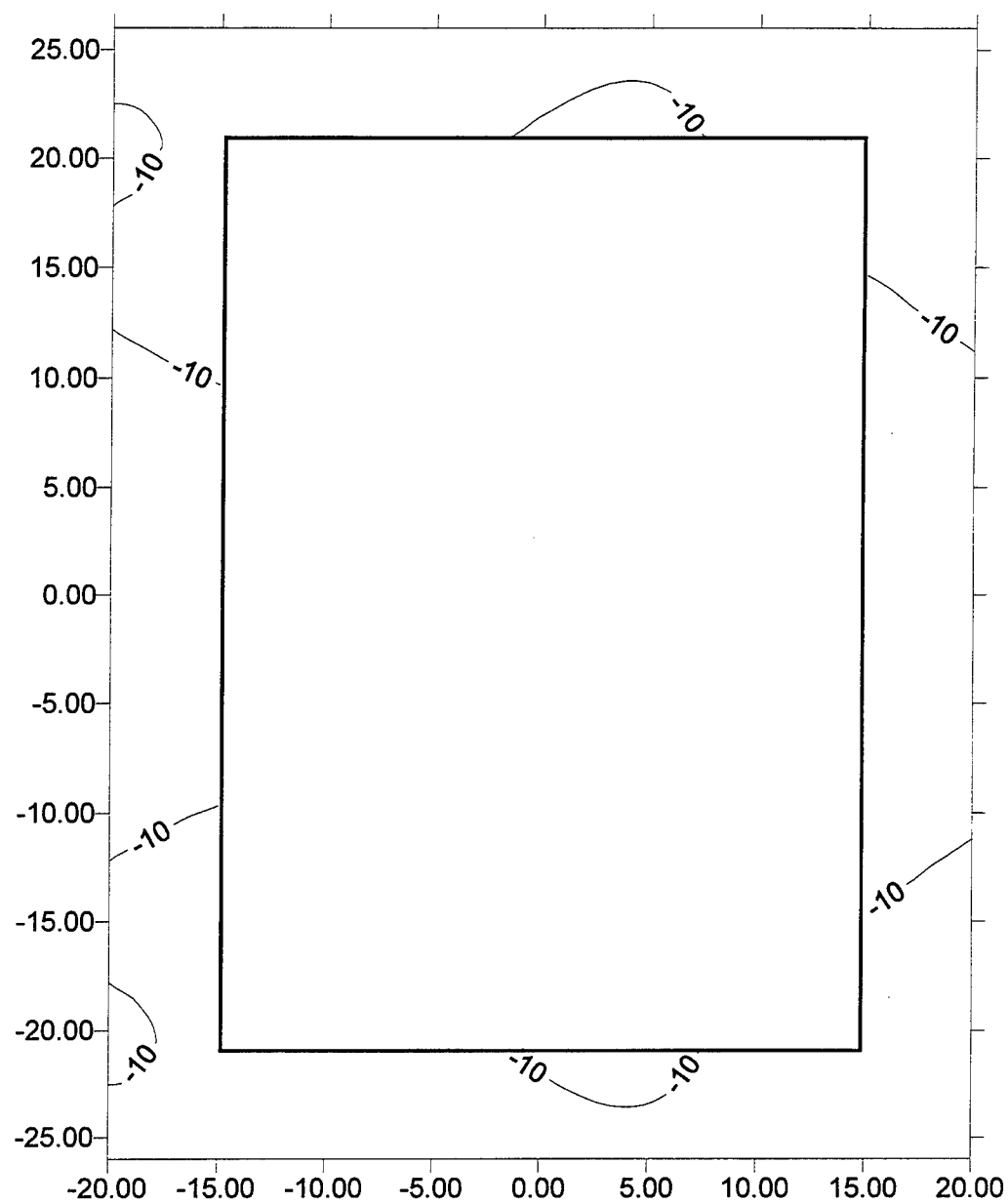


Figure C13. ITS-2 strains at 2 in. elevation, imposed deflection 0.0 in., cumulative travel of 0.2 in., that is, the bottom of the first leg of the first load cycle.

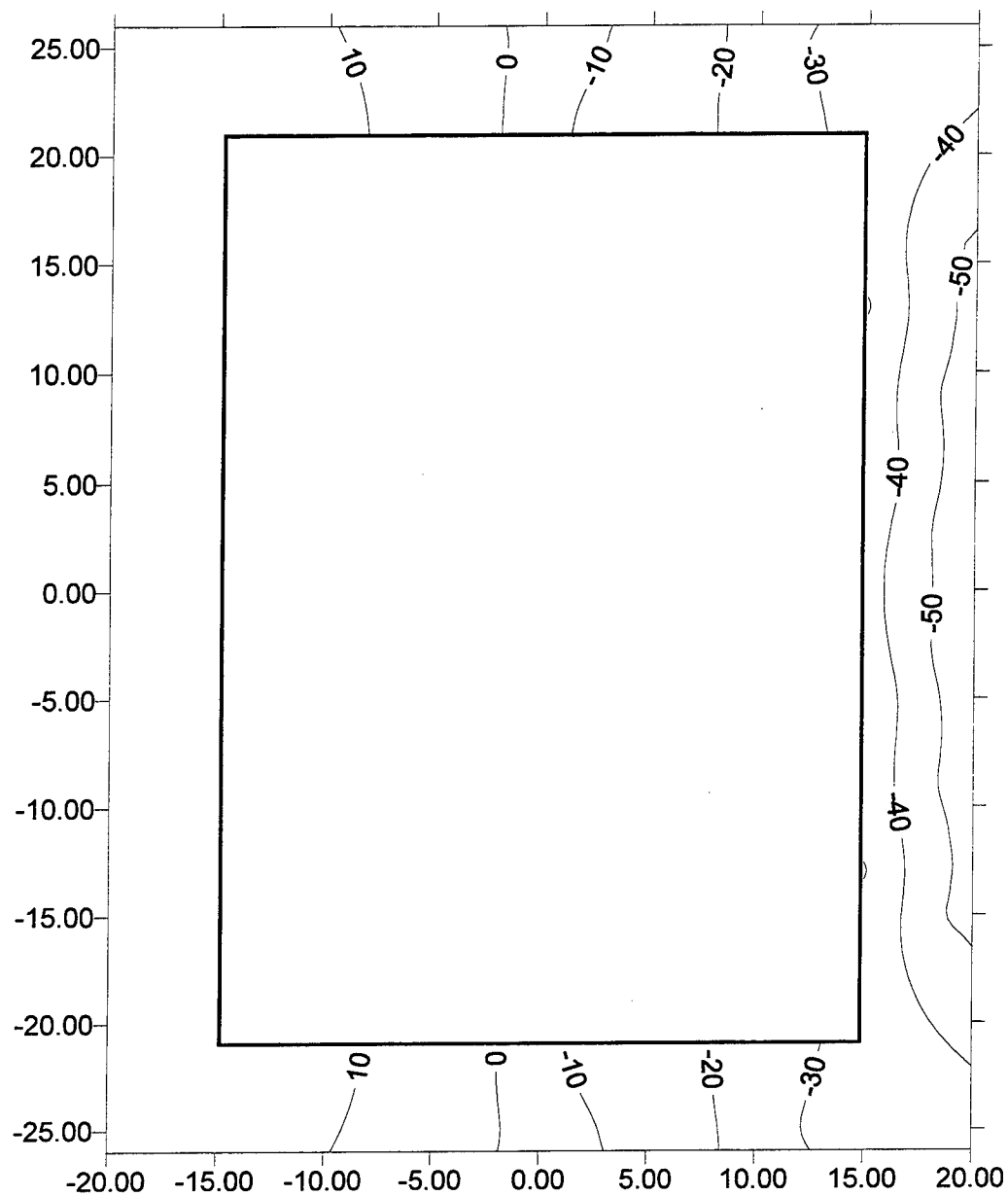


Figure C14. ITS-2 strains at 2 in. elevation, imposed deflection 0.1 in., cumulative travel of 0.3 in., that is, the top of the second leg of the first load cycle.

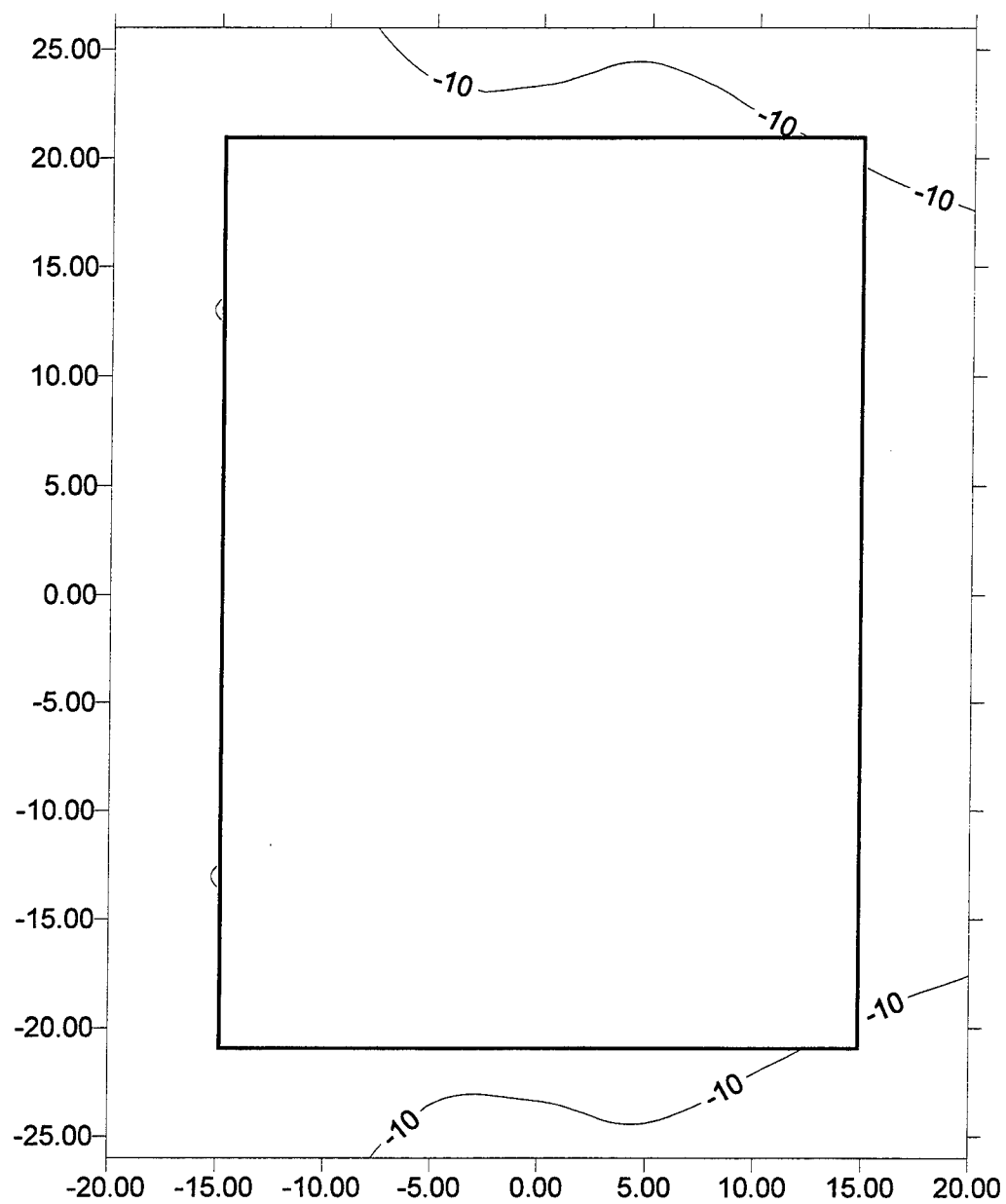


Figure C15. ITS-2 strains at 2 in. elevation, imposed deflection 0.0 in., cumulative travel of 0.4 in., that is, the bottom of the second leg of the first load cycle.

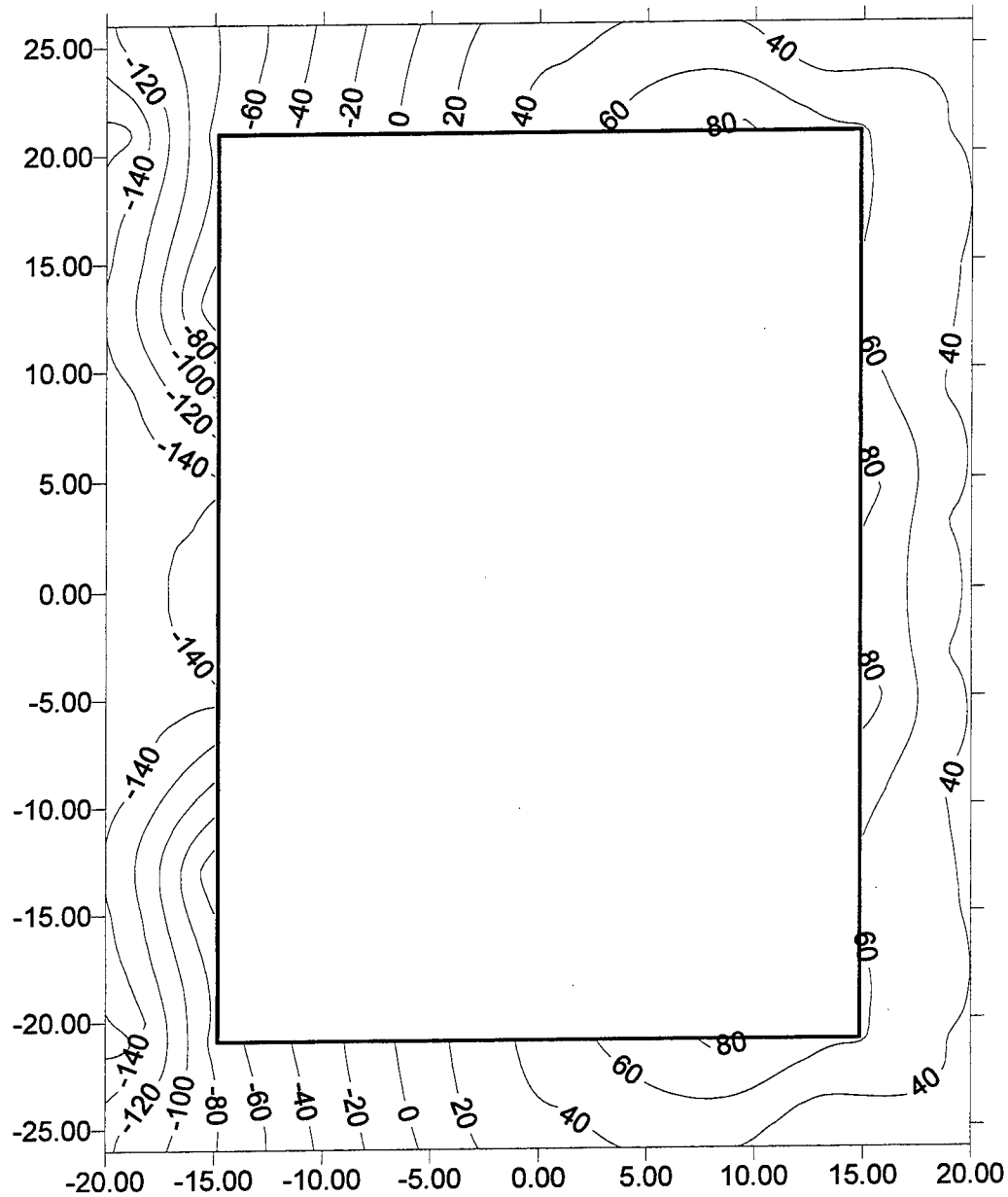


Figure C16. ITS-2 strains at 2 in. elevation, imposed deflection -0.2 in., cumulative travel of 0.6 in., that is, the top of the first leg of the second load cycle.

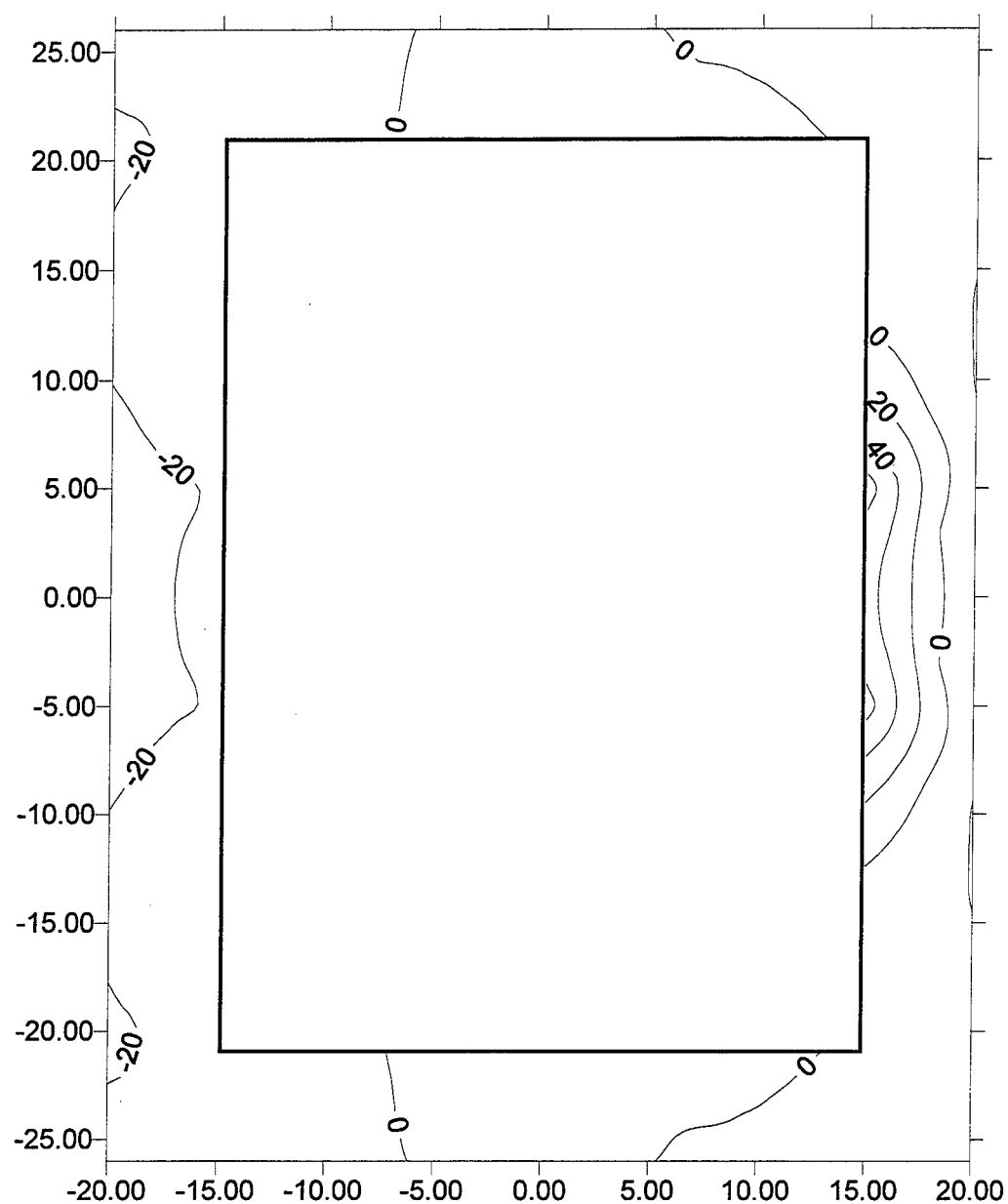


Figure C17. ITS-2 strains at 2 in. elevation, imposed deflection 0.0 in., cumulative travel of 0.8 in., that is, the bottom of the first leg of the second load cycle.

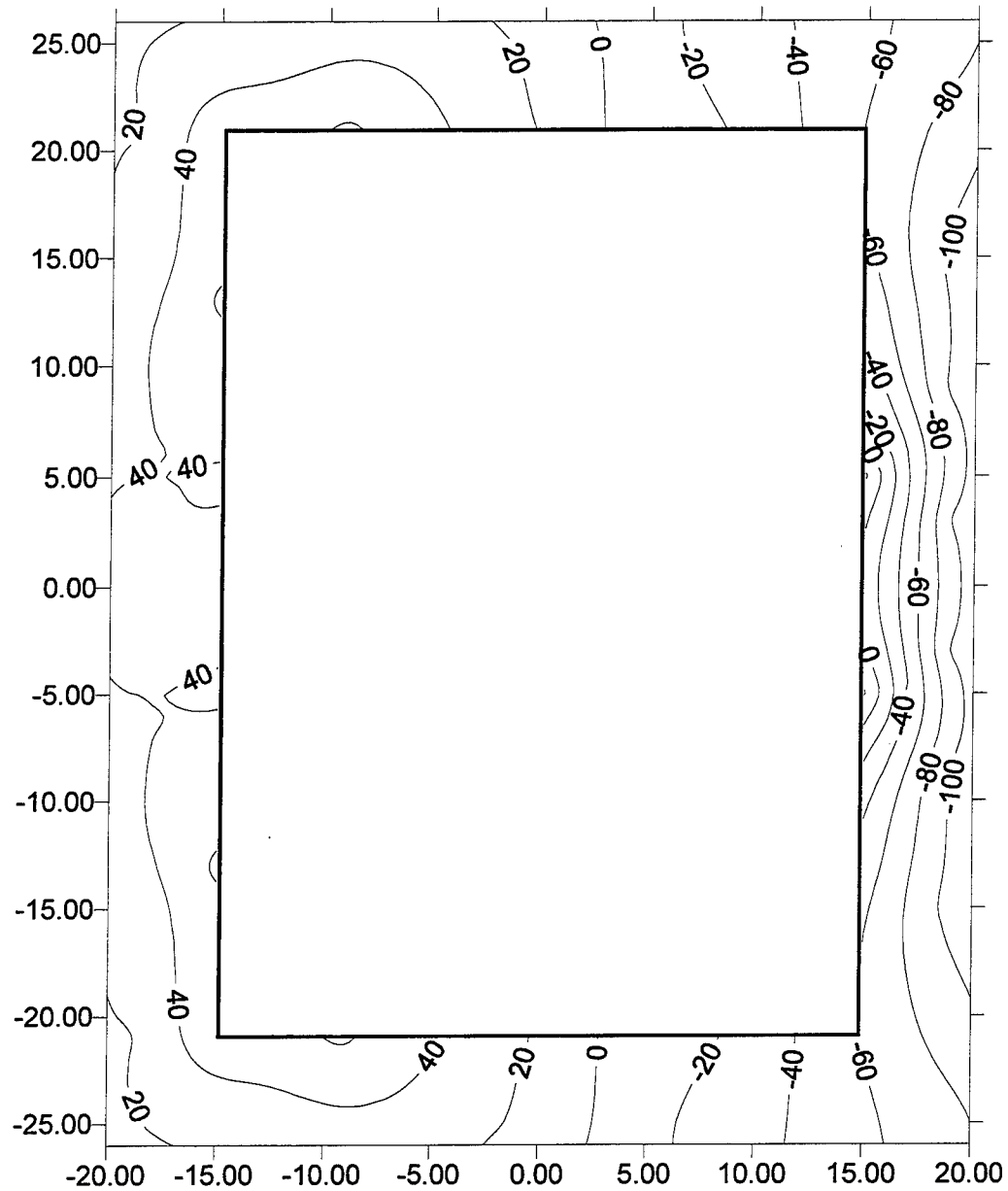


Figure C18. ITS-2 strains at 2 in. elevation, imposed deflection 0.2 in., cumulative travel of 1.0 in., that is, the top of the second leg of the second load cycle.

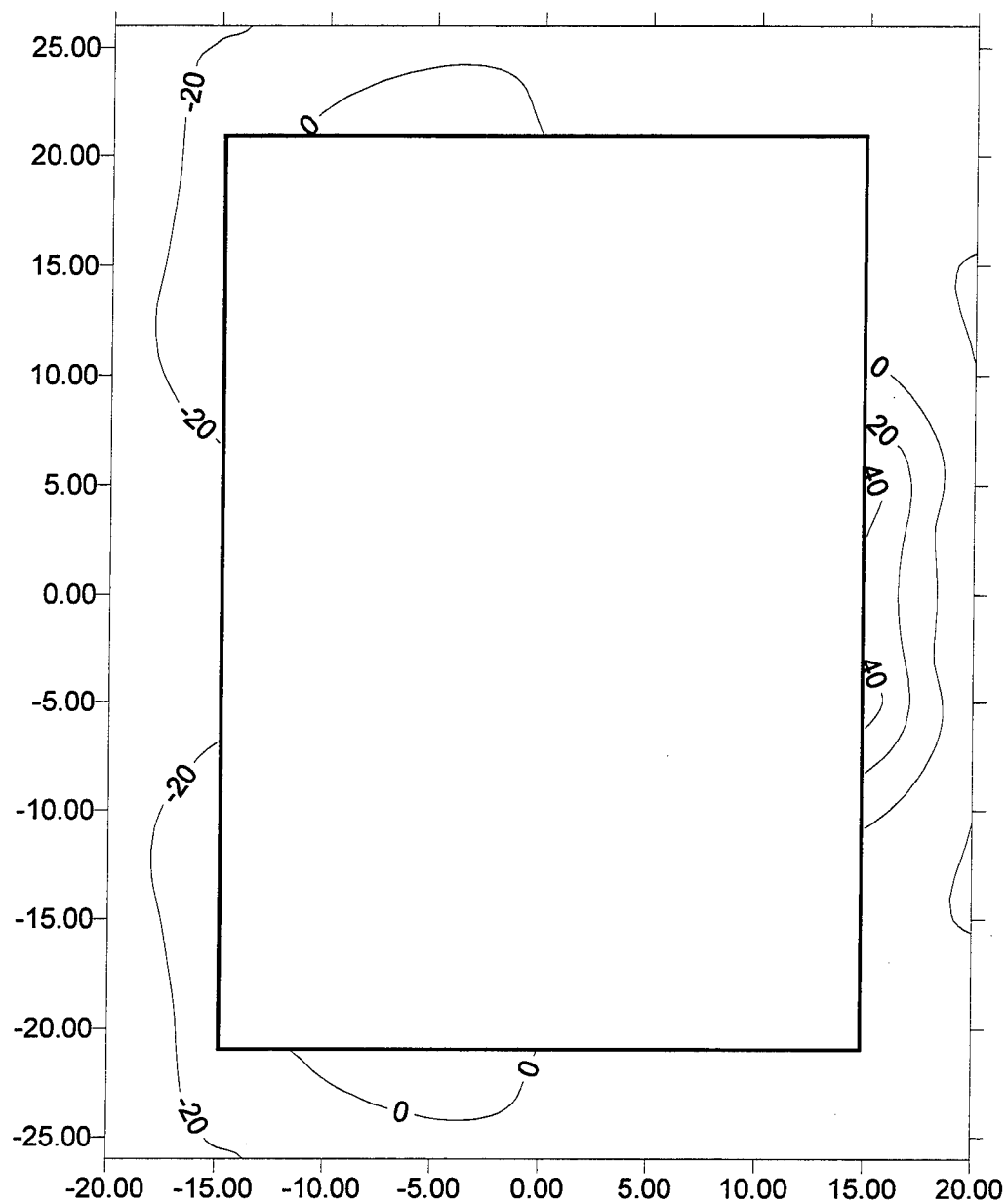


Figure C19. ITS-2 strains at 2 in. elevation, imposed deflection 0.0 in., cumulative travel of 1.2 in., that is, the bottom of the second leg of the second load cycle.

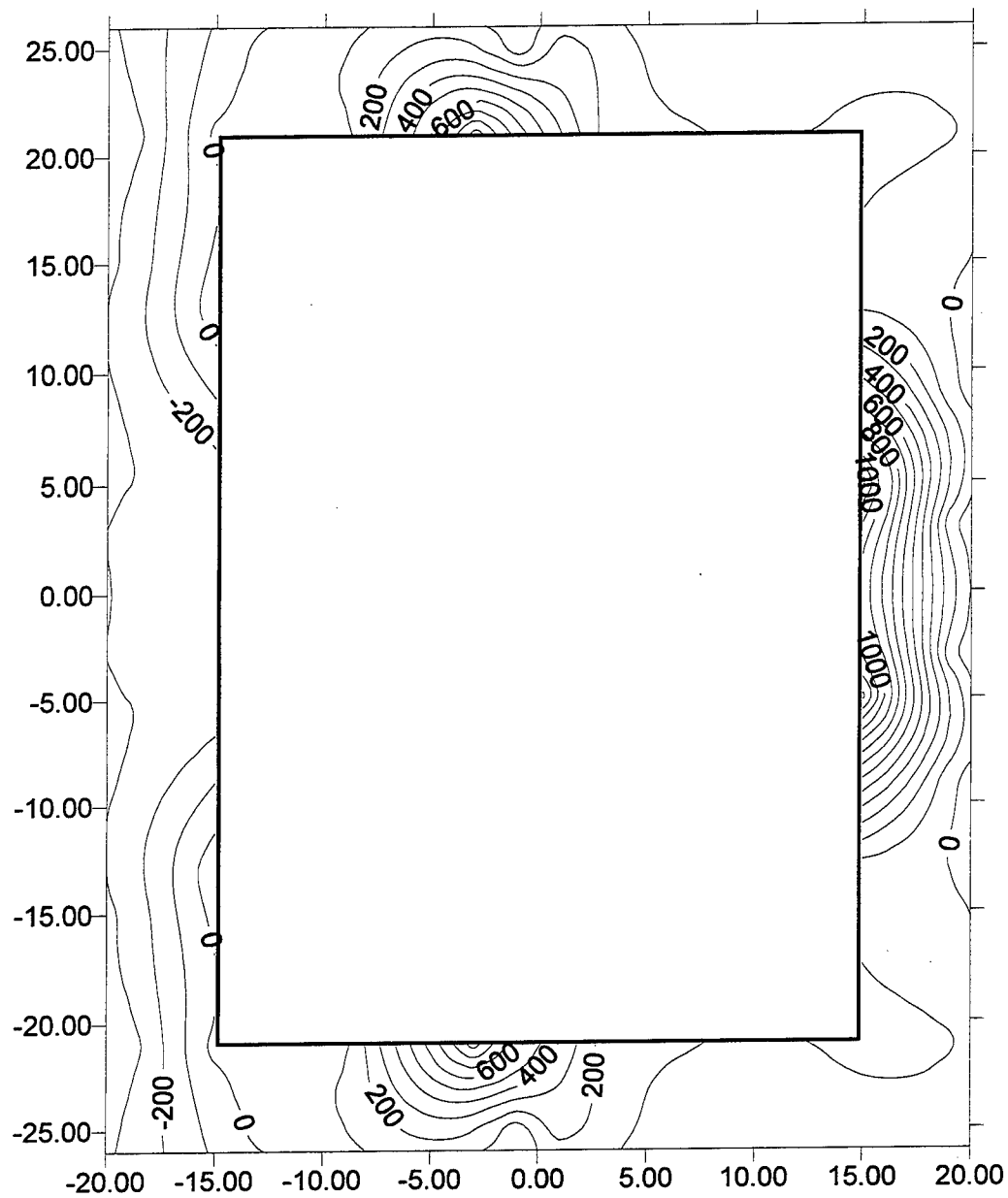


Figure C20. ITS-2 strains at 2 in. elevation, imposed deflection -0.3 in., cumulative travel of 1.5 in., that is, the top of the first leg of the third load cycle.

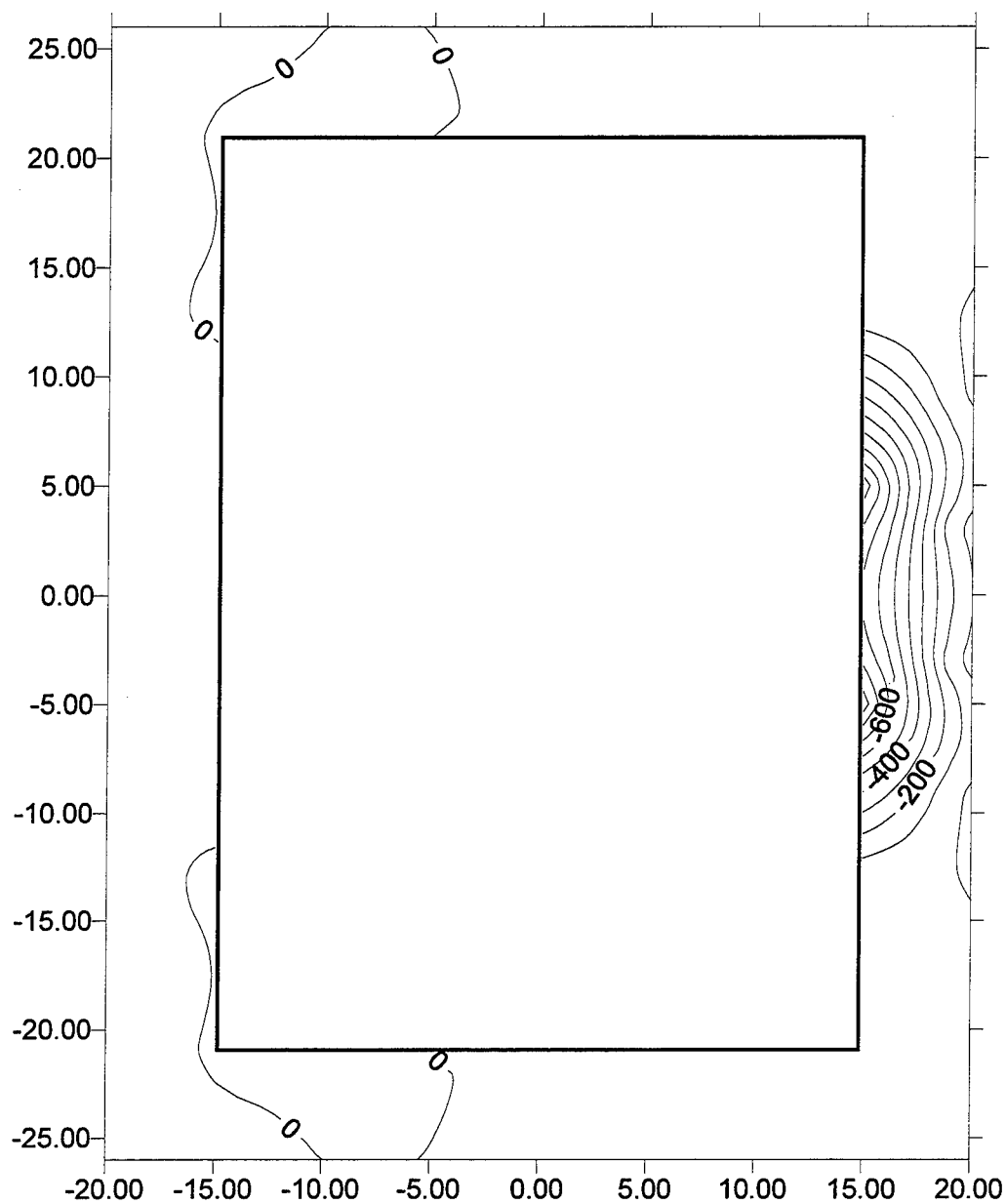


Figure C21. ITS-2 strains at 2 in. elevation, imposed deflection 0.0 in., cumulative travel of 1.8 in., that is, the bottom of the first leg of the third load cycle.

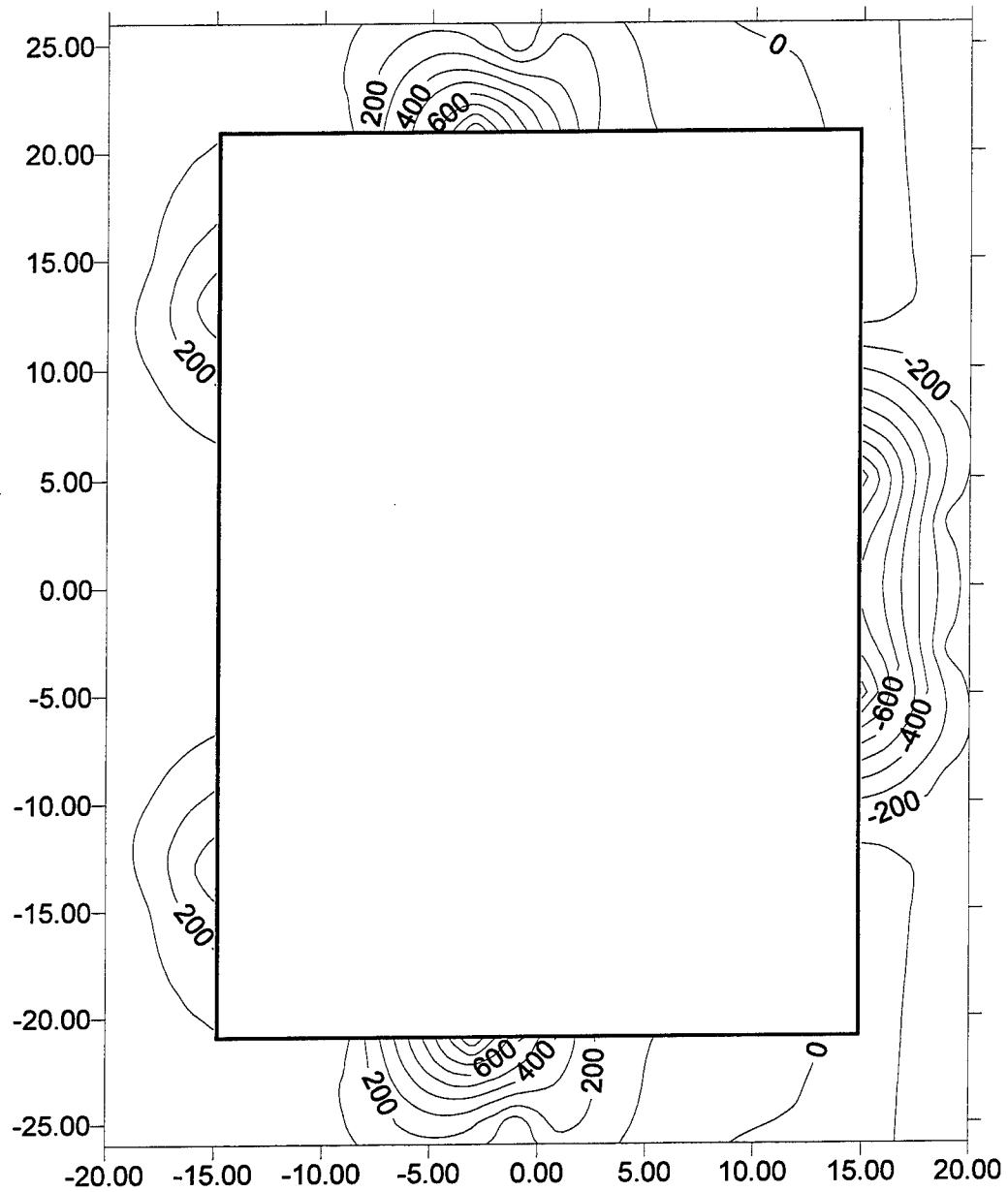


Figure C22. ITS-2 strains at 2 in. elevation, imposed deflection 0.3 in., cumulative travel of 2.1 in., that is, the top of the second leg of the third load cycle.

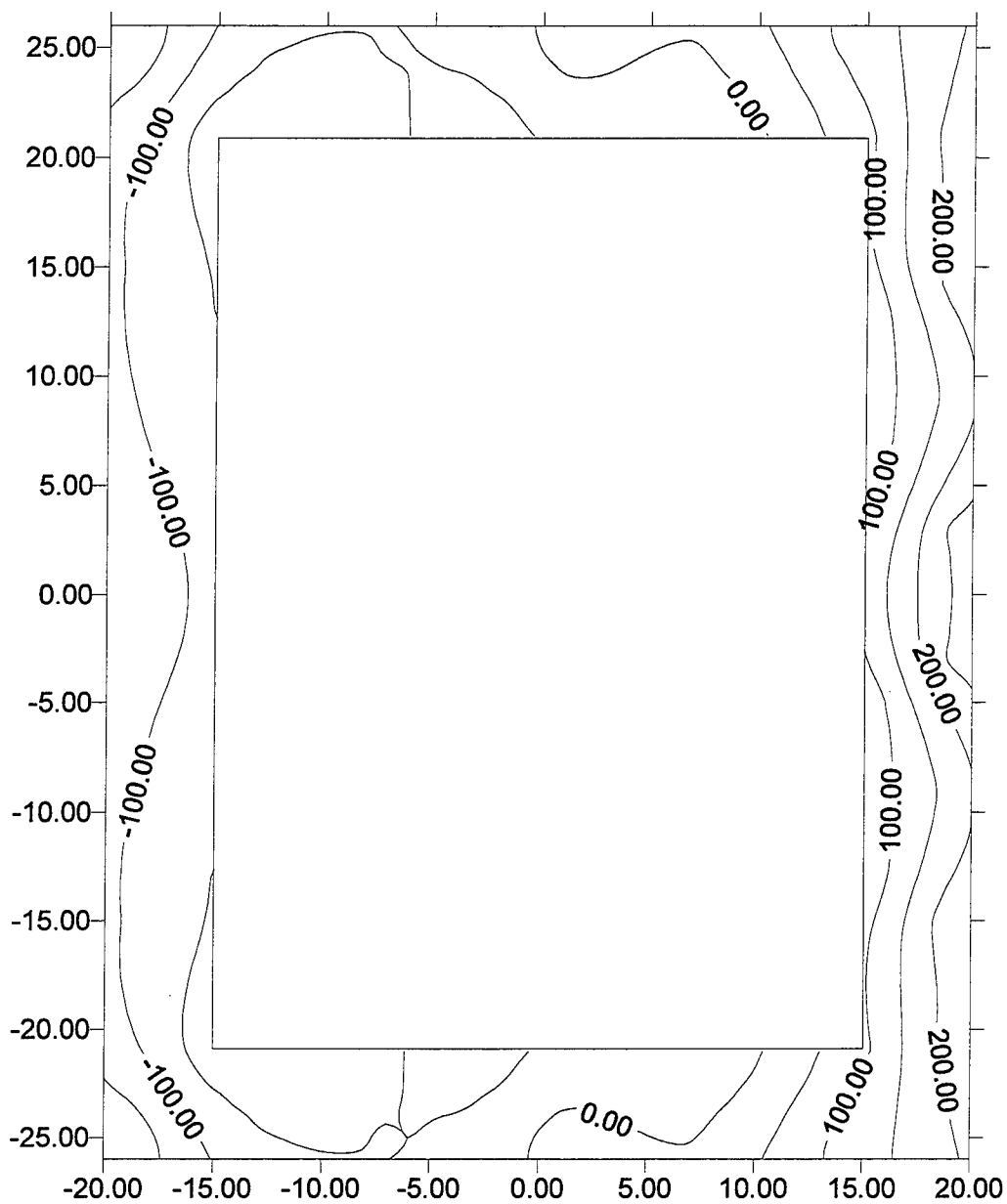


Figure C23. ITS-3 base strains, imposed deflection -0.1 in., cumulative travel of 0.1 in., that is, the top of the first leg of the first load cycle.

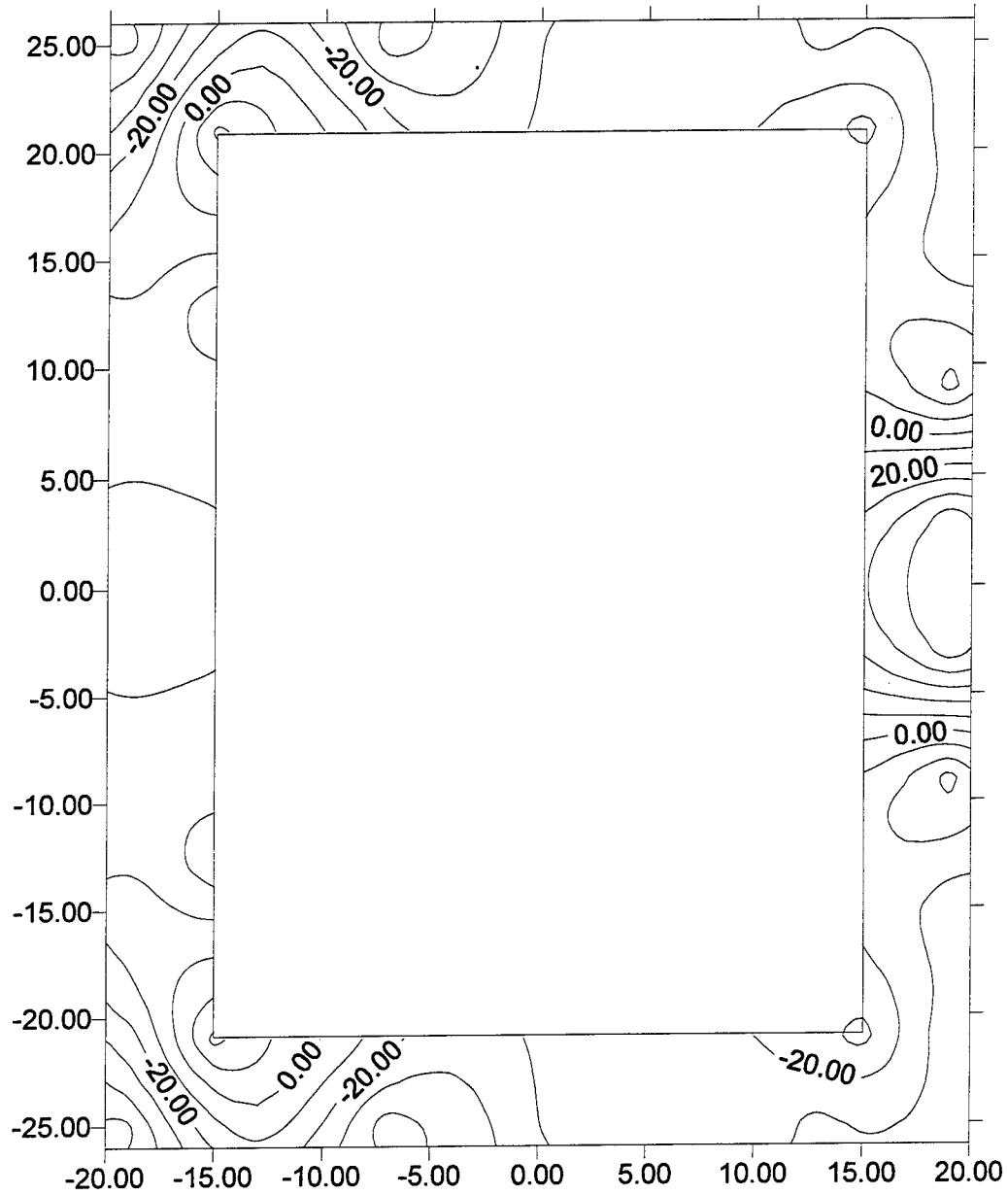


Figure C24. ITS-3 base strains, imposed deflection 0.0 in., cumulative travel of 0.2 in., that is, the bottom of the first leg of the first load cycle.

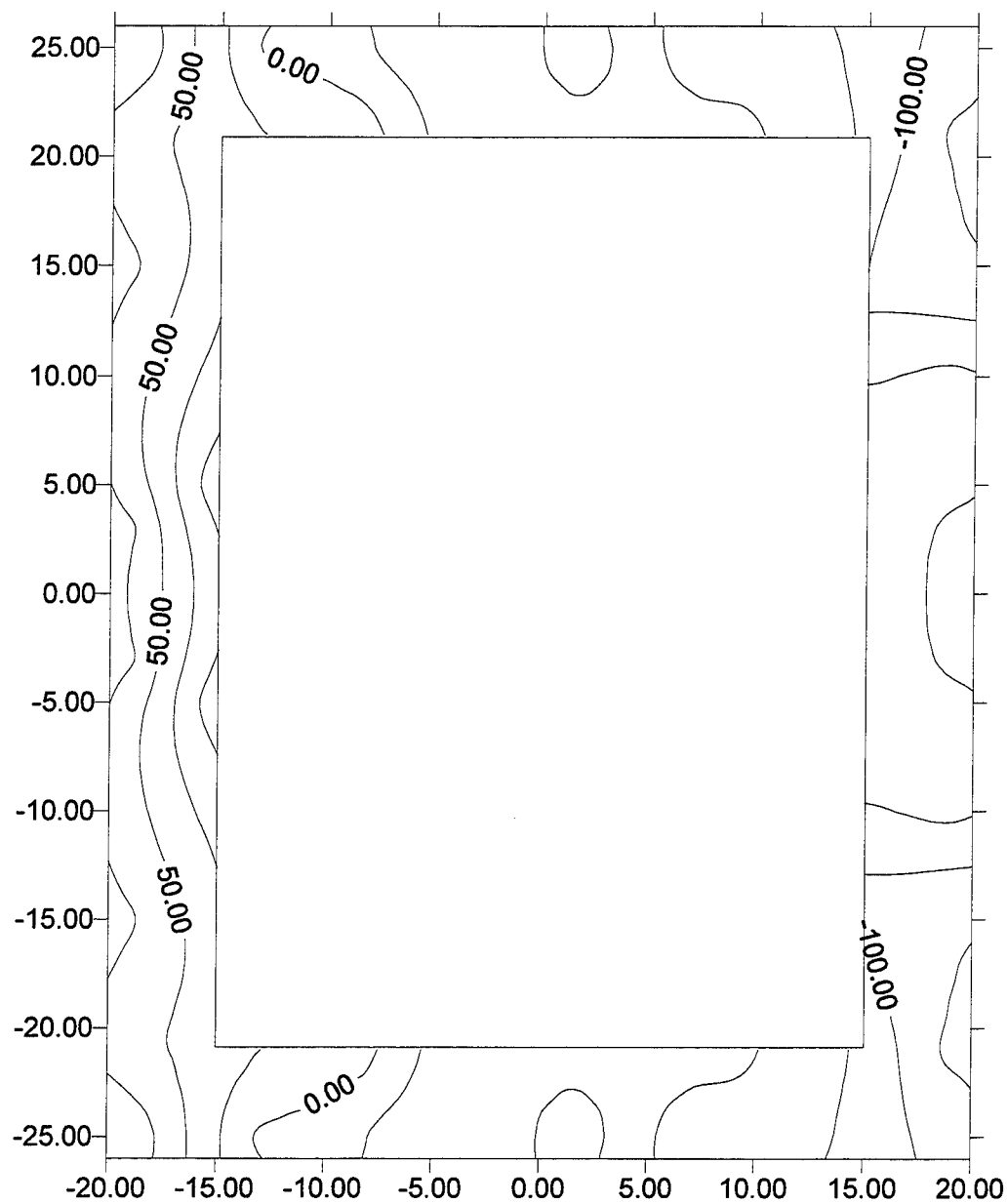


Figure C25. ITS-3 base strains, imposed deflection 0.1 in., cumulative travel of 0.3 in., that is, the top of the second leg of the first load cycle.

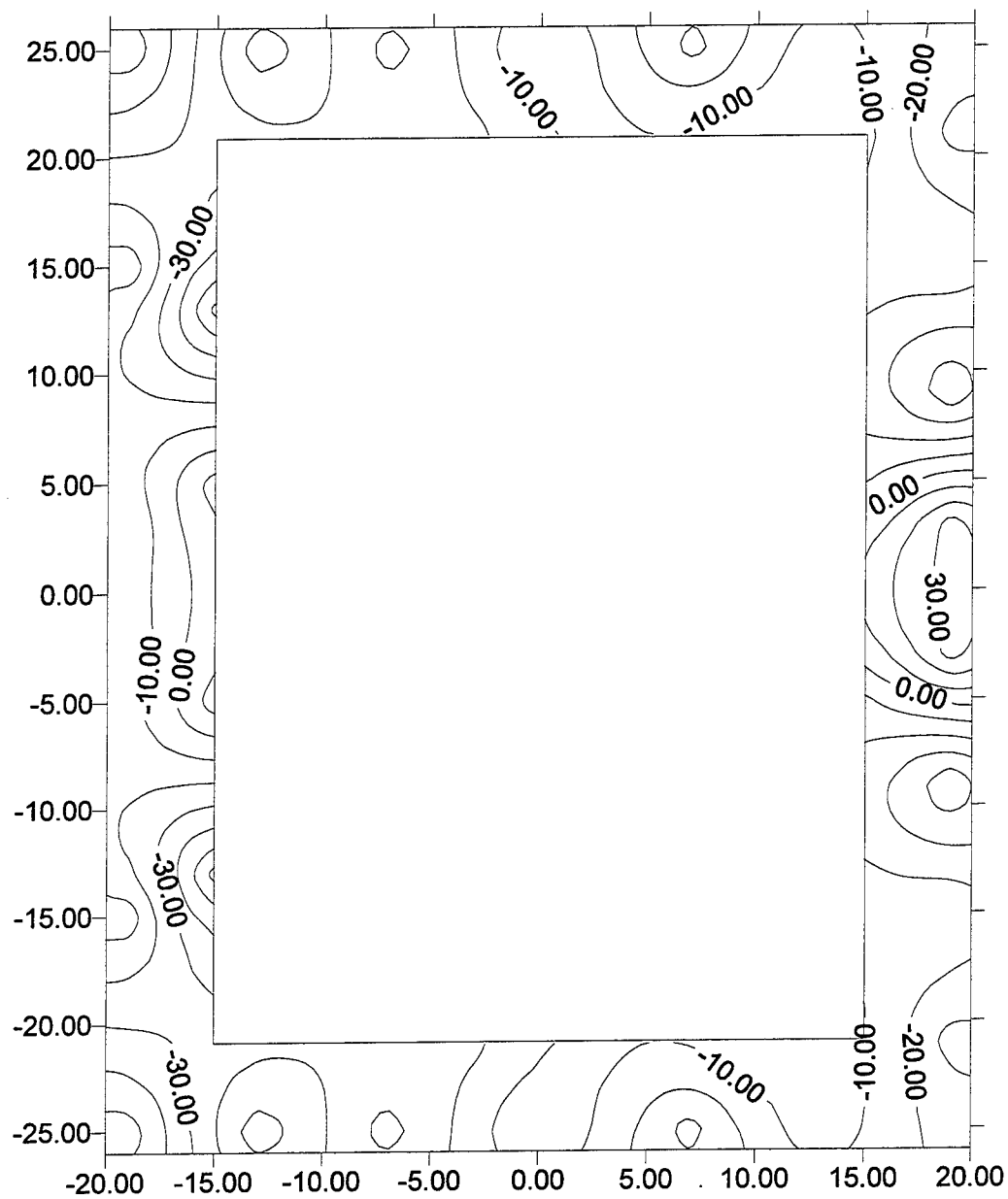


Figure C26. ITS-3 base strains, imposed deflection 0.0 in., cumulative travel of 0.4 in., that is, the bottom of the second leg of the first load cycle.

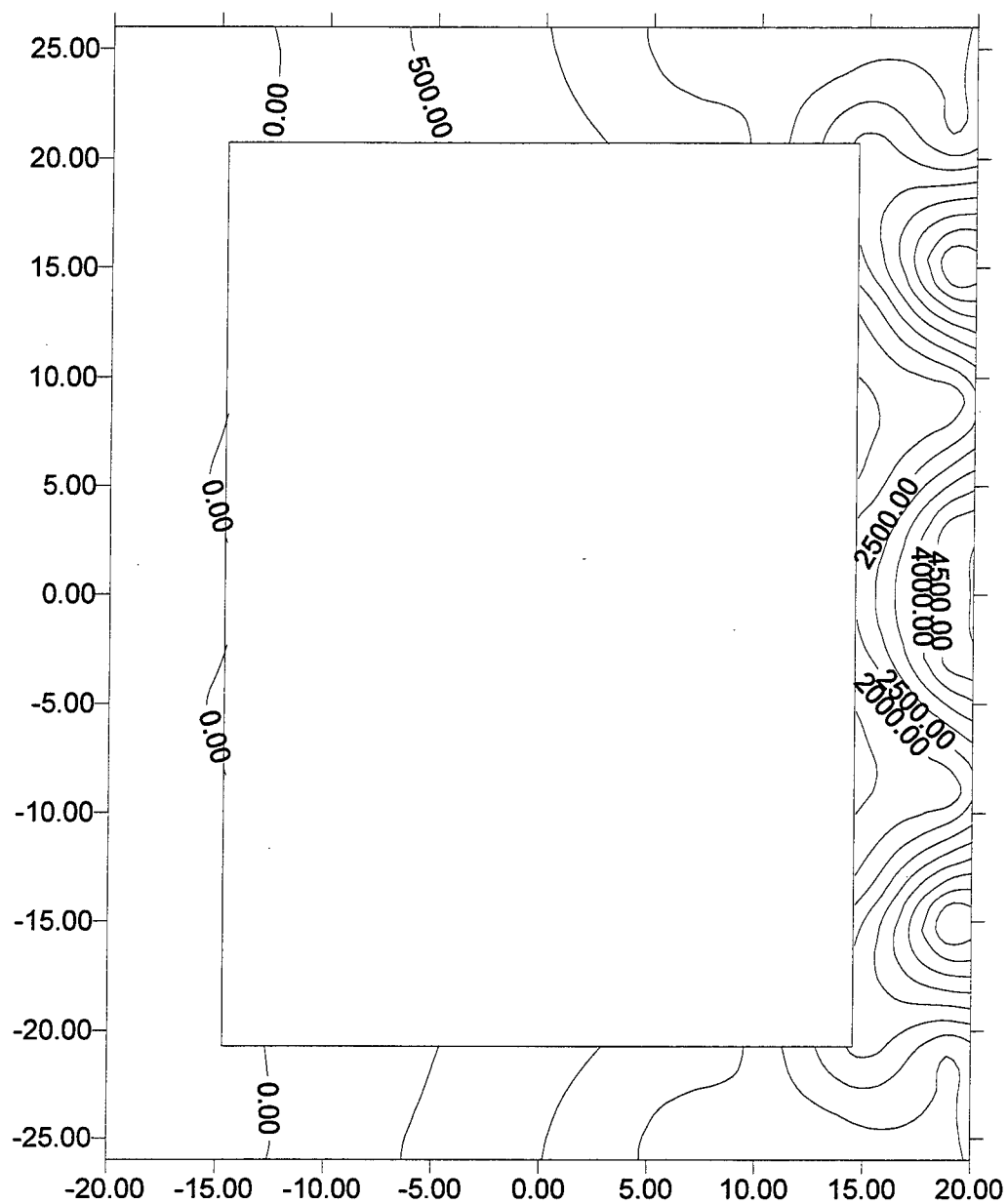


Figure C27. ITS-3 base strains, imposed deflection -0.2 in., cumulative travel of 0.6 in., that is, the top of the first leg of the second load cycle.

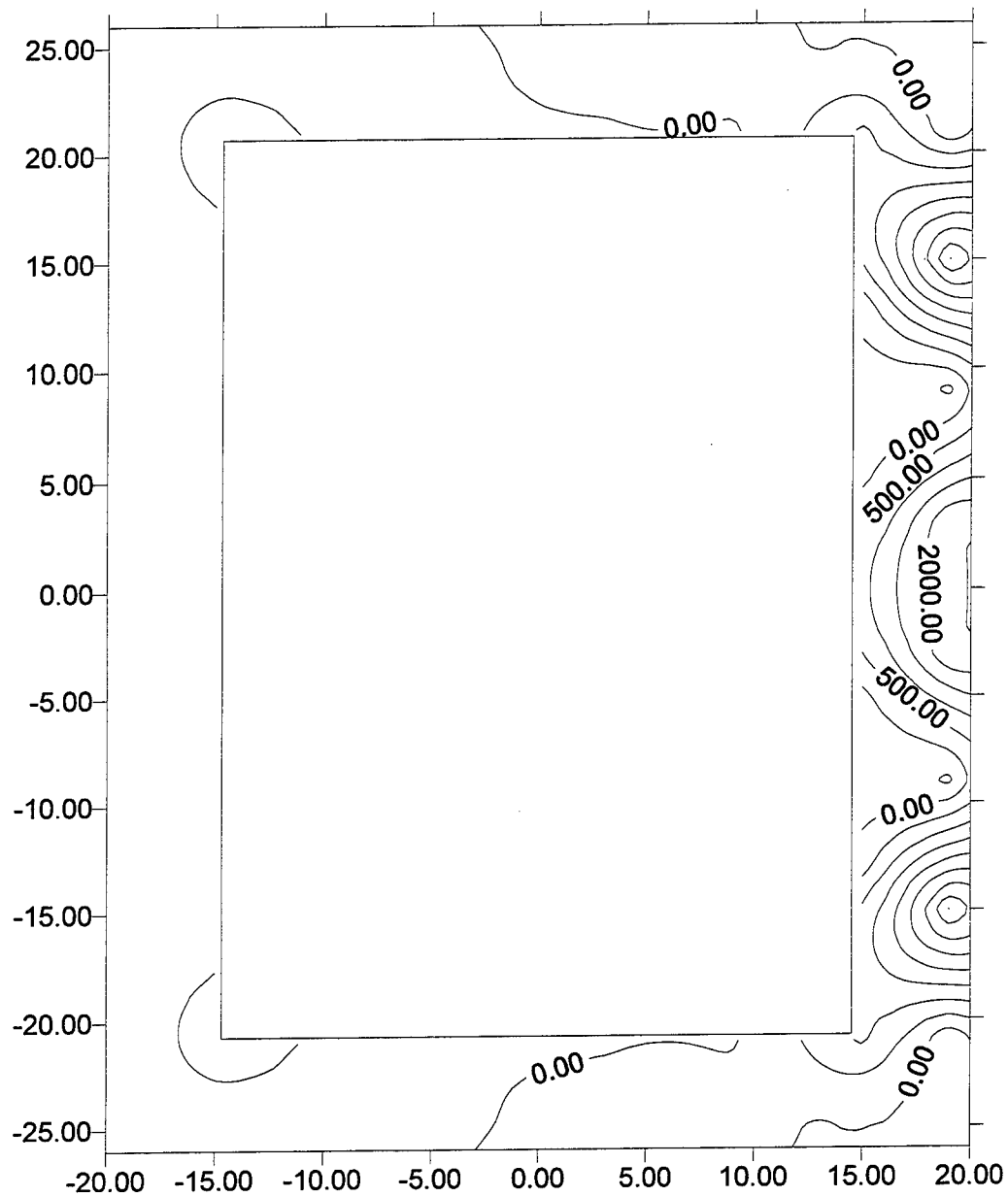


Figure C28. ITS-3 base strains, imposed deflection 0.0 in., cumulative travel of 0.8 in., that is, the bottom of the first leg of the second load cycle.

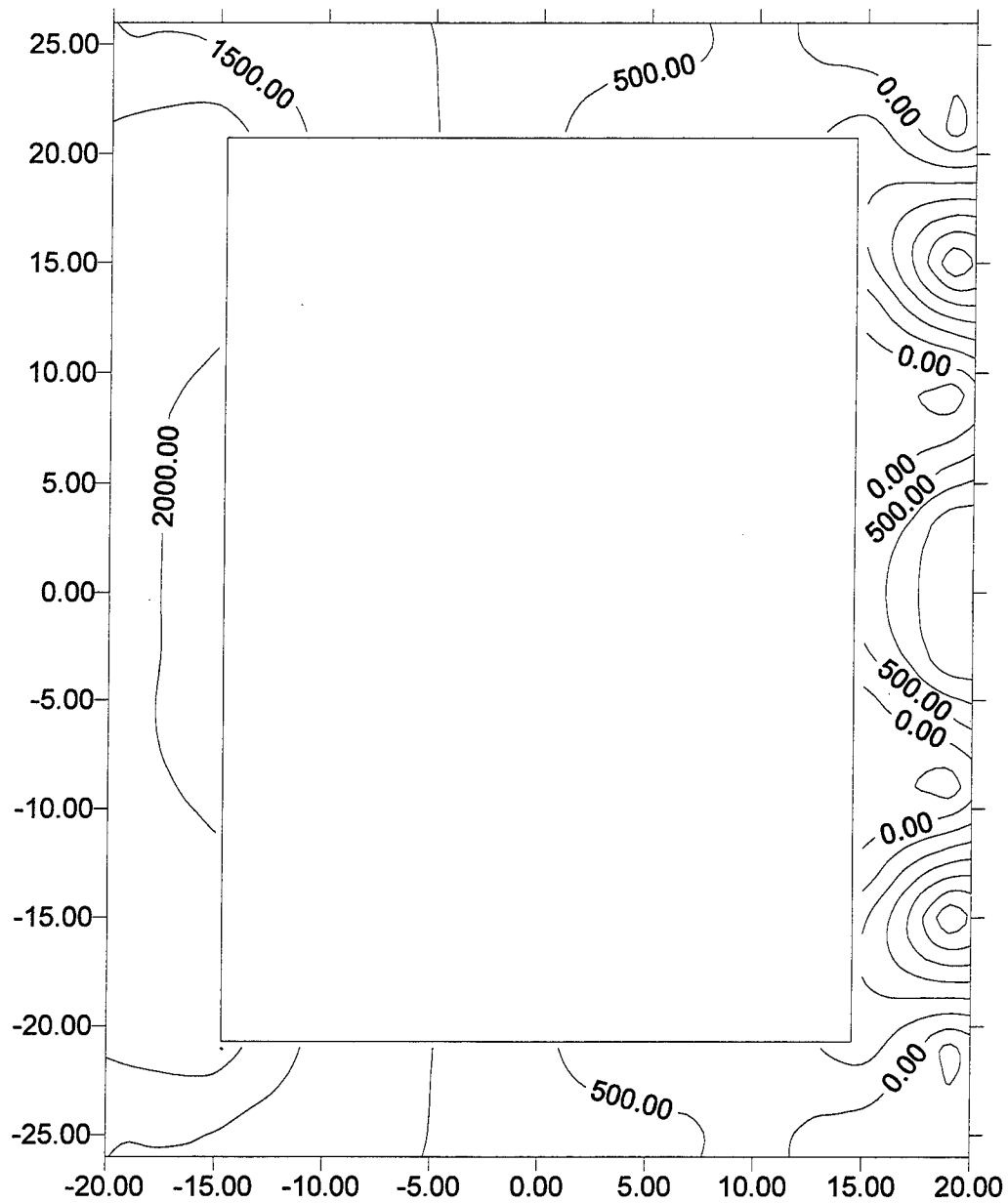


Figure C29. ITS-3 base strains, imposed deflection 0.2 in., cumulative travel of 1.0 in., that is, the top of the second leg of the second load cycle.

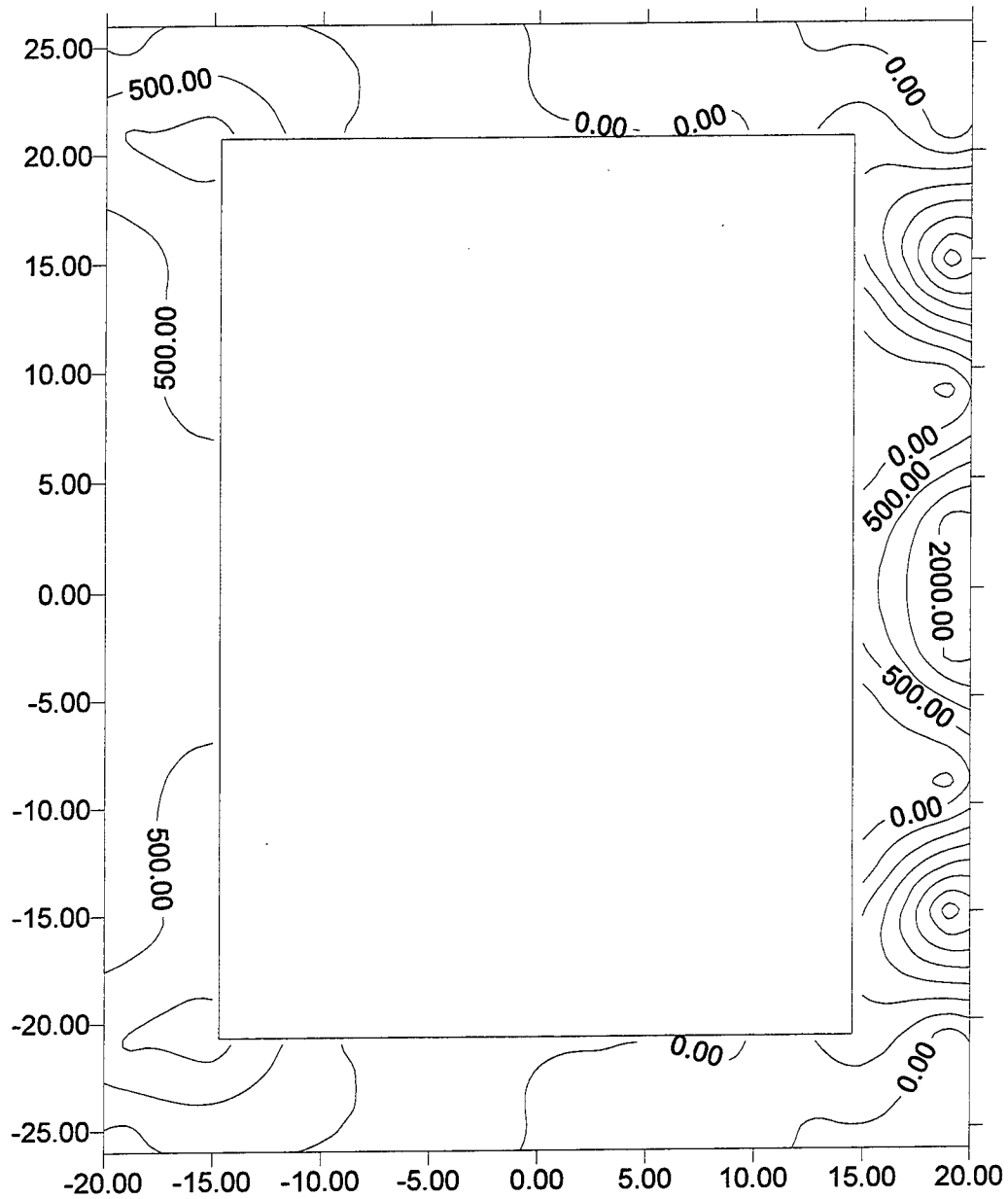


Figure C30 ITS-3 base strains, imposed deflection 0.0 in., cumulative travel of 1.2 in., that is, the bottom of the second leg of the second load cycle.

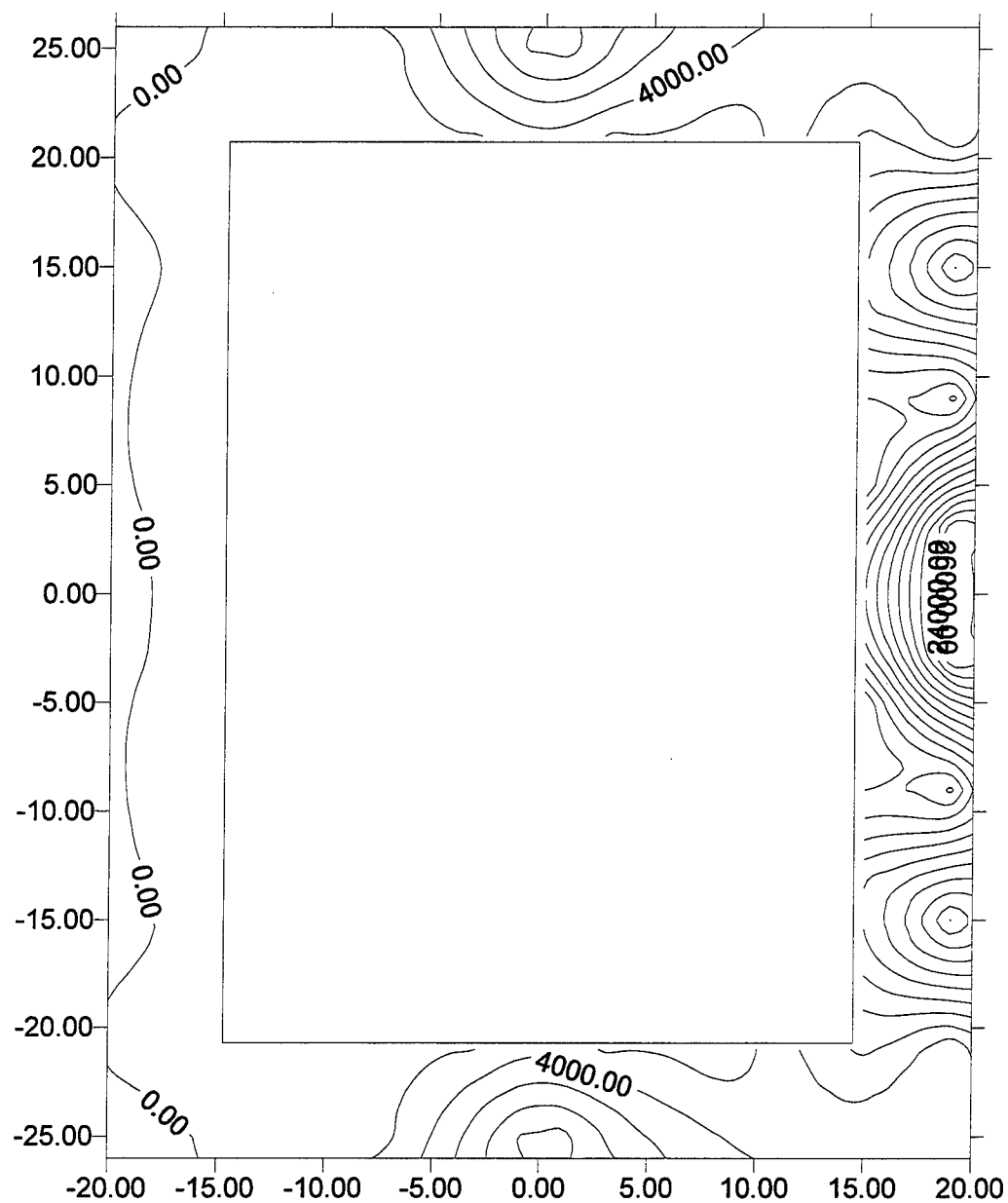


Figure C31. ITS-3 base strains, imposed deflection -0.3 in., cumulative travel of 1.5 in., that is, the top of the first leg of the third load cycle.

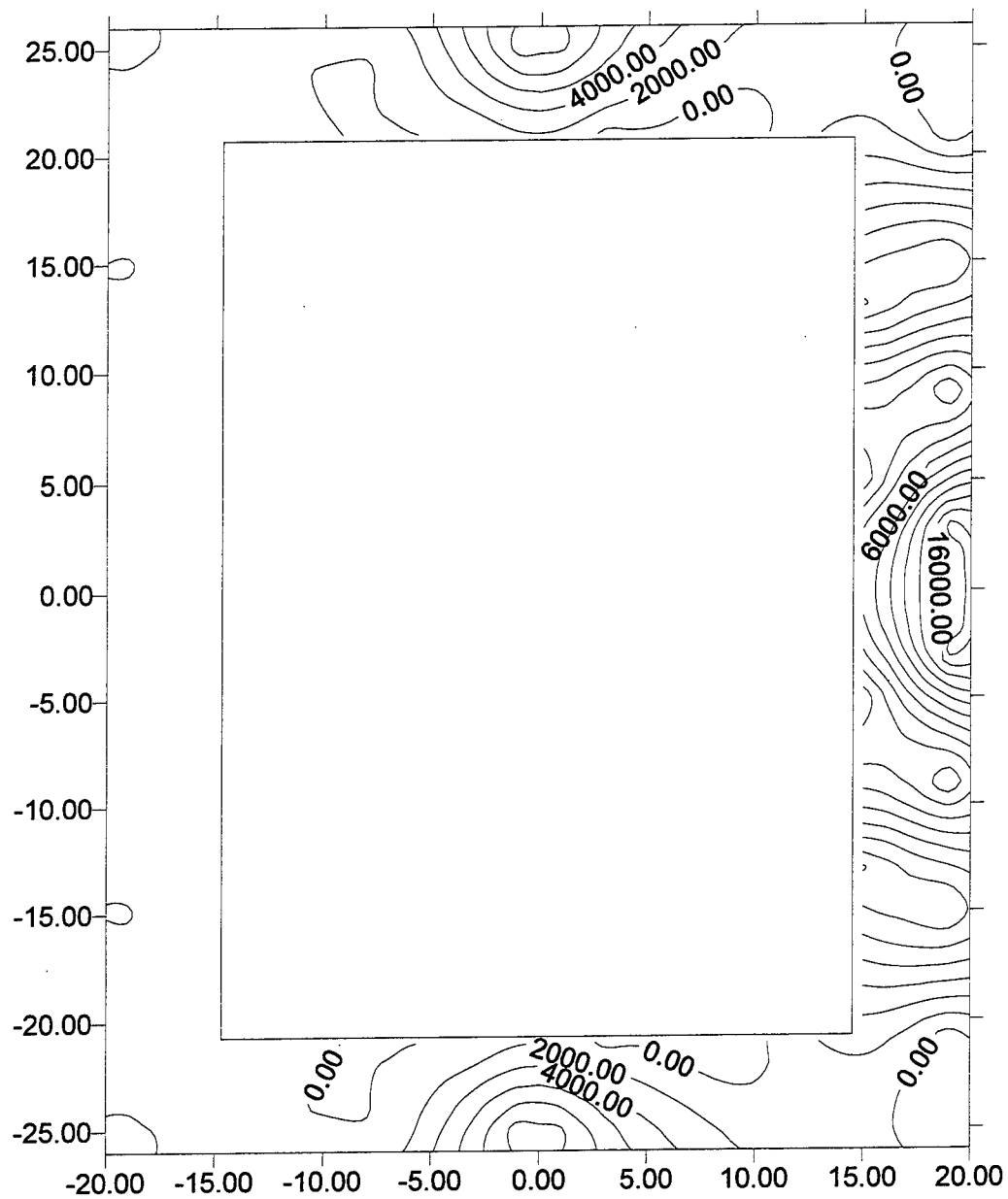


Figure C32. ITS-3 base strains, imposed deflection 0.0 in., cumulative travel of 1.8 in., that is, the bottom of the first leg of the third load cycle.

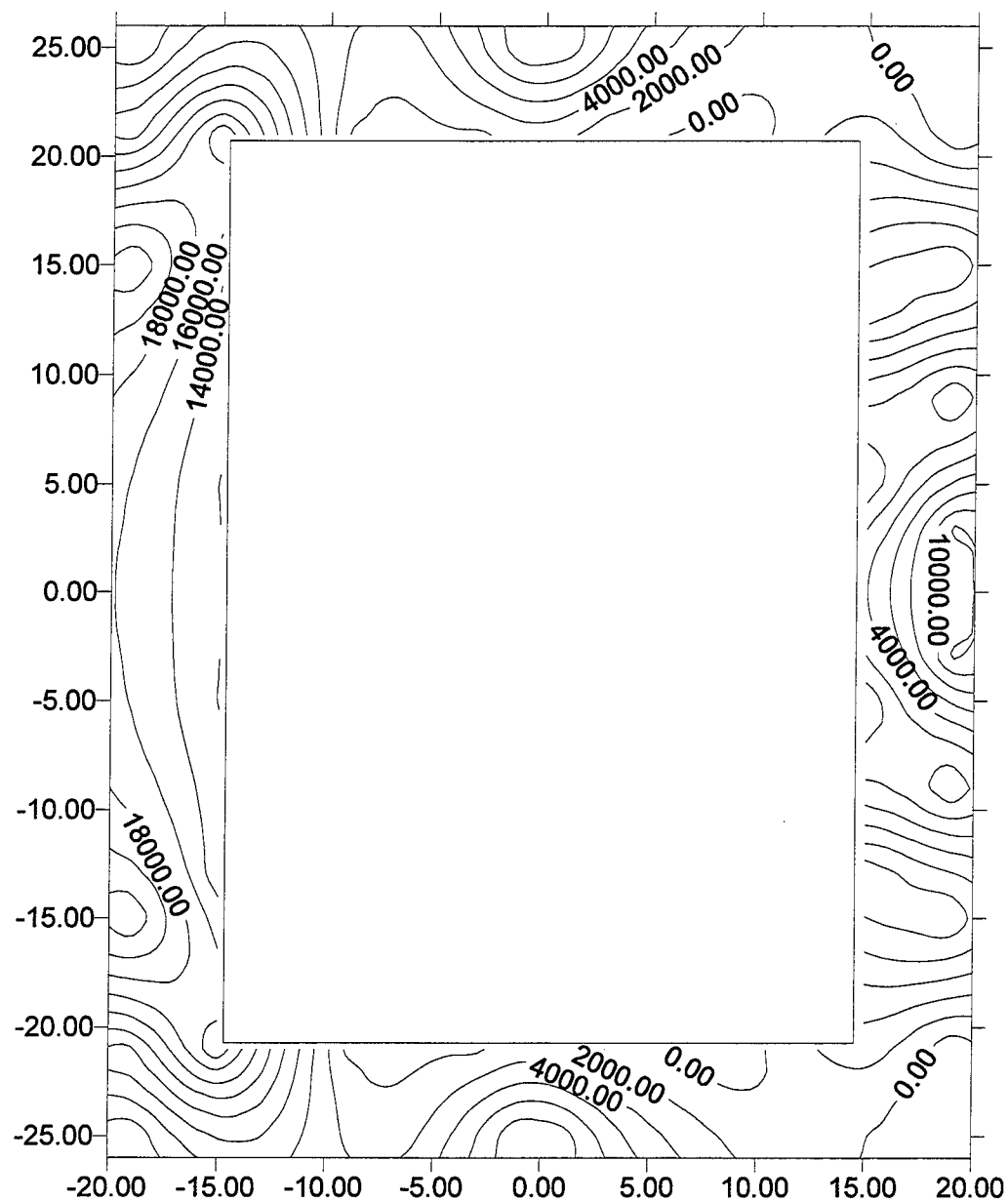


Figure C33. ITS-3 base strains, imposed deflection 0.3 in., cumulative travel of 2.1 in., that is, the top of the second leg of the third load cycle.

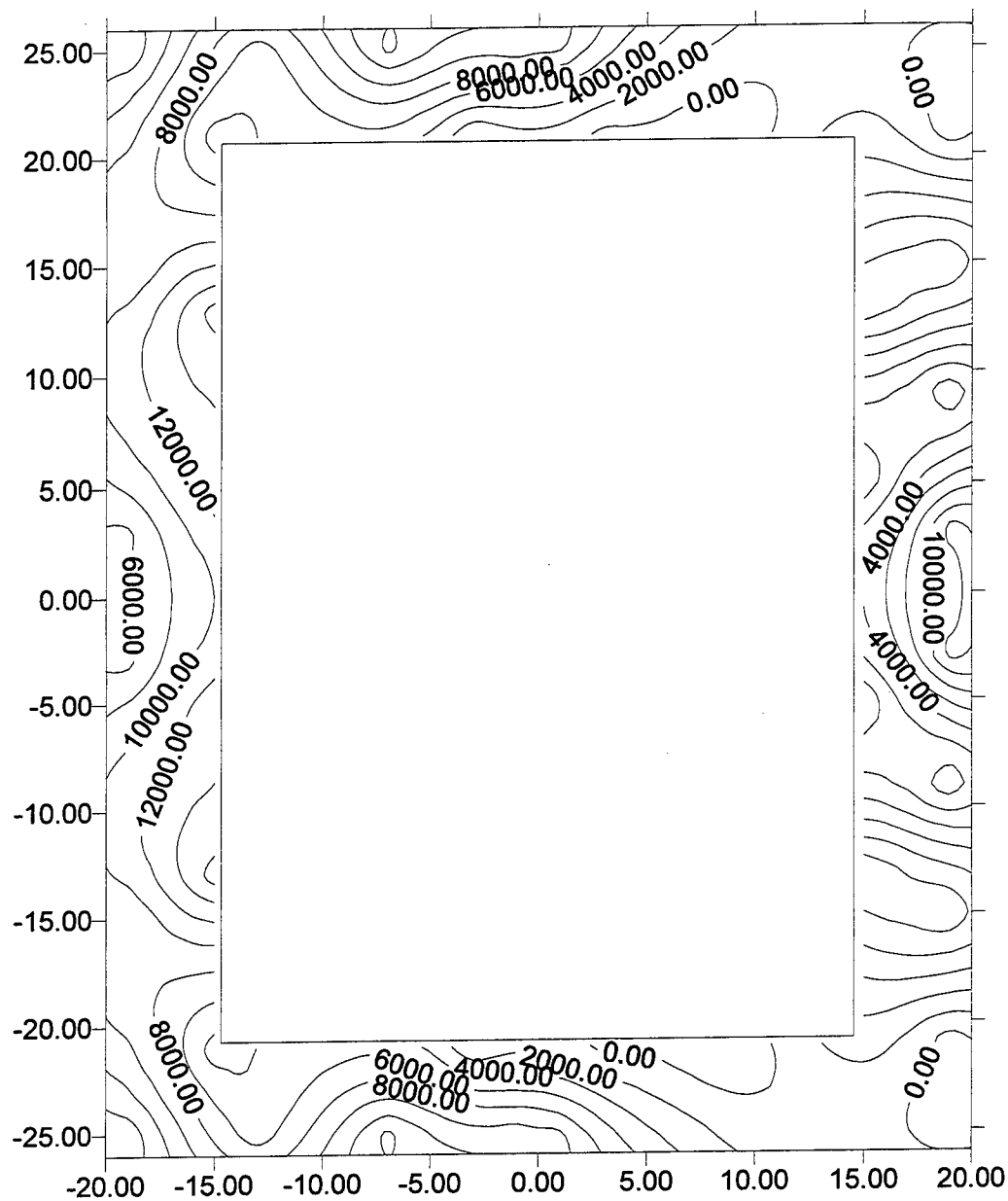


Figure C34. ITS-3 base strains, imposed deflection 0.0 in., cumulative travel of 2.4 in., that is, the bottom of the second leg of the third load cycle.

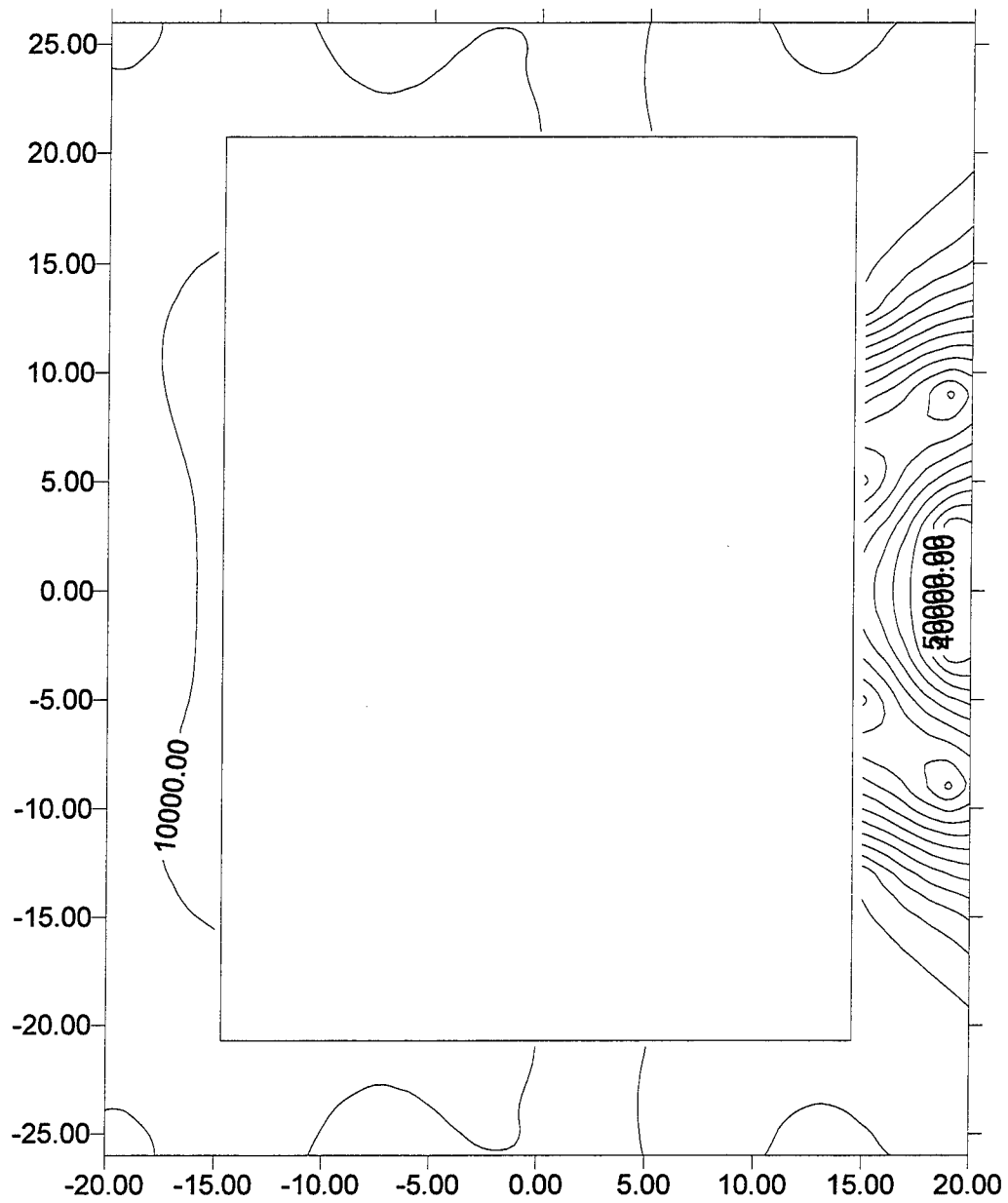


Figure C35. ITS-3 base strains, imposed deflection -0.4 in., cumulative travel of 2.8 in., that is, the top of the first leg of the fourth load cycle.

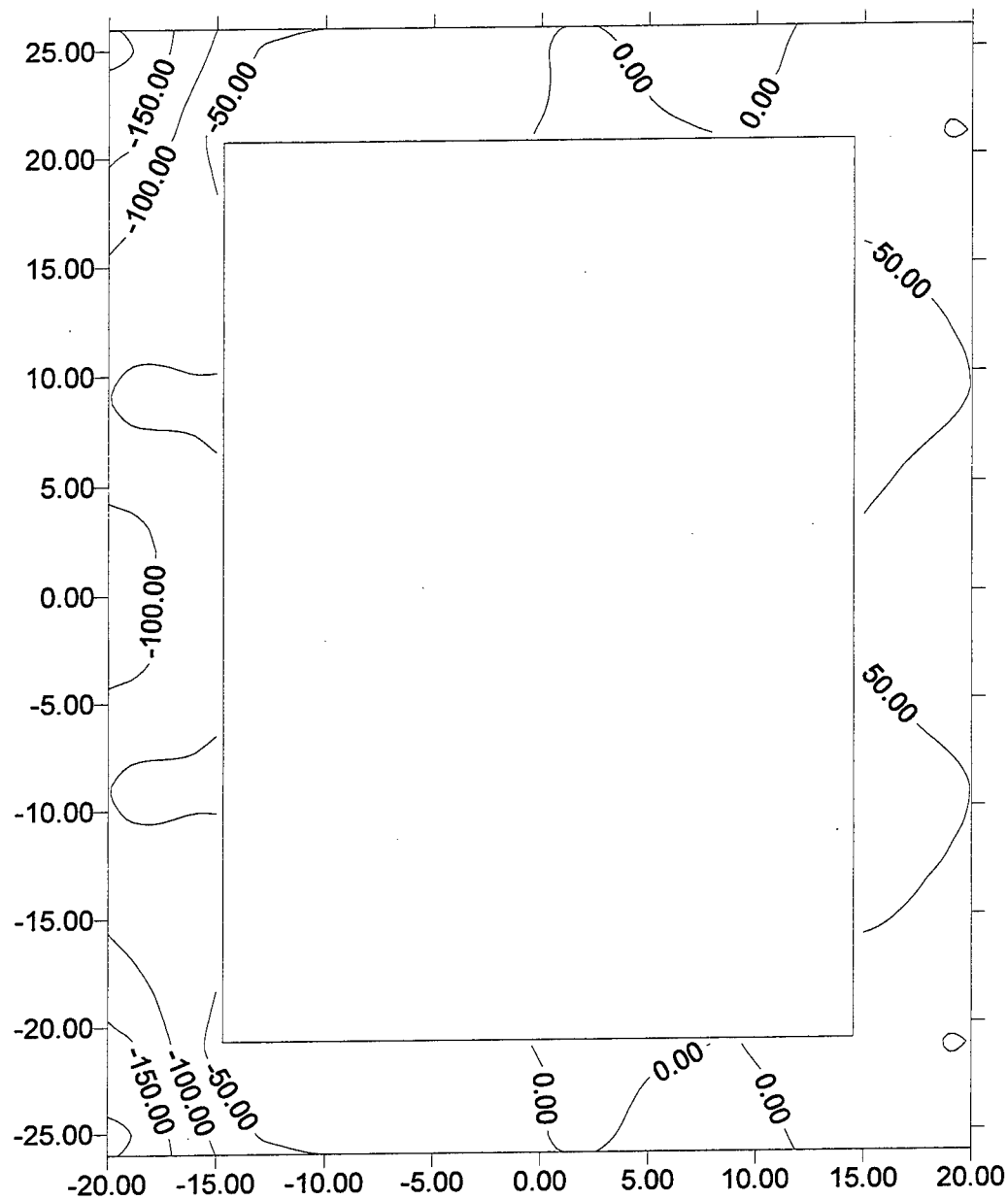


Figure C36. ITS-3 strains at 2 in. elevation, imposed deflection -0.1 in., cumulative travel of 0.1 in., that is, the top of the first leg of the first load cycle.

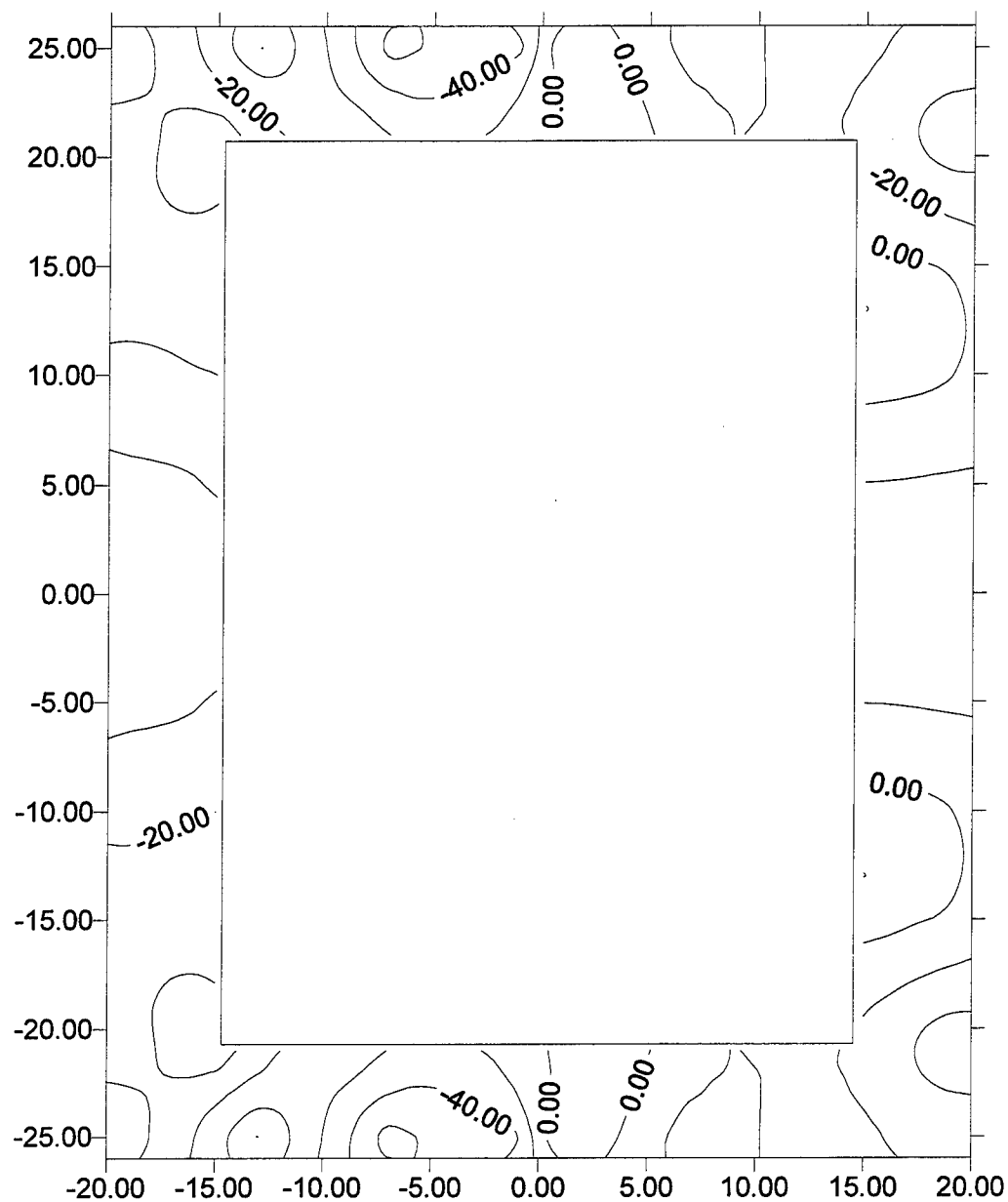


Figure C37. ITS-3 strains at 2 in. elevation, imposed deflection 0.0 in., cumulative travel of 0.2 in., that is, the bottom of the first leg of the first load cycle.

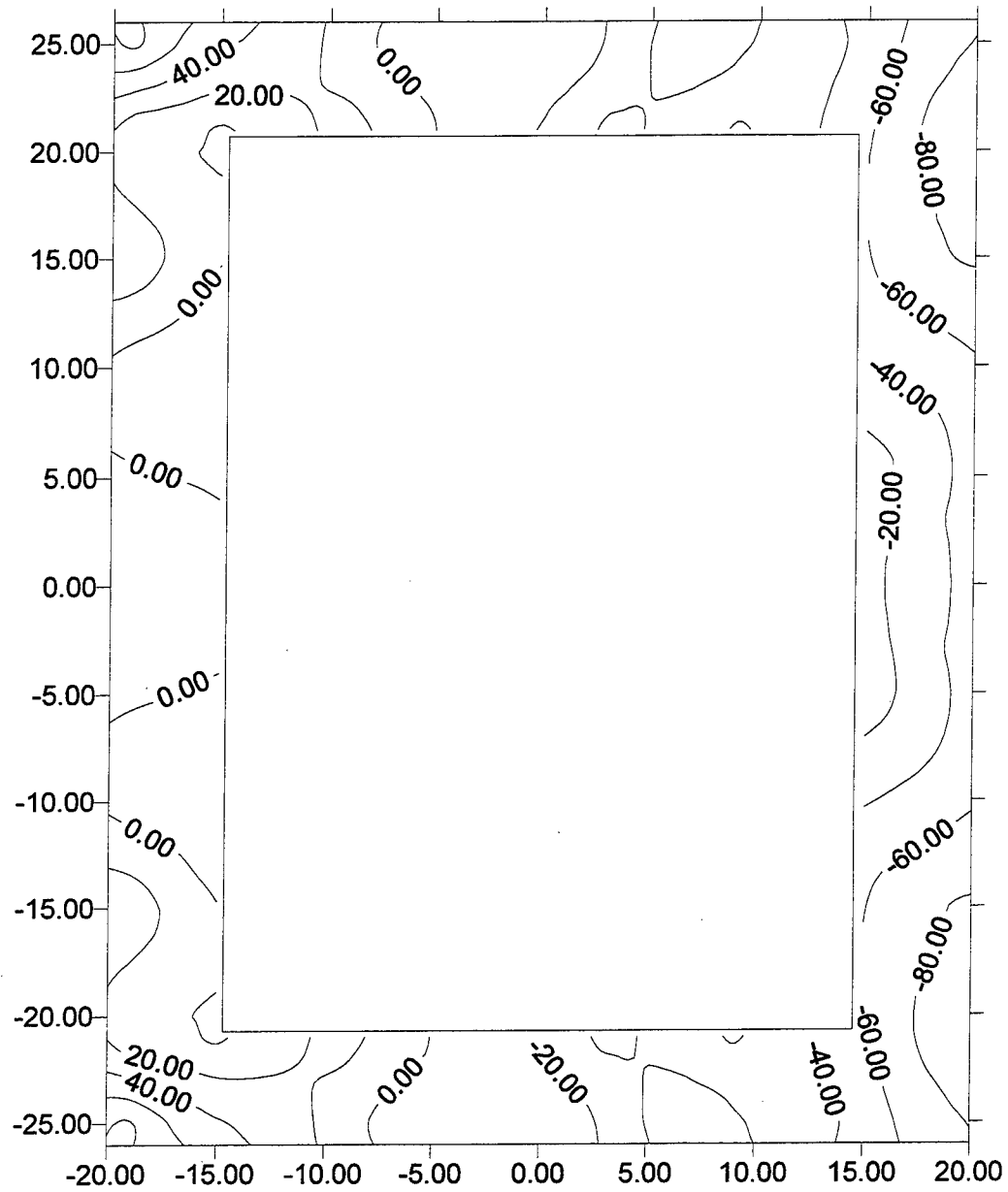


Figure C38. ITS-3 strains at 2 in. elevation, imposed deflection 0.1 in., cumulative travel of 0.3 in., that is, the top of the second leg of the first load cycle.

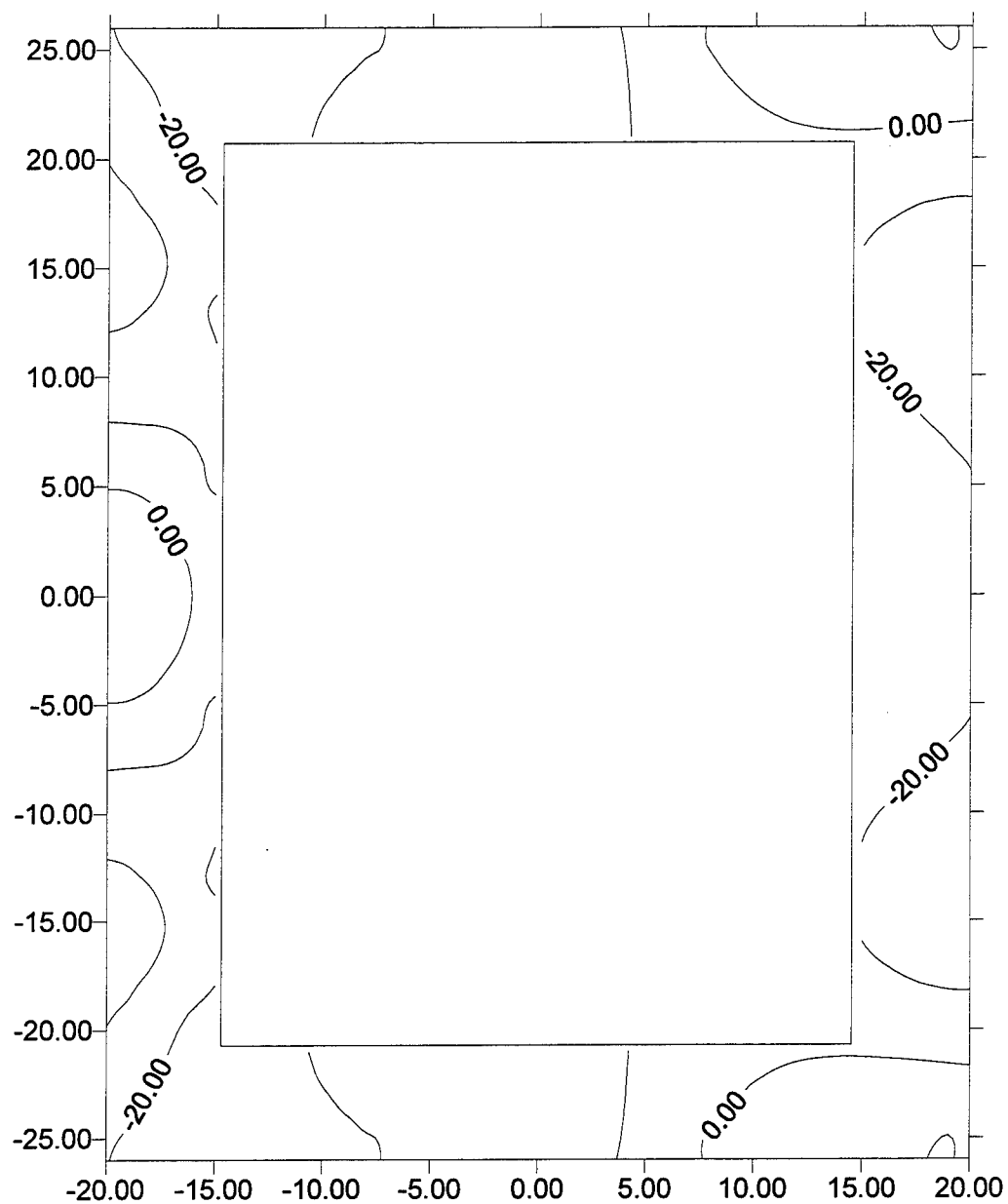


Figure C39. ITS-3 strains at 2 in. elevation, imposed deflection 0.0 in., cumulative travel of 0.4 in., that is, the bottom of the second leg of the first load cycle.

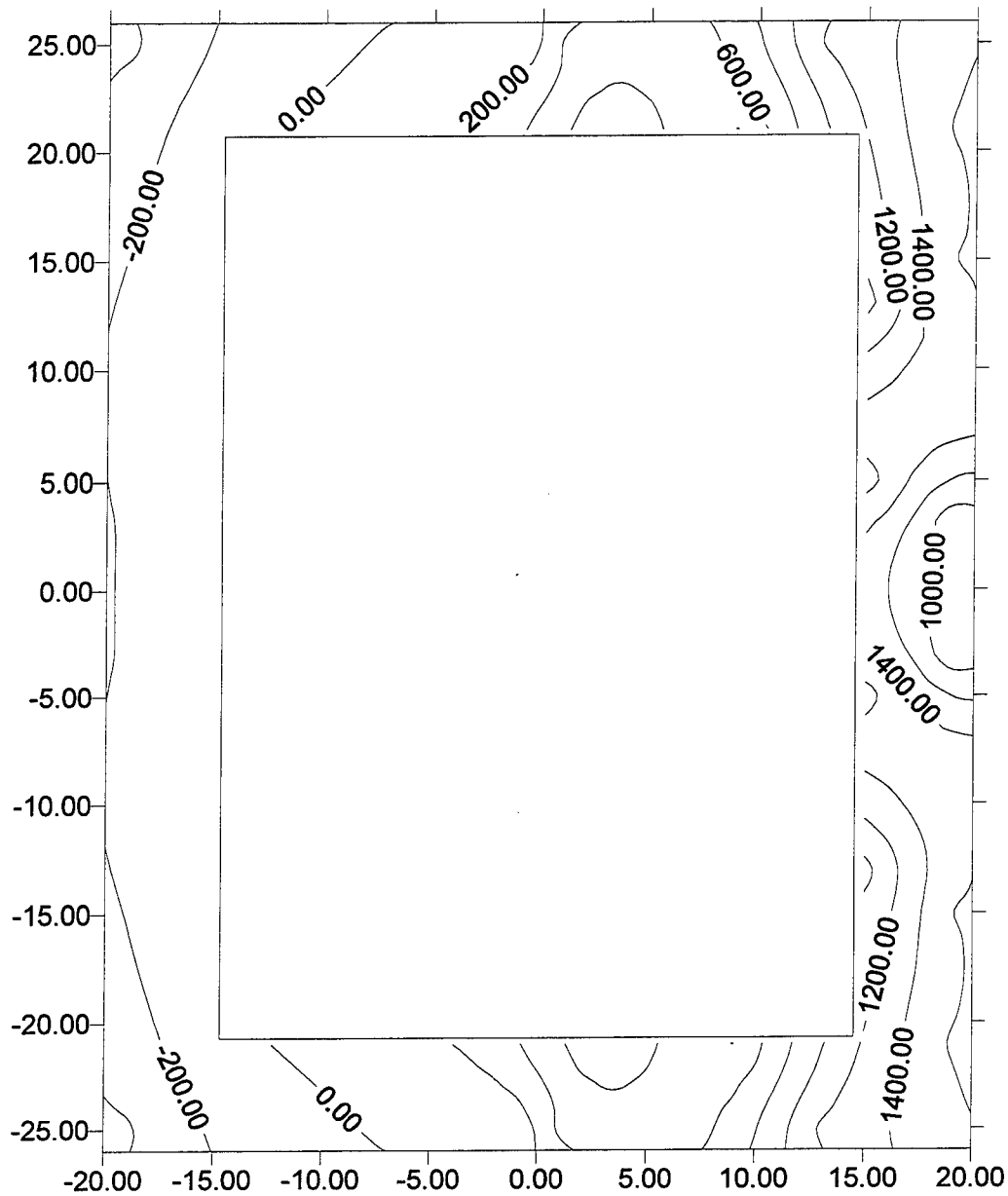


Figure C40. ITS-3 strains at 2 in. elevation, imposed deflection -0.2 in., cumulative travel of 0.6 in., that is, the top of the first leg of the second load cycle.

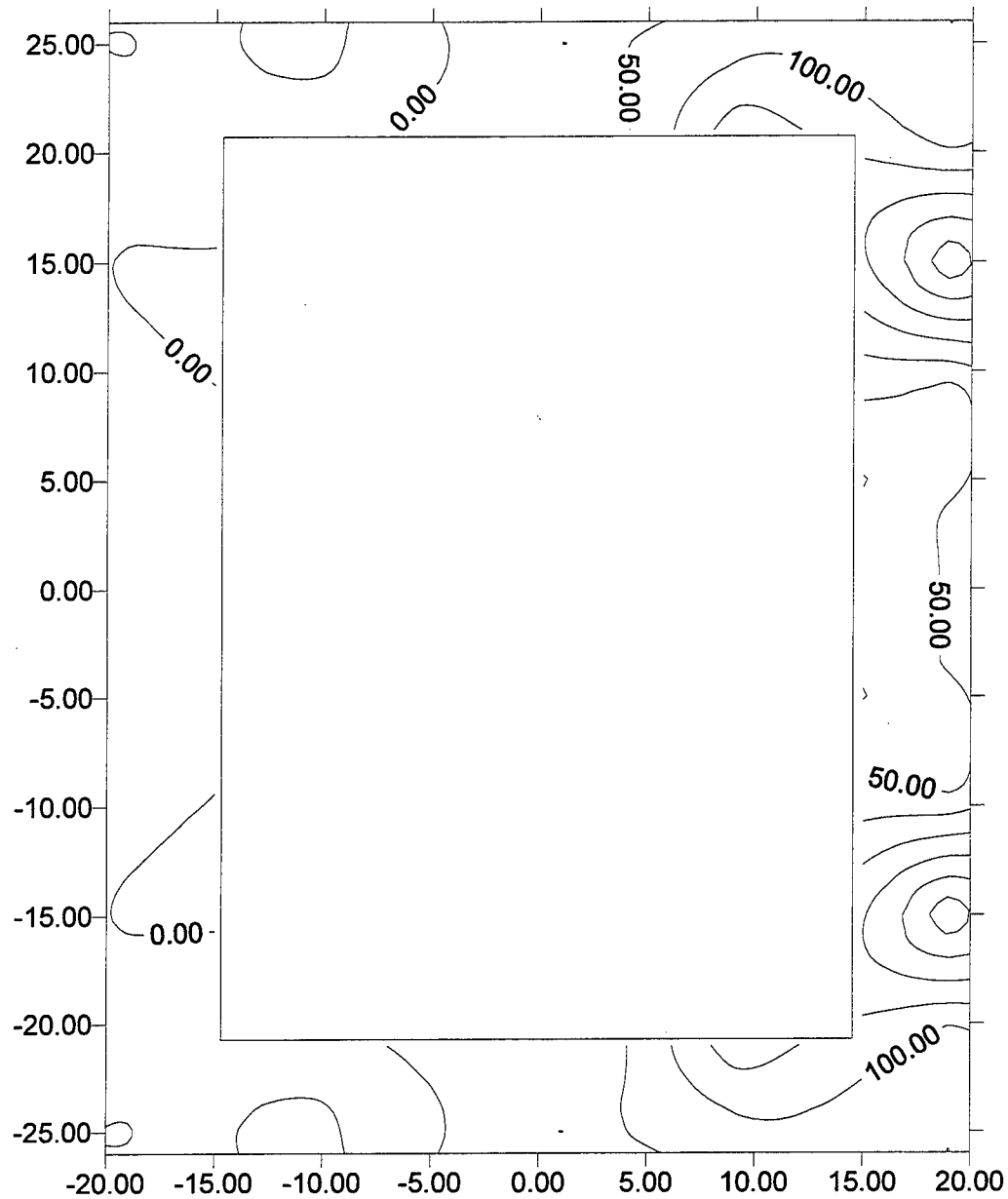


Figure C41. ITS-3 strains at 2 in. elevation, imposed deflection 0.0 in., cumulative travel of 0.8 in., that is, the bottom of the first leg of the second load cycle.

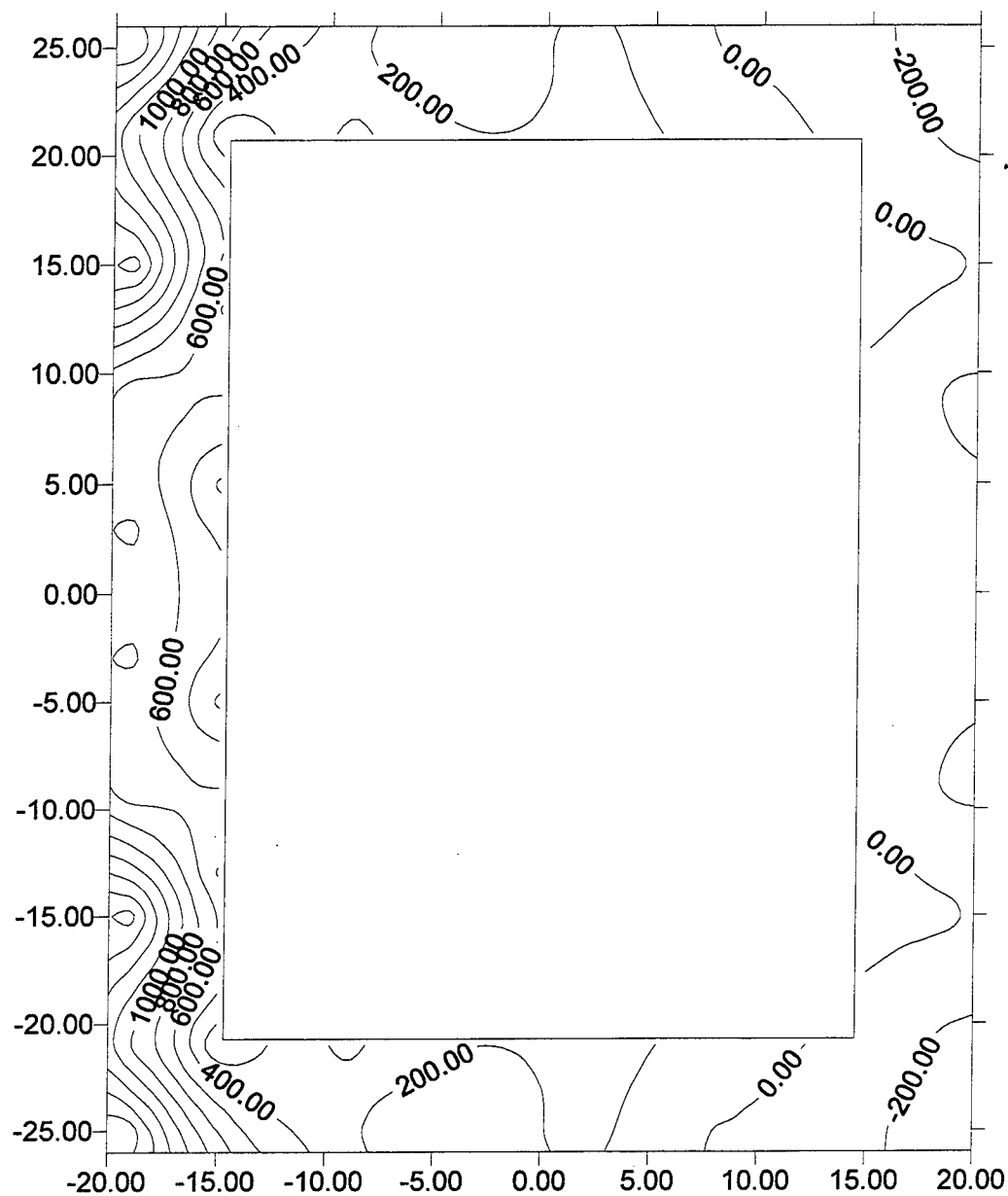


Figure C42. ITS-3 strains at 2 in. elevation, imposed deflection 0.2 in., cumulative travel of 1.0 in., that is, the top of the second leg of the second load cycle.

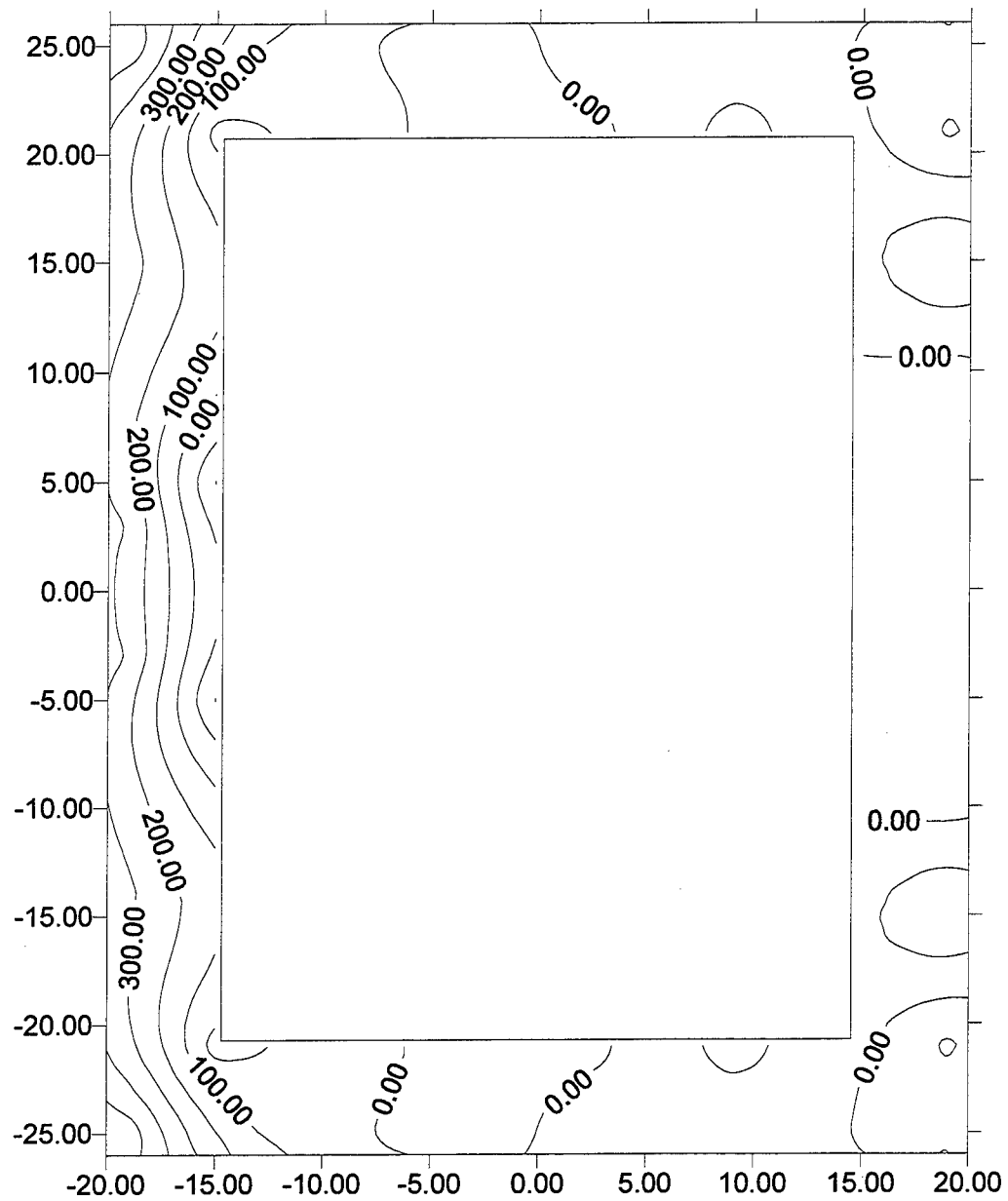


Figure C43. ITS-3 strains at 2 in. elevation, imposed deflection 0.0 in., cumulative travel of 1.2 in., that is, the bottom of the second leg of the second load cycle.

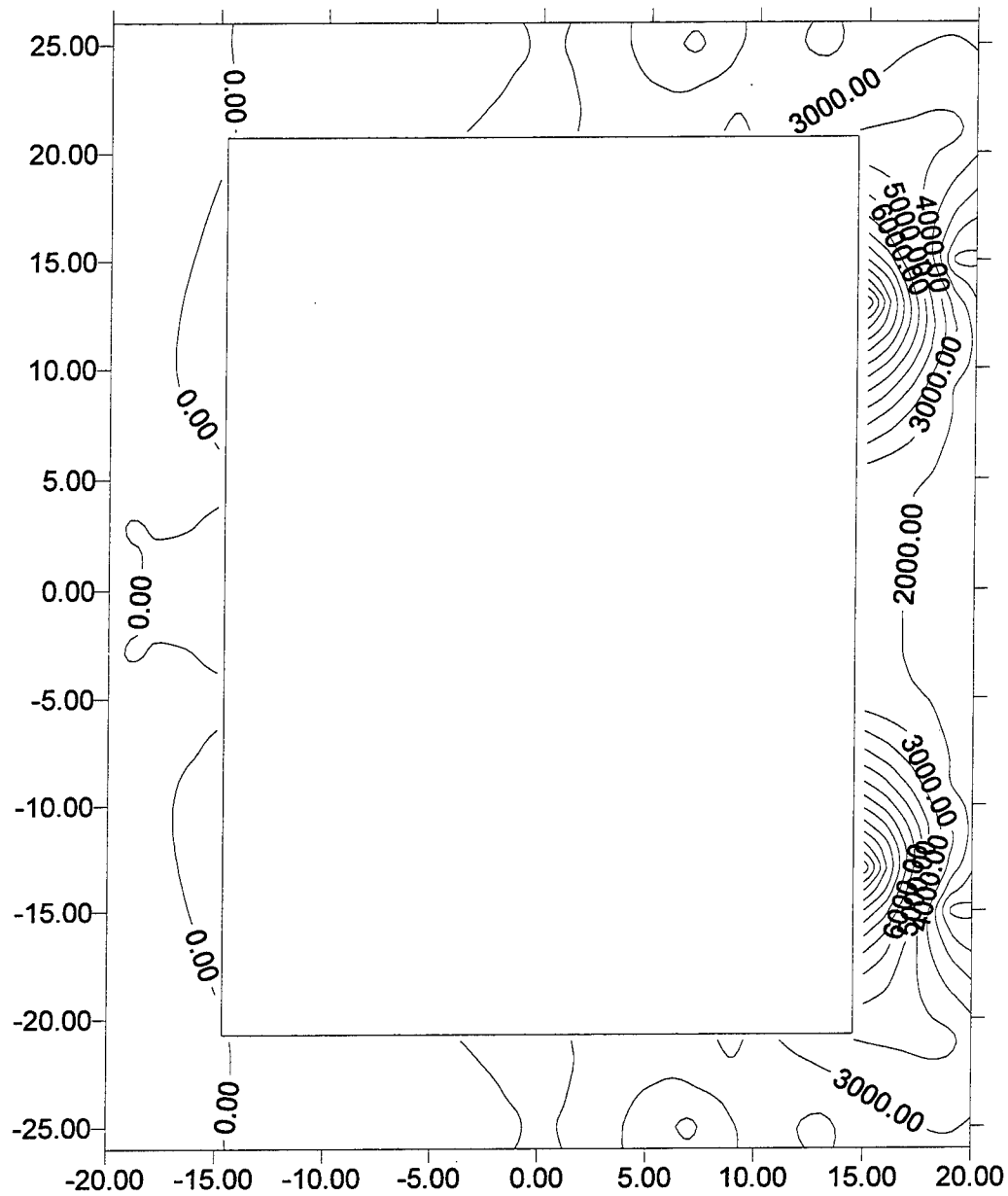


Figure C44. ITS-3 strains at 2 in. elevation, imposed deflection -0.3 in., cumulative travel of 1.5 in., that is, the top of the first leg of the third load cycle.

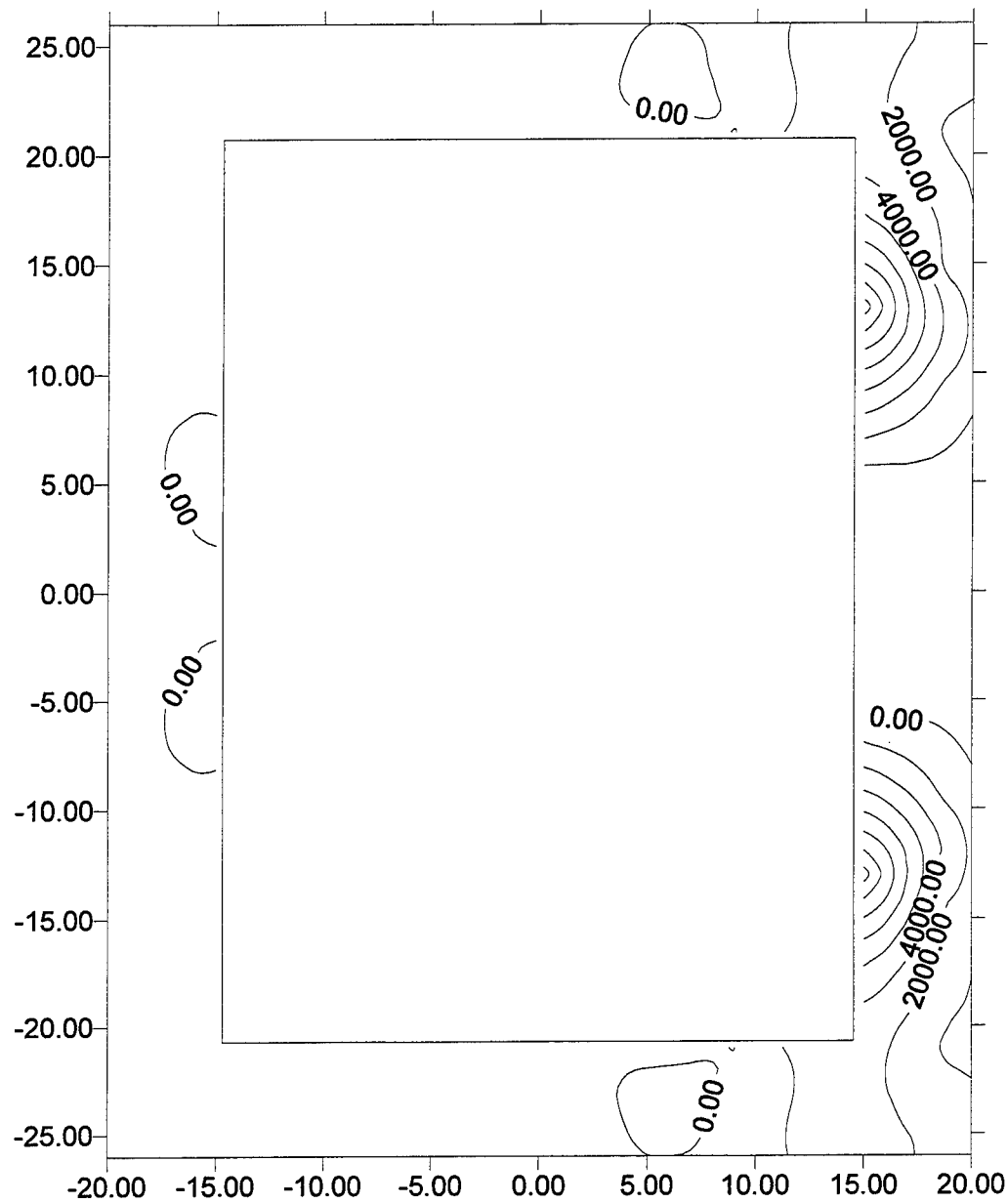


Figure C45. ITS-3 strains at 2 in. elevation, imposed deflection 0.0 in., cumulative travel of 1.8 in., that is, the bottom of the first leg of the third load cycle.

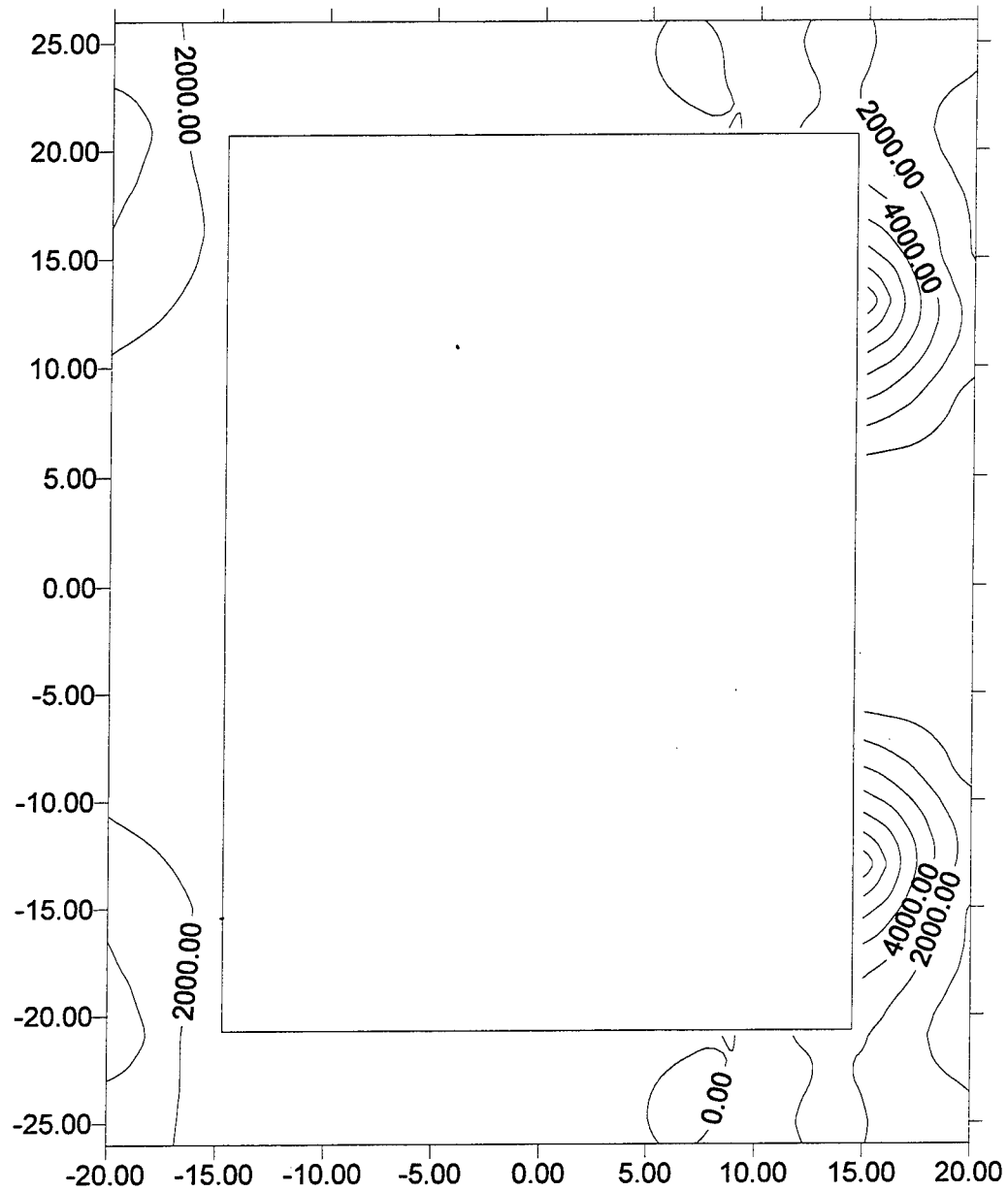


Figure C46. ITS-3 strains at 2 in. elevation, imposed deflection 0.3 in., cumulative travel of 2.1 in., that is, the top of the second leg of the third load cycle.

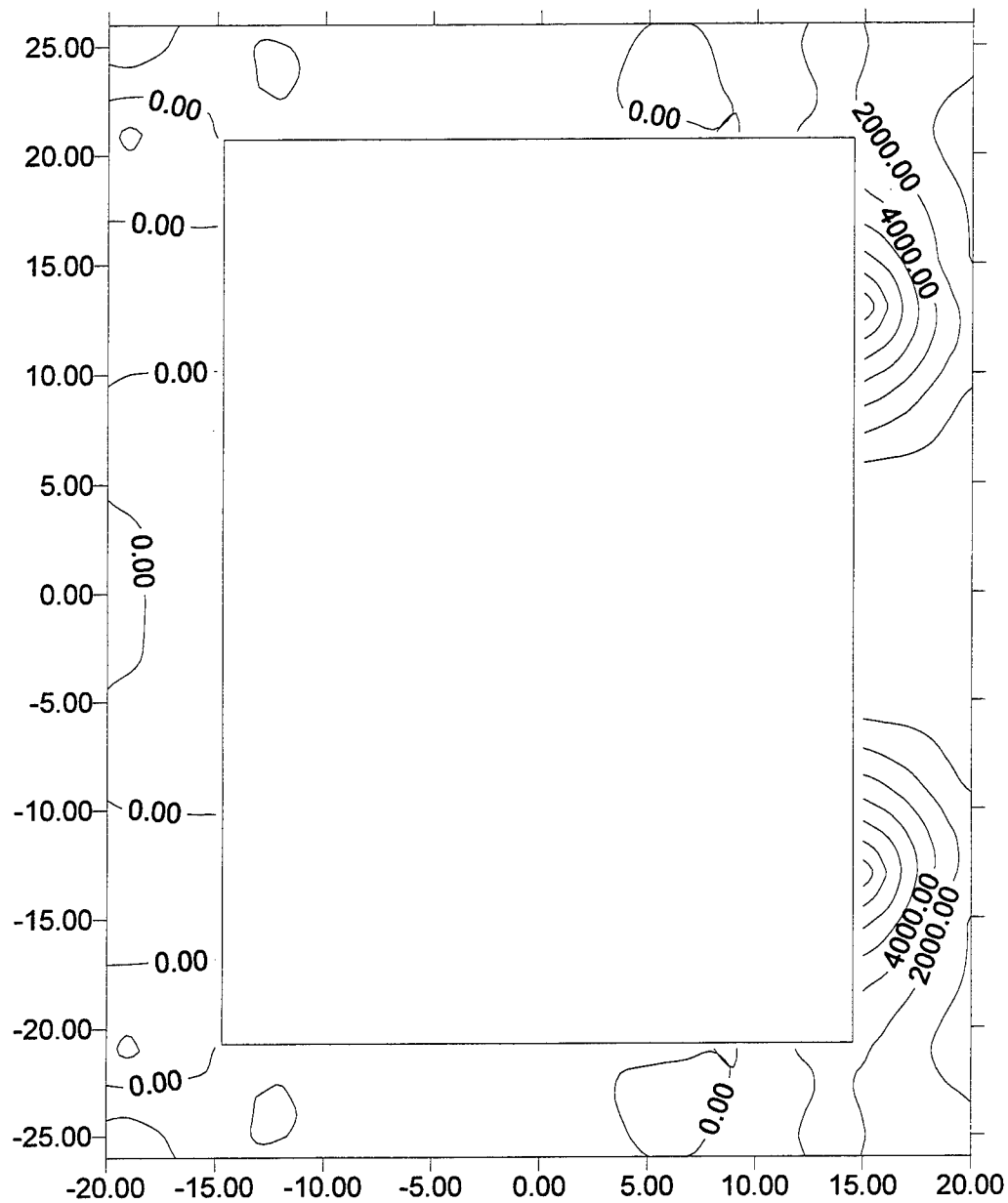


Figure C47. ITS-3 strains at 2 in. elevation, imposed deflection 0.0 in., cumulative travel of 2.4 in., that is, the bottom of the second leg of the third load cycle.

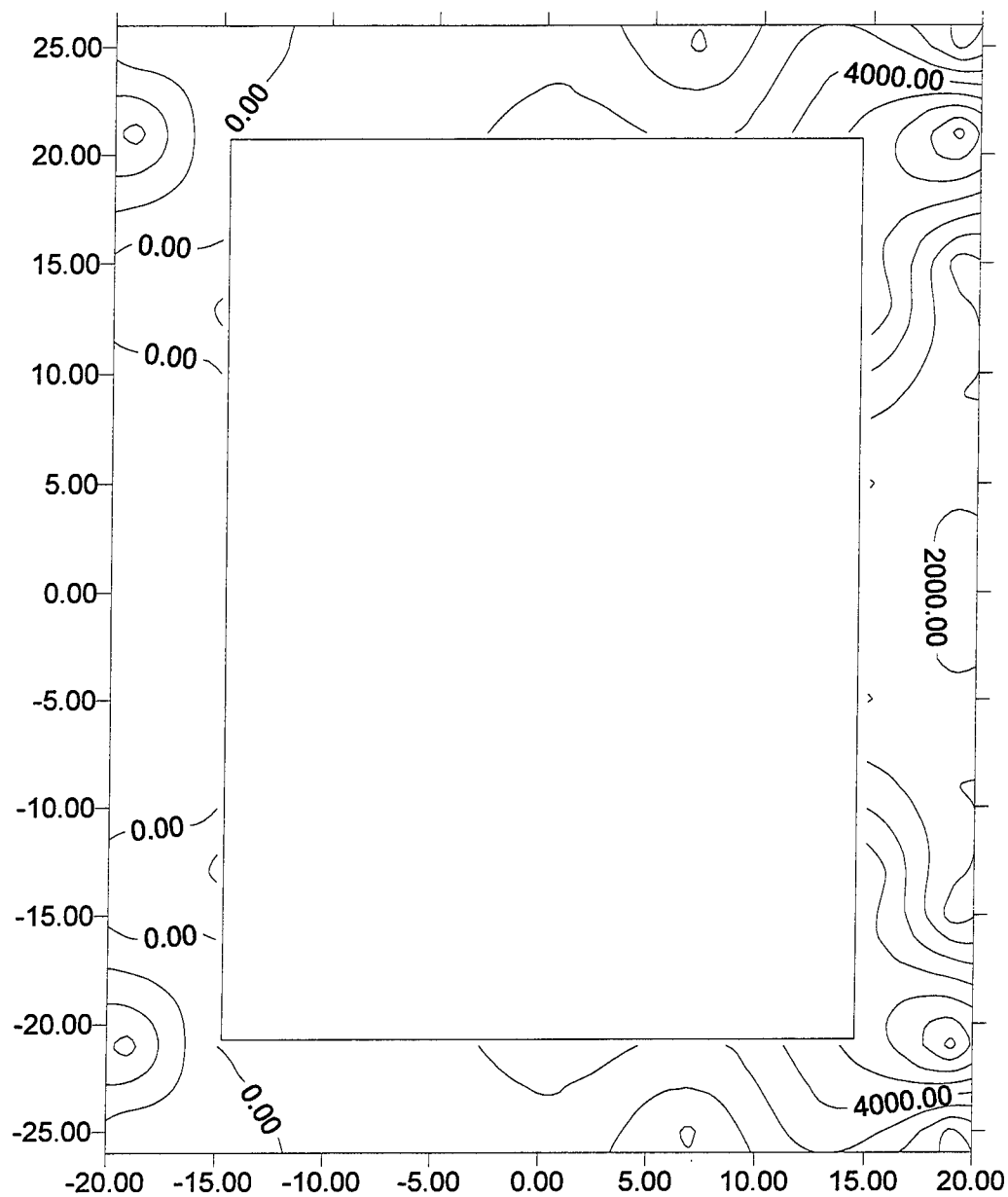


Figure C48. ITS-3 strains at 2 in. elevation, imposed deflection -0.4 in., cumulative travel of 2.8 in., that is, the top of the first leg of the fourth load cycle.

APPENDIX D
MODE SHAPES

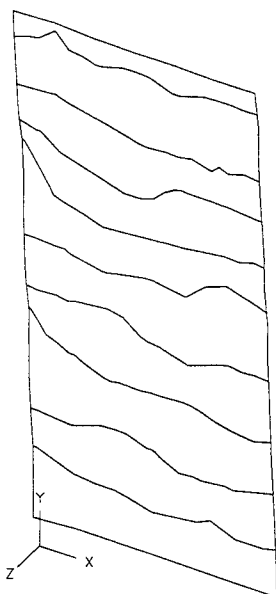


Figure D1. ITS-2 pre-experiment first bending mode at 44 Hz.

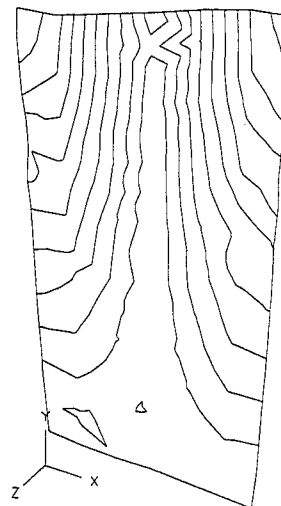


Figure D3. ITS-2 pre-experiment higher order torsional mode at 157 Hz.



Figure D2. ITS-2 pre-experiment torsional mode at 121 Hz.

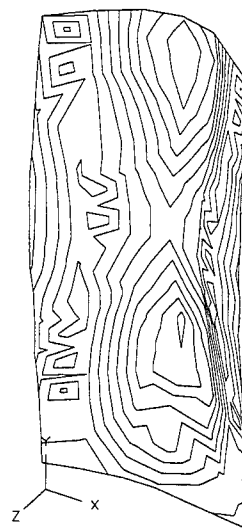


Figure D4. ITS-2 pre-experiment second bending mode at 457 Hz.

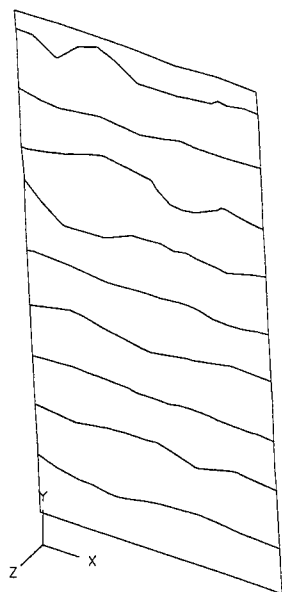


Figure D5. ITS-2 post-experiment first bending mode at 23 Hz.

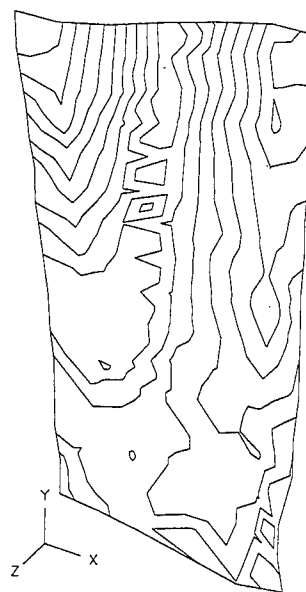


Figure D7. ITS-2 post-experiment higher order torsion mode at 157 Hz.

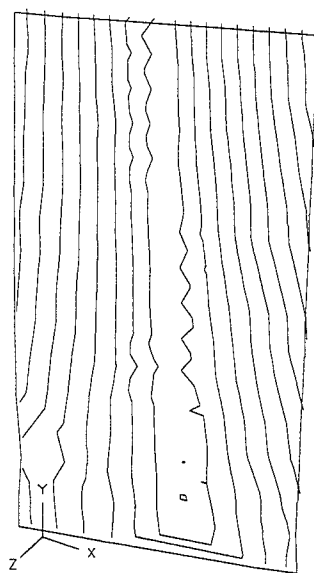


Figure D6. ITS-2 post-experiment torsion mode at 94 Hz.

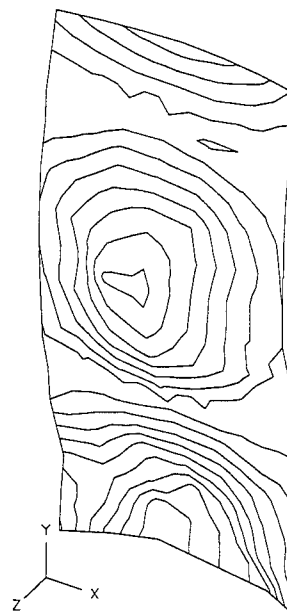


Figure D8. ITS-2 post-experiment second order bending mode at 340 Hz.



Figure D9. ITS-3 pre-experiment first bending mode at 51 Hz.

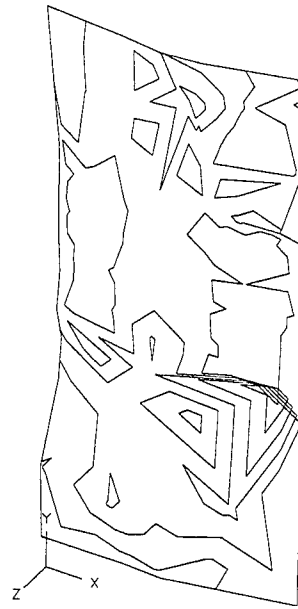


Figure D11. ITS-3 pre-experiment second bending mode at 440 Hz.

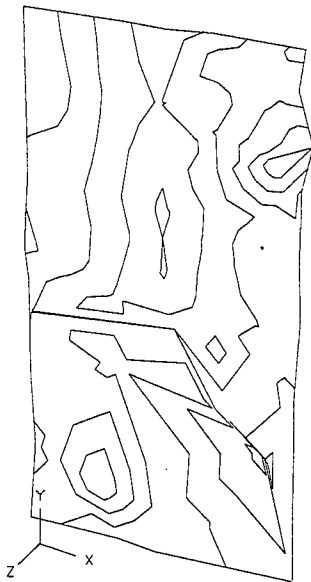


Figure D10. ITS-3 pre-experiment torsional mode at 143 Hz.

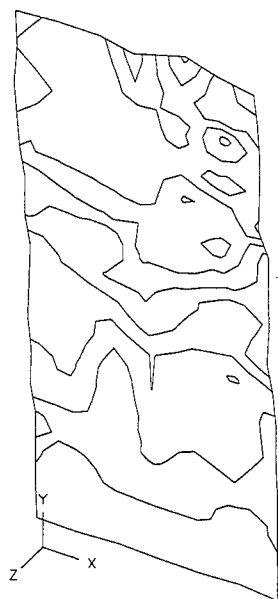


Figure D12. ITS-3 post-failure first bending mode at 23 Hz.

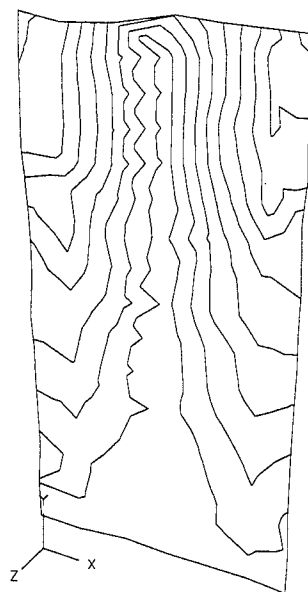


Figure D14. ITS-3 post-failure higher order torsional mode at 155 Hz.

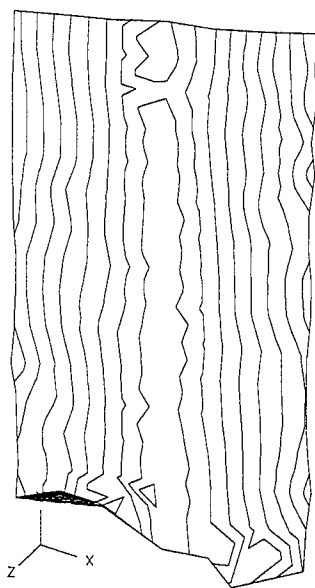


Figure D13. ITS-3 post-failure torsional mode at 45 Hz.



Figure D15. ITS-3 post-failure second bending mode at 426 Hz.

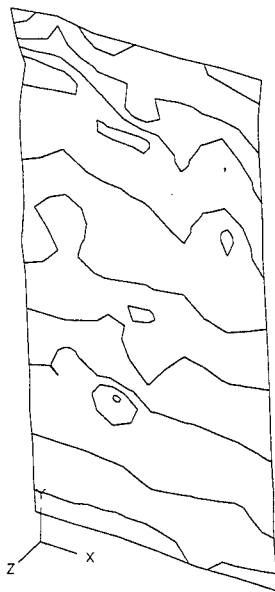


Figure D16. ITS-3 post-experiment first bending mode at 17 Hz.

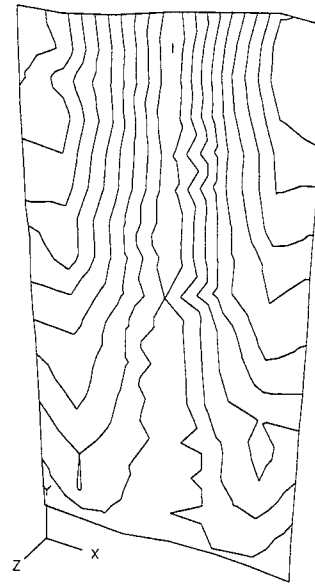


Figure D18. ITS-3 post-experiment higher order torsional mode at 152 Hz.

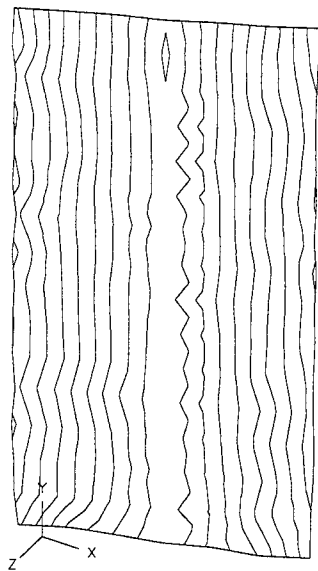


Figure D17. ITS-3 post-experiment torsional mode at 32 Hz.

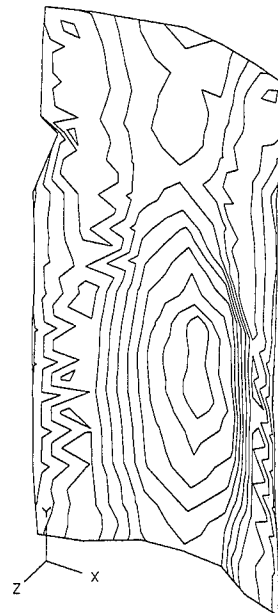


Figure D19. ITS-3 post-experiment wall bending mode at 421 Hz.

APPENDIX E

DISPLACEMENT ANALYSIS PLOTS

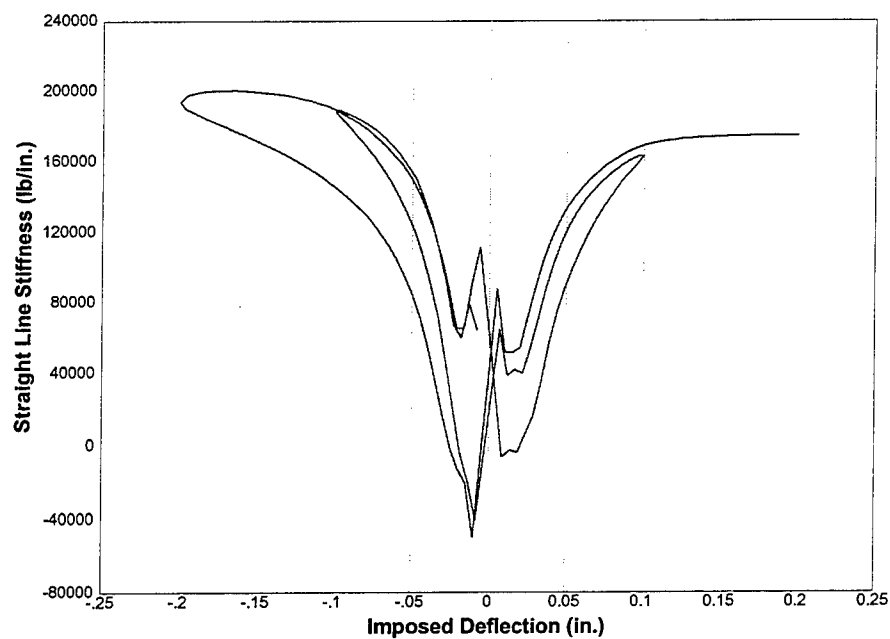


Figure E1. Initial stiffness of ITS-2 structure generated from imposed deflection and measured load.

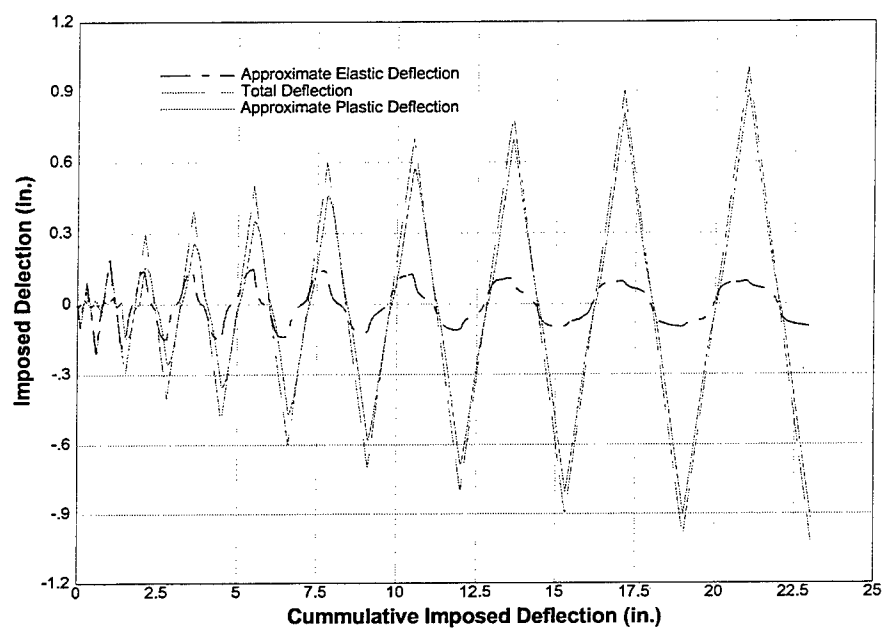


Figure E2. ITS-2 plastic deflection approximated by subtracting estimated elastic from total deflection.

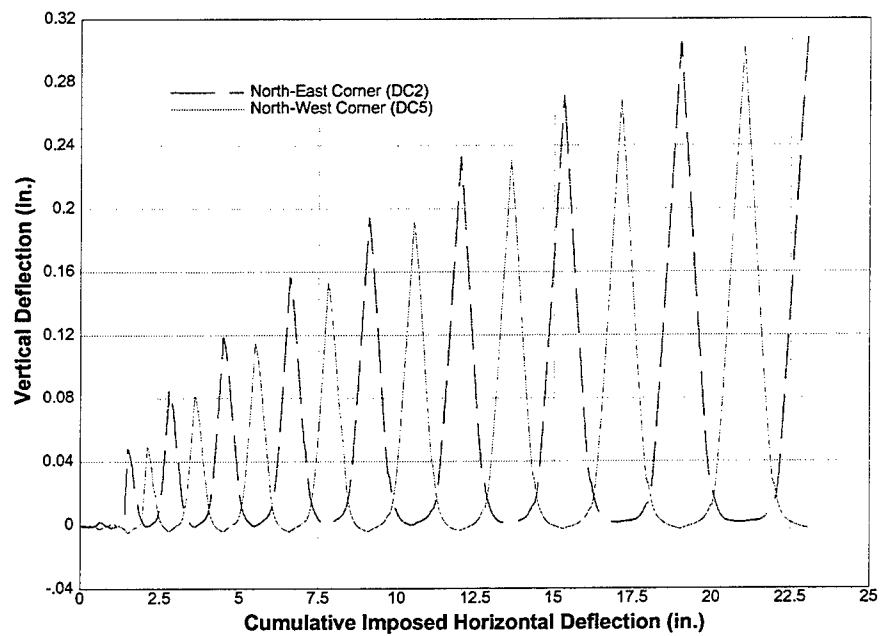


Figure E3. Vertical deflection measured at base of ITS-2 model.

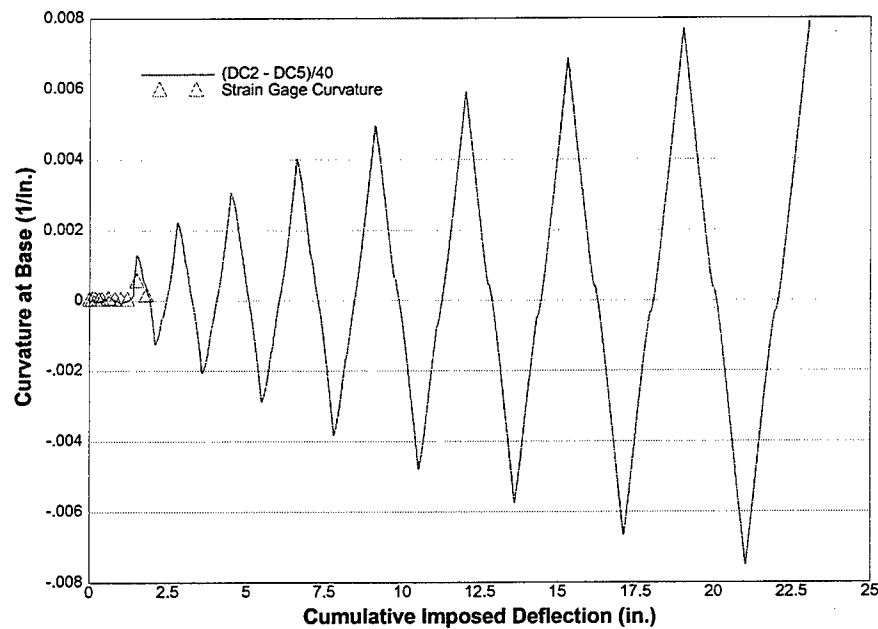


Figure E4. Curvature at base of ITS-2 model calculated from vertical deflections and internal strains.

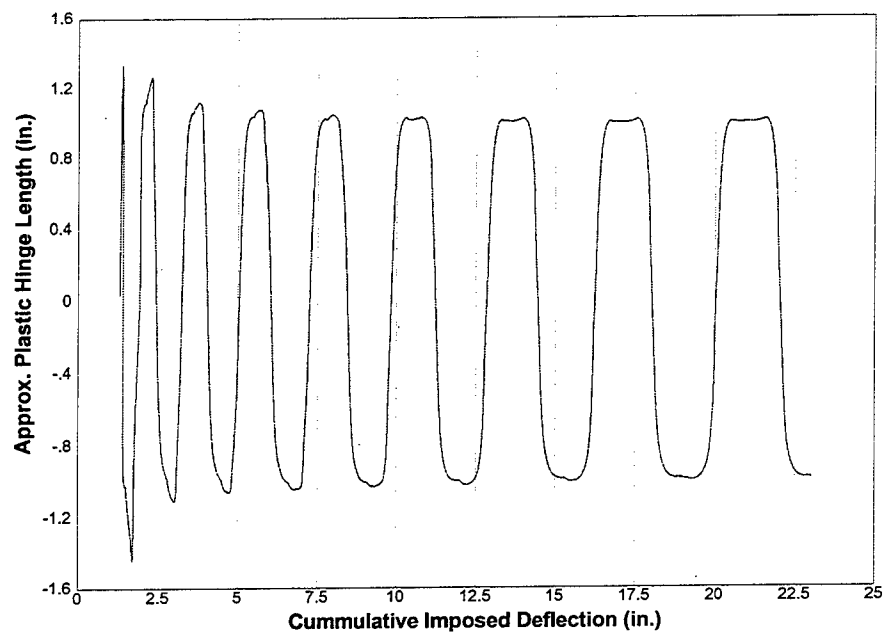


Figure E5. Plastic hinge length, calculated from experimental elastic and plastic deflection and curvature.

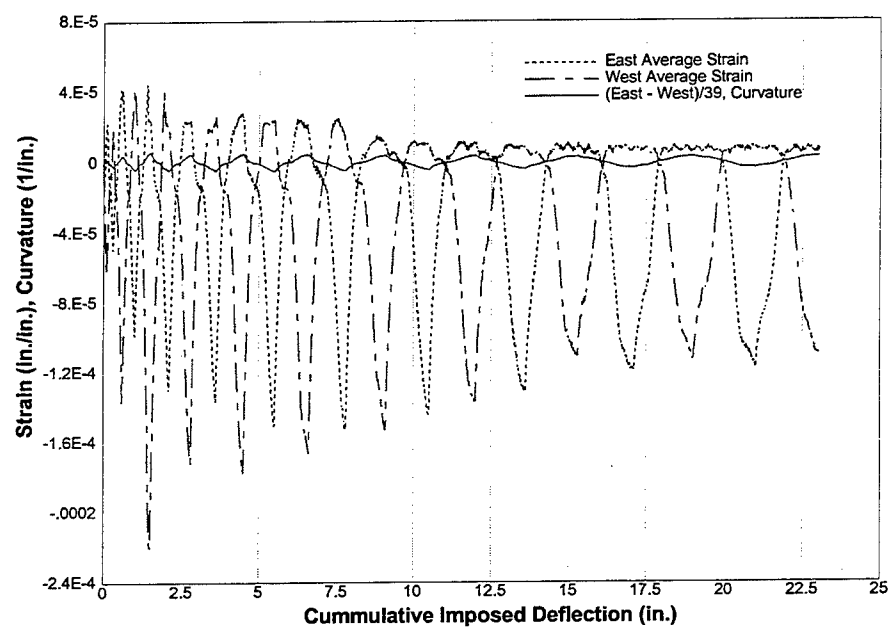


Figure E6. Section curvature generated from vertical strains at a 6 in. elevation.

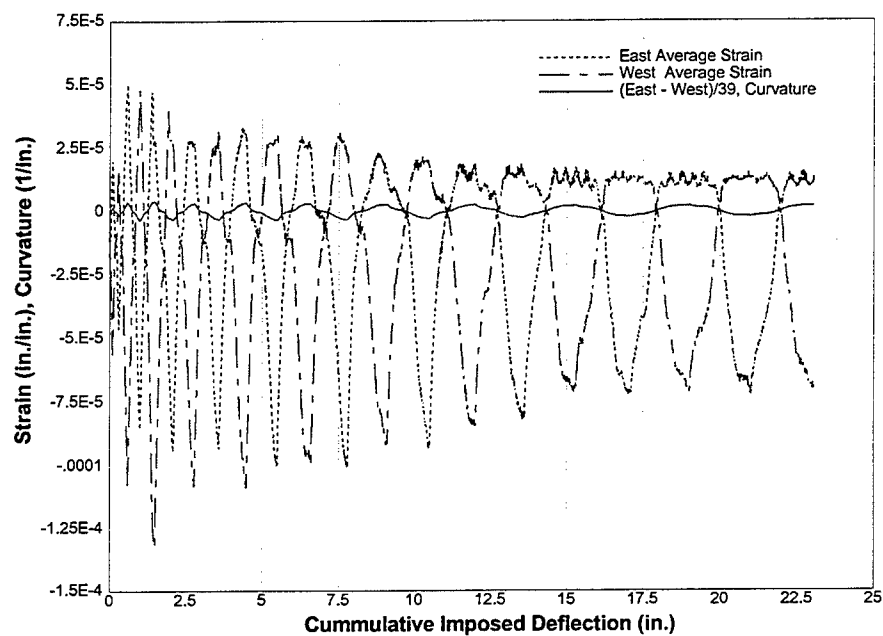


Figure E7. Section curvature generated from vertical strains at a 12 in. elevation.

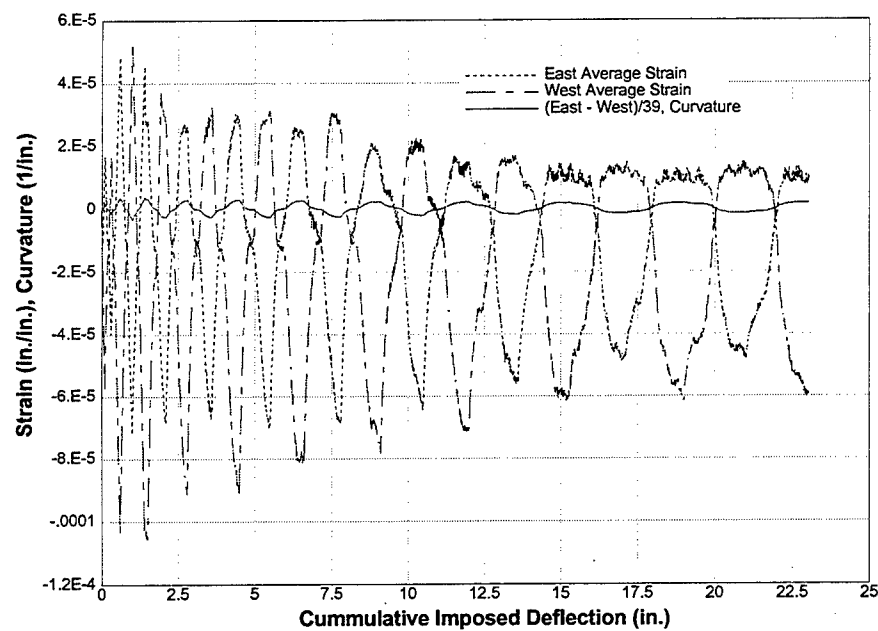


Figure E8. Section curvature generated from vertical strains at an 18 in. elevation.

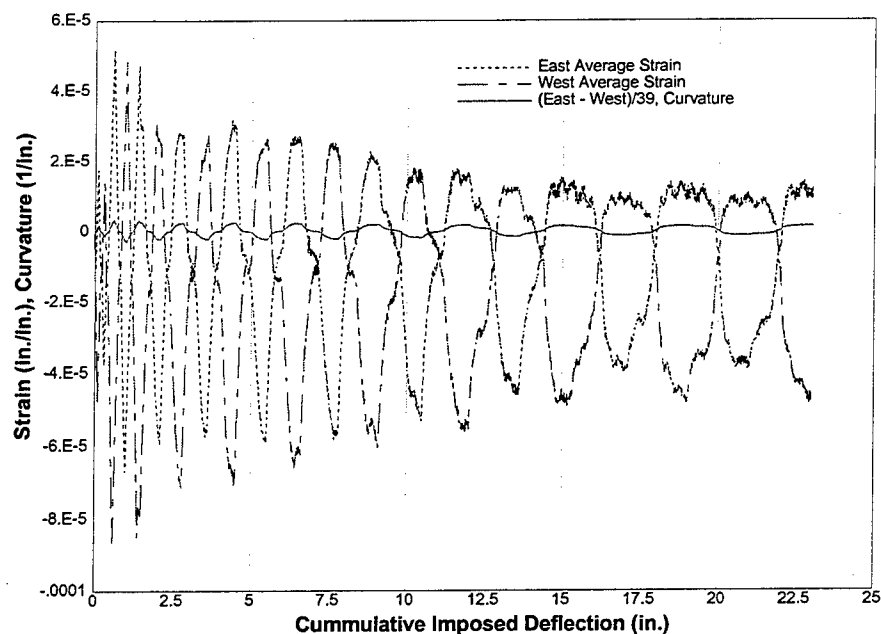


Figure E9. Section curvature generated from vertical strains at a 24 in. elevation.

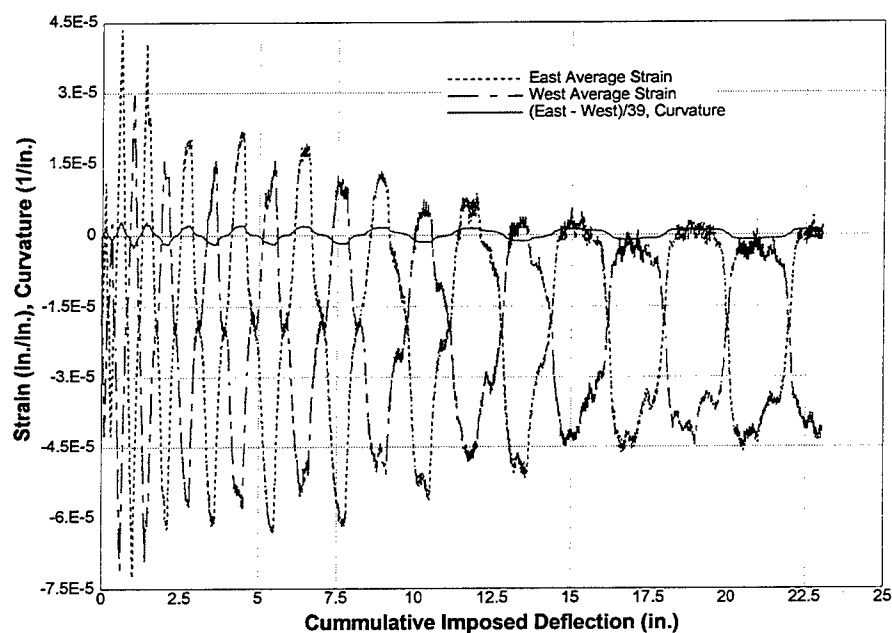


Figure E10. Section curvature generated from vertical strains at a 48 in. elevation.

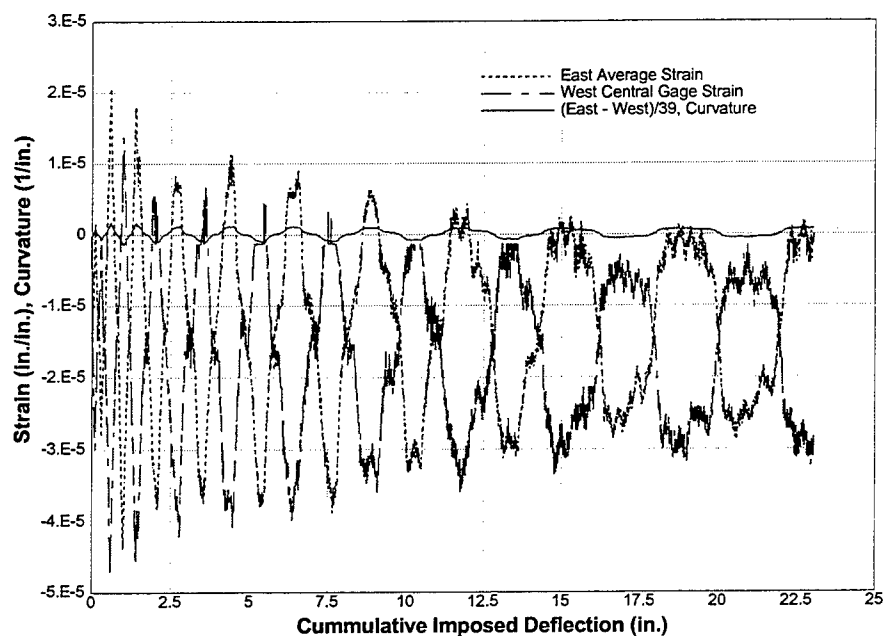


Figure E11. Section curvature generated from vertical strains at a 72 in. elevation.

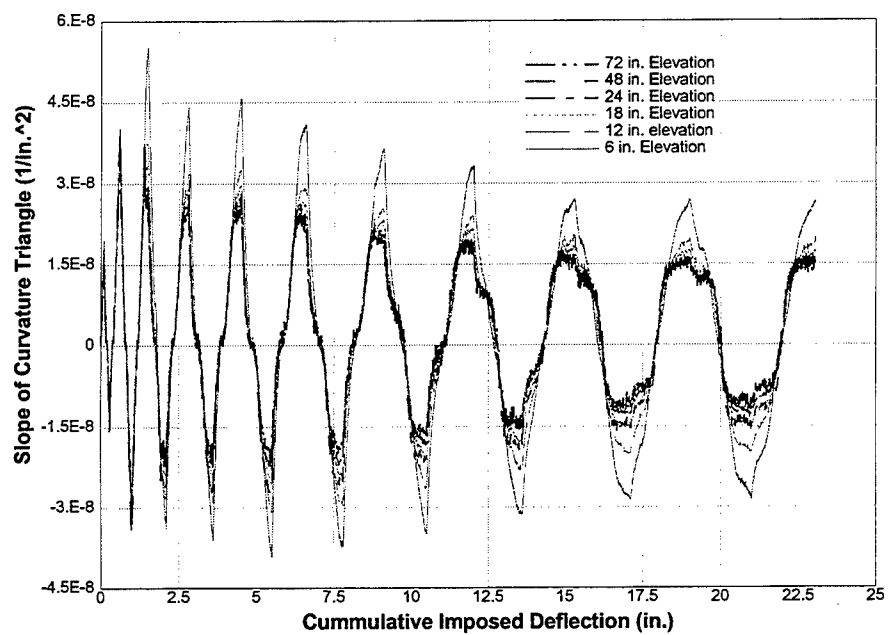


Figure E12. Slope of the curvature triangle at various elevations.

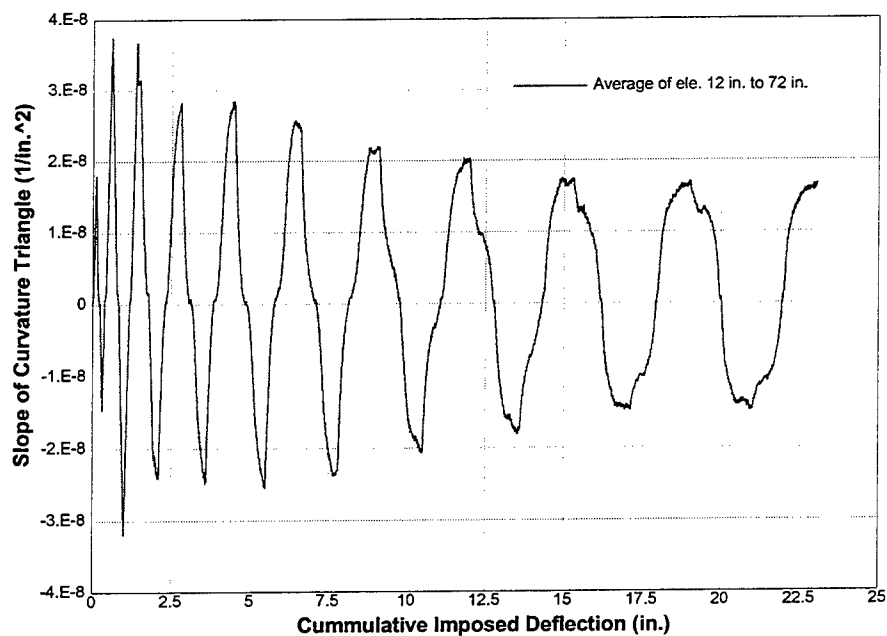


Figure E13. Average slope of the curvature triangle for 12 in. to 72 in. elevations.

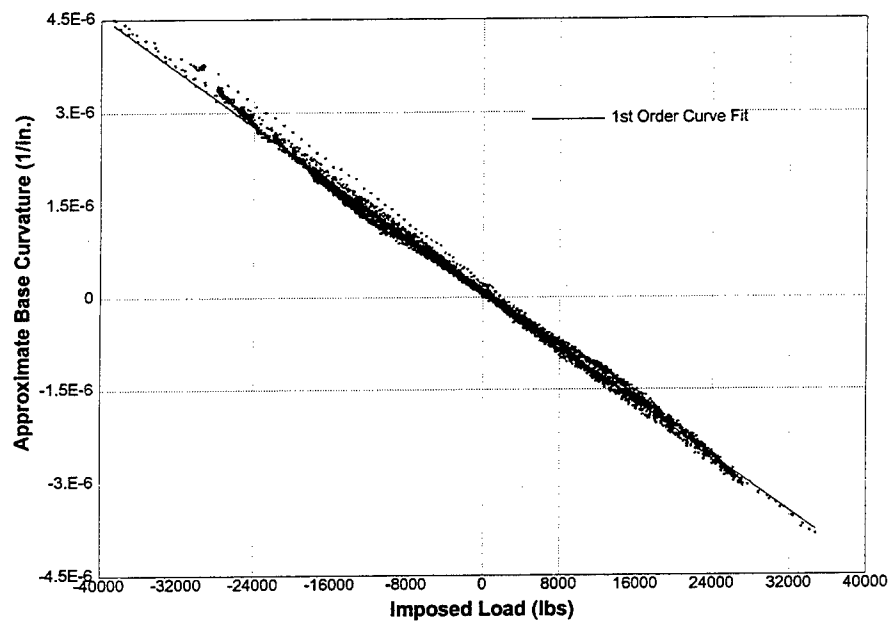


Figure E14. Curvature at the base of ITS-2 as derived from the estimated initial structural stiffness.

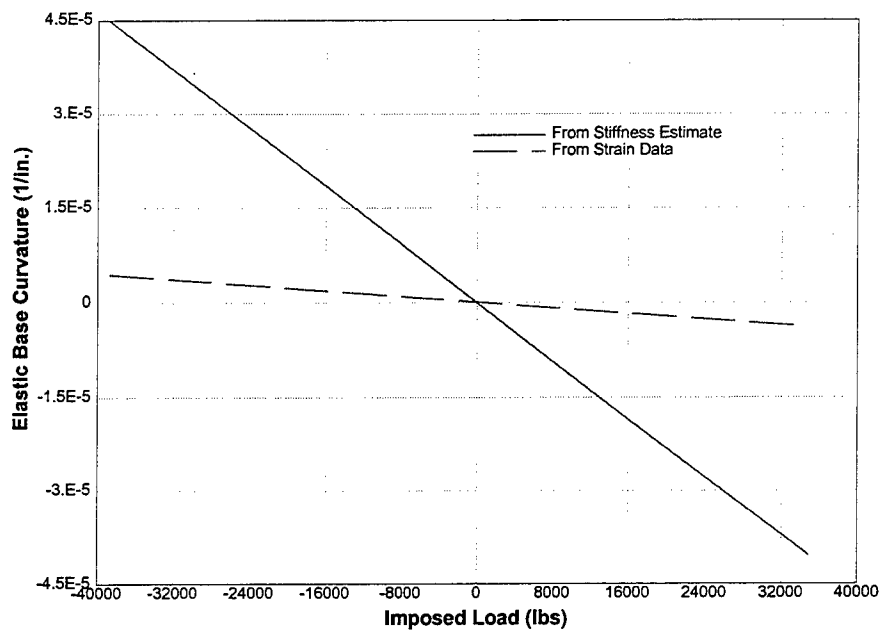


Figure E15. Curvature at the base of ITS-2 as derived from the estimated initial structural stiffness compared to that derived from body strain measurements.

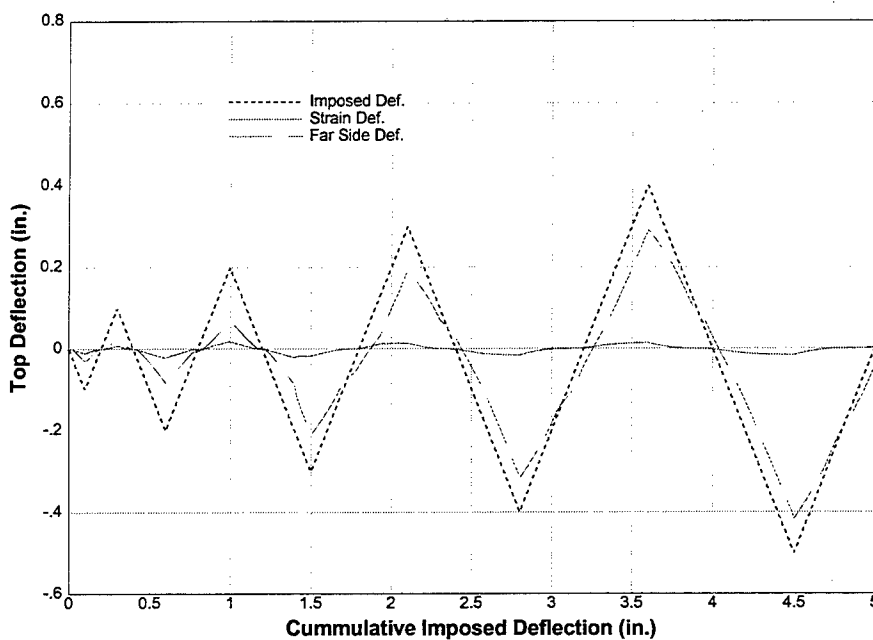


Figure E16. Comparison of imposed and measured horizontal deflections to the deflection calculated from the strains measured in ITS-2 model.

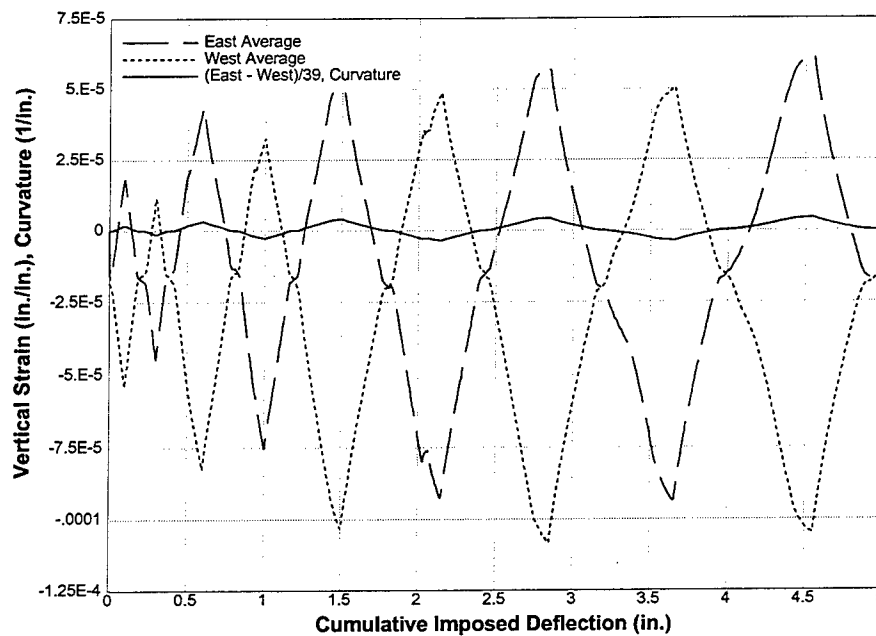


Figure E17. ITS-3 section curvature generated from vertical strains at a 24 in. elevation.

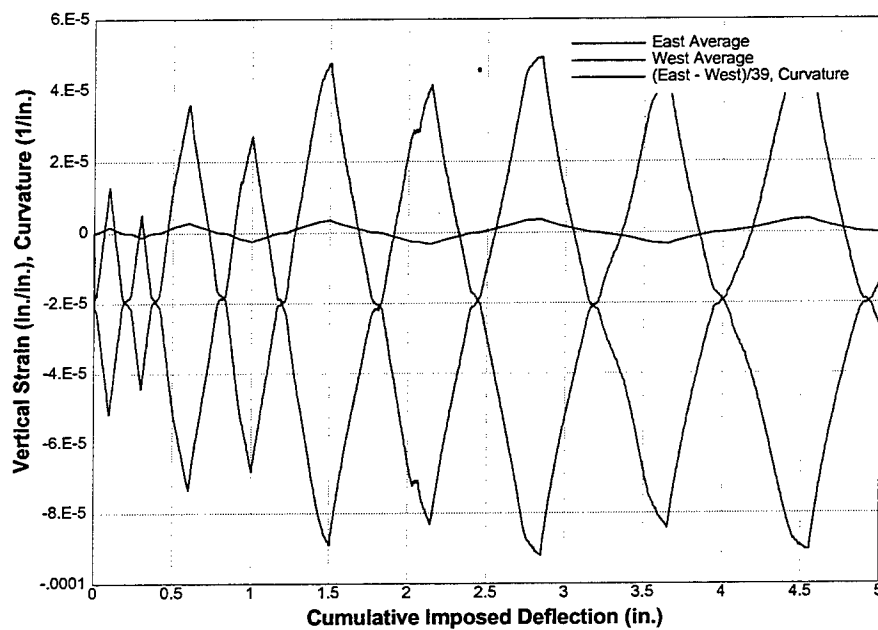


Figure E18. ITS-3 section curvature generated from vertical strains at a 48 in. elevation.

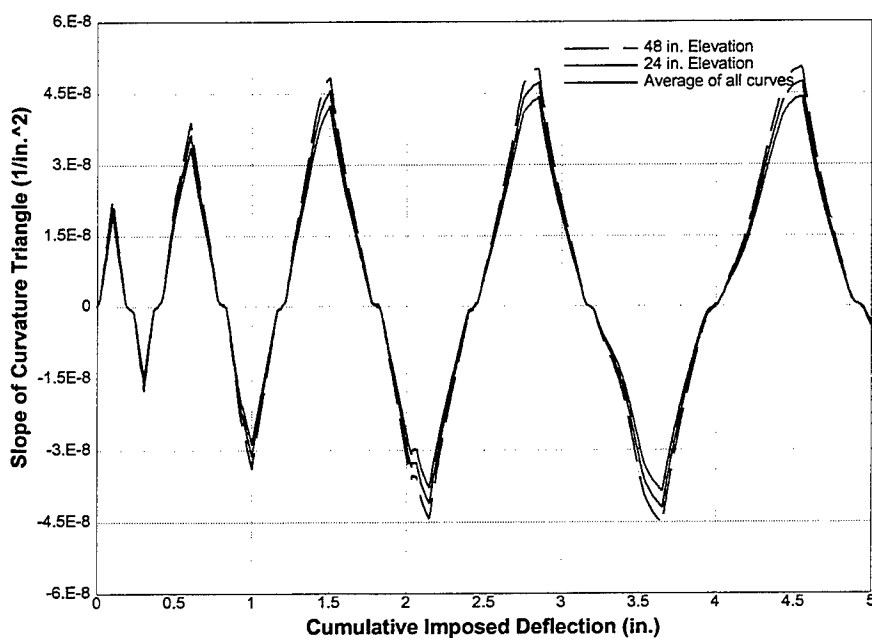


Figure E19. ITS-3 average slope of the curvature triangle for 24 in. and 48 in. elevations.

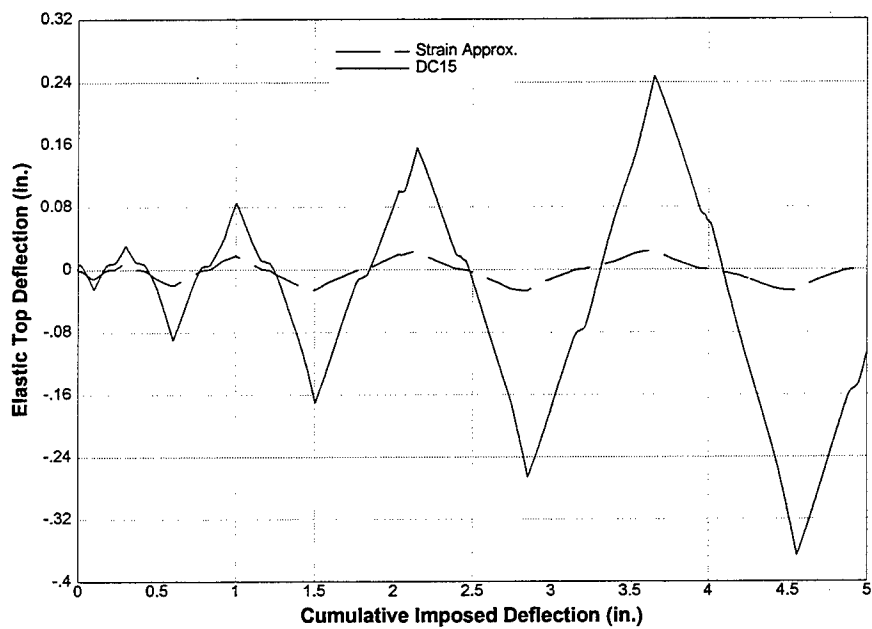


Figure E20. Comparison of imposed and measured horizontal deflections to the deflection calculated from the strains measured in ITS-3 model.

REPORT DOCUMENTATION PAGE

Form Approved
OMB No. 0704-0188

Public reporting burden for this collection of information is estimated to average 1 hour per response, including the time for reviewing instructions, searching existing data sources, gathering and maintaining the data needed, and completing and reviewing the collection of information. Send comments regarding this burden estimate or any other aspect of this collection of information, including suggestions for reducing this burden, to Washington Headquarters Services, Directorate for Information Operations and Reports, 1215 Jefferson Davis Highway, Suite 1204, Arlington, VA 22202-4302, and to the Office of Management and Budget, Paperwork Reduction Project (0704-0188), Washington, DC 20503.

1. AGENCY USE ONLY (Leave blank)		2. REPORT DATE March 1998	3. REPORT TYPE AND DATES COVERED Final report													
4. TITLE AND SUBTITLE Performance of Lightly Reinforced Concrete Intake Towers Under Selected Loadings			5. FUNDING NUMBERS Research Program 387 Work Unit 32911													
6. AUTHOR(S) Richard Charles Dove																
7. PERFORMING ORGANIZATION NAME(S) AND ADDRESS(ES) U.S. Army Engineer Waterways Experiment Station 3909 Halls Ferry Road Vicksburg, MS 39180-6199			8. PERFORMING ORGANIZATION REPORT NUMBER Technical Report SL-98-1													
9. SPONSORING/MONITORING AGENCY NAME(S) AND ADDRESS(ES) U.S. Army Corps of Engineers Washington, DC 20314-1000			10. SPONSORING/MONITORING AGENCY REPORT NUMBER													
11. SUPPLEMENTARY NOTES Available from National Technical Information Service, 5285 Port Royal Road, Springfield, VA 22161.																
12a. DISTRIBUTION/AVAILABILITY STATEMENT Approved for public release; distribution is unlimited.			12b. DISTRIBUTION CODE													
13. ABSTRACT (Maximum 200 words) <p>In the event of an earthquake, it is vitally important that the catastrophic failure of a dam and subsequent sudden release of the reservoir be prevented. An important part of the prevention of such a failure is maintaining the ability to control the release of water after the earthquake. For most earthen dams, and some concrete dams, the release of water is controlled through a reinforced concrete intake tower. Most existing intake towers are very lightly reinforced. The functional survival of such lightly reinforced towers is the main concern of this research effort. The ultimate objective of this research was the evaluation and/or development of approximate or simplified analysis procedures for the evaluation of the ductility of existing intake towers. The first phase of the research was a statistical analysis of the inventory of existing intake towers. This tower inventory quantified the distribution and variation of the structural characteristics of the U.S. Army Corps of Engineers' inventory of existing intake towers as related to their earthquake location hazard and assisted in the identification of possible failure mechanisms. The information generated was used in planning the second, experimental, phase of this research effort. The second phase consisted of a series of three experiments, each of which was composed of the static loading to failure of 1/8th-scale models of a typical intake tower configuration. Both cyclic and monotonic bending loads were applied to the models. Extremes encountered in existing towers. These experiments were successful in demonstrating that the scale</p> <p style="text-align: right;">(Continued)</p>																
14. SUBJECT TERMS <table border="0"> <tr> <td>Civil works</td> <td>Earthquake</td> <td>Reinforced concrete</td> </tr> <tr> <td>Deflection based analysis</td> <td>Hydraulic structures</td> <td>Seismic</td> </tr> <tr> <td>Ductility</td> <td>Intake tower</td> <td></td> </tr> <tr> <td>Earth dams</td> <td>Nonlinear response</td> <td></td> </tr> </table>			Civil works	Earthquake	Reinforced concrete	Deflection based analysis	Hydraulic structures	Seismic	Ductility	Intake tower		Earth dams	Nonlinear response		15. NUMBER OF PAGES 284	
			Civil works	Earthquake	Reinforced concrete											
Deflection based analysis	Hydraulic structures	Seismic														
Ductility	Intake tower															
Earth dams	Nonlinear response															
		16. PRICE CODE														
17. SECURITY CLASSIFICATION OF REPORT UNCLASSIFIED	18. SECURITY CLASSIFICATION OF THIS PAGE UNCLASSIFIED	19. SECURITY CLASSIFICATION OF ABSTRACT	20. LIMITATION OF ABSTRACT													

13. (Concluded).

models of typical intake towers had significant ductility available. Information on the specific response of these models was used to suggest modifications of the deflection-based analysis procedure for application to the evaluation of the ductility of existing intake towers.